A Momentum Variable Calculation Procedure for Solving Flow at all Speeds

by

Masoud Darbandi

A thesis
presented to the University of Waterloo
in fulfilment of the
thesis requirement for the degree of
Doctor of Philosophy
in
Mechanical Engineering

Waterloo, Ontario, Canada, 1996

National Library
of Canada

Acquisitions and
Bibliographic Services

395 Wellington Street
Ottawa ON K1A 0N4
Canada

Bibliothèque nationale
du Canada

Acquisitions et
services bibliographiques

395, rue Wellington
Ottawa ON K1A 0N4
Canada

Your file Votre référence

Our file Notre référence

0-612-21337-4

Canada

Abstract

The main purpose of this PhD research is to develop a numerical method for solving flow at all speeds using momentum component variables instead of the regular velocity ones. The different nature of compressible and incompressible governing equations of fluid flow generally classify the solution techniques into two main categories of compressible and incompressible methods. However, one extended purpose of this research is to develop an approach which permits incompressible methods to be extended to compressible ones using the analogy of flow equations. The proposed momentum component variables play a significant role for transferring the individual characteristics of the two formulations to each other in their adapted forms. In this regard, the two-dimensional Navier-Stokes equations are treated to solve time-dependent laminar flows from very low speeds, i.e. real incompressible flow, to supersonic flow. The approach is fully implicit and employs a control-volume-based finite-element method with momentum components, pressure, and temperature as dependent variables. The proper definitions for considering the dual role of momentum components at control surfaces plus the strong connective expressions between the variables on control volume surfaces and the main nodal values remove the possibility of velocity-pressure decoupling and allow the use of a colocated grid arrangement.

The performance of this new formulation is illustrated by solving different types of flow including incompressible and compressible (subsonic to supersonic), viscid and inviscid, and steady and unsteady options. No CFL number limit was encountered for the test models except in supersonic cases. The results demonstrate excellent performance of the flow analogy.

Acknowledgement

I would like to express my sincere appreciation to my supervisor, Professor G.E. Schneider, for his advice and guidance throughout the course of this work.

I also wish to express my thanks to my former and present office mates (Mr. R.W. Macdonald and Mr. B. Van Heyst) and the other members of the Computational Fluid Dynamics group at the University of Waterloo with whom I have been closely involved and with whom I have had many informative discussions. Special thanks are due to Mr. P. Zwart for his special help and Mr. M. Ashrafizaadeh for his many efforts to maintain the computer system for the group and to help the users, including myself.

I would like to thank the Ministry of Culture and Higher Education of Iran for the postgraduate scholarship awarded to me during the course of this study.

My deepest appreciation is extended to my wife, Fatemeh, who bravely faced the hardest period of our lives during the first half of this four-year period. The illness of our son turned our that first period into the most bitter one that we had ever seen.

Finally, I would like to dedicate this work to my parents, Hossein and Afagh, for their strong support of all of my academic endeavours, and to my children, Adel, Hamed, and Zahra.

Contents

3 One-Dimensional Investigation and Results 40

List of Tables

List of Figures

Nomenclature

A^{---}_{--}	coefficients matrix of variables in element conservation equations
A^{--}_{-}	right-hand-side vector in element conservation equations
a^{---}_{--}	coefficient matrix of ip variables in element conservation equations
C^{---}_{--}	coefficient matrix of nodal variables in integration point equations
C^{--}_{-}	vector of known values in integration point equations
c^{---}_{--}	coefficient matrix of ip variables in integration point equations
$\mathbb{C}$	Courant number, Eq.(3.30)
$\mathcal{C}$	influence coefficient matrix
c_p	specific heat at constant pressure
c_v	specific heat at constant volume
D^{--}	coefficients of elemental stiffness matrix, Eq.(4.167)
D^{-}	right-hand-side coefficients in elemental stiffness matrix, Eq.(4.167)
dS	outward normal vector to surface, Figure 2.3
E, e	total energy per unit mass at node and integration point
F, f	x-momentum (mass flux) component at node and integration point
G, g	y-momentum (mass flux) component at node and integration point
h	enthalpy per unit mass
H	distance between two plates, Figure 5.9
$\hat{\imath}, \hat{\jmath}$	unit vector of global coordinate system
J	Jacobian of transformation
$\mathbf{k}$	thermal conductivity
k, k', k''	constants or optional coefficients
L_d	diffusion length scale, Eq.(I.4)

L^{+}_{hy}	the hydrodynamic entrance length, Eq.(5.3)
$L_{up,dn}$	(up & down)stream lengths, Figure 4.2
M	Mach number
$\dot{m}$	mass flow
N_i	finite element shape functions
$\aleph$	the total number of grid nodes in solution domain
P, p	pressure at nodes and integration points, respectively
$\mathbb{P}$	Peclet number, Eq.(3.29)
q_x, q_y	heat flux components
R	gas constant
$\mathbb{R}$	momentum force
Re	Reynolds number
s	volumetric source
s_m	mass source term
s_f, s_g	x-momentum and y-momentum source terms
s_e	energy source term
S	control-volume surface area, Table 4.1
T, t	temperature at node and integration point
$U,\ u$	x-velocity at node and integration point
$V,\ v$	y-velocity at node and integration point
$\vec{V}$	velocity vector, $u\hat{i} + v\hat{j}$
V_{tot}	$\sqrt{u^2 + v^2}$
x, y	global Cartesian coordinates
X_e	the entrance length, Figure 5.9

Greek

α	weighting coefficient, see Eq.(3.52)
β	the slope of the tangent line at the boundary, Figure 4.3
Γ	efficient diffusion coefficient
γ	ratio of specific heats
$\triangle\theta$	time step
ϵ	convergence criterion
ζ	vorticity
Θ	dissipation term
θ	time
μ	viscosity
μs	micro seconds
ξ,η	local non-orthogonal coordinate system, Figure A.2
ϱ,ρ	density at node and integration point
τ	stress tensor components
σ_n,σ_t	normal and tangential surface stresses
Φ,ϕ	scalar at integration point and node
φ	stream function
Ψ,ψ	conserve quantity vector at node and integration point, Eq.(2.19)

Miscellaneous

$\mathcal{F},\mathcal{G}$	convection fluxes, Eq.(2.20)
$\mathcal{R},\mathcal{T}$	diffusion fluxes, Eq.(2.21)
$\mathcal{V}$	the area or the volume per unit depth of control volume

Subscripts

dn	indicates the downstream values, Figure 4.2
ip	integration point, Figure 2.2
e,w	integration points, see Fig.3.1
E,P,W	nodal points, see Fig.3.1
n	normal
t	tangential
up	indicates the upstream values, see Figure 4.2

Superscripts

o	previous time step value

Accents

$\dot{}$	time rate of change
$\hat{}$	convecting parameters
$\bar{}$	lagged from previous inner iteration

Acronyms

AR	aspect ratio or $\frac{A_{in}}{A_{throat}}$
bip	boundary integration points, Figure 4.3
IEC	irrotational entry condition
ip	integration points, Figure 2.1
NOI	number of iterations
RMS	Root-Mean-Square, Eq.(5.1)
SCV	sub-control-volume, Figure 2.1
S*i*,SS*i*	control-volume edge in xy plane, Figure 2.1 and Table 4.1
UEC	uniform entry condition

Chapter 1

Introduction

In this chapter, we are concerned with the general position and specific situation of this research, the purpose of this research, and its contributions. In this regard, a preliminary background is introduced in Section 1.1. It is followed by a literature review which presents the previous related works in Section 1.2. The objectives of this research are presented and discussed in Section 1.3. The outline of the thesis is presented in Section 1.4, where the progress of the subject during this investigation is discussed.

1.1 Background

This research is concerned with the branch of fluid dynamics known as *Computational Fluid Dynamics*, or CFD, i.e., computer modeling and solving of fluid flow problems, which plays an important role in aerodynamics, fluid dynamics, and heat transfer.

Prediction of fluid flow and heat transfer problems has traditionally been obtained by experimental investigations and theoretical calculations. It is apparent that the most reliable information about a physical process is often given by actual measurement. However, full scale equipment that gives more accurate results for experimental methods is expensive and often difficult to construct. The majority of fluid flow problems of interest in engineering cannot be solved analytically because of the complexity of the governing coupled partial differential equations.

In numerical methods, the differential equations are modeled by a set of algebraic equations which must be solved by computer. Fortunately, the development of numerical methods and the availability of large digital computers have enabled practical problems to be solved successfully. Indeed, CFD has made rapid progress since computers were first used as a tool in computational research. The contribution of CFD to the related sciences is remarkably high. CFD has also shown great contribution to experimental science where accurate design of experimental apparatus is necessary. Although research progress in numerical methods has been considerable, there is still room for significant progress. Almost all research in this branch is focused on not only eliminating the limitations and drawbacks of previous work but also on achieving an easy and optimum algorithm which would be capable of solving all real fluid flow and heat transfer problems. Accuracy of the results and stability of the method are two out of the many important goals in developing CFD codes.

The behavior of fluid flow from very low Mach number to hypersonic flow is not the same. Various methods have been presented for solving different flows and Mach number ranges. Most of these methods have not been successful for other ranges. Many algorithms have been developed for solving the Euler and Navier-Stokes equations. Also, different computational methods have been developed through the years to deal with compressible and incompressible flows because of the differences in the nature of these two types of flow. Recently, many works have focused on algorithms capable of solving both compressible and incompressible flows. Most of these methods employ primitive variables (velocities, pressure, and temperature) as the dependent variables.

The main objective of this research is to solve compressible and incompressible laminar flows where the dependent variables are momentum components, pressure, and temperature. Although the basic idea for turning from velocity variables to momentum variables was to explore and identify advantages while removing previous drawbacks, there are other reasons for this switch which are presented in the following sections.

A brief literature review of related works in this field is presented in the next section.

1.2 Literature Review

The literature in the CFD area is vast and it is not desirable to review it all. In this section a brief review of the relevant literature is given. All different methods in CFD have advantages and disadvantages. In some circumstances, it is very difficult to decide which outweighs the other.

CFD numerical methods are classified into different categories depending on the nature of the flow and governing equations. For example, a numerical approach may solve only compressible or incompressible, viscous or inviscid, steady or unsteady, or subsonic or supersonic flows. However, the distinction between two different flow types is sometimes so strong that it does not permit extension from one method to another. This difficulty has been experienced in extending compressible and incompressible methods to each other. The important role of density (and pressure) in the fluid governing equations has focused attention towards these two completely distinct branches of CFD. Various methods and techniques have been developed through the years to deal with each of them, but there are significant limitations for each in the range of the applicability of the other. From the mathematical viewpoint, the nature of the compressible and incompressible flow equations is also another issue which affects the development of compressible methods to solve incompressible flows. The unsteady compressible equations are parabolic-hyperbolic in nature, but the incompressible equations are of elliptic-parabolic type. This incompatibility between the nature of the equations causes computational difficulties in extending methods developed for one regime to the other. These restrictions and obstacles have prompted an increasing effort in CFD for developing codes capable of solving flows for different options including both compressible and incompressible flows. This is also the main concern in the current study.

One important and critical issue in developing codes for solving compressible and incompressible flow is the selection of the dependent variable set. There are several different options of dependent variables, but here we consider only the primitive variables. The primitive variables may include either velocity or momentum components. The distinction is immaterial for pure incompressible flow, where density is constant. However, using momentum components is very attractive for compressible flows, for several reasons. First of all, this formulation may permit existing solution methods for incompressible flows to be extended to cover the entire flow speed range. Secondly, the need to linearize the terms of the governing equations which include momentum variables is removed. For example, the conservative form of the continuity equation is preserved and it no longer needs to be linearized. Finally, mass flux is a constant parameter passing through a shock wave while velocity undergoes large changes. Using momentum components may result in fewer oscillation around certain discontinuities in the flow. These advantages will be discussed further in Section 2.4. Many of these have encouraged compressible flow solvers to use momentum components instead of velocity components.

Although our interest in this research is in solving the Navier-Stokes equations, the literature review is not restricted to Navier-Stokes methods. Methods for solving incompressible, compressible, pseudo-compressible, and compressible-incompressible flows are considered in turn.

1.2.1 Incompressible Flows

The primary difficulty in modeling incompressible flows lies in the fact that only gradients of pressure appear in the momentum equation and pressure does not explicitly show up in the continuity equation, although it is the continuity constraint that is used to determine the pressure. This difficulty may lead to decoupling in the velocity and pressure fields which creates non-physical solutions, Patankar [1]. This difficulty has led to methods like stream function-vorticity formulations which eliminate pressure from the governing equations. Although stream function-vorticity formulations have been successful for predicting two-dimensional incompressible flow, they are difficult to extend to three-dimensional flows. Alternatively, the considerable advantages of the primitive variable formulation have attracted more investigators toward developing incompressible numerical methods. The staggered grid arrangement is a well-known technique for treating the velocity-pressure decoupling in the primitive variable formulation of finite difference methods. In this technique, pressure and velocity variables are treated on two separate grids [1]. The Marker and Cell (MAC) method of Harlow and Welch [2] could be named as one of the successful pioneering works which uses primitive variables in a staggered grid arrangement.

The segregation of variables has been a well-liked technique to solve for the primitive variables implicitly. Generally speaking, segregated methods convert the indirect information in the continuity equation into a direct algorithm for the calculation of pressure. This means that they determine velocities from the solution of momentum conservation equations based on the best possible estimate of the pressure field. Then, pressure is determined from the solution of one or two Poisson-like equations. This process must be repeated for updating the velocity and pressure fields. The segregated solution can satisfy both mass and momentum conservation equations if the correcting pressures and velocities vanish. Raithby and Schneider [3], and Patankar [4] have developed methods based on the segregated approach. Using staggered grids in finite-difference segregated methods guarantees the coupling of the velocity and pressure fields [3, 4]. There are alternative methods which do not use a segregated approach. Zedan and Schneider [5] employed a Simultaneous Variable Approach (SVA), that uses the strong coupling between variables and solves all dependent variables simultaneously. In their method, the equation for pressure is obtained by substituting the momentum conservative equation, without approximation for the corresponding velocity, into the mass conservation equation.

Since the innovation of control-volume methods in CFD, there have been considerable efforts to use these in solving fluid flow problems including incompressible ones. The main advantage of these schemes is the conservation of the conservative quantities in each finite control volume. Most of the control-volume-based methods return to the original work of Patankar and Spalding [6] which is based on a pressure correction technique. They employed a semi-implicit segregated scheme, the Semi-Implicit Method for Pressure-Linked Equations (SIMPLE), which requires a heavy under-relaxation for the pressure correction to ensure convergence of the solution. A number of improved variants of the original SIMPLE algorithm including SIMPLER were later developed for solving incompressible flows [4]. The SIMPLE-based methods generally use staggered grid arrangement.

Contrary to a staggered grid arrangement in control-volume methods, it is the colocated grid arrangement which needs special treatment for the coupling of velocity and pressure. Colocated grid arrangements are mainly non-segregated. The main idea in a colocated arrangement is to consider the role of pressure as an active parameter in the continuity equation to remedy the decoupling. There are different approaches for removing the checkerboard problem in a colocated grid. Baliga and Patankar [7] used unequal order velocity-pressure interpolation to remove the decoupling problem in their control-volume-based finite-element method. Unequal-order means, pressure is computed at much fewer grid points than velocity. Prakash and Patankar [8] also developed a non-segregated approach using a control-volume-based finite-element method with equal-order velocity-pressure interpolation. Rhie and Chow [9] proposed a new technique for removing the decoupling of velocity and pressure in their colocated grid approach for solving incompressible flows. Their technique includes a new method for treating the convected terms at control volume surfaces. These terms are interpolated between main grid points. Schneider and Raw [10, 11] used a colocated grid approach in their control-volume-based finite-element method which considers the physical influence aspects of the flow in integration point equations. Later, Schneider and Karimian [12] showed that this derived formulation cannot guarantee the coupling of velocity and pressure under certain circumstances. Consequently, they proposed a second integration point velocity variable in order to remove the deficiencies of the previous formulation. With this remedy, a strong coupling between pressure and velocity was obtained and the checkerboard problem was totally removed. Darbandi and Schneider [13] have also investigated the checkerboard problem in their pressure-based momentum-component procedure. They remove the decoupling problem by introducing a second momentum-component variable at the control volume surface in their colocated grid arrangement.

Peric, Kessler, and Scheuerer [14] present a detailed comparison of two finite-volume solution methods for two-dimensional fluid flows, one with a staggered and the other with a colocated numerical grid. They show that the colocated scheme generally represents more advantages.

1.2.2 Compressible Flows

Compressible flows can be mainly divided into steady and unsteady methods. Most of the steady methods use the unsteady governing equations to integrate over time to reach steady flow conditions. Absolute steady methods are mainly space marching methods. The space marching method is used for solving equations which are parabolic in at least one spatial direction, the marching direction. Alishahi and Darbandi [15] solved supersonic flow for wing-body configuration problem by marching in centerline direction and using discrete zonal approach.

Unsteady methods are divided into explicit and implicit methods. Explicit schemes are subject to one or more stability restrictions on the temporal and spatial step sizes. These restrictions are usually given in terms of a Courant-Friedrich-Lewy (CFL) and viscous stability condition, which limits the time step. A number of early methods such as Palumbo and Rubin [16] implemented a two-step Lax-Wendroff scheme which advanced the solutions through time explicitly. MacCormack [17] forwarded an important progress in explicit methods by introducing a predictor-corrector finite-difference algorithm to solve Euler equations. The inclusion of artificial viscosity in this algorithm has enabled it to solve flows with shock. Modifications have been done on this explicit Euler algorithm, which severly suffers from the stiffness of the discrete Navier-Stokes approximation, to solve for viscous flow, e.g. MacCormack [18]. The method of Ref. [18] consists of two steps. The first step is an explicit predictor-corrector finite difference stage and yields second order accuracy in time and space. The second step is an implicit stage. The second step removes the sever stability limitation of the first explicit method step.

Many advantages of implicit formulations have generally shifted interests toward these schemes. There are several important implicit schemes that use a finite-difference formulation. Beam and Warming [19, 20] treated the conservation form of the governing equations by an ADI based approximate factorization formulation to produce a block tridiagonal linear system of equations. Density, momentum components, and total energy are dependent variables in their method. Shamroth, McDonald, and Briley [21] changed the momentum components to velocity ones. Briley and McDonald [22] presented another implicit approximate factorization method for solving the Navier-Stokes equations. The addition of artificial diffusion is required for stability of their method and to catch shock waves. Indeed, the handling of boundary conditions becomes more severe when approximate factorization is used to break a multidimensional problem into a set of one-dimensional problems. Since the innovation of finite-element methods, there have been parallel works for solving compressible flows using finite-element schemes. For example, Baker and Soliman [23] presented an implicit finite-element algorithm to solve compressible flows.

Besides the progress of control-volume methods for incompressible flows, there have been many attempts to develop SIMPLE-based incompressible methods into compressible one. One method was developed by Issa and Lockwood [24] who used an approximate form of the momentum equation to relate velocity corrections to pressure corrections in an staggered grid arrangement. Expressing continuity in terms of density and velocity corrections, these relations can then be used to determine an equation for pressure correction. Han [25] has also tried to extend the SIMPLE procedure for compressible flow calculations. However, details of flow discontinuities were not captured well due to excessive numerical smearing in Refs. [24, 25]. More related works are presented in Section 1.2.4.

Most of the schemes for compressible flow use density as a primary dependent variable and extract pressure from an equation of state, e.g. [18]. Since the role of density at low Mach numbers is very small, this approach cannot be used for incompressible flows as it is discussed in Section 1.2.3. There are also many other factors for each compressible method that prevent the use of these algorithms for low Mach numbers. Methods that use pressure as a primary dependent variable do not have the difficulties of the density-based methods because the change of pressure is always finite, irrespective of the flow Mach number. Therefore, it is possible to modify pressure-based methods to cover the entire spectrum of Mach numbers. Rhie [26] has presented a pressure-based segregated method for solving Navier-Stokes equations in compressible flows. This method is an extension of his previous incompressible methods [9]. He uses a multi-step pressure correction procedure, with implicit treatment of density, to correct the pressure field.

1.2.3 Pseudo-Compressible Flows

There are various design applications, such as automobile, ship, and turbomachinery design which typically solve very low speed flows using compressible algorithms.

Moreover, compressible algorithms are also important in the field of heat transfer where density has significant changes. As said in the previous sub-sections, the difference in nature between incompressible and compressible flows has spawned various computational schemes to be developed to treat these two types of flow. In the case of compressible flows, methods have been developed that use density as a primary variable. Such methods are known as density-based methods [18, 20]. Contrary to density-based methods, there are pressure-based ones which use pressure as a primary variable instead of density in the incompressible flow cases [10, 26, 27, 28].

If it is realized that the incompressible governing equations are derived from compressible ones, it is reasonable to recognize slightly compressible flow as being constructed from the incompressible one. Van Dyke [29] states that slightly compressible flow is a regular perturbation of incompressible flow. This promotes the idea of solving low speed flows using either compressible or incompressible algorithms. There are works which extend the original transonic flow solvers to low Mach number applications [30, 31]. On the other hand, there are works which are the extension of incompressible schemes and solve for compressible flows [28, 32, 33].

The simultaneous solution of the governing equations in compressible methods enhances the stability compared with the segregated approaches of the incompressible techniques, Merk et al [34]. This has encouraged many incompressible investigators toward using compressible algorithms in applications [35]. However this intention in switching encounters some major drawbacks. The speed of sound approaches infinity in the incompressible limit; implementing compressible codes for simulating incompressible flows is not computationally efficient. The hyperbolic time-dependent Navier-Stokes equations become *stiff* at low Mach numbers because of the great difference between the largest and the smallest magnitudes of the system eigenvalues, Feng and Merkle [36]. Since the eigenvalues are the speeds of the waves carrying information, one class of information related to the smallest one would be slowly transported within the region, while the time step is limited by the speed of the fastest traveling wave. Nevertheless, the number of time steps needed to reach the steady-state solution will approach infinity for an incompressible algorithm. Hence, convergence to a steady-state solution is usually slow and for time-dependent solutions the permitted time step becomes very small. This is why most compressible algorithms become either very inefficient or inaccurate at low Mach number speeds. Briley et al [37] rescale the equations to improve the convergence, however, the performance and the accuracy of their time-dependent compressible schemes are inadequate at low Mach numbers, say M_∞ <0.1. Volpe [30] compares the results of three widely-used two-dimensional compressible codes of which two are Euler codes, using finite-volume scheme, and the other is a Navier-Stokes solver, using a finite-difference scheme. These codes are examined for simple-low speed test cases with the solution accuracy enhanced by reducing the mesh-size. This reduction in turn causes deterioration of the convergence rates.

There are methods to overcome the difficulty of using a compressible scheme to solve for incompressible flows. One method is *preconditioning* which modifies the time term. This can be made to appear as a new matrix multiplying the time term in the vector form of the system of equations, Pletcher and Chen [38]. For steady problems, preconditioning is achieved by altering the physical time-derivative terms in the equations. On the other hand, for unsteady problems, an additional *pseudo-time* term of a particular form is added to the equations, which changes the nature of the hyperbolic problem which is being advanced in pseudo time. Chorin [39] and Steger and Kutler [40] used artificial compressibility in solving the mass conservation equation. They fabricated a hyperbolic time-dependent system of equations by adding a time derivative of the pressure term to the continuity equation. Kwak et al [41] developed a code using pseudocompressible methods to compute specifically incompressible flows. Choi and Merkle [42] similarly used a small time step to overcome the difficulties of low Mach number speeds in their implicit factorization scheme.

Merkle and Choi [43] used asymptotic expansions of the Euler equations in their *perturbation method* to solve for low Mach numbers. They added an artificial time derivative term to the energy equation. Perturbation schemes become inefficient when the Mach number is not very low. Another method for solving low Mach number flows is *flux-vector splitting method* which treats the stiff terms not only differently in time but also in space [44].

In addition to the three presented methods which focus on low Mach number flows, there are compressible-incompressible and all-speed-flow methods which solve for both incompressible and a wide range of compressible flows [32, 33, 45]. However there are few researchers who report the performance of their methods in solving very low Mach number problems, e.g. Chen and Pletcher [45]. Following the methods for solving both compressible and incompressible methods, Darbandi and Schneider [46] developed an analogy based on momentum component variables which enables existing incompressible methods to be extended to solve for compressible flows. The performance of the resulting method was illustrated by applying to various test cases from very low to transonic Mach numbers.

1.2.4 Compressible-Incompressible and All-Speed Flows

There are few numerical methods which are applicable to both incompressible and compressible flows. The idea of solving for all flow speeds with just one algorithm, however, is not new. The important question is how to consider the dual role of pressure in compressible and incompressible flows. Generally speaking, the idea of solving flow at all speeds has been studied using different approaches including finite-element, finite-difference, and control volume methods. The search for an algorithm suitable for all speeds goes back to the work of Harlow and Amsden [47]. They extended the MAC method for solving time dependent fluid flow problems for all Mach numbers. Their method suffers from a stability restriction and its scope of applicability is limited. Zienkiewicz, Szmelter, and Peraire [48] presented a semi-implicit algorithm for the calculation of both compressible and incompressible flows using a finite-element approach. Zienkiewicz and Wu [49] later developed this finite-element algorithm into a general explicit and semi-explicit method. However, their work is restricted to relatively low supersonic Mach numbers because the use of the non-conservative form of the equations may lead to inaccurate shock prediction. Hauke and Hughes [31] have similarly worked in finite-element context to develop their original compressible method to solve for incompressible limits.

The advantages of control-volume-based methods have encouraged recent work using this approach. Most of the control-volume-based methods for flow at all speeds return to the incompressible work of Patankar and Spalding [6] which is based on a pressure correction technique. Van Doormal, Raithby, and McDonald [50] have shown that a pressure-based method can be extended to include compressible flows. They used modified versions of the SIMPLE code with a staggered grid arrangement. Karki and Patankar [32] presented another control-volume-based finite-difference method which is based on the compressible form of the SIMPLER algorithm. The steady-state form of the Navier-Stokes equations was solved in a staggered grid arrangement with generalized non-orthogonal coordinates. Their method suffers from sensitivity to grid smoothness which is due to the presence of the curvature terms in the equations. Demirdzic, Lilek, and Peric [51] employed Cartesian based vectors instead of locally fixed based vectors of Karki et al [32], and removed the sensitivity to grid smoothness. Shyy, Chen, and Sun [52] have also developed a similar procedure for flow at all speeds using a multigrid algorithm. Lien and Leschziner [53] have included the turbulent effects in their control-volume based method for solving compressible and incompressible flows.

Chen and Pletcher [45] presented a colocated pressure-based technique for solving the time-dependent Navier-Stokes equations applicable to low Mach numbers. They found that smoothing was not needed to control oscillations in pressure for subsonic flows despite the use of central differences in their finite difference approach. Raw, Galpin, and Raithby [54] have presented a colocated control-volume method to solve compressible and incompressible flow fields. Special integration point equations were derived at control volume surfaces to connect them to neighboring nodal values. Since the pressure of other nodal points also appear in their formulation they change them to lagged values. Karimian and Schneider [33] used the approach of Ref. [50] and developed the incompressible work of Ref. [10] to solve for compressible flows.

Most of the all-speed methods are extensions of incompressible methods to compressible flows, e.g. [32, 33, 50, 52]. Hence, they apply the incompressible primitive variables, i.e., velocity components, as the dependent variables for extending their work to compressible flows. The main objective of this work is to use the momentum components as the unknown variables. The idea of using momentum component variables instead of velocity variables was introduced by Darbandi and Schneider [13, 55]. They also examine the performance of their momentum-component formulation in the context of a flow analogy for solving flow at all speeds [56]. Their implicit scheme is based on a colocated grid arrangement.

1.3 Objectives of this Research

To derive numerical solutions for the nodal values of the dependent variables, it is necessary to develop algebraic relations which approximate the governing differential conservation equations. While no single method yet contains all desirable features while being void of disadvantages, the following attributes and features are sought in the present formulation:

1. *Control Volume Basis*

   Since the fluid flow governing equations are intrinsically conservative it is preferable to use numerical methods that retain this property. Control-volume-based approaches have two major advantages. Firstly, they allow exact numerical conservation of the conserved quantities in each finite control volume. This means that mass, momentum, and energy are exactly conserved over any number of control volumes and consequently over the entire fluid flow domain. Secondly, they provide a physically meaningful interpretation of the various terms such as fluxes and source terms in the discretized form of the governing equations.

2. *Finite Element Method*

   The finite-element concept generally returns calculus and vector field theory to the construction of discrete simulation algorithms. The most important advantage of the finite element method is its great flexibility for handling highly complex solution domains. In the finite element method, the variation of dependent variables consists of grid point values and interpolation between them.

3. *Momentum Components as Dependent Variables*

   This formulation may permit existing solution methods for incompressible flows to be extended to cover the entire flow speed range. The need for linearizing the terms of the governing equations which include momentum variables is removed. For example, the conservative form of the continuity equation is preserved and it no longer needs to be linearized. Mass flux does not change through shock waves in supersonic flows and this may cause less oscillations around discontinuities in the solution.

4. *Pressure as a Dependent Variable*

   Pressure is selected as a dependent variable in preference to density because the pressure changes are finite at all flow speeds as opposed to the density changes which become very small at low Mach numbers. Therefore, pressure-based methods can be extended to solve incompressible flows.

5. *Colocation of Dependent Variables*

   The use of a non-staggered grid arrangement may produce a wavy non-physical pressure field while still satisfying the discrete momentum equations. The geometrical simplicity of the colocated grid arrangement is very attractive and it will be significant if the cause of the pressure oscillation can be removed. Boundary condition implementation difficulty and excessive book-keeping are two major objections to staggered grid methods. In addition, the velocities that satisfy mass do not necessarily conserve momentum in the same control volume. However, the use of one velocity field, instead of two velocity fields which are used in colocated grid methods, is an advantage of staggered grid method.

6. *Fully Implicit Formulation*

   Although explicit methods are relatively simple to set up, they need very small time steps to maintain stability. Conversely, the stability of the implicit methods can be maintained over much larger time steps. Large time steps may reduce accuracy of the transient solution, however, this is not important if only the steady-state solution is desired. In contrast to segregated methods, all dependent variables are solved simultaneously in our *fully* implicit formulation. This reduces the need for tracking the solution of dependent variables through sequential iteration or time step advancement.

1.4 Thesis Outline

A numerical method calculates the values of the dependent variables at a finite number of locations, named *grid points*, in the calculation domain. To calculate the domain variables on grid points, it is necessary to discretize the governing equations. A discretized equation is an algebraic relation that connects the values of the dependent variables for a group of grid points. The development of an algebraic representation of equations includes a number of steps.

First, the differential equations to be modeled and the dependent variables to be used must be determined. This task is accomplished in Chapter 2. In addition, the research motivation is another issue which is discussed in this chapter. Second, the domain must be discretized. Chapter 2 describes the control volume approach and Appendix A presents the finite-element formulations which are used to expand the necessary geometry relationships. Third, the algebraic representation which approximates the differential equations must be developed. This duty is elaborated in two chapters. In Chapter 3, a preliminary investigation is done in a one-dimensional context in order to avoid unnecessary multi-dimensionality complexities, to discover and study the deficiencies of the formulation, and to solve them with appropriate techniques. For example, the pressure-velocity decoupling issue is one which is considered in this chapter. The extension to two-dimensional modeling is accomplished in Chapter 4 to further illustrate points and demonstrate applicability to multi-dimensional flows. The developed method is examined for several different test models in Chapter 5. The test models try to cover the entire range of flow speed conditions. The final chapter, Chapter 6, is where the major contributions and conclusions of this work are summarized and where the recommendations for future work are presented.

Chapter 2

Governing Equations and Research Motivation

The main purpose of this chapter is to introduce the governing equations, to present the method for discretizing the solution domain, and to provide the research motivation. The general form of the governing equations is introduced in Section 2.1. In Section 2.2, the discretization of the solution domain is briefly explained. The options for dependent variables are presented in Section 2.3, together with a discussion on the roles of pressure and density in compressible and incompressible flows. The motivation for the current research is that choosing momentum variables has a number of conceptual advantages over velocity components; This is discussed further in Section 2.4.

2.1 Governing Equations

The differential equations governing the conservation of mass, momentum components, energy, and other scalars such as mass fraction and turbulence of kinetic energy can be cast into a general form as, Patankar [1],

$$\frac{\partial}{\partial\theta}(\rho\phi) + \nabla\cdot(\rho\vec{V}\phi - \Gamma\nabla\phi) = s \tag{2.1}$$

where ϕ is a general dependent variable and s denotes the volumetric source (or sink) of ϕ. The two terms inside the parenthesis represent convective and diffusive fluxes respectively. The cases where ϕ represents mass, momentum, and energy are of particular interest. Assume a Newtonian fluid, with constant viscosity and conductivity, and which obeys Stokes' law, the two-dimensional Cartesian form of these equations is

$$\left\{\frac{\partial\rho}{\partial\theta}\right\} + \frac{\partial(\rho u)}{\partial x} + \frac{\partial(\rho v)}{\partial y} = s_m \tag{2.2}$$

$$\frac{\partial(\rho u)}{\partial\theta} + \frac{\partial(\rho uu)}{\partial x} + \frac{\partial(\rho vu)}{\partial y} + \frac{\partial p}{\partial x} = \frac{\partial\tau_{xx}}{\partial x} + \frac{\partial\tau_{yx}}{\partial y} + s_f \tag{2.3}$$

$$\frac{\partial(\rho v)}{\partial\theta} + \frac{\partial(\rho uv)}{\partial x} + \frac{\partial(\rho vv)}{\partial y} + \frac{\partial p}{\partial y} = \frac{\partial\tau_{xy}}{\partial x} + \frac{\partial\tau_{yy}}{\partial y} + s_g \tag{2.4}$$

$$\frac{\partial(\rho e)}{\partial\theta} + \frac{\partial(\rho uh)}{\partial x} + \frac{\partial(\rho vh)}{\partial y} = \frac{\partial(u\tau_{xx} + v\tau_{xy} - q_x)}{\partial x} + \frac{\partial(u\tau_{yx} + v\tau_{yy} - q_y)}{\partial y} + s_e \tag{2.5}$$

where external heat generation and body forces have been neglected. These equations are derived in many texts, e.g. [57], and are referred to as the Navier-Stokes equations. The components of the stress tensor are

$$\tau_{xx} = 2\mu\frac{\partial u}{\partial x} - \left\{\frac{2}{3}\mu\left(\frac{\partial u}{\partial x} + \frac{\partial v}{\partial y}\right)\right\} \tag{2.6}$$

$$\tau_{xy} = \tau_{yx} = \mu\left(\frac{\partial u}{\partial y} + \frac{\partial v}{\partial x}\right) \tag{2.7}$$

$$\tau_{yy} = 2\mu\frac{\partial v}{\partial y} - \left\{\frac{2}{3}\mu\left(\frac{\partial u}{\partial x} + \frac{\partial v}{\partial y}\right)\right\} \tag{2.8}$$

Using Fourier's laws of heat conduction, the components of heat flux in Eq.(2.5) are written as

$$q_x = -\mathbf{k}\frac{\partial t}{\partial x} \tag{2.9a}$$

$$q_y = -\mathbf{k}\frac{\partial t}{\partial y} \tag{2.9b}$$

The braces, $\{\}$, indicate those terms which vanish in the incompressible limit. In addition to the above differential equations, one auxiliary equation, the equation of state, is needed

$$\rho = \rho(p, t) \tag{2.10}$$

If the fluid is assumed to be a calorically perfect gas, the equation of state is written

$$p = \rho R t \tag{2.11}$$

The following relationships also exist for a perfect gas

$$c_p - c_v = R \tag{2.12a}$$

$$\gamma = \frac{c_p}{c_v} \tag{2.12b}$$

Although c_p, c_v, and R vary slightly with temperature, they are assumed constant in this study. If the change in potential energy is neglected, the total energy and enthalpy of the fluid per unit mass for a perfect gas are

$$e = c_v t + \frac{1}{2}(u^2 + v^2) \tag{2.13}$$

$$h = c_p t + \frac{1}{2}(u^2 + v^2) \tag{2.14}$$

Alternatively, for compressible flows at very low Mach numbers, the pressure and density become less dependent on each other and; in the idealized limit of incompressible flow, they are completely decoupled. For incompressible flow, the equation of state, Eq.(2.10), collapses to

$$\rho = \rho(t) \tag{2.15}$$

For isothermal flow, this equation is reduced to

$$\rho = \text{ constant } = \rho_o \tag{2.16}$$

In this case, the transient term in Eq.(2.2) vanishes and the continuity equation becomes

$$\nabla \cdot \vec{V} = 0 \tag{2.17}$$

Therefore, for the idealized incompressible flow case the equation of state, Eq.(2.10), is replaced by Eq.(2.16) with e given by Eq.(2.13) as for the perfect gas.

Vector Form of Governing Equations

Since the two-dimensional discretization of the governing equations is done based on the vector form of Navier-Stokes equations, it is useful to present this form of the equations here. Equations (2.2-2.5) are expressed in vector form as

$$\frac{\partial \psi}{\partial \theta} + \frac{\partial \mathcal{F}(\psi)}{\partial x} + \frac{\partial \mathcal{G}(\psi)}{\partial y} = \frac{\partial \mathcal{R}(\psi)}{\partial x} + \frac{\partial \mathcal{T}(\psi)}{\partial y} + \mathbf{s} \tag{2.18}$$

where the conserved quantity vector is defined as

$$\psi = \begin{pmatrix} \rho \\ \rho u \\ \rho v \\ \rho e \end{pmatrix} \tag{2.19}$$

Using the definition of enthalpy, Eq.(2.14), the convection and diffusion flux vectors respectively are

$$\mathcal{F} = \begin{pmatrix} \rho u \\ \rho u u + p \\ \rho u v \\ \rho u h \end{pmatrix} , \quad \mathcal{G} = \begin{pmatrix} \rho v \\ \rho v u \\ \rho v v + p \\ \rho v h \end{pmatrix} \tag{2.20}$$

$$\mathcal{R} = \begin{pmatrix} 0 \\ \tau_{xx} \\ \tau_{xy} \\ u\tau_{xx} + v\tau_{xy} - q_x \end{pmatrix} , \quad \mathcal{T} = \begin{pmatrix} 0 \\ \tau_{yx} \\ \tau_{yy} \\ u\tau_{yx} + v\tau_{yy} - q_y \end{pmatrix} \tag{2.21}$$

The components of the stress tensor and the heat flux vector, in Eq.(2.21), are defined as before by Eqs.(2.6-2.8) and Eq.(2.9). The source vector is defined

$$\mathbf{s} = \begin{pmatrix} s_m \\ s_f \\ s_g \\ s_e \end{pmatrix} \tag{2.22}$$

Euler Flow Governing Equations

The Euler equations represent the special case of the Navier-Stokes equations where the dissipative transport phenomena of viscosity, mass diffusion, and thermal conduction are neglected. Considering this definition and assuming no source terms, Eq.(2.18) is reduced to

$$\frac{\partial \psi}{\partial \theta} + \frac{\partial \mathcal{F}(\psi)}{\partial x} + \frac{\partial \mathcal{G}(\psi)}{\partial y} = 0 \tag{2.23}$$

where $\mathcal{F}$ and $\mathcal{G}$ are given by Eq.(2.20).

2.2 Domain Discretization

The first step to solving conservation equations is domain discretization. The current numerical method uses a control-volume-based finite-element discretizations as introduced in Section 1.3. This technique was applied to the heat conduction problem by Schneider and Zedan [58] and extended to fluid flow problems by Schneider and Raw [10, 11]. While these works have selected quadrilateral elements throughout the domain, there are other works which employ the same approach with other finite-element shapes. For example, Baliga and Patankar [7] considered triangular elements. The present method is control-volume-based because the elements are used to construct the calculation domain with non-overlapping control-volumes which fill the solution domain. Nodes are located at the element corners, and will be the location of all unknowns. In this study we consider quadrilateral elements which consist of four edges and four vertices.

The basic relations and transformations of the finite element scheme are presented in Appendix A for quadrilateral elements. It will be advantageous if the control volumes are appropriately defined from the elements. If we imagine bounded domains around nodes which do not overlap each other and all together cover whole solution domain the preliminary tool for employing the control-volume part of the method is formed. In this regard, each element is broken up into four sub-elements by ξ=0 and η=0 lines, Figure 2.1. The assemblage of all sub-elements which touch a node form the required bounded domain which is called control-volume, Figure 2.2. It consists of eight line segments. Conservation balances for mass, momentums, and energy are applied for each control-volume. Since each sub-elements is used to define control-volumes, we rename it to a *sub-control-volume* or simply SCV. Figure 2.1 illustrates how ξ=0 and η=0 lines have divided the element into four

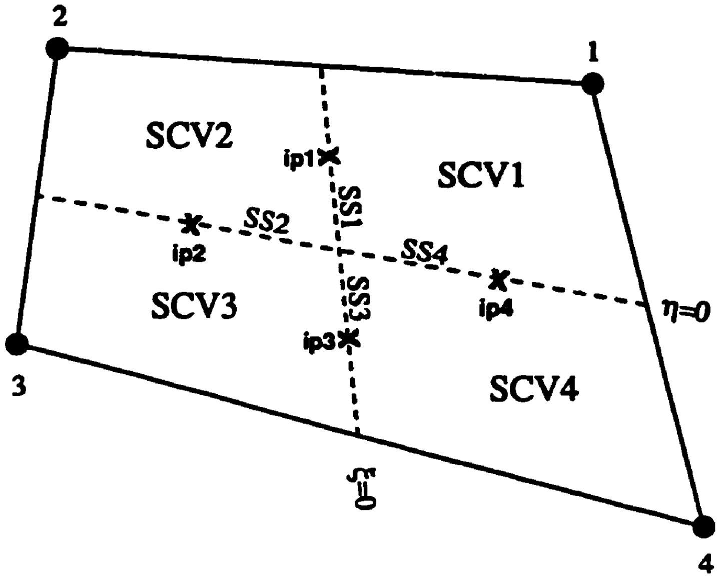

Figure 2.1: Definitions inside an element.

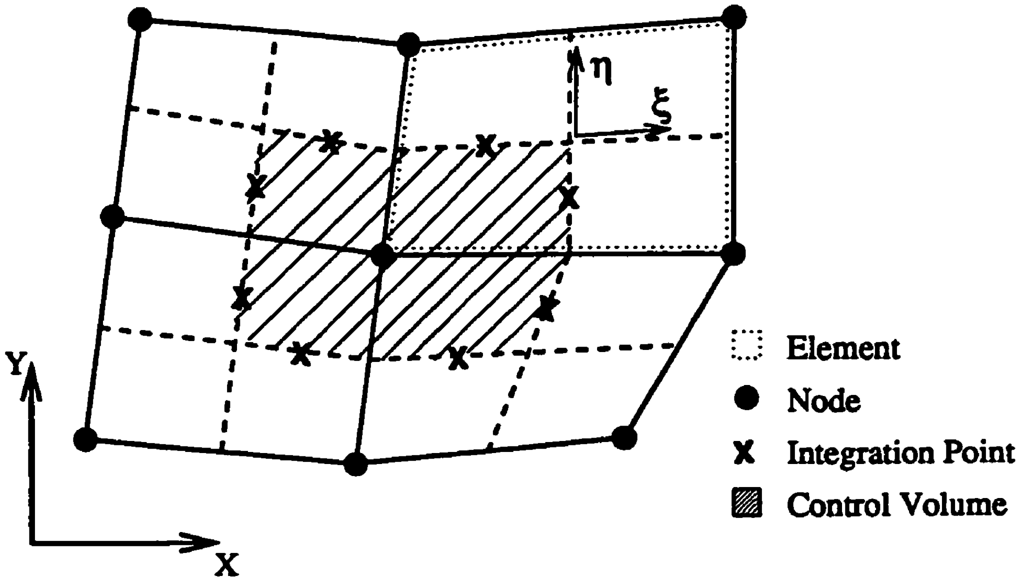

Figure 2.2: Two-dimensional domain discretization.

SCVs. A conservative flux discretization of the governing equations is accomplished by looking over all elements and then over all SCV faces within each element. The flux passing through each SCV face is assembled to the corresponding own control volumes. The fluxes are estimated by integrating over the SCV surface. The argument of such integrals is approximated by the mid-point of each surface. These mid-points are denoted as integration points and labeled by *ip*. They are illustrated in Figures 2.1 and 2.2 by crosses. As seen, the sub-surfaces are simply tagged by SS labels.

This grid arrangement is called the colocated grid because all unknowns of the problem are located at the same points. The geometric simplicity of the colocated grid arrangement is very attractive and it will be significant if the pressure checkerboard problem can be removed, as discussed in Section 1.2.1.

The integration over sub-surfaces require knowledge of the normal vector to each sub-surface. Assume that the sub-surface is stretched between points a with $(x,y)_a$ and b with $(x,y)_b$, Figure 2.3. $\overrightarrow{\Delta S}$ represents an outward normal vector to the segment line $\overline{ab}$ if we assume conventional counter-clockwise travel on the control-volume surface. It is written as

$$\overrightarrow{\Delta S} = (\Delta S)_x \, \hat{i} + (\Delta S)_y \, \hat{j} \tag{2.24}$$

where

$$(\Delta S)_x = \quad \Delta y = \quad (y_b - y_a) \tag{2.25a}$$

$$(\Delta S)_y = \quad -\Delta x = \quad -(x_b - x_a) \tag{2.25b}$$

In Chapter 3, the one-dimensional form of the governing equations is studied. Therefore, a one-dimensional domain discretization is needed. A simple uniform one-dimensional mesh is shown and described in Figure 3.1 and Section 3.2.

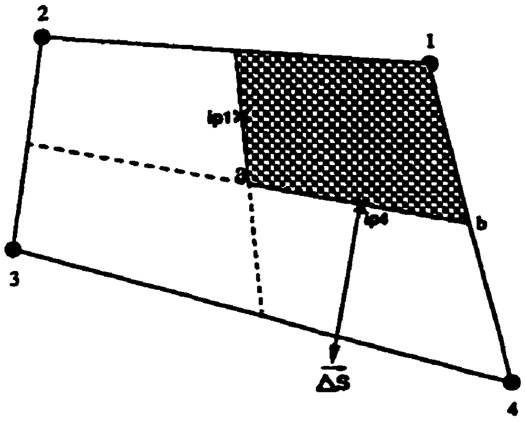

Figure 2.3: Surface vector demonstration.

2.3 Dependent Variables

The governing equations were introduced in Section 2.1. Each of these equations is frequently associated with one basic variable. This basic variable is explicitly represented by the time derivative part of each equation. Density, velocity components, and temperature (or enthalpy) are mainly associated with the mass, momentum, and energy equations, respectively.

Most compressible flow methods solve the Navier-Stokes equations for density, velocity, and temperature and derive pressure from the equation of state. However, in the incompressible limit, the density is no longer an unknown, and it vanishes from the continuity equation. Although some methods still use density as a dependent variable in the incompressible limit, they suffer from slow convergence, low accuracy, and instability, Volpe [30]. Instead, most methods for incompressible flow use pressure as the dependent variable and consider the pressure field to be set indirectly by the continuity equation. The choices for dependent variables were compared by Hauke and Hughes [31] who present a comparative study on the performance of three different set of dependent variables, excluding momentum variable set, to solve compressible flow for incompressible limits. They deduced that pressure is a good choice in the incompressible limit.

In the present work, pressure is selected as a dependent variable. The difficulty introduced with choosing pressure as a dependent variable is that checkerboard fields may arise, as discussed in Section 1.2.1. This problem is overcome with two different definitions for momentum integration point equations, which are discussed in Chapters 3 and 4. With this practice, both compressible and incompressible flows can be computed using the same computer program and specifying a proper pressure-density relationship.

For simple orthogonal coordinate systems such as Cartesian, as oppose to the non-orthogonal coordinate systems, the appropriate dependent variables in the momentum equations are the velocity components. There are other choices for non-orthogonal coordinate systems. The Cartesian velocity components have been widely used as the dependent variables in all speed solvers, Section 1.2.4. The advantage is that the governing equations are very simple and boundary condition application is easy. In this research, momentum components (or, equivalently, mass fluxes; i.e., $f=\rho u$ and $g=\rho v$) have been selected as dependent variables for the momentum equations. The reason for this is discussed in Section 2.4. For the energy equation either temperature or enthalpy could be chosen as the dependent variable. In the present work, temperature is chosen, as it facilitates boundary condition application.

2.4 Research Motivation

Generally speaking, there are different reasons for research in a branch of study. The research path is always open to problems which are unsolved. The status of the research for this type of problems is completely clear. However, the path of research is not ended as soon as the problem is solved. There are always room to improve the side factors of the method and its solution like stability, efficiency, accuracy, and so on. There are generally two types of research approach. In the first category, an existing method is developed by adding extra professional treatments. In the second one, a new approach, i.e. a novel work, is proposed and investigated in order to find the pros and cons comparing with the other existing approaches.

We categorize the current research as a novel work and in this section we take a deeper look at the motivation for the current research. The compressible-incompressible analogy, methods of linearization, and smooth fluxes through abrupt changes in flow parameters are issues which form the foundation for selecting momentum variables as the dependent variables in this research. These issues are separately addressed in this section.

2.4.1 Incompressible-Compressible Analogy

The concept of analogy in this study is to develop incompressible methods for solving compressible flows by switching the dependent variables. In order to express the concept of analogy, it is necessary to expand either the conservation equations or the control-volume level of these equations. In this section, we are concerned with the continuity and momentum equations. On the other hand, as a start to analogy implementation, we confine the discussion to Euler flow, which contains the basic physics of much high-speed flow.

As the first step, we study the control-volume level of conservation equations. Recall the steady form of the Euler equations, Eq.(2.23), with zero source term. This equations could be integrated over an arbitrary control volume. At this stage we are not interested in the details of integration but the final form of the control-volume level of conservation equations. These forms are derived in Chapter 3 for a one-dimensional study and in Chapter 4 for two-dimensional study. The integrated equations for an arbitrary quadrilateral control volume will result in the following set of equations:

$$\int_{c.s.} (\rho u)\hat{i}\cdot d\vec{S} + \int_{c.s.} (\rho v)\hat{j}\cdot d\vec{S} = 0 \tag{2.26a}$$

$$\int_{c.s.} (\rho u u)\hat{i}\cdot d\vec{S} + \int_{c.s.} (\rho v u)\hat{j}\cdot d\vec{S} + \int_{c.s.} p\hat{i}\cdot d\vec{S} = 0 \tag{2.26b}$$

$$\int_{c.s.} (\rho u v)\hat{i}\cdot d\vec{S} + \int_{c.s.} (\rho v v)\hat{j}\cdot d\vec{S} + \int_{c.s.} p\hat{j}\cdot d\vec{S} = 0 \tag{2.26c}$$

where $c.s.$ means integration over control surface and $d\vec{S}$ is a vector normal to the surface of control volume. For an incompressible flow, these equations reduce to

$$\int_{c.s.} (u)\hat{i}\cdot d\vec{S} + \int_{c.s.} (v)\hat{j}\cdot d\vec{S} = 0 \tag{2.27a}$$

$$\int_{c.s.} u(u)\hat{i}\cdot d\vec{S} + \int_{c.s.} v(u)\hat{j}\cdot d\vec{S} + \int_{c.s.} p^{*}\hat{i}\cdot d\vec{S} = 0 \tag{2.27b}$$

$$\int_{c.s.} u(v)\hat{i}\cdot d\vec{S} + \int_{c.s.} v(v)\hat{j}\cdot d\vec{S} + \int_{c.s.} p^{*}\hat{j}\cdot d\vec{S} = 0 \tag{2.27c}$$

where $p^{*} = p/\rho$. Here, u, v, and p^{*} are considered as the dependent variables. The variables outside of parentheses are due to non-linearities, and need to be linearized. Alternatively, for a compressible flow, Eqs.(2.26) can also be expressed as

$$\int_{c.s.} (f)\hat{i}\cdot d\vec{S} + \int_{c.s.} (g)\hat{j}\cdot d\vec{S} = 0 \tag{2.28a}$$

$$\int_{c.s.} u(f)\hat{i}\cdot d\vec{S} + \int_{c.s.} v(f)\hat{j}\cdot d\vec{S} + \int_{c.s.} p\hat{i}\cdot d\vec{S} = 0 \tag{2.28b}$$

$$\int_{c.s.} u(g)\hat{i}\cdot d\vec{S} + \int_{c.s.} v(g)\hat{j}\cdot d\vec{S} + \int_{c.s.} p\hat{j}\cdot d\vec{S} = 0 \tag{2.28c}$$

Here, f, g, and p are considered as the dependent variables. If equations, Eqs.(2.27) and Eqs.(2.28) are compared, it is seen that they are the same except for their vector of dependent variables. Equations (2.27) were developed for incompressible flows where u, v, and p^* were dependent variables. However, Eqs.(2.28) were developed for compressible flows where f, g, and p were dependent variables. Therefore, the analogy suggests that incompressible control-volume methods using u, v, and p^* as the dependent variables could be extended to solve compressible flows by switching to f, g, and p as the dependent variables.

This analogy can also be applied to the non-conservative form of the governing equations. This non-conservative form may be selected as either the main governing equations for solving the flow field or the equation for deriving integration-point operators in control-volume methods; in order to connect integration points to the main grid points. For incompressible flow, the steady form of the Euler equations becomes

$$\frac{\partial u}{\partial x} + \frac{\partial v}{\partial y} = 0 \tag{2.29a}$$

$$u\frac{\partial u}{\partial x} + v\frac{\partial u}{\partial y} + \frac{\partial p^*}{\partial x} = 0 \tag{2.29b}$$

$$u\frac{\partial v}{\partial x} + v\frac{\partial v}{\partial y} + \frac{\partial p^*}{\partial y} = 0 \tag{2.29c}$$

Here, u, v, and p^* are considered as the dependent variables. Alternatively, for compressible flow, Eq.(2.23) can be written as

$$\frac{\partial f}{\partial x} + \frac{\partial g}{\partial y} = 0 \tag{2.30a}$$

$$u\frac{\partial f}{\partial x} + v\frac{\partial f}{\partial y} + \frac{\partial p}{\partial x} = \text{ Terms} \tag{2.30b}$$

$$u\frac{\partial g}{\partial x} + v\frac{\partial g}{\partial y} + \frac{\partial p}{\partial y} = \text{ Terms} \tag{2.30c}$$

Here, f, g, and p are considered as the dependent variables. There are two more terms in the right-hand-side of the momentum equations which are a result of the nonlinear convection terms. These terms vanish in the incompressible limit. Again, comparing Eqs.(2.29) and Eqs.(2.30) shows that they are the same except for their dependent variables. Therefore, according to the analogy, incompressible governing equations which are arranged for u, v, and p^* as dependent variables could be extended to compressible governing equations by switching to f, g, and p as the dependent variables.

Therefore, this analogy provides an important argument for selecting momentum components as the dependent variables.

2.4.2 Fluxes versus Primitive Variables

In the conservation equations, Eqs.(2.2-2.5), it is seen that the left-hand sides involve the divergence of the flux of some physical quantities:

From Eq.(2.2)	$\rho\vec{V}$	mass flux
From Eq.(2.3)	$\rho u\vec{V}$	flux of x-component of momentum
From Eq.(2.4)	$\rho v\vec{V}$	flux of y-component of momentum
From Eq.(2.5)	$\rho e\vec{V}$	flux of total energy

Thus the conservation equations deal directly with the flux of mass, momentum, and energy rather than just the primitive variables such as p, ρ, and $\vec{V}$. The conservation equations can be cast in a common generic form as

$$\frac{\partial \mathbf{a}}{\partial \theta}+\frac{\partial \mathbf{b}}{\partial x}+\frac{\partial \mathbf{c}}{\partial y}=\mathbf{d} \tag{2.31}$$

In this generic form, all arguments of the $\frac{\partial}{\partial \theta}$, $\frac{\partial}{\partial x}$, and $\frac{\partial}{\partial y}$-terms in Eqs.(2.2-2.5) are collected in **a**, **b**, and **c** flux vectors, respectively. All non-differential terms are collected in $\mathbf{d}$ which is called the source vector. The term $\mathbf{a}$ is called the solution vector for an unsteady problem. Equation 2.31 is called the *strong* conservation form of the governing equations, in contrast to the Navier-Stokes equations which is a weak conservation form. Comparing with Eq.(2.18), we see that

$$\mathbf{a} = \psi \tag{2.32a}$$

$$\mathbf{b} = \mathcal{F} - \mathcal{R} \tag{2.32b}$$

$$\mathbf{c} = \mathcal{G} - \mathcal{T} \tag{2.32c}$$

$$\mathbf{d} = \mathbf{s} \tag{2.32d}$$

For an inviscid flow, Eq.(2.31) reduces to Eq.(2.23). For an unsteady Euler flow problem, the proper dependent variables are $\{\rho, \rho u, \rho v, \rho e\}$. However, for steady Euler problems, a marching method with marching in one space direction may be chosen where the components of $\mathcal{F}$ are considered as the dependent variables [59].

This form of governing equations is popular in CFD. There are reasons behind this popularity. For example, Anderson et al [60] have shown that the conservative form of the Euler equations allows shock waves to be captured as weak solutions, thereby circumventing the need to apply shock-fitting techniques. Furthermore, in flow fields involving shock waves, there are sharp discontinuities in p, ρ, u, t, etc., across the shock. Experience has shown that the conservation form of the governing equations is better to be used with shock-capturing methods. The use of the conservation form does not result in unsatisfactory spatial oscillations upstream and downstream of the shock wave, and the solution is generally smooth and stable [61]. This is sketched in Figure 2.4. This plot depicts the flow across a normal shock wave for a number of flow-field parameters and their combinations. There are sharp discontinuities for ρ, p, and u variables passing through a shock wave. If

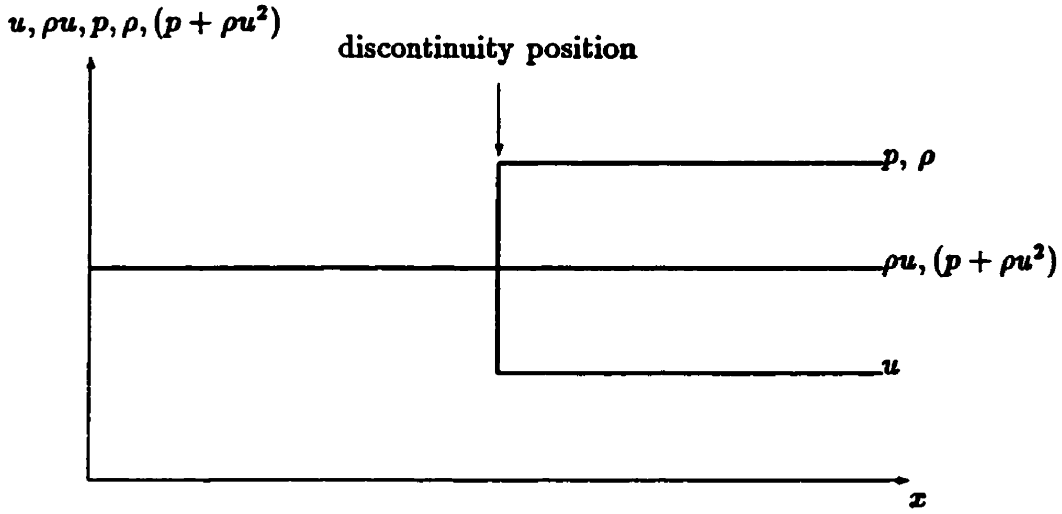

Figure 2.4: The change of flow properties across a normal shock wave.

these variables are chosen as dependent variables the equations would directly see a large discontinuity which in turn would result in numerical errors associated with their calculation.

On the other hand, the mass flux, ρu, is constant across the shock wave, i.e.,

$$\rho_1 u_1 = \rho_2 u_2 \tag{2.33}$$

Hence, if ρu is used as a dependent variable, the stability and accuracy of the solution would be increased. The investigation of the x-momentum equation will result a similar conclusion for the $p + \rho u^2$ term, i.e.,

$$p_1 + \rho_1 u_1^2 = p_2 + \rho_2 u_2^2 \tag{2.34}$$

Again, although p, ρ, and u have sharp discontinuities across the shock wave, the flux variable of $p + \rho u^2$ remains constant across the shock. If this flux variable is selected as the dependent variable, the conservation equations would see no error associated with sharp discontinuities in p, ρ, and u.

Since we are looking for developing a method capable of solving both steady and unsteady flows, the solution vector $\{\rho, \rho u, \rho v, \rho e\}$ is selected as the dependent variables. However, it was shown in Section 2.3 that pressure should be chosen as a dependent variable rather than density for incompressible flows.

Based on these arguments, we conclude that the appropriate choice for the vector of dependent variables is $\{p, \rho u, \rho v\}$. Another argument for the same choice is given in the next section.

2.4.3 Treating the Nonlinearities

The general form of the Navier-Stokes equations is non-linear regardless of the choice of dependent variables. In order to solve them using methods for linear equation systems, the non-linear terms must be linearized. There are many different linearization techniques such as lagging the coefficients, simple iterative update of the equations, Newton linearization to iteratively update the coefficients, Newton linearization with coupling, and many more, Anderson et al [62]. Each of these linearizations has advantages and disadvantages, and generally do not guarantee convergence. Thus they may be restricted to special applications.

Generally speaking, linearization introduces some errors, such as iterative errors, in solution domain during the process of solving the non-linear equations. Iteration is used to solve non-linear equations by choosing an initial guess and updating it by solving the linearized equations until the residuals are reduced to a preset level. Iterative errors vanish if residuals are enough small. Besides the method of linearization, the number of linearized terms within an equation is also important. In general, more linearization would cause higher numerical errors. We should choose a method which requires as few linearizations as possible.

Nonlinearities	Momentum Variable	Velocity Variable
$\frac{\partial \rho}{\partial \theta}$	Yes	Yes
$\frac{\partial(\rho u)}{\partial x}$	No	$\bar{\rho} u + \bar{u} \rho - \overline{\rho u}$
$\frac{\partial(\rho v)}{\partial y}$	No	$\bar{\rho} v + \bar{v} \rho - \overline{\rho v}$
$\frac{\partial(\rho u)}{\partial \theta}$	No	Yes
$\frac{\partial(\rho v)}{\partial \theta}$	No	Yes
$\frac{\partial(\rho u u)}{\partial x}$	$\bar{u}(\rho u)$	$\overline{\rho u} u$
$\frac{\partial(\rho v u)}{\partial y}$	$\bar{v}(\rho u)$	$\overline{\rho v} u$
$\frac{\partial(\rho u v)}{\partial x}$	$\bar{u}(\rho v)$	$\overline{\rho u} v$
$\frac{\partial(\rho v v)}{\partial y}$	$\bar{v}(\rho v)$	$\overline{\rho v} v$
$\frac{\partial u}{\partial x}$	$\frac{1}{\bar{\rho}}\left(\frac{\partial f}{\partial x} - \bar{u}\overline{\frac{\partial \rho}{\partial x}}\right)$	No
$\frac{\partial v}{\partial x}$	$\frac{1}{\bar{\rho}}\left(\frac{\partial g}{\partial x} - \bar{v}\overline{\frac{\partial \rho}{\partial x}}\right)$	No
$\frac{\partial u}{\partial y}$	$\frac{1}{\bar{\rho}}\left(\frac{\partial f}{\partial y} - \bar{u}\overline{\frac{\partial \rho}{\partial y}}\right)$	No
$\frac{\partial v}{\partial y}$	$\frac{1}{\bar{\rho}}\left(\frac{\partial g}{\partial y} - \bar{v}\overline{\frac{\partial \rho}{\partial y}}\right)$	No

Table 2.1: Treatment of the nonlinearities in the mass and momentum equations.

We now consider the number of linearizations required if the velocity or momentum components are chosen as dependent variables. Table 2.1 provides a comprehensive comparison of important terms in Eqs.(2.2-2.4) for both velocity and momentum variables. It is important to note that the linearization is done for the control-volume level of discretization where the differential forms disappear by integrating over the control-volume surfaces and volume. Therefore, the first column shows the real appearance of the nonlinear term in the general form of the governing equations and the other two columns show the linearization of the same term in the control volume discretized form. The words of "Yes" and "No" are used to identify whether the term needs or does not need linearization with respec to the selected variables. In this table we see that for the continuity equation, the transient term needs linearization with both formulations, while the other two terms need to be linearized only when using velocity components. The method of linearization could be different for different flow-fields and solution method. Compressible-incompressible solvers may use a Newton-Raphson linearization which retains the important role of density for compressible flows but shifts this role to velocity in the incompressible limit, i.e.

$$\rho u = \bar{\rho} u + \bar{u} \rho - \overline{\rho u} \tag{2.35}$$

For the momentum equations, the convection terms need to be linearized for velocity or momentum formulations. However, the transient term needs to be linearized only for the velocity formulation. The diffusion terms must be linearized for the momentum formulations, as discussed in Appendix D.

Here it must be noted that we are not to compare just the number of nonlinearities in these two formulations and reach a conclusion. The method of linearization is another issue which surmounts the number of linearizations. For example, the relative weights of diffusion and convection in the momentum equations are not the same. Diffusion terms are always discretized using elliptical schemes. Since the same technique is used for all diffusion terms, linearization then does not pose a major problem. However, the linearization of mass flux terms in the continuity equation and convection terms in the momentum equations require more improved treatment. This is because each component of the linearized term, e.g. ρ and u in the ρu term, may require special treatment consistent with the physics of the original nonlinear term. Therefore, a suitable treatment of the nonlinearities is much important than reducing the number of linearizations.

Therefore, we see that the selection of momentum components over velocity components provides additional simplicity in the linearization of the governing equations, specially, the continuity equation. This is another reason for using the momentum components as the dependent variables.

2.5 Closure

In this chapter, the general conservation equation and several versions of the Navier-Stokes equations were introduced. This was followed by a discussion on the selected dependent variables. It was also explained that if a computational scheme is to be valid for both incompressible and compressible flows, pressure should be selected as a dependent variable in preference to density. In addition, several reasons were given for selecting momentum components instead of velocity components as dependent variables. An analogy was introduced which enables incompressible methods to be extended to solve compressible flows. The smoothness of the fluxes through the discontinuities in the flow-field was another reason to switch to momentum components. Finally, it was shown that the momentum-variable formulation leads to fewer linearization difficulties and introduces less erroneous linearization.

Chapter 3

One-Dimensional Investigation and Results

3.1 Introduction

The development of a numerical method requires several steps. The initial steps are very important in the progress of subsequent stages. In a multi-dimensional method, there is no better way to test the method initially than for the simple case of one-dimensional flow. In this chapter, we examine the method for one-dimensional investigations or formulations with some special applications. The procedure is started by discretizing the solution domain in Section 3.2. Then in Section 3.3, we introduce the one-dimensional governing equations and write the statement of conservative for them. Next, we derive the one-dimensional integration point expressions and operators in Section 3.4. These derived expressions are first checked for sound physical behaviour for special flow cases. Later in Section 3.5, they are checked for the velocity-pressure decoupling problem. The modeling of the velocity-based formulation is accomplished in Section 3.6. In Section 3.7, the method is tested for a number of test problems. In this regard, a source and sink combination is put in the one-dimensional flow and the resulting velocity and pressure field distributions are studied. The results confirm the decoupling problem under special circumstances. The one-dimensional test is followed by checking the formulation for high speed flows with shocks. In this regard, the shock tube problem is selected and tested for one-dimensional inviscid flow and the results are compared with the analytical solution. Finally, a direct comparison between the momentum-variable procedure and velocity-variable procedure, including their results, is presented.

3.2 One-Dimensional Domain Discretization

The two-dimensional discretization of the solution domain has been fully discussed in Section 2.2 and Appendix A. For a one-dimensional study, the grid distribution is very simple. The number of nodes, integration points, and SCVs in each element are reduced considerably. Figure 3.1 illustrates a simple uniform one-dimensional grid distribution. The Y and Z dimensions have unit lengths.

Control volumes are located between the two crosses while elements are located between the solid circles. The notation used to denote relative control volume location is illustrated in this figure. The subscripts E and W are used to denote the nodal quantities associated with the control volume to the east and west of node P. Similarly, e and w are east and west surfaces of the control volume centered at point P. Upper case letters are associated with quantities at main nodal grid points, while lower case letters refer to quantities at integration points. This convention is normally respected throughout this thesis.

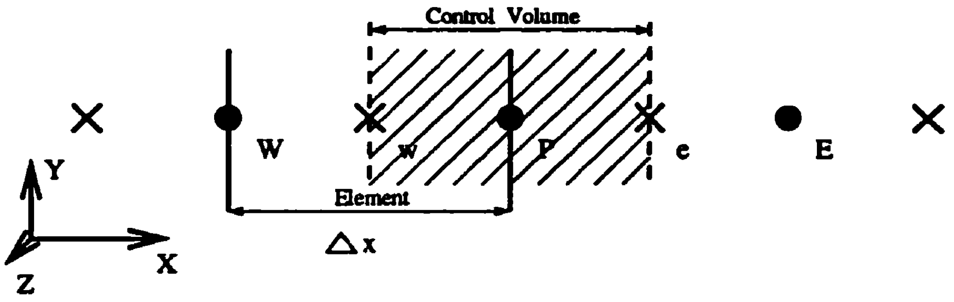

Figure 3.1: One-dimensional domain discretization.

3.3 Discretization of Governing Equations

In this section the algebraic representation for different terms of the mass, momentum, and energy equations are derived according to control-volume-based methods. These algebraic equations have a nonlinear form. These nonlinearities need to be linearized properly in order to use solution techniques applicable to linear algebraic equation systems. The one-dimensional conservative form of the governing equations for mass, momentum, and energy are respectively derived from Eqs.(2.2-2.5) for flow in x direction as

$$\frac{\partial \rho}{\partial \theta} + \frac{\partial (\rho u)}{\partial x} = s_m \tag{3.1}$$

$$\frac{\partial (\rho u)}{\partial \theta} + \frac{\partial (\rho u u)}{\partial x} + \frac{\partial p}{\partial x} = \frac{\partial}{\partial x}(\Gamma \frac{\partial u}{\partial x}) + s_f \tag{3.2}$$

$$\frac{\partial (\rho e)}{\partial \theta} + \frac{\partial (\rho u e + u p)}{\partial x} = \frac{\partial}{\partial x}(\Gamma u \frac{\partial u}{\partial x}) - \frac{\partial q_x}{\partial x} + s_e \tag{3.3}$$

where $\Gamma = \frac{4}{3}\mu$. The auxiliary equation is the equation of state for compressible flow, Eq.(2.11), and the constant density assumption for incompressible flow, Eq.(2.16). The other necessary parameters, like total energy and enthalpy, are calculated from Section 2.1 considering the one-dimensionality.

3.3.1 Conservation of Mass Equation

Integrating the equation of mass, Eq.(3.1), over a control volume and using the divergence theorem will yield

$$\int_{\mathcal{V}_P} \frac{\partial \rho}{\partial \theta}\, d\mathcal{V} + \int_{S_P} f\, dS = \int_{\mathcal{V}_P} s_m\, d\mathcal{V} \tag{3.4}$$

where $\int_{\mathcal{V}_P}$ and $\int_{S_P}$ are taken over the volume and the surfaces normal to the x-axis of the control volume, Figure 3.1. The transient term is approximated by a *lumped mass* approach in our fully implicit method

$$\int_{\mathcal{V}_P} \frac{\partial \rho}{\partial \theta}\, d\mathcal{V} \approx J_P\left(\frac{\varrho_P - \varrho_P^o}{\Delta\theta}\right) \tag{3.5}$$

where J represents the volume of the control volume. The superscript "o" denotes the old values of the corresponding parameter. The subscript P refers to the nodal point P. Since ϱ is not a major dependent variable it is properly linearized for compressible flow using Eq.(B.5). The result is $\varrho = \bar{\varrho} + \frac{1}{RT}\ P - \frac{\bar{P}}{RT^2}\ T$. Similarly, the source term is approximated as the source strength evaluated at point P times the volume of control volume

$$\int_{\mathcal{V}_P} s_m\, d\mathcal{V} \approx (s_m)_P\ \ J_P \tag{3.6}$$

The remaining flux term is simply integrated over the boundary surface of the control volume

$$\int_{S_P} f\, dS \approx f_e - f_w \tag{3.7}$$

f_e and f_w are evaluated at the integration points which are not nodal locations. The expressions which relate them to the main grid nodes are derived in Section 3.5.

3.3.2 Conservation of Momentum Equation

Integrating the momentum conservation equation, Eq.(3.2), over an arbitrary control volume will yield

$$\int_{\mathcal{V}_P} \frac{\partial f}{\partial \theta}\, d\mathcal{V} + \int_{S_P} (uf)\, dS + \int_{S_P} p\, dS = \int_{S_P} \Gamma \frac{\partial u}{\partial x}\, dS + \int_{\mathcal{V}_P} s_f\, d\mathcal{V} \tag{3.8}$$

The transient and source terms can be treated as before

$$\int_{\mathcal{V}_P} \frac{\partial f}{\partial \theta}\, d\mathcal{V} \approx J_P \left(\frac{F_P - F_P^o}{\Delta \theta} \right) \tag{3.9}$$

$$\int_{\mathcal{V}_P} s_f\, d\mathcal{V} \approx (s_f)_P \;\; J_P \tag{3.10}$$

The convection term is simply integrated over the control volume surfaces

$$\int_{S_P} (uf)\, dS \approx (uf)_e - (uf)_w \tag{3.11}$$

These nonlinear terms at the control volume surfaces must also be linearized. It is possible to linearize them respect to f variable or both f and u variables. The details are given in Appendix C and the result is written here by employing Eq.(C.14)

$$\int_{S_P} (uf)\, dS \approx 2k'[\bar{u}_e f_e - \bar{u}_w f_w] - k''(\bar{u}_e^2 \bar{\rho}_e - \bar{u}_w^2 \bar{\rho}_w) \tag{3.12}$$

The pressure term is written as

$$\int_{S_P} p\, dS \approx p_e - p_w \tag{3.13}$$

The last term is the diffusion term which is treated in a similar manner

$$\int_{S_P} \Gamma \frac{\partial u}{\partial x}\, dS \approx (\Gamma \frac{\partial u}{\partial x})_e - (\Gamma \frac{\partial u}{\partial x})_w \tag{3.14}$$

The results do not directly involve the main dependent variables and an appropriate substitution is needed. Appendix D represents different methods to linearize terms similar to the $\frac{\partial u}{\partial x}$ term. Here, the scheme of Eq.(D.2) is used to linearize the diffusion term. After substituting, the results are written as

$$\int_{S_P} \Gamma \frac{\partial u}{\partial x}\, dS \approx \Gamma \left[\left(\frac{1}{\bar{\rho}} \frac{\partial f}{\partial x} \right)_e - \left(\frac{1}{\bar{\rho}} \frac{\partial f}{\partial x} \right)_w \right] - \Gamma \left[\left(\frac{\bar{u}}{\bar{\rho}} \frac{\partial \rho}{\partial x} \right)_e - \left(\frac{\bar{u}}{\bar{\rho}} \frac{\partial \rho}{\partial x} \right)_w \right] \tag{3.15}$$

The terms in the second bracelet can be evaluated by either using the lagged values of the density or by employing the method of Appendix B and considering them as active terms. As is seen, all terms except the transient and source terms need to be evaluated at the integration points which are not nodal locations. The necessary connections are developed in Section 3.4.

3.3.3 Conservation of Energy Equation

In this research, different methods for treating the one-dimensional energy equation have been used because the number of nonlinear terms is much more than the number in the momentum equation and they can be linearized differently. The final formulation which is presented in this sub-section presents just one which the final one-dimensional results are based on. Integrating the equation of energy, Eq.(3.3), over an arbitrary control volume will yield

$$\int_{\mathcal{V}_P} \frac{\partial(\rho e)}{\partial \theta}\, d\mathcal{V} + \int_{S_P} (fe)\, dS + \int_{S_P} up\, dS = \int_{S_P} \Gamma u \frac{\partial u}{\partial x}\, dS - \int_{S_P} q_x\, dS + \int_{\mathcal{V}_P} s_e\, d\mathcal{V} \tag{3.16}$$

The transient and source terms can be treated as before. However, the nonlinear transient term, i.e. ρe, is linearized with respect to ρ and e using Eq.(B.6) in Appendix B. This gives $\rho e = \bar{\rho} e + \bar{e} \rho - \overline{\rho e}$ where a simple linearization for e is

$$e = c_v\, T + \frac{\bar{u}}{2\bar{\rho}}\, f \tag{3.17}$$

Using Eq.(B.5) for density and substituting it and Eq.(3.17) into the linearized form of ρe will finally yield

$$\int_{\mathcal{V}_P} \frac{\partial(\rho e)}{\partial\theta}\, d\mathcal{V} \approx \frac{J_P}{\Delta\theta}\left[\frac{\bar{U}}{2}\, F + \frac{\bar{E}}{R\bar{T}}\, P + (\bar{\varrho}c_v - \frac{\overline{\varrho E}}{\bar{T}})\, T - (\varrho E)^o\right]_P \tag{3.18}$$

The subscript P for the terms in braces means that all terms are evaluated at the nodal location P. On the other hand, the convection term in Eq.(3.16), fe, is first linearized with respect to f and e using Eq.(B.6). Then one more linearization is done for the definition of e, Eq.(3.17). A combination of these two linearizations will result in the following linearized form for the convection term,

$$\int_{S_P} fe\; dS \approx [\bar{k}_e f_e - \bar{k}_w f_w] + c_v[\bar{f}_e t_e - \bar{f}_w t_w] - [(\overline{fe})_e - (\overline{fe})_w] \tag{3.19}$$

where $k = c_v t + u^2$. The viscous term in Eq.(3.16) is treated similarly to the viscous term of the momentum equation. The extra u in the viscous term of the energy equation is lagged. The conduction term in Eq.(3.16) is approximated at control volume surfaces by writing a central difference involving its neighboring nodal temperatures. The pressure term is changed to $up = u(\rho Rt) = R\, f\, t$. Then using Eq.(B.6) we obtain

$$\int_{S_P} up\; dS \approx R\{[\bar{t}_e f_e - \bar{t}_w f_w] + [\bar{f}_e t_e - \bar{f}_w t_w] - [(\overline{ft})_e - (\overline{ft})_w]\} \tag{3.20}$$

As before, all terms except the transient term were derived at integration points. The necessary connecting expressions between integration points and the main grid points are derived in the next section.

3.4 Integration Point Operators

The conservative treatment of mass, momentum, and energy was presented in the last section. However, to make the system of algebraic equations well-posed, the derived discretized forms require that the dependent variables at control volume surfaces be represented in terms of nodal variables. Therefore, it is necessary to derive expressions for the major dependent variables of the formulation (i.e., momentum component, pressure, and temperature variables) at control volume surfaces in terms of nodal values.

3.4.1 Momentum Component Variable

Although the continuity equation is treated as an equation for pressure it does not directly involve pressure in itself. This is critical for incompressible flow conditions. A simple connection of f_e and f_w in Eq.(3.7) to the neighbouring nodal F's does not directly brings the effect of pressure into the continuity equation. Moreover, it ensures the checkerboard problem will exist [1]. Various techniques have been adopted to overcome this shortcoming in the continuity equation. Many of them have paid attention to a better modeling of the integration point variables. In this regard, new schemes have tried to bring the correct physical aspects of the flow into the integration point equation. Baliga et al [7, 63], Prakash and Patankar [8], and Prakash [64] are few among many works who have presented profiles that attempt to include the relevant physics of the problem. Consequently, Schneider and Raw [10] employed a different approach that uses the governing equations, themselves, to derive the integration point equations. According to their work, an algebraic approximation to the appropriate differential equation is generated at each integration point which consequently will include all of the physics and relevant couplings for that variable. This method will be employed in this work to derive the necessary integration point equations.

Following the work of Schneider and Raw [10], momentum integration point equations are derived by approximating the non-conservative form of the momentum equation, which is derived from Eq.(3.2). It is

$$\frac{\partial f}{\partial \theta} + u\frac{\partial f}{\partial x} + f\frac{\partial u}{\partial x} + \frac{\partial p}{\partial x} = \frac{\partial}{\partial x}(\Gamma\frac{\partial u}{\partial x}) + s_f \tag{3.21}$$

The terms of this equation are treated in a manner that represents the correct physical aspects of the flow. If there is a strong flow along a specific direction, then significant influences travel only from upstream to downstream in this direction. So, the conditions at a particular point can be affected significantly by upstream conditions. The balance between diffusion and convection terms depends on their relative strengths. If convection is large enough then it overwhelms the elliptic effect of the diffusion term. Considering a correct physical treatment would require a central difference approximation for the pressure gradient term and an upwind approximation for the convection term. A central differencing scheme is also used for the diffusion term which reflects the elliptical influence of parameters in the flow field. The transient term is treated as before by a backward difference in time. So, the terms of Eq.(3.21) are discretized as

$$\frac{\partial f}{\partial \theta} \approx \frac{f_e - f_e^o}{\Delta\theta} \tag{3.22}$$

$$u\frac{\partial f}{\partial x} \approx \bar{u}_e\frac{f_e - F_P}{\Delta x/2} \tag{3.23}$$

$$f\frac{\partial u}{\partial x} \approx \bar{f}_e\frac{f_e/\bar{\varrho}_e - F_P/\bar{\varrho}_P}{\Delta x/2} \tag{3.24}$$

$$\frac{\partial p}{\partial x} \approx \frac{P_E - P_P}{\Delta x} \tag{3.25}$$

$$\frac{\partial^2 u}{\partial x^2} \approx \frac{F_P/\bar{\varrho}_P - 2f_e/\bar{\rho}_e + F_E/\bar{\varrho}_E}{(\Delta x/2)^2} \tag{3.26}$$

Here, both convection terms are treated in an upwind manner. Appendix C presents a comprehensive discussion on the role of the velocity components in the momentum's convection terms. These roles could have a direct effect on the way that these convection terms are discretized. However, it is shown that if $\frac{\partial f}{\partial x}$ is treated in a central difference manner it produces poor results, Appendix E. Another form of treatment for Eq.(3.24) is

$$f\frac{\partial u}{\partial x} \approx \overline{\frac{\partial u}{\partial x}}\, f \tag{3.27}$$

This scheme will include just f_e and is directly transferred to the unknown part of the equation on the left hand side. The reason for avoiding this scheme is the possibility of poor stability of the method as is shown in Appendix E.

Substitution of the discretized terms into Eq.(3.21) and rearrangement yield the following expression for the momentum integration point equation

$$\begin{aligned} f_e = {} & \frac{1}{2}\frac{\bar{\rho}_e}{\bar{\varrho}_P}\left(\frac{2+\mathbb{P}+\frac{\bar{\varrho}_P}{\bar{\rho}_e}\mathbb{P}}{(\frac{1}{4\mathbb{C}}+1)\mathbb{P}+2}\right)F_P + \frac{\bar{\rho}_e}{\bar{\varrho}_E}\left(\frac{1}{(\frac{1}{4\mathbb{C}}+1)\mathbb{P}+2}\right)F_E \\ & + \frac{1}{4\bar{u}_e\left[(\frac{1}{4\mathbb{C}}+1)+\frac{2}{\mathbb{P}}\right]}(P_P - P_E) + \frac{f_e^o}{1+4\mathbb{C}+\frac{8\mathbb{C}}{\mathbb{P}}} + \frac{\Delta x}{4\bar{u}_e\left[(\frac{1}{4\mathbb{C}}+1)+\frac{2}{\mathbb{P}}\right]}s_f \end{aligned} \tag{3.28}$$

where $\mathbb{P}$ and $\mathbb{C}$ are the grid Peclet and Courant numbers, i.e.,

$$\mathbb{P} \equiv \frac{\bar{\rho}_e \bar{u}_e \Delta x}{\Gamma} \tag{3.29}$$

$$\mathbb{C} = \frac{\bar{u}_e \Delta \theta}{\Delta x} \tag{3.30}$$

As is seen, there is a strong connection between the momentum integration point variable and neighbouring nodal dependent variables. The use of this expression in the mass conservation equation, Eq.(3.7), provides a coupling of pressure and momentum-variables and helps to eliminate the need for a staggered grid. Although this procedure reduces the necessity of using a staggered grid, it may still reveal the checkerboard problem under special circumstances which are described in the next section.

If $\mathbb{P}$ is changed from zero to infinity, the influence of upstream and downstream nodal values is properly seen. This is examined for limiting values of the Peclet number in steady-state condition

$$\mathbb{P} \to 0 \qquad f_e = \frac{1}{2}\frac{\bar{\rho}_e}{\bar{\varrho}_P}F_P + \frac{1}{2}\frac{\bar{\rho}_e}{\bar{\varrho}_E}F_E + \frac{\Delta x}{8\Gamma}\bar{\rho}_e(P_P - P_E) + \frac{(\Delta x)^2}{8\Gamma}\bar{\rho}_e s_f \tag{3.31}$$

$$\mathbb{P} \to \infty \qquad f_e = \frac{1}{2}(1 + \frac{\bar{\rho}_e}{\bar{\varrho}_P})F_P + \frac{1}{4\bar{u}_e}(P_P - P_E) + \frac{\Delta x}{4\bar{u}_e}s_f \tag{3.32}$$

The influence of the momentum nodal values properly changes from that of fully elliptic for $\mathbb{P} \to 0$, to that of fully parabolic for $\mathbb{P} \to \infty$. This demonstrates a correct behaviour of the derived expression for the momentum component at the integration point. In the next sub-section, the other integration point variables are examined.

3.4.2 Other Variables

There is no direct equation to be used for deriving an integration point equation for pressure. Schneider and Raw [10] used the pressure Poisson equation as an explicit partial differential equation to show that pressure is a strongly elliptic variable in incompressible flows. Thus, a linear interpolation is used to determine the integration point pressure which is analogous to conventional procedures insofar as its implementation is concerned.

$$p_e \approx \frac{P_P + P_E}{2} \tag{3.33}$$

The temperature integration point equation is obtained by directly discretizing the energy governing equation. The one-dimensional energy equation for transient flow could be written in the following form

$$\rho c_v \frac{\partial t}{\partial \theta} + \rho u c_v \frac{\partial t}{\partial x} + p \frac{\partial u}{\partial x} = \frac{\partial}{\partial x}(\Gamma u \frac{\partial u}{\partial x}) - \frac{\partial q_x}{\partial x} \tag{3.34}$$

The terms of this equation are approximated very similar to the approximations in Eqs.(3.22-3.26). The transient term is discretized by a backward difference, an upwind difference is considered for the second term on left-hand-side, and the third term of the left-side is approximated by a central difference. The substitution of these approximations into Eq.(3.34) yields

$$c_v \bar{\rho}_e \frac{t_e - t_e^o}{\Delta\theta} + c_v \bar{f}_e \frac{t_e - T_P}{\Delta x/2} + \bar{p}_e \frac{F_E/\bar{\varrho}_E - F_P/\bar{\varrho}_P}{\Delta x/2} \approx \bar{\Theta} \tag{3.35}$$

where the lagged dissipation term, $\bar{\Theta}$, is treated in the following form:

$$\bar{\Theta} \approx \Gamma \left[\frac{\bar{U}_E - \bar{U}_P}{\Delta x}\right]^2 + \Gamma \bar{u}_e \frac{\bar{U}_P - 2\bar{u}_e + \bar{U}_E}{(\Delta x/2)^2} + \mathbf{k} \frac{\bar{T}_P - 2\bar{t}_e + \bar{T}_E}{(\Delta x/2)^2} + s_e \tag{3.36}$$

Thus, the temperature integration point equation could be derived after some rearrangement in Eq.(3.35), i.e.,

$$t_e = \frac{2\mathbb{C}}{1+2\mathbb{C}} T_P + \frac{\bar{p}_e}{2c_v \bar{\bar{f}}_e} \frac{2\mathbb{C}}{1+2\mathbb{C}} \left[\frac{F_E}{\bar{\varrho}_E} - \frac{F_P}{\bar{\varrho}_P}\right] + \frac{2\mathbb{C}}{1+2\mathbb{C}} \frac{\bar{\Theta}}{2c_v \bar{\bar{f}}_e} \tag{3.37}$$

The steady-state form of this equation is reduced to

$$t_e = T_P + \frac{\bar{p}_e}{2c_v \bar{\bar{f}}_e} \left[\frac{F_E}{\bar{\varrho}_E} - \frac{F_P}{\bar{\varrho}_P}\right] + \frac{\bar{\Theta}}{2c_v \bar{\bar{f}}_e} \tag{3.38}$$

The unknown density at an integration point can be calculated from either the equation of state or the nonlinear form of the continuity equation. The importance of this variable is for connecting the momentum and velocity-variable quantities at integration points. In the first case, the equation of state is linearized with respect to pressure and temperature, Appendix B, and then the pressure and temperature integration point equations are substituted. This form of linearization was not employed in solving the test cases which are presented in Section 3.7. The second case employs the non-conservative form of the continuity equation, i.e.,

$$\frac{\partial \rho}{\partial \theta} + u\frac{\partial \rho}{\partial x} + \rho\frac{\partial u}{\partial x} = 0 \tag{3.39}$$

Using a backward scheme for the transient term and an upwind scheme for the second term will result in

$$\rho_e = \frac{2\mathbb{C}}{1+2\mathbb{C}}\rho_P + \frac{\rho_e^o}{1+2\mathbb{C}} + \frac{\Delta x}{2\bar{u}_e}\frac{2\mathbb{C}}{1+2\mathbb{C}}\left(\rho\frac{\partial u}{\partial x}\right)_e \tag{3.40}$$

in which the last term of Eq.(3.39) has been lagged. Note that the role of density integration point equation in momentum-variable formulation is not as critical as it is for velocity-variable procedures which uses density directly in the conservative treatment of the continuity equation.

The remaining variables which are not mentioned here , like velocity, do not appear in the formulation with an active role but passive and lagged from previous iterations. Velocity is obtained by using the $u = \frac{f}{\rho}$ definition. Other similarly lagged variables are properly calculated by their basic definitions, Section 2.1, using the magnitude of major dependent variables at integration points.

3.5 Pressure-Velocity Decoupling Issue

The absence of pressure in the continuity equation and the use of a central difference for the pressure term in the momentum equation permit the pressure field to accept a zig-zag solution in incompressible flows, Patankar [1]. Such a zig-zag field, which is known as the pressure checkerboard problem, is not physical. Any number of additional solutions can be constructed by adding a checkerboard pressure field to a smooth pressure field solution.

In this section, the pressure checkerboard problem is investigated for the derived discretized equations of Section 3.3 when the integration point equations of Section 3.4 are employed. This study is started by simplifying the formulations for steady incompressible flow and testing it for special domain situations.

3.5.1 Decoupling in One-Dimensional Formulation

We have already derived the momentum integration point equation, Eq.(3.28), which illustrates a strong coupling between the pressure and velocity fields. This compensates for the absence of pressure in the continuity equation. There remains a question of whether the velocity-pressure decoupling issue has been eliminated. It is interesting to investigate this in our colocated formulation which includes pressure effects in the discretized form of the continuity equation. Consider the control volume located at point P in Figure 3.1, the control-volume discretized equations of mass and momentum for steady-state, incompressible, Euler flow without any source terms are written

$$f_e - f_w = 0 \tag{3.41a}$$

$$2[\bar{u}_e f_e - \bar{u}_w f_w] - (\bar{u}_e^2 \rho_e - \bar{u}_w^2 \rho_w) + p_e - p_w = 0 \tag{3.41b}$$

Here, f_e and f_w are derived from Eq.(3.31) considering incompressible flow conditions with no source term. They are

$$f_e = \quad F_P + \tfrac{1}{4\bar{u}_e}(P_P - P_E) \tag{3.42a}$$

$$f_w = \quad F_W + \tfrac{1}{4\bar{u}_w}(P_W - P_P) \tag{3.42b}$$

The value of p_e is obtained from Eq.(3.33). A similar interpolation for P_w is $p_w = \frac{P_P+P_W}{2}$. If these four integration point expressions are substituted into Eqs.(3.41) the following results are obtained after some rearrangement

$$-F_W + F_P - \frac{1}{4\bar{u}_w}P_W + \frac{1}{4}(\frac{1}{\bar{u}_w} + \frac{1}{\bar{u}_e})P_P - \frac{1}{4\bar{u}_e}P_E = 0 \tag{3.43a}$$

$$-2[\bar{u}_w F_W - \bar{u}_e F_P] + P_P - P_W = (\bar{u}_e^2 \rho_e - \bar{u}_w^2 \rho_w) \tag{3.43b}$$

If the continuity and the momentum equations are respectively multiplied by $\frac{\dot{m}}{\rho}$ and $\frac{\varrho}{\rho}$, the consideration of

$$\dot{m} = (\rho u)_e = (\rho u)_w = \text{mass flow rate} = \text{constant} \tag{3.44}$$

will reduce these equations to

$$\frac{4\dot{m}}{\rho}(F_P - F_W) \quad - \quad (P_W - 2P_P + P_E) \quad = 0 \tag{3.45a}$$

$$\frac{2\dot{m}}{\rho}(F_P - F_W) \quad + \quad (P_P - P_W) \quad = 0 \tag{3.45b}$$

Here, the pressure term in the continuity equation acts as a source term to correct the momentum field. Schneider and Karimian [12] have shown that a zig-zag pressure field results in a zig-zag velocity field in their similar formulation. Following their work, a pressure field similar to

$$\begin{aligned} P_W &= +P_a \\ P_P &= -P_a \\ P_E &= +P_a \end{aligned} \tag{3.46}$$

can result in a zig-zag momentum field like

$$\begin{aligned} F_W &= f_a \\ F_P &= f_a + \frac{P_a}{U_a} \\ F_E &= f_a \end{aligned} \tag{3.47}$$

indicating that only every other node is connected. The non-physical solution set, Eqs.(3.46 and 3.47), satisfies Eq.(3.45). In other words, a non-physical solution satisfies the discretized governing equations.

A similar conclusion is obtained by direct examining of Eqs.(3.41). If $u_e = u_w$ and $\rho_e = \rho_w$, then Eqs.(3.41) become

$$f_e - f_w = 0 \tag{3.48a}$$

$$2u(f_e - f_w) + p_e - p_w = 0 \tag{3.48b}$$

Now, irrespective of any definition used for f_e and f_w, substitution of the first equation into the second one gives

$$p_e - p_w = 0 \tag{3.49}$$

Considering the $p_e = \frac{P_E + P_P}{2}$ and $p_w = \frac{P_P + P_W}{2}$ approximations will result

$$P_E - P_W = 0 \tag{3.50}$$

This shows that the possibility of a checkerboard problem still exists in this colocated grid arrangement even with the strong coupling of pressure and momentum dependent variables. Thus, the appearance of pressure in the continuity equation is not the complete remedy for a colocated grid approach. The next sub-section introduces a remedy to eliminate this checkerboard difficulty.

3.5.2 A Solution to the Decoupling Problem

A general remedy to the pressure-velocity decoupling problem is the employment of a staggered grid scheme [1]. However, the current method has been established on a colocated grid arrangement which is proposed as being an advantage of the method, Section 1.3. The difficulty could be overcome by introducing a new set of momentum components at integration points. The new set should not only involve all aspects and physics of the flow but also consider the satisfaction of mass which the single integration point equation does not. This proposed new set of variables could be used in conjunction with the continuity equation and wherever conservation of mass is addressed. Karimian and Schneider [33] present an argument to obtain the best new set of velocity components at integration points. It is deduced that the equation which involves both momentum and continuity equation errors works well. Following their conclusion, a two-parts equation is presented to derive the second set of momentum components at integration points

$$\text{(Momentum Equation Error)} - u\text{(Continuity Equation Error)} = 0 \qquad (3.51)$$

The main idea is to invoke the role of conservation of mass in the integration point equations. Such an equation has the effect of invoking momentum and mass conservation, even though it is indirect. We write a general form of this equation using Eqs.(3.1 and 3.2)

$$\left[\frac{\partial f}{\partial \theta} + f\frac{\partial u}{\partial x} + u\frac{\partial f}{\partial x} + \frac{\partial p}{\partial x} - \frac{\partial}{\partial x}\Gamma\frac{\partial u}{\partial x} - s_f\right] - \alpha u\left[\frac{\partial \rho}{\partial \theta} + \frac{\partial f}{\partial x} - s_m\right] = 0 \qquad (3.52)$$

where α is an arbitrary coefficient which determines the degree to which the continuity equation error is involved. The discretization of this equation is exactly similar to what was done for the momentum integration point equation, Eqs.(3.22-3.26). In this regard, similar terms in the two braces are added and transient terms are treated like previous treatments for the transient terms. The final result is

$$\begin{aligned}\hat{f}_e \;=\; & \frac{1}{2}\frac{\bar{\rho}_e}{\bar{\varrho}_P}\left(\frac{2+\mathbb{P}+(1-\alpha)\frac{\bar{\varrho}_P}{\bar{\rho}_e}\mathbb{P}}{(\frac{1}{4\mathbb{C}}+1-\frac{\alpha}{2})\mathbb{P}+2}\right)F_P+\frac{\bar{\rho}_e}{\bar{\varrho}_E}\left(\frac{1}{(\frac{1}{4\mathbb{C}}+1-\frac{\alpha}{2})\mathbb{P}+2}\right)F_E \\ & +\frac{1}{4\bar{u}_e[\frac{1}{4\mathbb{C}}+1-\frac{\alpha}{2}+\frac{2}{\mathbb{P}}]}(P_P-P_E)+\frac{f_e^o}{1+2\mathbb{C}(2-\alpha)+\frac{8\mathbb{C}}{\mathbb{P}}} \\ & +\frac{\alpha\Delta x}{4[\frac{1}{4\mathbb{C}}+1-\frac{\alpha}{2}+\frac{2}{\mathbb{P}}]}\overline{\frac{\partial\rho}{\partial\theta}}+\frac{\Delta x}{4\bar{u}_e[\frac{1}{4\mathbb{C}}+1-\frac{\alpha}{2}+\frac{2}{\mathbb{P}}]}(s_f-\alpha\bar{u}_e s_m) \qquad (3.53)\end{aligned}$$

This new integration point expression is different from Eq.(3.28). We name it *convecting momentum* or *mass conserving momentum* because the conservation of mass is included in it. The hat on this variable, $\hat{f}$, distinguishes it from the *convected* one, f, which was presented before by Eq.(3.28). Comparing Eq.(3.53) with Eq.(3.28) shows that the convecting momentum and convected momentum are the same for α=0. The general convecting expression can be simplified to the special case of steady-state, Euler flow, i.e.,

$$\hat{f}_e=\frac{(1-\alpha)+\frac{\bar{\rho}_e}{\bar{\varrho}_P}}{2-\alpha}F_P+\frac{1}{2\bar{u}_e(2-\alpha)}(P_P-P_E)+\frac{\Delta x}{2\bar{u}_e(2-\alpha)}(s_f-\alpha\bar{u}_e s_m) \qquad (3.54)$$

Differing values of the arbitrary coefficient, α, will change the influence of nodal parameter values. This is shown for two different values of α in incompressible flow

$$\alpha=0 \qquad \hat{f}_e=F_P+\frac{1}{4\bar{u}_e}(P_P-P_E)+\frac{\Delta x}{4\bar{u}_e}s_f \qquad (3.55)$$

$$\alpha=1 \qquad \hat{f}_e=F_P+\frac{1}{2\bar{u}_e}(P_P-P_E)+\frac{\Delta x}{2\bar{u}_e}(s_f-2\bar{u}_e s_m) \qquad (3.56)$$

Before closing this section, it is instructive to show that the use of two integration point equations for the momentum components does not permit the checkerboard problem to persist. In this regard, Eqs.(3.48) are written in the forms that involve both convected and convecting momentums

$$\hat{f}_e - \hat{f}_w = 0 \tag{3.57a}$$

$$2u(f_e - f_w) + p_e - p_w = 0 \tag{3.57b}$$

where f_e and f_w are substituted from Eqs.(3.42). Similar convecting momentums are derived from Eq.(3.56) considering incompressible flow conditions with no source term

$$\hat{f}_e = \quad F_P + \tfrac{1}{2\bar{u}_e}(P_P - P_E) \tag{3.58a}$$

$$\hat{f}_w = \quad F_W + \tfrac{1}{2\bar{u}_w}(P_W - P_P) \tag{3.58b}$$

By comparing with Eqs.(3.42), it is possible to relate the convected and convecting momentums, i.e.,

$$\hat{f}_e = \quad f_e + \tfrac{1}{4\bar{u}_e}(P_P - P_E) \tag{3.59a}$$

$$\hat{f}_w = \quad f_w + \tfrac{1}{4\bar{u}_w}(P_W - P_P) \tag{3.59b}$$

These expressions are substituted in Eq.(3.57a). Assuming u_e=u_w will result in

$$f_e - f_w = \frac{1}{4\bar{u}}(P_W - 2P_P + P_E) \tag{3.60}$$

This result can be substituted in Eq.(3.57b) where p_e and p_w are approximated by linear interpolation of the neighboring nodal pressures. The result is

$$P_E - P_P = 0 \tag{3.61}$$

Contrary to Eq.(3.50), here adjacent nodes are connected and thus the checkerboard problem as we know it does not arise. A similar investigation shows that a zig-zag pressure field like Eq.(3.46) cannot result in a zig-zag momentum/velocity field like

Eq.(3.47). This new *momentum convecting* equation is a remedy for elimination of the checkerboard problem. In the next section, other possible techniques for deriving convecting momentum-variables are described.

3.5.3 Other Possible Solutions

Although the discretization of Eq.(3.52) was done similar to what had been done for Eq.(3.21), it is possible to treat the convection terms in different manners to get different formulations. Both the convected equation, Eq.(3.31), and the convecting equation, Eq.(3.54), show that the momentum integration value is related to its upstream nodal momentum value for steady-state Euler flow. However, it can be argued that the integration point values should depend on both upstream and downstream nodal values. To examine this, the $u\frac{\partial(\rho u)}{\partial x}$ term, which is a common term in both the continuity and momentum equations, is discretized in different ways. Once more, Eq.(3.52) is repeated here while the concern is only on $u\frac{\partial(\rho u)}{\partial x}$ terms in those two braces, i.e.,

$$\underbrace{\left[\ldots + u\frac{\partial(\rho u)}{\partial x} + \ldots\right]}_{\text{Momentum Error}} - \alpha u \underbrace{\left[\ldots + \frac{\partial(\rho u)}{\partial x} + \ldots\right]}_{\text{Continuity Error}} = 0 \qquad (3.62)$$

Considering the physical interpretation of the $u\frac{\partial(\rho u)}{\partial x}$ term in both the continuity and momentum equation parts could result in different discretizing options. Table 3.1 summarizes some of the possibilities. The first row of the table represents Method I which was used in the preceding sub-section to derive $\hat{f}_e$. The results of that formulation were presented there. Now, if central differencing is employed to the term in both braces the method is named Method II. The result of this approach

	in Momentum Equation	in Continuity Equation
Method I	Upwind Difference	Upwind Difference
Method II	Central Difference	Central Difference
Method III	Upwind Difference	Central Difference
Method IV	Central Difference	Upwind Difference

Table 3.1: Different method of treating $\frac{\partial(\rho u)}{\partial x}$ in mass conserving equation.

for steady-state Euler flow is

$$\hat{f}_e = \frac{\bar{\rho}_e}{\bar{\varrho}_P} F_P + \frac{\alpha - 1}{2}(F_E - F_P) + \frac{1}{2\bar{u}_e}(P_P - P_E) + \frac{\Delta x}{2\bar{u}_e}(s_f - \alpha \bar{u}_e s_m) \tag{3.63}$$

The influence of neighbouring momentum nodal values is again changed if α is changed. This is examined for incompressible flow

$$\alpha = 1 \qquad \hat{f}_e = F_P + \frac{1}{2\bar{u}_e}(P_P - P_E) + \frac{\Delta x}{2\bar{u}_e}(s_f - \bar{u}_e s_m) \tag{3.64}$$

$$\alpha = 2 \qquad \hat{f}_e = \frac{F_P + F_E}{2} + \frac{1}{2\bar{u}_e}(P_P - P_E) + \frac{\Delta x}{2\bar{u}_e}(s_f - 2\bar{u}_e s_m) \tag{3.65}$$

The change of α from 1 to 2 provides for this interpolation to be changed from an absolute upwind to an absolute average of neighbouring nodal momentum values.

Another way for treating the $u\frac{\partial(\rho u)}{\partial x}$ term is a combination of upwind differencing for the momentum part and central differencing for the continuity part, Method III. This form ratifies the convecting prescription for the continuity equation and the convected prescription for the momentum equation. The result for steady-state Euler flow is

$$\hat{f}_e = \frac{1}{2}(1 + \frac{\bar{\rho}_e}{\bar{\varrho}_P})F_P + \frac{\alpha}{4}[F_E - F_P] + \frac{(P_P - P_E)}{4\bar{u}_e} + \frac{\Delta x}{4\bar{u}_e}(s_f - \alpha \bar{u}_e s_m) \tag{3.66}$$

When $\alpha \rightarrow 0$, this equation approaches the limiting convected equation, Eq.(3.31). In this case, both convected and convecting momentums are the same. However, for α=2 in incompressible flows, the average of neighbouring nodal momentums results for approximating the integration point equation,

$$\alpha = 2 \qquad \hat{f}_e = \frac{F_P + F_E}{2} + \frac{1}{4\bar{u}_e}(P_P - P_E) + \frac{\Delta x}{4\bar{u}_e}(s_f - 2\bar{u}_e s_m) \tag{3.67}$$

There is a fourth method, Method IV, which uses central differencing for the momentum part and upwind differencing for the continuity part. The upwind model was used to treat the continuity parts in Method I where the purpose was to make a consistent discretization for similar differential terms of the equation. Generally speaking, the main idea in deriving a convecting equation is to employ upwind differencing for momentum convection terms and central differencing for the continuity terms, however, Method IV is presented as yet another possible option. The result of this case for steady-state Euler flow is

$$\begin{aligned} \hat{f}_e \;=\; & \frac{\alpha - \frac{\bar{\rho}_e}{\bar{\varrho}_P}}{\alpha - 1} F_P + \frac{1}{2(1-\alpha)}(F_P + F_E) + \frac{1}{2\bar{u}_e(1-\alpha)}(P_P - P_E) + \\ & \frac{\Delta x}{2\bar{u}_e(1-\alpha)}(s_f - \alpha \bar{u}_e s_m) \end{aligned} \tag{3.68}$$

Considering α=0 reduces this equation to the following form for incompressible flow conditions:

$$\alpha = 0 \qquad \hat{f}_e = \frac{3}{2}F_P + \frac{1}{2}F_E + \frac{1}{4\bar{u}_e}(P_P - P_E) + \frac{\Delta x}{4\bar{u}_e}(s_f - 2\bar{u}_e s_m) \tag{3.69}$$

which is an inappropriate expression for approximating the momentum integration point value. However, considering α=2 improves it to an appropriate expression

$$\alpha = 2 \qquad \hat{f}_e = \frac{F_P + F_E}{2} + \frac{1}{2\bar{u}_e}(P_P - P_E) + \frac{\Delta x}{2\bar{u}_e}(s_f - 2\bar{u}_e s_m) \tag{3.70}$$

These different methods were studied in a one-dimensional procedure for which results are presented in Section 3.7.

3.6 Velocity Component Based Formulation

At this stage, the one-dimensional modeling for the momentum component formulation is complete. This formulation provides the mechanism with which to examine different one-dimensional test problems with regards to its ability to solve such problems. However, the solution of these test problems by itself does not provide any advantages or disadvantages with respect to the velocity-variable formulation. Where feasible, a comparison will be made of the results of the momentum-variable formulation with those of the velocity-variable formulation. In this respect, we will be concerned with methods which have been developed for solving compressible and incompressible flows at all-speeds. The work of Karimian and Schneider [33] is the best among the available methods for such flows. They provide a damping mechanism in their formulation in order to avoid spatial oscillations in the vicinity of discontinuities and shocks. This damping also results in improved convergence. Since the current method is free from employing any damping mechanism, a comparison between the two formulations will be performed on the basis of there being no damping or density averaging in either method.

In order to pursue this latter idea, the one-dimensional approach of Karimian and Schneider [65], who apply it to the shock tube problem, is formulated in the following. A clearer comparison will be obtained if the energy equation can be separated from the continuity and momentum equations. In this way only the flow couplings are considered and the additional complications of the energy equation and its couplings are avoided. Thus, an isothermal flow is assumed throughout the domain and a constant temperature field is specified via the energy equation. The statement of conservative for the mass and momentum equations can be obtained from Eqs.(3.1 and 3.2) assuming zero diffusion and source terms. The final form of these statements can be directly written from Sections 3.3.1 and 3.3.2 as

$$\frac{J_P}{\Delta\theta}(\varrho_P - \varrho_P^o) + (\rho u)_e - (\rho u)_w = 0 \tag{3.71}$$

$$\frac{J_P}{\Delta\theta}((\varrho U)_P - (\varrho U)_P^o) + (\rho uu)_e - (\rho uu)_w + p_e - p_w = 0 \tag{3.72}$$

The transient term in the continuity equation and the pressure term in the momentum equation are treated as in Sections 3.3.1 and 3.3.2, respectively. The convection term in the momentum equation is simply linearized respect to the velocity-variable, i.e. $\rho uu = (\overline{\rho u})u$. However, the mass flux terms in the continuity equation require special treatment. They are treated by using a Newton-Raphson linearization, Eq.(B.6). This treatment, which was introduced in Section 2.4.3, allows the strong importance of density in highly compressible flows to shift to that of velocity in the incompressible limit. The mass flux is given by

$$\rho u = \bar{\rho} u + \bar{u}\rho - \overline{\rho u} \tag{3.73}$$

The non-linear density in the second term on the right-hand-side is determined by

$$\rho_e = \frac{1}{R\bar{T}_P} P_P + \frac{\bar{\varrho}_E - \bar{\varrho}_P}{2} \tag{3.74}$$

The non-linear transient term in the momentum equation is first treated by a Newton-Raphson linearization, i.e. $\varrho U = \bar{\varrho} U + \bar{U}\varrho - \overline{\varrho U}$. Then, the non-linear density is treated by using Eq.(B.5).

In the next step, the convected velocity at the integration point is derived from the non-conservative form of the momentum equation, i.e.,

$$\rho\frac{\partial u}{\partial\theta} + \rho u\frac{\partial u}{\partial x} + \frac{\partial p}{\partial x} = 0 \tag{3.75}$$

Writing a backward difference in time, an upwind difference approximation for the convection term, and a central difference approximation for the pressure term and rearranging the resulting terms give the following expression

$$u_e = \frac{2\mathbb{C}}{1+2\mathbb{C}}\, U_P + \frac{\mathbb{C}}{\bar{\rho}_e \bar{u}_e (1+2\mathbb{C})}\, (P_P - P_E) + \frac{u_e^o}{1+2\mathbb{C}} \tag{3.76}$$

This integration point velocity is the convected one which is substituted into the convection term of the momentum equation. Similarly, the convecting velocity at the integration point is derived from the following equation

$$(\rho\frac{\partial u}{\partial \theta} + \rho u \frac{\partial u}{\partial x} + \frac{\partial p}{\partial x}) - u(\frac{\partial \rho}{\partial \theta} + u\frac{\partial \rho}{\partial x} + \rho\frac{\partial u}{\partial x}) = 0 \tag{3.77}$$

where the term in the first parenthesis is modeled using central differencing for the spatial derivatives and backward differencing in time for the transient term. The following result is obtained after some rearrangement

$$\hat{u}_e = \frac{\mathbb{C}}{1+2\mathbb{C}}\, (U_P + U_E) + \frac{\mathbb{C}}{\bar{\rho}_e \bar{u}_e (1+2\mathbb{C})}\, (P_P - P_E) + \text{TERMS} \tag{3.78}$$

where

$$\text{TERMS} = \frac{\bar{u}_e}{\bar{\rho}_e(1+2\mathbb{C})}\, (\bar{\rho}_e - \rho_e^o) + \frac{\bar{u}_e \mathbb{C}}{\bar{\rho}_e(1+2\mathbb{C})}\, (\bar{\varrho}_E - \bar{\varrho}_P) + \frac{u_e^o}{1+2\mathbb{C}} \tag{3.79}$$

This convecting velocity at the integration point is substituted into the mass flux terms of the continuity equation, Eq.(3.73).

Now, the modeling of velocity-variable formulation is now complete. However, Karimian and Schneider [65] improve this formulation by treating TERMS in Eq.(3.78) and the second term on right-hand side of Eq.(3.74) using an *absolute harmonic interpolation* scheme. This treatment damps oscillations in the vicinity of shock waves and discontinuities in the numerical solution.

3.7 Applications

To check the accuracy of our numerical solutions, a comparison will be made with an exact analytical solution for incompressible and compressible Euler flows. Although our interest in this research is in solving the complete Navier-Stokes equations, the Euler equations are of importance in many flows and do exhibit the strong coupling between velocity, pressure, and density. They therefore provide a good preliminary tool to evaluate the performance of a Navier-Stokes solver. In this section, source and sink test cases are first applied to incompressible flows and the results are examined. Subsequently, the shock tube problem is examined to examine the compressible part of the method. Finally, a direct comparison between the results of momentum-based and velocity-based formulations is provided.

3.7.1 Incompressible Flow

The main purpose here is to examine the checkerboard problem in a flow field when a sudden positive or negative change in mass or pressure is imposed. Therefore, the source terms in the continuity and momentum equations have non-zero values. The test case is a one-dimensional, steady-state, Euler flow through a constant area channel with unit length and with mass/pressure-source/sink inside it. There are twenty-one uniform node distributions. The source and sink divide the domain into three equal parts, Figure 3.2. For the sake of space, some part of domain has not been shown in this figure. The mass is specified at the upstream boundary and pressure is defined at the downstream boundary of the domain for boundary condition implementation. Also, mass and pressure are nondimensionalized with respect to inlet momentum component, F_{in}, and inlet dynamic pressure, $(\frac{1}{2}\rho U_{in}^2)$, respectively. Two different possible arrangements are considered for each source/sink. They are

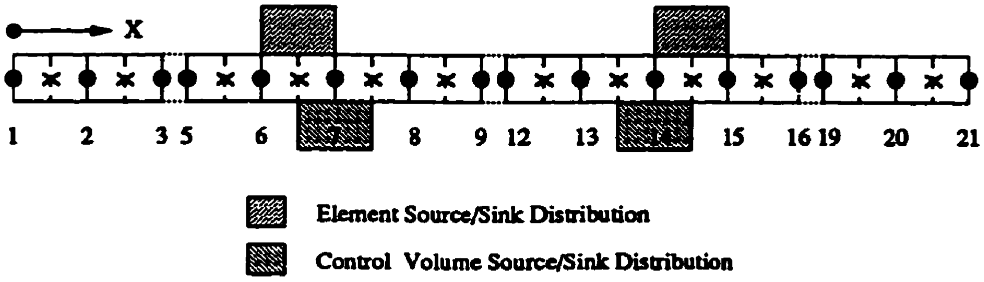

Figure 3.2: Source and sink distribution in one-dimensional domain.

defined by either two neighbouring nodes, named an element source/sink, or by two neighbouring integration points, named a control volume source/sink, Figure 3.2. If the source is distributed within an element, it is equally split between the two control volumes of that element.

The discretized equations of continuity and momentum have analytical solution for mass and pressure variables when element pressure-source/sink is located in the domain. For this case, the results of the code are confirmed by the analytical solution, Figure 3.3. This analytical solution cannot be obtained for other types of source and sink distributions. For the control-volume source/sink, there is some oscillations around the source and sink in the numerical results. These local oscillations around the source and sink do not reflect the checkerboard problem. For example, Figure 3.4 shows the results of code for locating a control-volume mass-source/sink in the domain. The numerical result does not fit the required distribution in the domain. In these distributions, the migration from before to after a source happens within more than one discrete distance between two integration points or nodes. Figures 3.5 and 3.6 show the results of the code for locating an element mass-source/sink in the domain. One applies the mass conserving approach and the other does not. If the mass conserving equation is not applied in the

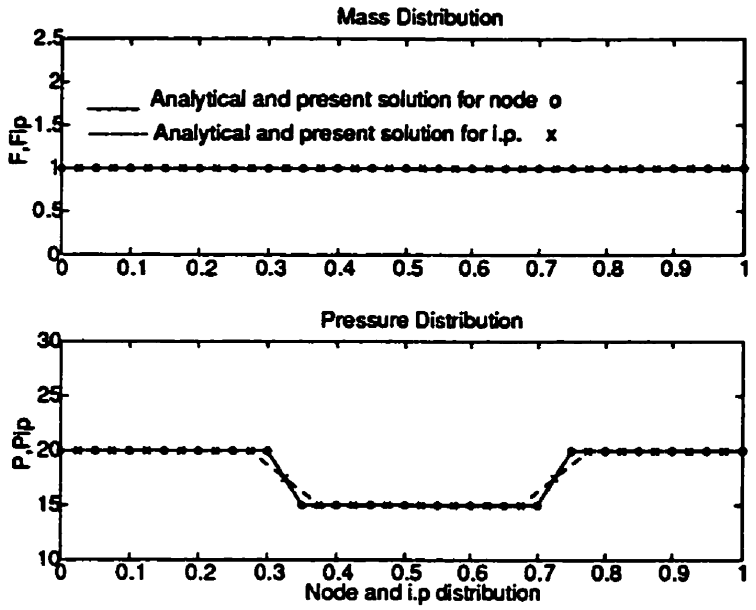

Figure 3.3: The effect of element pressure-source/sink on pressure and velocity distributions.

continuity equation instead of convected one, the pressure checkerboard problem appears, Figure 3.5, while the use of a convecting equation does not allow the growth of non-physical oscillations in the domain, Figure 3.6. This has also been shown for the other type of source/sink configuration in the domain. For example, Figures 3.7 and 3.8 illustrate the difference for a control-volume pressure-source/sink considerations. The lack of mass conserving equation will result non-physical solution in domain.

All the results of this section (up to here) were obtained by employing the convecting momentum expression of Method I into the continuity equation and considering α=1, Eq.(3.56). The depicted figures show that mass is constant in passing through pressure-source/sink while pressure is not constant passing through a mass-source/sink. The use of momentum convecting equations in continuity equa-

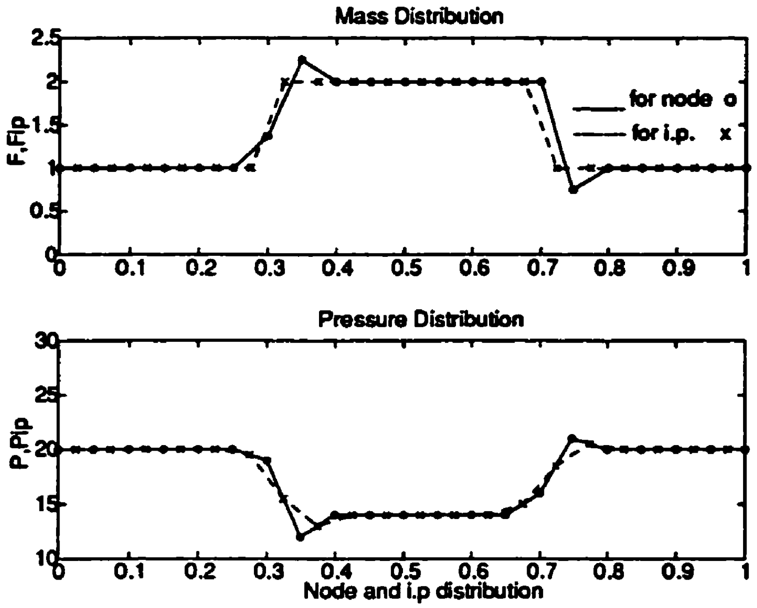

Figure 3.4: The effect of control-volume mass-source/sink on pressure and velocity distributions.

equation removes the checkerboard problem and restricts oscillations to three nodes or less.

There are also many other results with employing Method II and Method III of Section 3.5.3. They show satisfactorily results in removing the pressure checkerboard problem. These results have been compared with each other. Generally, Method I shows better or similar results compared with Method II and Method III. For example, Figure 3.9 shows the pressure distribution comparison when control-volume pressure-source/sink is located in the domain. The Method II with α=2, Eq.(3.65), shows overshoot and undershoot in the neighbouring nodal values but Method I with α=1, Eq.(3.56), shows just one stronger overshoot downstream of the source or sink. Three nodal points are affected by the sink/source in the Method II while this is decreased to two nodes in Method I. The reason for the difference in

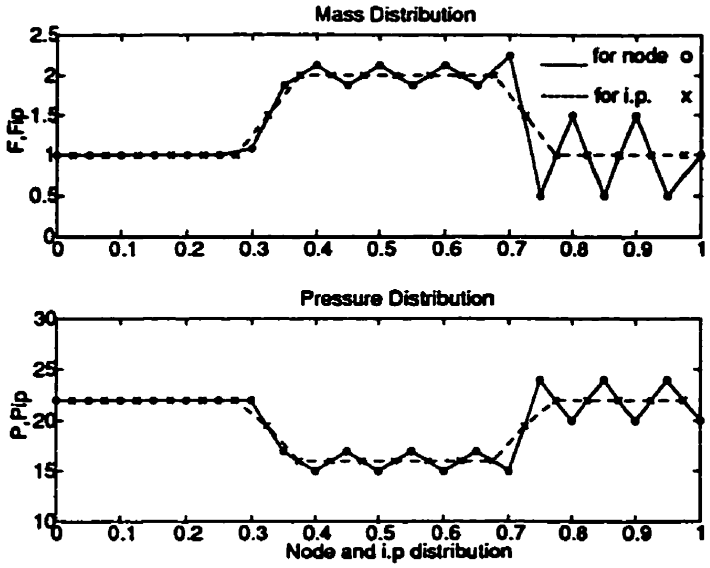

Figure 3.5: The effect of element mass-source/sink on pressure and velocity distributions without using *convecting momentum* equation.

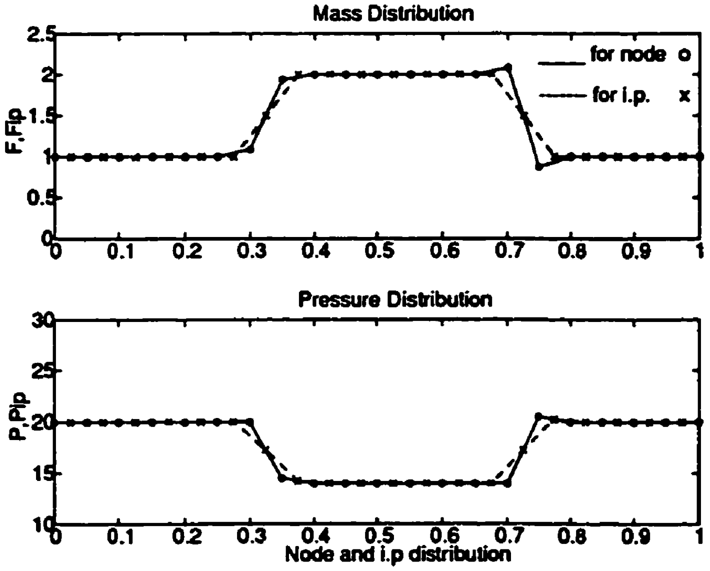

Figure 3.6: The effect of element mass-source/sink on pressure and velocity distributions.

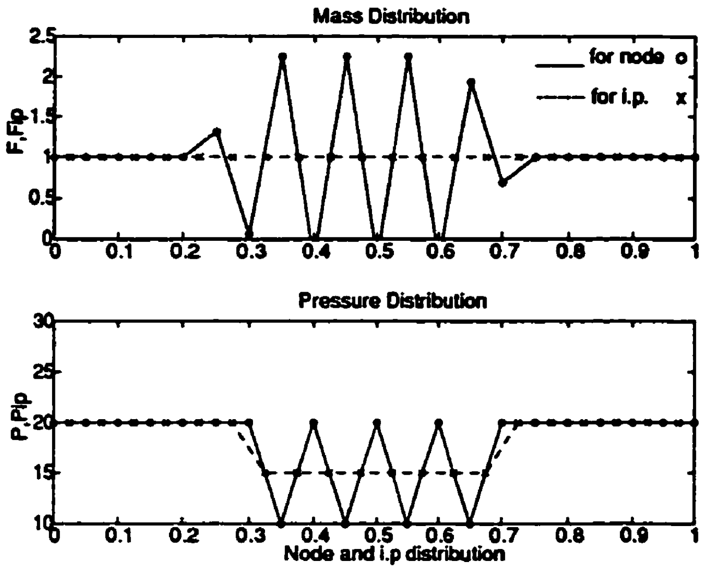

Figure 3.7: The effect of control-volume pressure-source/sink pressure and velocity distributions without using *convecting momentum* equation.

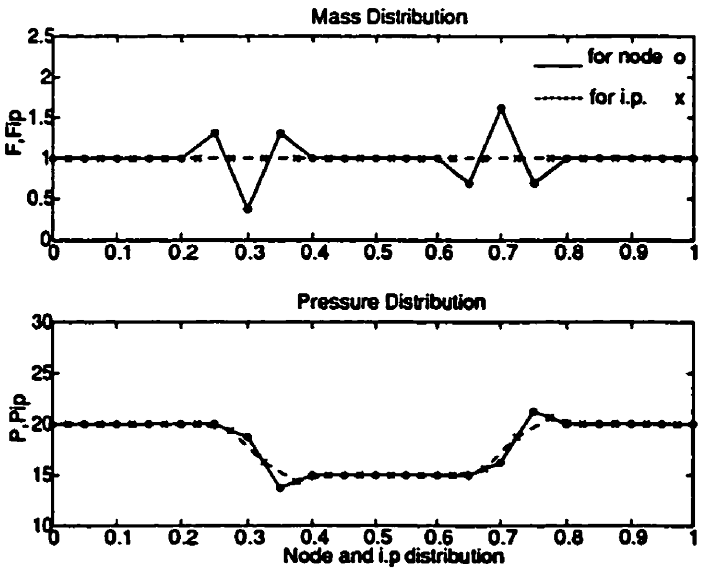

Figure 3.8: The effect of control-volume pressure-source/sink on pressure and velocity distributions.

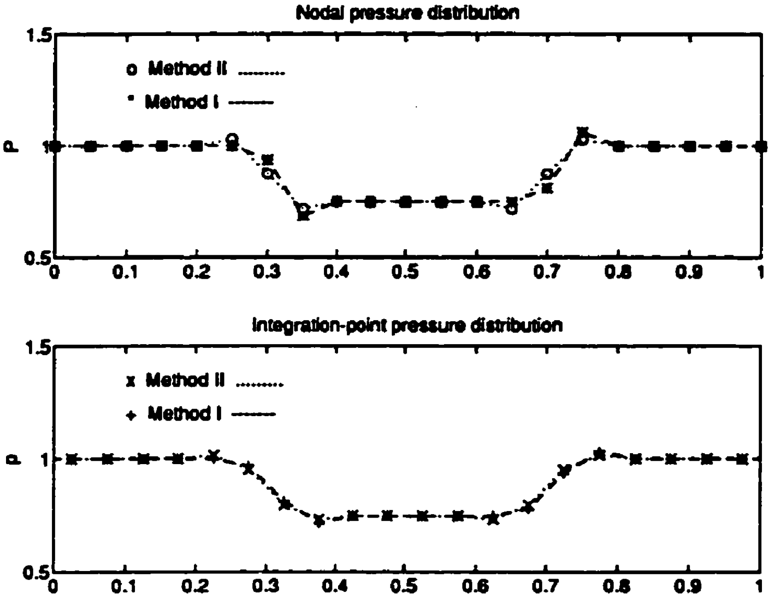

Figure 3.9: Comparing the numerical results of Method I and II using control-volume pressure-source/sink in domain.

solutions returns to the connection of momentum components at integration point to its neighbouring nodes. In an upwind scheme, the integration point is affected by upstream values while in central differencing scheme, the effect is from both upstream and downstream values.

3.7.2 Compressible Flow

Here, the shock tube problem has been selected to present the results of the one-dimensional formulation for compressible flow. The selection of the shock tube problem as a test case is due to the availability of its analytical solution which enables us to examine the accuracy of the numerical solution. On the other hand, this transient problem includes both transient flow features and a wide range of Mach number, i.e., a moving normal shock wave, expansion waves, a contact discontinuity, and having subsonic, transonic, and supersonic regimes.

The shock tube geometry and wave pattern is shown in Figure 3.10. The pressures at the left and right of the diaphragm are taken as 1000kPa and 100kPa, respectively. The temperature is uniform throughout the shock tube at 25 $^{\circ}C$ before rupturing the diaphragm. Gas properties are $c_v = 720\ J/kgK$, $R = 287.0\ J/kgK$, and $\gamma = 1.4$. To the left of the contact line, gas expansion causes a reduction in temperature, whereas to the right of the discontinuity, the compressed wave raises the temperature of the gas. At the contact line, there is a discontinuity in the temperature profile and hence the density profile.

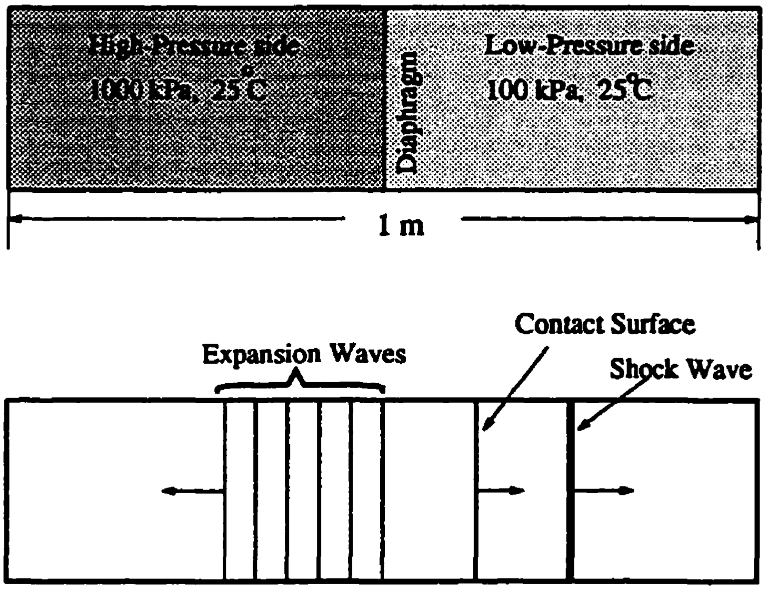

Figure 3.10: Shock tube problem and its wave pattern.

The results show the mass flux, pressure, temperature, and density distributions throughout the shock tube 500 μs after rupturing the diaphragm. The exact solution is superposed in all figures. 201 nodes are chosen with a time step of 0.7 μs. The pressure and temperature are nondimensionalized by lower pressure side values and the initial temperature of the shock tube, respectively. The convergence criterion in each time step is checked for all nodes,

$$Max\left\| \frac{P_i - \bar{P}_{i-1}}{P_i} \right| , \left| \frac{T_i - \bar{T}_{i-1}}{T_i} \right\|_{i=1,N} < \epsilon \tag{3.80}$$

where i indicates the node number and $\epsilon=10^{-5}$.

The shock tube problem is examined both for different Courant numbers and for Methods I, II, and III. Figure 3.11 shows the results employing the mass conserving procedure of Method I. The moving shock wave is captured within a few nodes, but some overshoot is seen downstream of the shock wave. The Courant number for this case is 0.4. In order to find the limits of stability for our implicit algorithm, the time step is gradually increased to increase the Courant number. Figures 3.12 and 3.13 show the results with larger time step sizes, i.e., Δt=12μs and Δt=17μs, respectively. They show that the method is stable for higher Courant numbers of

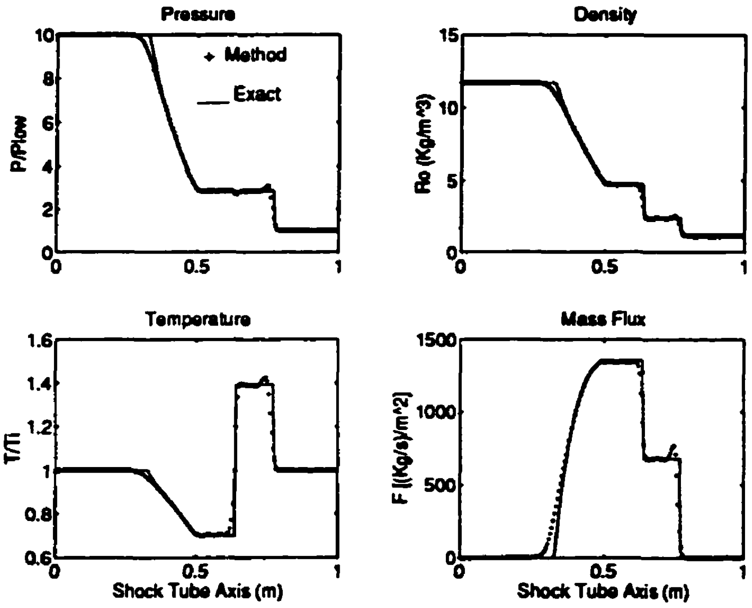

Figure 3.11: Shock tube results for Method I with α =1, C=0.4, and 201 nodes.

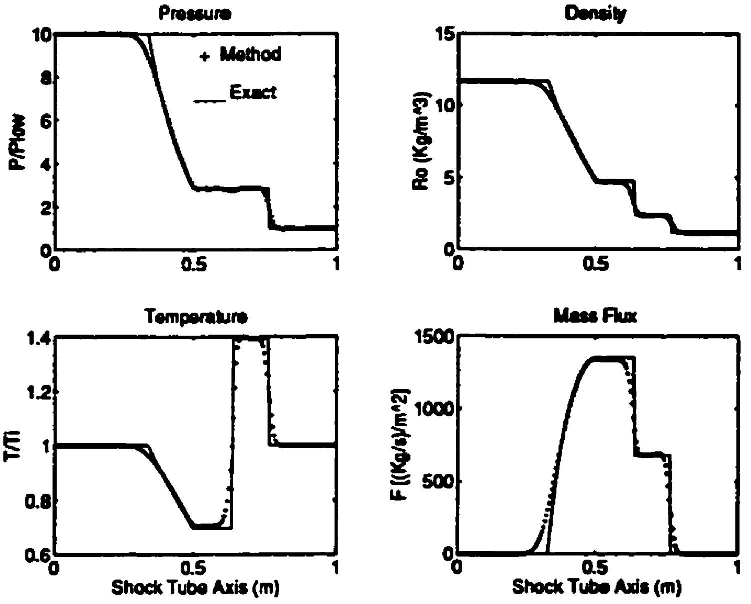

Figure 3.12: Shock tube results for Method I with α=1, C=0.7, and 201 nodes.

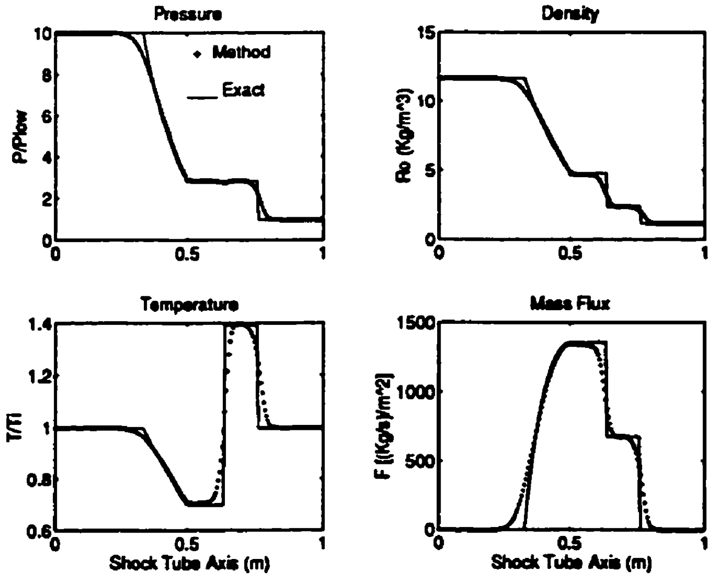

Figure 3.13: Shock tube results for Method I with α=1, C=1.0, and 201 nodes.

C=0.7 and C=1.0, respectively. The increase in Courant number does cause more smearing around discontinuities because the transient details are not captured accurately in fully implicit methods with large time steps. No limits were encountered for higher Courant numbers. There are results available for Courant number of C=6.3 which are not presented here.

In the second stage, compressible flow is tested for two more test cases involving Method II and Method III. The results have been depicted in Figures 3.14 and 3.15 for Method II with α=1 and for Method III with α=2, respectively. The results of Method II are identical with the results of Method I because their formulation become identical for the defined α's in this test case. It is interesting to note that discontinuities are predicted within a fewer number of nodes in Method III, but at the cost of higher undershoot and overshoot around discontinuities.

The final stage is to study the effect of mesh refinement. Following the results presented in Figure 3.11, C=0.4 is selected as constant and Δt is changed for a total number of 151 nodes to maintain C=0.4. The results are seen in Figure 3.16. As is expected, sharp changes of the parameters are smeared and there would be less accuracy than the case of Figure 3.11 with 50 more nodes.

As the results show, all methods remove the checkerboard problem and provide the desired coupling between pressure and the momentum components. These preliminary results show good agreement with the theoretical solution although neither artificial viscosity nor other overshoot treatment is explicitly considered in the formulation. Moreover, no smoothing or damping function has been used to reduce oscillations. The results of this section confirm the success of the one-dimensional formulation for treating high speed flows.

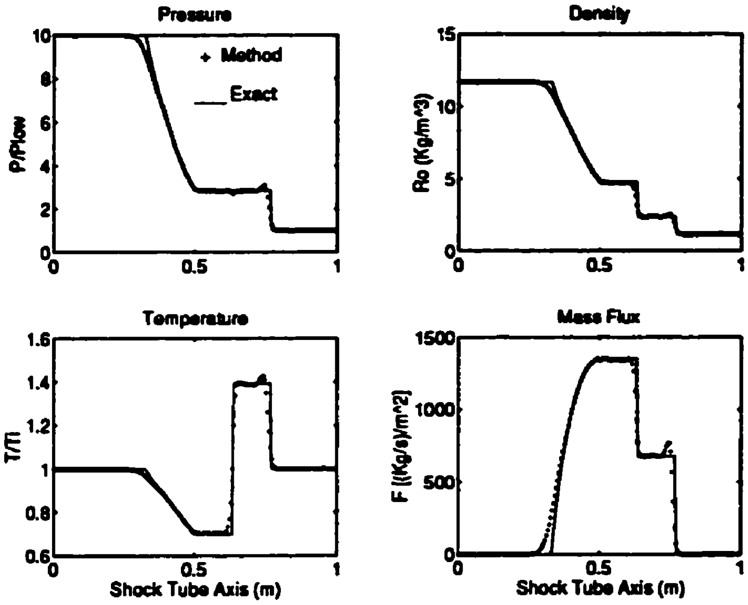

Figure 3.14: Shock tube, using Method II with α=1, C=0.4, and 201 nodes.

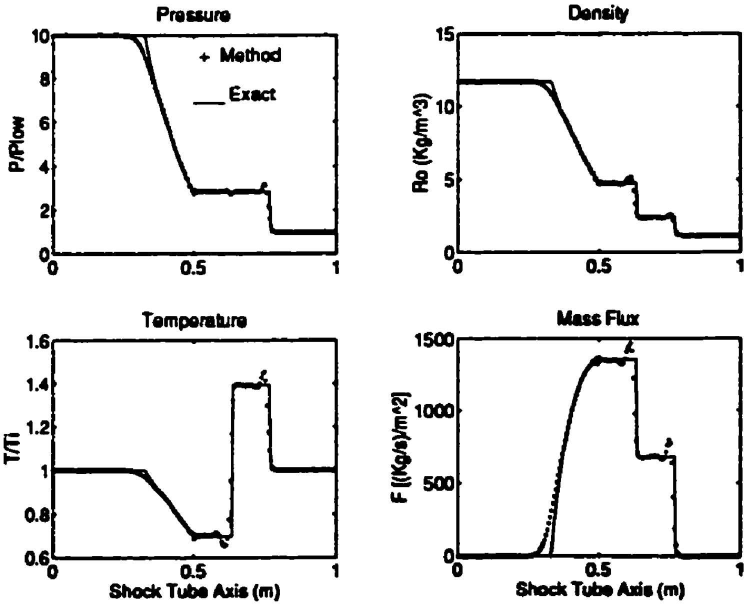

Figure 3.15: Shock tube, using Method III with α=2, C=0.4, and 201 nodes.

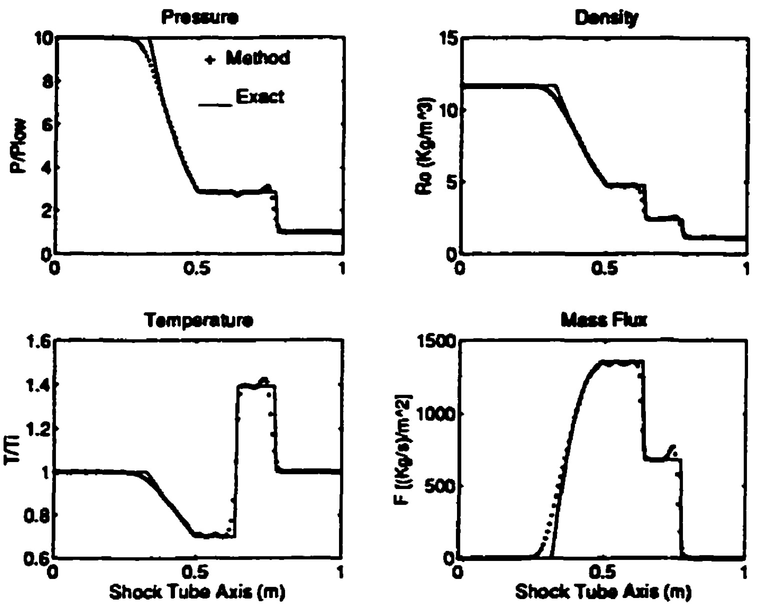

Figure 3.16: Shock tube results for Method I with α=1, C=0.4, and 151 nodes.

3.7.3 Comparison Between Velocity and Momentum Formulations

As the final step of the one-dimensional investigation, the performance of the momentum component formulation is compared with that of the velocity component formulation. In this way we are able to investigate some of the potential advantages of the momentum component formulation. One advantage relates to the benefits of using mass flux variable instead of the velocity-variable, Section 2.4.2, for flows involving discontinuities, and another relates to the benefits of simplifying the difficult treatment of nonlinearities, Section 2.4.3. The shock tube problem and the quasi-one-dimensional converging-diverging nozzle problem are two one-dimensional test problems which can be used to investigate the potential advantages of the momentum-variable formulation in high speed flows with shocks. In this section, we pursue this investigation for the shock tube problem which is a more difficult problem as was mentioned in Section 3.7.2. The initial conditions, the gas properties, and the nodes distributions are defined as before. This investigation is restricted to isothermal flow in order to provide a clearer comparison between the two formulations. Equation 3.80 is used as a measure of convergence for the pressure.

Figures 3.17 to 3.20 present the results obtained by both the velocity-based and the momentum-based formulations. They show the distributions throughout the shock tube $500\mu s$ after rupturing the diaphragm. The convergence criterion had been set $\epsilon=10^{-3}$ for both formulations in this test. The velocity-based results have been obtained by modeling the equations as presented in Section 3.6 which represents the work of Karimian and Schneider [65] except for the exclusion of the damping mechanisms of their formulation. They have presented a detailed study of their approach in solving the shock tube problem. The momentum-based formulation has been treated in a manner which provides more consistency with the velocity-based formulation. For example, the momentum convection term in this formulation, Eq.(3.12), is linearized very similar to the one in the velocity-based formulation, i.e. $k'=\frac{1}{2}$ and $k''=0$.

Several conclusions can be derived from this study and from examination of the presented figures. Generally speaking, the velocity-based formulation suffers from severe oscillations in the vicinity of the shock. Experience showed that there was also a maximum Courant number for the velocity-variable formulation that enabled solutions to be obtained. This value, $\mathbb{C}=0.1$, is the one for which the presented results have been obtained. Above this value, the method was unstable and diverged. However, the momentum-variable method converged for higher Courant numbers, up to $\mathbb{C}=2.2$, although the accuracy of the solution was degraded with increasing

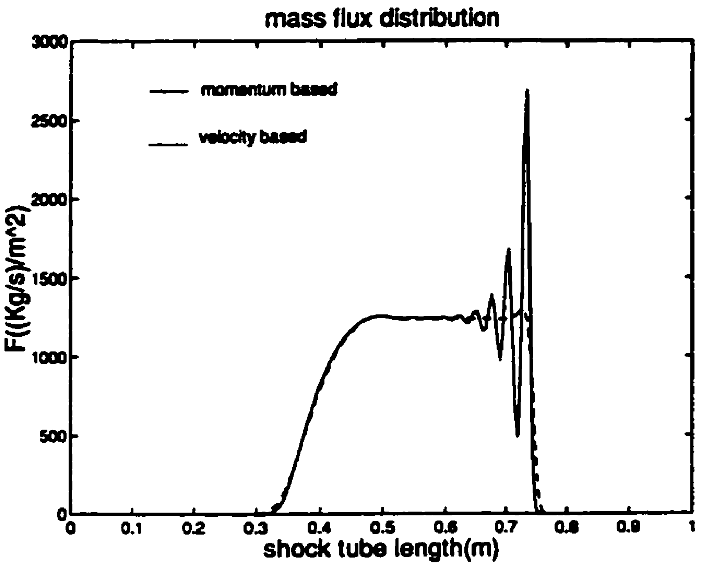

Figure 3.17: The comparison of mass flux distributions between velocity-variable and momentum-variable formulations, $\epsilon=10^{-3}$.

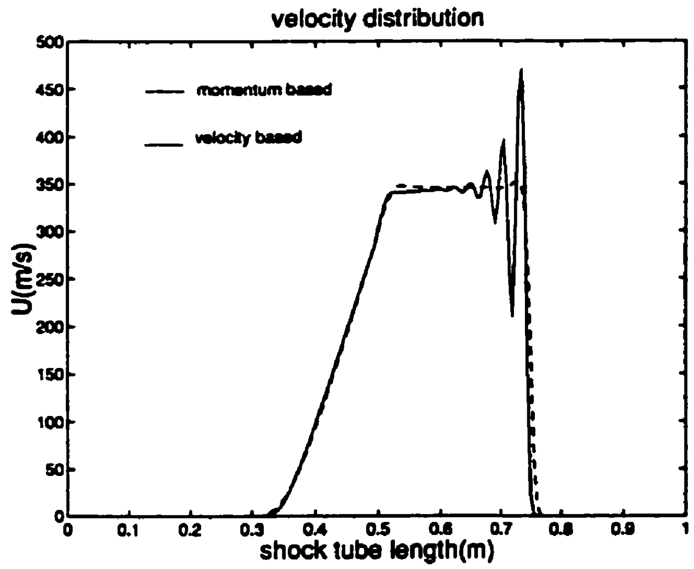

Figure 3.18: The comparison of velocity distributions between velocity-variable and momentum-variable formulations, $\epsilon=10^{-3}$.

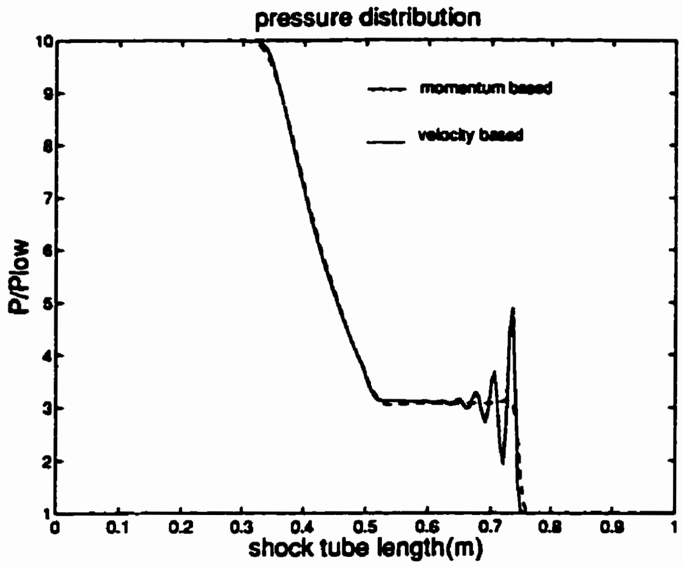

Figure 3.19: The comparison of pressure distributions between velocity-variable and momentum-variable formulations, ϵ=10^{-3}.

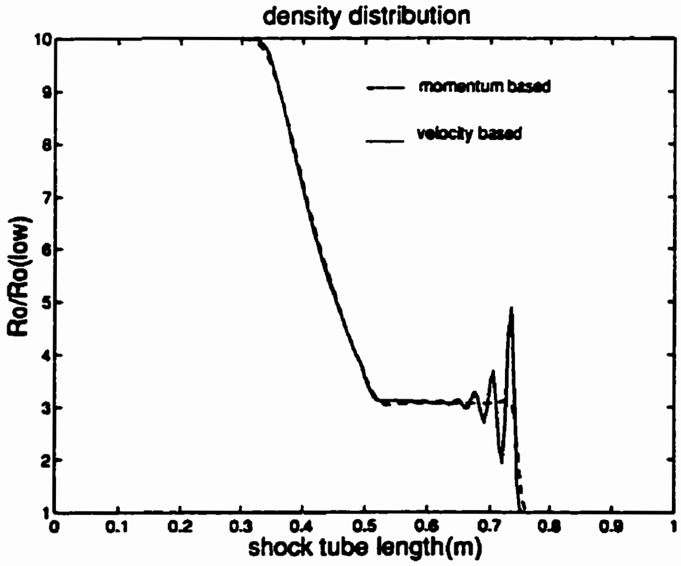

Figure 3.20: The comparison of density distributions between velocity-variable and momentum-variable formulations, ϵ=10^{-3}.

the Courant number. The presented results for the momentum-based formulation were obtained using C=0.35.

The distributions of the flow parameters in this isothermal study show fewer discontinuities than the corresponding distributions in Figures 3.11 to 3.16. This has been shown in Figure 3.21 by performing a rough comparison between the isothermal and non-isothermal exact solutions. In this figure, we are concerned only with the general distribution of the parameters rather than their exact values and positions. As seen, a constant temperature field results in no discontinuity in the form of a contact surface. However, there is still a sharp discontinuity with the moving shock which appears in all distributions including the mass flux distribution. These discontinuities are due to the nature of the problem which is a highly transient one. As a reminder, we were concerned with the two potential

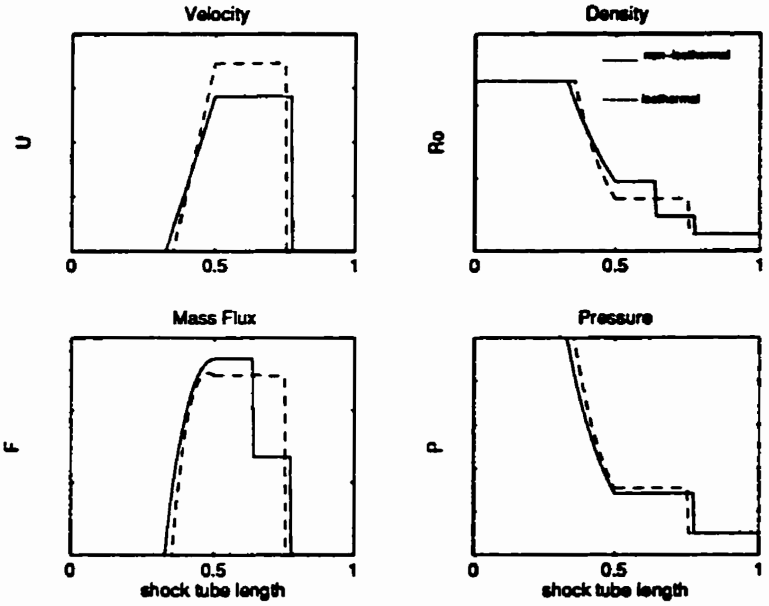

Figure 3.21: A rough comparison between isothermal and non-isothermal exact solutions in the shock tube problem.

advantages of the momentum-variable formulation, i.e. the constant mass flux through discontinuity and the nonlinearity treatment. Figure 3.21 shows that the number of discontinuities in the mass flux distribution is never less than the number of them in the velocity distribution. In other words, whereas F is indeed constant across a shock in steady flow, here it is not. This problem therefore demonstrates that the other aspects of the momentum-based formulation, related to linearization requirements, have resulted in superior results to those from the velocity-based formulation.

One more step was taken in this comparative study in order to check the stability of the two formulations for meeting lower convergence criterion. In this regard, the convergence criterion for the pressure was decreased from 10^{-3} to 10^{-5}. In this case, the velocity-based formulation diverged for the previous Courant number, $\mathbb{C}$=0.1. The maximum Courant number which enabled solutions to be obtained with this lower convergence criterion was $\mathbb{C}$=0.03. The results for this Courant number have been illustrated in Figures 3.22 and 3.23. They show much stronger oscillations in the domain comparing with the previous results. The results for the momentum-based formulation have been obtained for Courant number 0.35, as before, and an extremely low convergence criterion of 10^{-9}. The decrease of the convergence criterion from 10^{-3} to 10^{-9} increased the average number of iterations per time step from 5 to 14.

3.8 Closure

A one-dimensional investigation was performed in this chapter. The main purpose of this investigation was to ensure that the developed momentum-component procedure works well in its one-dimensional form and that all proposed objectives have

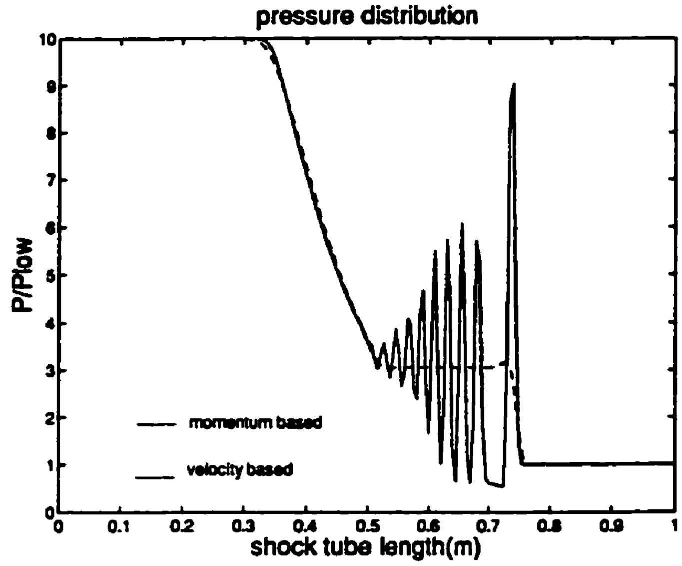

Figure 3.22: Comparison of pressure distributions between velocity-variable and momentum-variable formulations, ϵ=10^{-5}.

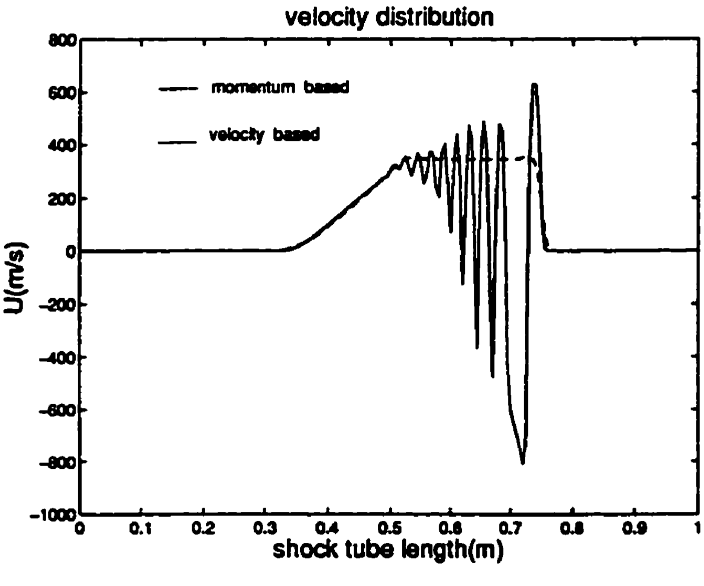

Figure 3.23: Comparison of velocity distributions between velocity-variable and momentum-variable formulations, ϵ=10^{-5}.

been satisfactorily achieved. In this regard, the control-volume-based formulation was applied to the one-dimensional governing equations. The related integration point operators were derived based on incorporating the correct physical influence of the flow and other relevant schemes. The simplified forms of the derived expressions were tested for special flow cases with different Peclet and Courant numbers for which the results illustrated a behaviour consistent with the physics of the flow. The pressure checkerboard problem was removed using convecting integration point operators for momentum components. In this regard, several integration point expressions were derived for use in the continuity equation which showed satisfactory results in coupling the velocity and pressure fields. The ability of the method to remove the pressure checkerboard problem was tested by putting a mass/pressure source/sink in one-dimensional compressible flows. The method worked effectively. In compressible flow, the new formulation was tested for the shock tube problem which has many features of high speed compressible flows including moving normal shock and expansion waves. There was no CFL number limit observed for the presented implicit algorithm.

A direct comparison of the velocity-based and momentum-based formulations was performed. It was shown that the velocity-based formulation produces severe spatial oscillations if an explicit damping mechanism is not employed. These oscillations subsequently resulted in increasing the number of iterations per time step and lowering the accuracy of the solution. Then, it was concluded that the momentum-based procedure produced more accurate and stable solution than the velocity-based procedure without damping.

The results of this chapter support the objectives of the current research and enable us to move towards extending the one-dimensional formulation to a two-dimensional momentum-component formulation.

Chapter 4

Computational Modeling in Two Dimensions

4.1 Introduction

The preliminary investigations and results for one-dimensional flow were accomplished in Chapter 3 and shown to be satisfactory. Here we extend the proposed approach to two-dimensions. In this regard, the necessary steps of the discretization procedure for the two-dimensional Navier-Stokes equations are presented in this chapter. These steps are similar to those taken in Chapter 3.

After the introduction, Section 4.2 provides definitions and descriptions which are used throughout this chapter. In order to discretize the two-dimensional governing equations, a control-volume-based finite-element approach is employed to integrate them over the control volumes in Section 4.3. The discretized equations which are derived in this manner require the evaluation of the dependent variables at control volume surfaces. Thus, the necessary integration point operators are derived in Section 4.4. This is where some important issues of convection-diffusion modeling and velocity-pressure coupling are discussed. The convecting momentum equations are obtained in Section 4.5. The results of previously-mentioned three sections are assembled in Section 4.6 where the element stiffness matrix is built. Finally, the techniques used to invoke boundary conditions are explained in Section 4.7.

4.2 Preliminary Definitions and Descriptions

In the following sections, the details of the discretization technique will be presented. In order to unify all definitions and conventions which are used during discretization, it is helpful to present them in an introductory section. This is accomplished in the current section.

The discretization is started by integrating the governing equations over control volumes. In the employed control-volume-based approach, the procedure of integration is accomplished in an element-by-element manner. The process, within all elements, is started from SCV1 (Sub Control Volume 1) of the element and extends to SCV4 of that element, Figure 2.1 in Section 2.2. In order to distinguish the sub-control-volumes, we use the index of i, $i = 1 \ldots 4$, at the end of SCV to identify the SCV in question, Table 4.1. Furthermore, i is the relevant node number in that SCV. There are four sides in each SCV only two of which are coincident with the corresponding control volume edges. For example, SS4 and SS1 are the edges when SCV1 is treated. For an arbitrary SCVi, these sub-surfaces are $S1i$ and $S2i$ for which the numbers represent the sub-surfaces when a counter-clockwise rotation is selected around the center of the element for traveling from one sub-surface of the SCVi to another. Table 4.1 also shows the arrangement of $S1i$ and $S2i$ for

SCVi	SCV1	SCV2	SCV3	SCV4
S1i,S2i	SS4,SS1	SS1,SS2	SS2,SS3	SS3,SS4
$\int_{S_i}$	$\int_{S_{SS4}} + \int_{S_{SS1}}$	$\int_{S_{SS1}} + \int_{S_{SS2}}$	$\int_{S_{SS2}} + \int_{S_{SS3}}$	$\int_{S_{SS3}} + \int_{S_{SS4}}$
$\mathcal{V}_i$	$\mathcal{V}_{SCV1}$	$\mathcal{V}_{SCV2}$	$\mathcal{V}_{SCV3}$	$\mathcal{V}_{SCV4}$

Table 4.1: Abbreviations and parameter definitions.

different SCVs of an element. The integration over these two sub-surfaces is briefly addressed by a single digit number index. For SCV1, it is given by

$$\int_{S_1} = \int_{S_{SS4}} + \int_{S_{SS1}} \tag{4.1}$$

Similar definitions have been tabulated for other SCVs in Table 4.1. Other parameters of the SCVi may be identified directly by adding the subscripts i to them. For example, the volume per unit depth of SCVi is shown by

$$\mathcal{V}_i = \mathcal{V}_{SCVi} \tag{4.2}$$

Approximation of the governing equations will algebraically require the modeling of each of the operators in terms of at most four nodes and four integration points in each element. This results in two sets of 4×1 array of unknowns which will repeatedly be encountered in this chapter. The first set represents the magnitude of dependent variable or unknowns at nodes, i.e., $\{P\}$, $\{F\}$, $\{G\}$, and $\{T\}$, and the other set represents them at integration points, i.e., $\{p\}$, $\{f\}$, $\{g\}$, and $\{t\}$. The latter are not nodal unknowns and must therefore be related to these nodal dependent variables.

Generally speaking, there are four major governing equations, four sub-control-volumes, four nodes, four integration points, etc. which make their tracking complicated. In order to have an organized procedure, many useful definitions are presented here. For example, the results of integration over each SCV are required to be stored in arrays. Special combination of subscripts and superscripts are used to recognize the identity of the elements of the arrays. They are generally written as

$$A_{sb1,sb2}^{sp1,sp2,sp3} \qquad a_{sb1,sb2}^{sp1,sp2,sp3} \tag{4.3}$$

The upper and lower cases for $[A]$ and $[a]$ mean the matrices multiply by the array of nodes or of integration points of an element, respectively. The notation sp1 refers to the related governing equation, i.e., p:continuity, f:x-momentum, g:y-momentum, and t:energy. The notation sp2 stands for the multiplier array to the matrix, i.e., p, f, g, and t for P, F, G, and T arrays, respectively. The notation sp3 means to which term the matrix belongs, e.g. θ:transient term, c:convection term, d:diffusion term, p:pressure term, and etc. The notation sb1 stands for SCV number in question within element, and sb2 counts either the element node numbers, if the coefficient is upper case, or integration point number, if it is lower case.

A well-posed discretization will require the representation of integration point values in terms of nodal ones. This procedure will result in matrices similar to Eq.(4.3) which are identified by $[C]$ and $[c]$, i.e.,

$$C_{sb1,sb2}^{sp1,sp2,sp3} \qquad c_{sb1,sb2}^{sp1,sp2,sp3} \tag{4.4}$$

All subscripts and superscripts are identically defined as those in Eq.(4.3) except for sb1 which refers to integration point number now. The array of known values in right-hand-side of elemental matrices, Eq.(4.3), and integration point matrices, Eq.(4.4), are identified by $\{A\}$ and $\{C\}$, respectively, i.e.,

$$A_{sb1}^{sp1,sp3} \qquad C_{sb1}^{sp1,sp3} \tag{4.5}$$

Their subscripts and superscripts have the same definition as before in terms of sp1, sp2, sp3, sb1, and sb2.

4.3 Discretization of the Governing Equations

The general form of the governing equations was introduced in Section 2.1 by Eq.(2.18). Considering no source terms, these equations can be integrated over SCV*i* of an arbitrary element

$$\int_{\mathcal{V}_i} \frac{\partial\psi}{\partial\theta} d\mathcal{V} + \int_{\mathcal{V}_i} \frac{\partial\mathcal{F}}{\partial x} d\mathcal{V} + \int_{\mathcal{V}_i} \frac{\partial\mathcal{G}}{\partial y} d\mathcal{V} = \int_{\mathcal{V}_i} \frac{\partial\mathcal{R}}{\partial x} d\mathcal{V} + \int_{\mathcal{V}_i} \frac{\partial\mathcal{T}}{\partial y} d\mathcal{V} \qquad (4.6)$$

Using the divergence theorem, the volume integral of space derivatives is replaced by a surface integral which is evaluated over the surface of SCV*i*

$$\int_{\mathcal{V}_i} \frac{\partial\psi}{\partial\theta} d\mathcal{V} + \int_{\mathcal{S}_i} \left(\mathcal{F}\hat{i} + \mathcal{G}\hat{j}\right) \cdot d\vec{\mathcal{S}} = \int_{\mathcal{S}_i} \left(\mathcal{R}\hat{i} + \mathcal{T}\hat{j}\right) \cdot d\vec{\mathcal{S}} \qquad (4.7)$$

where $d\vec{\mathcal{S}}$ is the outward normal vector to the surface, Figure 2.3. Integration on surfaces is broken into two sub-surface integration according to Table 4.1

$$\int_{\mathcal{V}_i} \frac{\partial\psi}{\partial\theta} d\mathcal{V} + \int_{\mathcal{S}1i} \left(\mathcal{F}\hat{i} + \mathcal{G}\hat{j}\right) \cdot d\vec{\mathcal{S}} + \int_{\mathcal{S}2i} \left(\mathcal{F}\hat{i} + \mathcal{G}\hat{j}\right) \cdot d\vec{\mathcal{S}} =$$

$$\int_{\mathcal{S}1i} \left(\mathcal{R}\hat{i} + \mathcal{T}\hat{j}\right) \cdot d\vec{\mathcal{S}} + \int_{\mathcal{S}2i} \left(\mathcal{R}\hat{i} + \mathcal{T}\hat{j}\right) \cdot d\vec{\mathcal{S}} \qquad (4.8)$$

where $\mathcal{S}1i$ and $\mathcal{S}2i$ indicate the integration point number on the sub-surfaces. Since the method is fully implicit, all terms except the transient term are evaluated at the advanced time and the transient term is approximated by a *lumped mass* approach, i.e., ψ at each SCV is approximated by the nodal value of its corresponding node

$$\int_{\mathcal{V}_i} \frac{\partial\psi}{\partial\theta} d\mathcal{V} \approx J_i\left(\frac{\Psi_i - \Psi_i^o}{\Delta\theta}\right) \qquad (4.9)$$

where J_i is the Jacobian of transformation and represents the volume of the subcontrol volume per unit width, Eq.(A.15). A linear variation of the integral argument is considered over each sub-surface integrals. As a result, the value of the surface integral is approximated by the value at the mid-point of that sub-surface, i.e., integration point, times the area of the sub-surface. By this mid-point approximation, the arguments of the integrals are taken out of the integral and the areas of the sub-surfaces are computed using Eqs.(2.25), i.e.,

$$(\Delta S_x)_{ipi} = \int_{SSi} dS_x \tag{4.10a}$$

$$(\Delta S_y)_{ipi} = \int_{SSi} dS_y \tag{4.10b}$$

Considering this mid-point approximation and substitution of Eq.(4.9) into Eq.(4.8) results in the final conservative discretization form of the governing equations for SCVi

$$\begin{aligned} J_i \frac{\Psi_i - \Psi_i^o}{\Delta\theta} + [\mathcal{F}(\Delta S_x) + \mathcal{G}(\Delta S_y)]_{S1i} + [\mathcal{F}(\Delta S_x) + \mathcal{G}(\Delta S_y)]_{S2i} = \\ [\mathcal{T}(\Delta S_x) + \mathcal{R}(\Delta S_y)]_{S1i} + [\mathcal{T}(\Delta S_x) + \mathcal{R}(\Delta S_y)]_{S2i} \end{aligned} \tag{4.11}$$

where the subscript i of Ψ refers to SCVi. This general equation consists of all transient, convection, and diffusion flux terms of the four governing equations.

Recalling the definition of $\mathcal{F}$, $\mathcal{G}$, $\mathcal{R}$, and $\mathcal{T}$, Eqs.(2.20 and 2.21), shows that there are two major obstacles to solve Eq.(4.11). The first obstacle returns to the nonlinear nature of the system of equations. In order to use linear algebraic equation solvers, these equations must be linearized. The second obstacle is the location of the unknown fluxes and flows. As seen, the locations of the unknowns are integration points which are not our nodal locations and they must somehow be related to the main nodal values. These difficulties are treated in the present and the following sections.

4.3.1 Conservation of Mass Equation

The discretized form of conservation of mass could be extracted from the general form of Eq.(4.11) and recalling the definition of $\mathcal{F}$ and $\mathcal{G}$ from Eq.(2.20)

$$J_i \frac{\varrho_i - \varrho_i^o}{\Delta\theta} + \sum_{k=1}^{2} [(\Delta S_x)f + (\Delta S_y)g]_{S_{ki}} = 0 \tag{4.12}$$

The transient term is a non-linear term because ϱ is not a major dependent variable and needs to be linearized properly. The density in incompressible flow is constant, Eq.(2.16), and does not need any treatment. The equation of state is used to convert density in compressible flow. Appendix B presents methods for density linearization. Regarding the results of this appendix, Eq.(B.5) is selected to linearize ϱ with respect to both P and T dependent variables

$$\varrho_i = \frac{1}{R\bar{T}_i} P_i - \frac{\bar{\varrho}_i}{\bar{T}_i} T_i + \bar{\varrho}_i \tag{4.13}$$

Thus, the transient term is written as

$$\int_{\mathcal{V}_i} \frac{\partial \rho}{\partial \theta} d\mathcal{V} \approx J_i \frac{\varrho_i - \varrho_i^o}{\Delta\theta} = \underbrace{\frac{J_i}{\Delta\theta} \frac{1}{R\bar{T}_i}}_{\sum_{j=1}^{4} A_{i,j}^{pp\theta}} P_i + \underbrace{\left(-\frac{J_i}{\Delta\theta} \frac{\bar{\varrho}_i}{\bar{T}_i} \right)}_{\sum_{j=1}^{4} A_{i,j}^{pt\theta}} T_i - \underbrace{\frac{J_i}{\Delta\theta} (\varrho_i^o - \bar{\varrho}_i)}_{A_i^{p\theta}} \tag{4.14}$$

As seen, the results are easily converted to the compact summation form. It should be noted that three of the four components of each summation are zero in this general form, i.e.,

$$A_{i,j}^{pp\theta} = \begin{cases} \frac{J_i}{\Delta\theta} \frac{1}{R\bar{T}_i} & j = i \\ 0 & j \neq i \end{cases} \tag{4.15}$$

$$A_{i,j}^{pt\theta} = \begin{cases} -\frac{J_i}{\Delta\theta} \frac{\bar{\varrho}_i}{\bar{T}_i} & j = i \\ 0 & j \neq i \end{cases} \tag{4.16}$$

$$A_i^{p\theta} = \frac{J_i}{\Delta\theta}(\varrho_i^o - \bar{\varrho}_i) \tag{4.17}$$

Now, the transient term, Eq.(4.14), is written in summation form for an arbitrary sub-control-volume of i as

$$\int_{\mathcal{V}_i} \frac{\partial\rho}{\partial\theta} d\mathcal{V} \approx \sum_{j=1}^{4} A_{i,j}^{pp\theta} P_j + \sum_{j=1}^{4} A_{i,j}^{pt\theta} T_j - A_i^{p\theta} \tag{4.18}$$

A similar procedure could be repeated for the mass flux terms of the continuity equation. Recall Eq.(4.8) and consider the bracketed terms of Eq.(4.12), the summation form becomes

$$\int_{S_i} \left(f\hat{i} + g\hat{j}\right) \cdot d\vec{S} \approx \sum_{j=1}^{4} a_{i,j}^{pfm} f_j + \sum_{j=1}^{4} a_{i,j}^{pgm} g_j \tag{4.19}$$

Here, two of the four elements in each summation are zero, i.e.,

$$a_{i,j}^{pfm} = \begin{cases} (\Delta S_x)_{S1i} & j = S1i \\ (\Delta S_x)_{S2i} & j = S2i \\ 0 & \text{else} \end{cases} \tag{4.20}$$

$$a_{i,j}^{pgm} = \begin{cases} (\Delta S_y)_{S1i} & j = S1i \\ (\Delta S_y)_{S2i} & j = S2i \\ 0 & \text{else} \end{cases} \tag{4.21}$$

The two discretized equations, Eq.(4.18) and Eq.(4.19), can now be assembled and written in the usual matrix form for an arbitrary sub-control-volume of i

$$\sum_{j=1}^{4} A_{i,j}^{pp\theta} P_j + \sum_{j=1}^{4} A_{i,j}^{pt\theta} T_j + \sum_{j=1}^{4} a_{i,j}^{pfm} f_j + \sum_{j=1}^{4} a_{i,j}^{pgm} g_j = A_i^{p\theta} \tag{4.22}$$

It should be noted that the above equation is written only for one portion of a four-control-volume element. It is not expected that it conserves the mass within that sub-control-volume of i. The conservation of mass is only valid for a whole control volume which consists of an assemblage of four sub-control-volume equations, Figure 2.2. If all four sub-control-volume equations of an element are put together they take the following matrix form:

$$[A^{pp\theta}]\{P\} + [A^{pt\theta}]\{T\} + [a^{pfm}]\{f\} + [a^{pgm}]\{g\} = \{A^{p\theta}\} \tag{4.23}$$

where the brackets are 4×4 square matrices and the braces are 4×1 column vectors. The rows of arrays represent the sub-control-volume number and the columns represent the node number.

Notice that Eq.(4.23) has discretized the mass flux terms into an algebraic expression involving the integration point variables as well as nodal variables. This expression is not complete at this stage and needs to be modified. This modification is done in Section 4.5.

4.3.2 Conservation of Momentum Equation

Discretization of the momentum conservation equations is much more complex than that for the continuity equation. The complexity of the equation arises due to the appearance of different types of nonlinear terms, and from the large number of them. The one-dimensional discretization of Section 3.3.2 will facilitate the procedure of discretization in this section. The transient term does not need any linearization and it is easily discretized by plugging the definition of ψ from Eq.(2.19) into Eq.(4.11), using a mass-lumped approach,

$$\int_{\mathcal{V}_i} \frac{\partial f}{\partial \theta} d\mathcal{V} \approx J_i \frac{F_i - F_i^o}{\Delta\theta} = \frac{J_i}{\Delta\theta} F_i - \frac{J_i}{\Delta\theta} F_i^o \tag{4.24}$$

A summation form similar to Eq.(4.18) could be arranged for an arbitrary sub-control-volume i

$$\int_{\mathcal{V}_i} \frac{\partial f}{\partial \theta} d\mathcal{V} \approx \sum_{j=1}^{4} A_{i,j}^{ff\theta} F_j - A_i^{f\theta} \tag{4.25}$$

where

$$A_{i,j}^{ff\theta} = \begin{cases} \frac{J_i}{\Delta\theta} & j = i \\ 0 & j \neq i \end{cases} \tag{4.26}$$

$$A_i^{f\theta} = \frac{J_i}{\Delta\theta} F_i^o \tag{4.27}$$

As the next step, the convection terms are treated. In this regard, the appropriate terms of $\mathcal{F}$ and $\mathcal{G}$, Eq.(2.20), are substituted in the integral form of the convection terms

$$\int_{S_i} \left((\rho uu + p)\,\hat{\imath} + \rho vu\,\hat{\jmath} \right) \cdot d\vec{S} = \int_{S_i} (\rho uu\,\hat{\imath} + \rho vu\,\hat{\jmath}) \cdot d\vec{S} + \int_{S_i} p\,\hat{\imath} \cdot d\vec{S} \tag{4.28}$$

We first treat the pressure integration term which is linear. Considering the previous procedure, we write

$$\int_{S_i} p\,\hat{\imath} \cdot d\vec{S} \approx \sum_{k=1}^{2} [p(\Delta S_x)]_{Ski} \tag{4.29}$$

Using our previous definitions, this equation is reformed in general summation form for an arbitrary sub-control-volume i as

$$\int_{S_i} p\,\hat{\imath} \cdot d\vec{S} \approx \sum_{j=1}^{4} a_{i,j}^{fpp} p_j \tag{4.30}$$

where the coefficients of $a_{i,j}^{fpp}$ and those of $a_{i,j}^{pfm}$ in Eq.(4.20) are the same, i.e.,

$$[a^{fpp}] = [a^{pfm}] \tag{4.31}$$

As seen, the pressure term is also represented by integration point variables which in turn should be represented in terms of nodal variables. This will be accomplished in Section 4.4.1.

The first integration on the right-hand-side of Eq.(4.28) can be expanded for sub-control-volume i as

$$\int_{S_i} (\rho u u\,\hat{i} + \rho v u\,\hat{j}) \cdot d\vec{S} \approx \sum_{k=1}^{2} [(\rho u u)(\Delta S_x) + (\rho v u)(\Delta S_y)]_{Ski} \tag{4.32}$$

As seen, the discretized equation is nonlinear and needs to be linearized properly. Appendix C has a comprehensive study on different methods of linearization for the convection terms of the conservative momentum equation. Providing a simpler approach at this stage, Eqs.(C.10 and C.11) with $k' = 0$ are used to linearize the nonlinearities, i.e.,

$$\rho u u \approx \bar{u} f \tag{4.33a}$$

$$\rho v u \approx \bar{v} f \tag{4.33b}$$

where $\bar{u}$ and $\bar{v}$ are calculated explicitly from known values of the previous iteration which will be explained later in Section 4.5. Using these linearizations in Eq.(4.32), we obtain

$$\int_{S_i} (\rho u u\,\hat{i} + \rho v u\,\hat{j}) \cdot d\vec{S} \approx \sum_{k=1}^{2} [\bar{u} f(\Delta S_x) + \bar{v} f(\Delta S_y)]_{Ski} \tag{4.34}$$

The general summation form for an arbitrary sub-control-volume i is

$$\int_{S_i} (\rho u u\,\hat{i} + \rho v u\,\hat{j}) \cdot d\vec{S} \approx \sum_{j=1}^{4} a_{i,j}^{ffc} f_j \tag{4.35}$$

where the coefficients are

$$a_{i,j}^{ffc} = \begin{cases} [\bar{u}(\Delta S_x) + \bar{v}(\Delta S_y)]_{S1i} & j = S1i \\ [\bar{u}(\Delta S_x) + \bar{v}(\Delta S_y)]_{S2i} & j = S2i \\ 0 & \text{else} \end{cases} \tag{4.36}$$

As the second step, integration point values which appear in linearized terms have to be calculated as a function of the nodal variables in the element. The appropriate equations for f and g are derived in Section 4.4.1.

To complete the momentum conservation equation, the diffusion terms must be treated. Modeling of the diffusion terms is relatively more routine than the convection terms due to their elliptic nature. Following the previous procedure, the right-hand-side of Eq.(4.11) could be extended to the momentum equations using the definition of $\mathcal{R}$ and $\mathcal{T}$ from Eq.(2.21). The result is

$$\int_{S_i} (\tau_{xx}\hat{i} + \tau_{yx}\hat{j}) \cdot d\vec{S} \approx \sum_{k=1}^{2} [\tau_{xx}(\Delta S_x) + \tau_{yx}(\Delta S_y)]_{S_{ki}} \tag{4.37}$$

Looking back to the definition of stress terms in Eqs.(2.6 and 2.7) shows that they are nonlinear in terms of momentum component variables. In the one-dimensional investigation, Section 3.3.2, the linearization scheme of Appendix D was selected to linearize the $\frac{\partial u}{\partial x}$ term. In the two-dimensional diffusion terms, the essence of nonlinearity is the same although they are more plentiful. As before, we use the approach presented by Eq.(D.2) in Appendix D to linearize the velocity differential forms. Employing this linearization scheme to the stress terms of Eqs.(2.6 and 2.7) results in

$$\tau_{xx} \approx \frac{2\mu}{3\bar{\rho}}\left(\{2\frac{\partial f}{\partial x} - 2\bar{u}\frac{\partial \bar{\rho}}{\partial x}\} - \{\frac{\partial g}{\partial y} - \bar{v}\frac{\partial \bar{\rho}}{\partial y}\}\right) \tag{4.38}$$

$$\tau_{xy} = \tau_{yx} \approx \frac{\mu}{\bar{\rho}}\left(\{\frac{\partial f}{\partial y} - \bar{u}\frac{\partial \bar{\rho}}{\partial y}\} + \{\frac{\partial g}{\partial x} - \bar{v}\frac{\partial \bar{\rho}}{\partial x}\}\right) \tag{4.39}$$

$$\tau_{yy} \approx \frac{2\mu}{3\bar{\rho}}\left(-\{\frac{\partial f}{\partial x} - \bar{u}\frac{\partial \bar{\rho}}{\partial x}\} + \{2\frac{\partial g}{\partial y} - 2\bar{v}\frac{\partial \bar{\rho}}{\partial y}\}\right) \tag{4.40}$$

The second terms in all braces vanish in the incompressible limit. These terms are now lagged and calculated explicitly from the known values of the previous iterations. This results in a source term on the right-hand-side of Eq.(4.8) in compressible flows. To reveal the elliptic nature of diffusion, all active and inactive differential terms are modeled through differentiation of the finite-element shape functions for the linear quadrilateral elements, Eq.(A.3). The following results are obtained after rearranging and sorting active and inactive terms together:

$$\tau_{xx} \approx \sum_{j=1}^{4} \left(\{ \frac{4\mu}{3\bar{\rho}} \frac{\partial N_j}{\partial x} F_j - \frac{2\mu}{3\bar{\rho}} \frac{\partial N_j}{\partial y} G_j \} + \{ -\frac{4\mu}{3\bar{\rho}} \bar{u} \frac{\partial N_j}{\partial x} \bar{\varrho}_j + \frac{2\mu}{3\bar{\rho}} \bar{v} \frac{\partial N_j}{\partial y} \bar{\varrho}_j \} \right) \tag{4.41}$$

$$\tau_{xy} = \tau_{yx} \approx \sum_{j=1}^{4} \left(\{ \frac{\mu}{\bar{\rho}} \frac{\partial N_j}{\partial y} F_j + \frac{\mu}{\bar{\rho}} \frac{\partial N_j}{\partial x} G_j \} + \{ -\frac{\mu}{\bar{\rho}} \bar{u} \frac{\partial N_j}{\partial y} \bar{\varrho}_j - \frac{\mu}{\bar{\rho}} \bar{v} \frac{\partial N_j}{\partial x} \bar{\varrho}_j \} \right) \tag{4.42}$$

$$\tau_{yy} \approx \sum_{j=1}^{4} \left(\{ -\frac{2\mu}{3\bar{\rho}} \frac{\partial N_j}{\partial x} F_j + \frac{4\mu}{3\bar{\rho}} \frac{\partial N_j}{\partial y} G_j \} + \{ \frac{2\mu}{3\bar{\rho}} \bar{u} \frac{\partial N_j}{\partial x} \bar{\varrho}_j - \frac{4\mu}{3\bar{\rho}} \bar{v} \frac{\partial N_j}{\partial y} \bar{\varrho}_j \} \right) \tag{4.43}$$

Now, Eqs.(4.41 and 4.42) are substituted in Eq.(4.37). The resulting equation can be rearranged and written in general summation form for an arbitrary SCVi

$$\int_{S_i} (\tau_{xx} \hat{i} + \tau_{yx} \hat{j}) \cdot d\vec{S} \approx -\sum_{j=1}^{4} A_{i,j}^{ffd} F_j - \sum_{j=1}^{4} A_{i,j}^{fgd} G_j + A_i^{fd} \tag{4.44}$$

where the coefficient of $A_{i,j}^{ffd}$ and $A_{i,j}^{fgd}$ are

$$A_{i,j}^{ffd} = -\sum_{k=1}^{2} \left[\frac{4\mu}{3\bar{\rho}} \frac{\partial N_j}{\partial x} (\Delta S_x) + \frac{\mu}{\bar{\rho}} \frac{\partial N_j}{\partial y} (\Delta S_y) \right]_{Ski} \tag{4.45}$$

$$A_{i,j}^{fgd} = -\sum_{k=1}^{2} \left[-\frac{2\mu}{3\bar{\rho}} \frac{\partial N_j}{\partial y} (\Delta S_x) + \frac{\mu}{\bar{\rho}} \frac{\partial N_j}{\partial x} (\Delta S_y) \right]_{Ski} \tag{4.46}$$

$$A_i^{fd} = \sum_{j=1}^{4} \sum_{k=1}^{2} \left(-\frac{4\mu}{3\bar{\rho}} \bar{u} \frac{\partial N_j}{\partial x} \bar{\varrho}_j + \frac{2\mu}{3\bar{\rho}} \bar{v} \frac{\partial N_j}{\partial y} \bar{\varrho}_j - \frac{\mu}{\bar{\rho}} \bar{u} \frac{\partial N_j}{\partial y} \bar{\varrho}_j - \frac{\mu}{\bar{\rho}} \bar{v} \frac{\partial N_j}{\partial x} \bar{\varrho}_j \right)_{Ski} \tag{4.47}$$

Now, we can assemble all the terms of the momentum equation. In this regard, Eqs.(4.25, 4.30, 4.35, and 4.44) are plugged into Eq.(4.7) and the result is

$$\sum_{j=1}^{4}(A_{i,j}^{ff\theta} + A_{i,j}^{ffd})F_j + \sum_{j=1}^{4} A_{i,j}^{fgd}G_j + \sum_{j=1}^{4} a_{i,j}^{ffc} f_j + \sum_{j=1}^{4} a_{i,j}^{fpp} p_j = A_i^{f\theta} + A_i^{fd} \qquad (4.48)$$

which could be cast into the matrix form as

$$[A^{ff\theta} + A^{ffd}]\{F\} + [A^{fgd}]\{G\} + [a^{ffc}]\{f\} + [a^{fpp}]\{p\} = \{A^{f\theta} + A^{fd}\} \qquad (4.49)$$

Similar to previous sections, these equations are not well-posed because they involve integration point values. Closure for these terms will be fulfilled in the next sections. All discussions in this section relate to the discretization of the x-momentum equation. A similar procedure is applied for the y-momentum equation. The results of this would be an equation similar to Eq.(4.49). Comparing with this equation, it is written

$$[A^{gfd}]\{F\} + [A^{gg\theta} + A^{ggd}]\{G\} + [a^{ggc}]\{g\} + [a^{gpp}]\{p\} = \{A^{g\theta} + A^{gd}\} \qquad (4.50)$$

where the elements of the matrices could be estimated by comparing the equivalent terms of two momentum equations and the resulting elements of the x-momentum equation matrices.

4.3.3 Conservation of Energy Equation

The discretization of the energy equation is not as straight forward as it was for mass and momentum equations. There are a variety of reasons behind this which cause the study of the energy equation to be not so routine as for the others. Among these reasons, one is the larger number of terms and the other is their higher complexity. This complexity however causes more complex nonlinearities for those terms. These complex nonlinearities can be treated using different techniques of linearization. However, more study and experience is needed to fully assess the pros and cons of different possible linearization. A poor linearization may cause oscillation in the solution which in turn may lead to divergence or slow convergence. All these reasons cause the study of the energy equation to be more difficult and ambiguous. Contrary to the important terms, there are a number of nonlinearities which are not so prominent. This permits us to ignore the active role of many terms and calculate them approximately using the known values from previous iterations.

We start the discretization by treating the transient part of the equation. Considering Eq.(4.9) and the definition of ψ from Eq.(2.19), the transient part of the equation is written as

$$\int_{\mathcal{V}_i} \frac{\partial(\rho e)}{\partial \theta} d\mathcal{V} \approx J_i \frac{(\varrho E)_i - (\varrho E)_i^o}{\Delta\theta} \tag{4.51}$$

There are different possible methods to derive the linearized form of this equation. Appendix F presents a few of them. Regarding the comments of the Appendix and the one-dimensional procedure, Section 3.3.3, we use Eq.(F.2) to linearize the transient term

$$\int_{\mathcal{V}_i} \frac{\partial(\rho e)}{\partial \theta} d\mathcal{V} \approx \frac{J_i \bar{U}_i}{2\Delta\theta} F_i + \frac{J_i \bar{V}_i}{2\Delta\theta} G_i + \frac{c_v J_i \bar{\varrho}_i}{\Delta\theta} T_i - \frac{J_i}{\Delta\theta} \varrho_i^o E_i^o] \tag{4.52}$$

This results in a general summation form for an arbitrary SCVi

$$\int_{\mathcal{V}_i} \frac{\partial(\rho e)}{\partial \theta} d\mathcal{V} \approx \sum_{j=1}^{4} A_{i,j}^{tf\theta} F_j + \sum_{j=1}^{4} A_{i,j}^{tg\theta} G_j + \sum_{j=1}^{4} A_{i,j}^{tt\theta} T_j - A_i^{t\theta} \tag{4.53}$$

where

$$A_{i,j}^{tf\theta} = \begin{cases} \frac{J_i \bar{U}_i}{2\Delta\theta} & j = i \\ 0 & j \neq i \end{cases} \tag{4.54}$$

$$A_{i,j}^{tg\theta} = \begin{cases} \frac{J_i \bar{V}_i}{2\Delta\theta} & j = i \\ 0 & j \neq i \end{cases} \tag{4.55}$$

$$A_{i,j}^{tt\theta} = \begin{cases} \frac{c_v J_i \bar{\varrho}_i}{\Delta\theta} & j = i \\ 0 & j \neq i \end{cases} \tag{4.56}$$

$$A_i^{t\theta} = \frac{J_i}{\Delta\theta} \varrho_i^o E_i^o \tag{4.57}$$

In the second step of discretization, the energy convection terms are discretized. Combining the proper components of $\mathcal{F}$ and $\mathcal{G}$ from Eq.(2.20) and the convection part of Eq.(4.7), we obtain

$$\int_{S_i} (\rho u h \,\hat{i} + \rho v h \,\hat{j}) \cdot d\vec{S} \approx \sum_{k=1}^{2} [(\rho u h)(\triangle S_x) + (\rho v h)(\triangle S_y)]_{Ski} \tag{4.58}$$

Similar to the momentum convective terms, this term is nonlinear and must be linearized in terms of momentum component variables. Appendix G presents different schemes of linearization for the above nonlinearities. At this stage, they are linearized using the scheme presented by Eq.(G.3). The employment of this scheme yields

$$\int_{S_i} (\rho u h \,\hat{i} + \rho v h \,\hat{j}) \cdot d\vec{S} \approx \sum_{k=1}^{2} \left[\frac{\bar{u}}{2} (\bar{u}\, f + \bar{v}\, g + 2 c_p \bar{\rho}\, t)(\Delta S_x) + \right.$$
$$\left. \frac{\bar{v}}{2} (\bar{u}\, f + \bar{v}\, g + 2 c_p \bar{\rho}\, t)(\Delta S_y) \right]_{Ski} \tag{4.59}$$

This equation is reformed to a general summation form for an arbitrary SCVi

$$\int_{S_i} (\rho u h \,\hat{i} + \rho v h \,\hat{j}) \cdot d\vec{S} \approx \sum_{j=1}^{4} a_{i,j}^{tfc} f_j + \sum_{j=1}^{4} a_{i,j}^{tgc} g_j + \sum_{j=1}^{4} a_{i,j}^{ttc} t_j \tag{4.60}$$

where the coefficients of the matrices are obtained from

$$a_{i,j}^{tfc} = \begin{cases} \left\{\frac{\bar{u}}{2}\left[\bar{u}(\Delta S_x) + \bar{v}(\Delta S_y)\right]\right\}_{S1i} & j = S1i \\ \left\{\frac{\bar{u}}{2}\left[\bar{u}(\Delta S_x) + \bar{v}(\Delta S_y)\right]\right\}_{S2i} & j = S2i \\ 0 & \text{else} \end{cases} \tag{4.61}$$

$$a_{i,j}^{tgc} = \begin{cases} \left\{\frac{\bar{v}}{2}\left[\bar{u}(\Delta S_x) + \bar{v}(\Delta S_y)\right]\right\}_{S1i} & j = S1i \\ \left\{\frac{\bar{v}}{2}\left[\bar{u}(\Delta S_x) + \bar{v}(\Delta S_y)\right]\right\}_{S2i} & j = S2i \\ 0 & \text{else} \end{cases} \tag{4.62}$$

$$a_{i,j}^{ttc} = \begin{cases} 2c_p\left\{\bar{\rho}\left[(\Delta S_x) + (\Delta S_y)\right]\right\}_{S1i} & j = S1i \\ 2c_p\left\{\bar{\rho}\left[(\Delta S_x) + (\Delta S_y)\right]\right\}_{S2i} & j = S2i \\ 0 & \text{else} \end{cases} \tag{4.63}$$

Despite a full discretization, the unknowns of this equation still need to be related to the main nodal variables. This is accomplished in the next sections. The last part of the discretization process is the modeling of the energy viscous work terms. As mentioned earlier, the elliptic nature of diffusion facilitates its treatment. To treat the diffusive conduction terms, Eq.(4.7) is recalled and the conduction terms of $\mathcal{R}$ and $\mathcal{T}$ in Eq.(2.21) is plugged in as

$$\int_{S_i} (q_x \hat{\imath} + q_y \hat{\jmath}) \cdot d\vec{S} \approx \sum_{k=1}^{2} \left[q_x(\Delta S_x) + q_y(\Delta S_y)\right]_{Ski} \tag{4.64}$$

Using the definition of q_x and q_y from Eq.(2.9) yields

$$\int_{S_i} (q_x \hat{\imath} + q_y \hat{\jmath}) \cdot d\vec{S} \approx -\mathbf{k} \sum_{k=1}^{2} \left[\frac{\partial T}{\partial x}(\Delta S_x) + \frac{\partial T}{\partial y}(\Delta S_y)\right]_{Ski} \tag{4.65}$$

The derivatives of the finite-element shape functions are employed to describe the differential forms, i.e.,

$$\int_{S_i} (q_x \hat{\imath} + q_y \hat{\jmath}) \cdot d\vec{S} \approx -\mathbf{k} \sum_{j=1}^{4} \sum_{k=1}^{2} \left[\frac{\partial N_j}{\partial x}(\Delta S_x) + \frac{\partial N_j}{\partial y}(\Delta S_y)\right]_{Ski} T_j \tag{4.66}$$

The general form of this for an arbitrary SCVi is

$$\int_{S_i} (q_x \hat{i} + q_y \hat{j}) \cdot d\vec{S} \approx \sum_{j=1}^{4} A_{ij}^{ttk} T_j \tag{4.67}$$

where

$$A_{ij}^{ttk} = -\mathrm{k} \sum_{k=1}^{2} \left[\frac{\partial N_j}{\partial x}(\Delta S_x) + \frac{\partial N_j}{\partial y}(\Delta S_y) \right]_{Ski} \tag{4.68}$$

For the remainder of the diffusion terms, we use again the definition of $\mathcal{R}$ and $\mathcal{T}$ from Eq.(2.21) and plug its energy part into Eq.(4.7). The result is

$$\int_{S_i} [(u\tau_{xx} + v\tau_{xy})\,\hat{i} + (u\tau_{yx} + v\tau_{yy})\,\hat{j}] \cdot d\vec{S} \approx \sum_{k=1}^{2} [(u\tau_{xx} + v\tau_{xy})(\Delta S_x) + (u\tau_{yx} + v\tau_{yy})(\Delta S_y)]_{Ski} \tag{4.69}$$

The nonlinearity of the viscous work terms is much complicated than the diffusion terms in momentum equation. This is due to the velocity components which multiply the stress components. At the first stage of the linearization, all these velocity components are evaluated using lagged values from the previous iteration and the treatment of the remainder of the nonlinearities are similar to those for the momentum equations. We start discretizing by plugging the linearized stress terms, Eqs.(4.41-4.43), into Eq.(4.69). The resulting equation can be rearranged for the active and inactive variables. The general form of the resulting equation is presented in summation form for an arbitrary SCVi as

$$\int_{S_i} [(u\tau_{xx} + v\tau_{xy})\,\hat{i} + (u\tau_{yx} + v\tau_{yy})\,\hat{j}] \cdot d\vec{S} \approx -\sum_{j=1}^{4} A_{i,j}^{tfd} F_j - \sum_{j=1}^{4} A_{i,j}^{tgd} G_j + A_i^{td} \tag{4.70}$$

where the matrix components are defined as

$$A_{ij}^{tfd} = -\mu \sum_{k=1}^{2} \left(\{ \frac{4\bar{u}}{3\bar{\rho}} \frac{\partial N_j}{\partial x} + \frac{\bar{v}}{\bar{\rho}} \frac{\partial N_j}{\partial y} \}(\Delta S_x) + \{ \frac{\bar{u}}{\bar{\rho}} \frac{\partial N_j}{\partial y} - \frac{2\bar{v}}{3\bar{\rho}} \frac{\partial N_j}{\partial x} \}(\Delta S_y) \right)_{Ski} \tag{4.71}$$

$$A_{ij}^{tgd} = -\mu \sum_{k=1}^{2} \left(\{ -\frac{2\bar{u}}{3\bar{\rho}} \frac{\partial N_j}{\partial y} + \frac{\bar{v}}{\bar{\rho}} \frac{\partial N_j}{\partial x} \} (\Delta S_x) + \{ \frac{\bar{u}}{\bar{\rho}} \frac{\partial N_j}{\partial x} + \frac{4\bar{v}}{3\bar{\rho}} \frac{\partial N_j}{\partial y} \} (\Delta S_y) \right)_{Ski} \tag{4.72}$$

$$A_i^{td} = \mu \sum_{j=1}^{4} \sum_{k=1}^{2} \left(\left[-\frac{4\bar{u}^2}{3\bar{\rho}} \frac{\partial N_j}{\partial x} + \frac{2\bar{u}\bar{v}}{3\bar{\rho}} \frac{\partial N_j}{\partial y} - \frac{\bar{u}\bar{v}}{\bar{\rho}} \frac{\partial N_j}{\partial y} - \frac{\bar{v}^2}{\bar{\rho}} \frac{\partial N_j}{\partial x} \right] (\Delta S_x) + \right. \tag{4.73}$$

$$\left. \left[-\frac{\bar{u}^2}{\bar{\rho}} \frac{\partial N_j}{\partial y} - \frac{\bar{u}\bar{v}}{\bar{\rho}} \frac{\partial N_j}{\partial x} + \frac{2\bar{u}\bar{v}}{3\rho} \frac{\partial N_j}{\partial x} - \frac{4\bar{v}^2}{3\bar{\rho}} \frac{\partial N_j}{\partial y} \right] (\Delta S_y) \right)_{Ski} \bar{\varrho}_j \tag{4.74}$$

Now, we can assemble all the terms of the energy equation in Eq.(4.7). In this regard, Eqs.(4.53, 4.60, 4.67, and 4.70) are plugged in Eq.(4.7) and the result is

$$\sum_{j=1}^{4} (A_{i,j}^{tf\theta} + A_{i,j}^{tfd}) F_j + \sum_{j=1}^{4} (A_{i,j}^{tg\theta} + A_{i,j}^{tgd}) G_j + \sum_{j=1}^{4} (A_{i,j}^{tt\theta} + A_{i,j}^{ttk}) T_j +$$

$$\sum_{j=1}^{4} a_{i,j}^{tfc} f_j + \sum_{j=1}^{4} a_{i,j}^{tgc} g_j + \sum_{j=1}^{4} a_{i,j}^{ttc} t_j = A_i^{t\theta} + A_i^{td} \tag{4.75}$$

which can be cast into the matrix form as

$$[A^{tf\theta} + A^{tfd}]\{F\} + [A^{tg\theta} + A^{tgd}]\{G\} + [A^{tt\theta} + A^{ttk}]\{T\} +$$

$$[a^{tfc}]\{f\} + [a^{tgc}]\{g\} + [a^{ttc}]\{t\} = \{A^{t\theta} + A^{td}\} \tag{4.76}$$

The treatment of integration point values is necessary as it was in preceding subsections. The next section will provide this treatment.

4.4 Integration Point Equations

The idea of connecting the integration point values to the corresponding nodal values has been largely investigated in control volume methods. In Section 4.3, we discretized the governing equations in a control volume manner. The resulting equations included the array of integration point unknowns which are not the major unknown nodal variables in our formulation. In order to have the discretization complete, it is required to represent the momentum components, pressure, and temperature at the integration points of an element in terms of their neighboring nodal values within that element. In Section 4.3.2, the nonlinear forms of $\mathcal{R}$ and $\mathcal{T}$, Eq.(2.21), were directly treated by invoking the elliptic nature of diffusion. On the other hand, time dependent terms were directly computed from nodal values. However, convective terms are left to be evaluated in a special manner because their treatment is not as direct as it was for the diffusion terms. Roughly, about (80 to 90)% of the difficulty in modeling of momentum equation terms returns to the complexity in modeling of convection terms, Patankar [66]. Central-difference schemes in finite-difference approaches and bilinear interpolation in finite-element approaches are the easiest ways to treat the convective integration point values within an element, however, they are limited to diffusion-dominated flows where Peclet number is less than 2.

For convective dominated flows, it is better to use upwinding-based methods which consider the higher influence of the upstream nodal values at integration points. Figure 4.1 schematically shows how the upstream influence should be regarded in evaluating convective integration point quantities. A pure upwind scheme works for all Peclet numbers, however, the accuracy of the solution is diminished. Raithby [67] has provided a comparative study on treating the convection terms by a number of upwind schemes and shows that they produce false-diffusion. Raithby [68] has also proposed a skewed upwind scheme which considers the real direction of the flow and consequently reduces the false-diffusion. The basic attempt in most recent schemes is to model the integration point values, ϕ_{ip}, by upstream values,

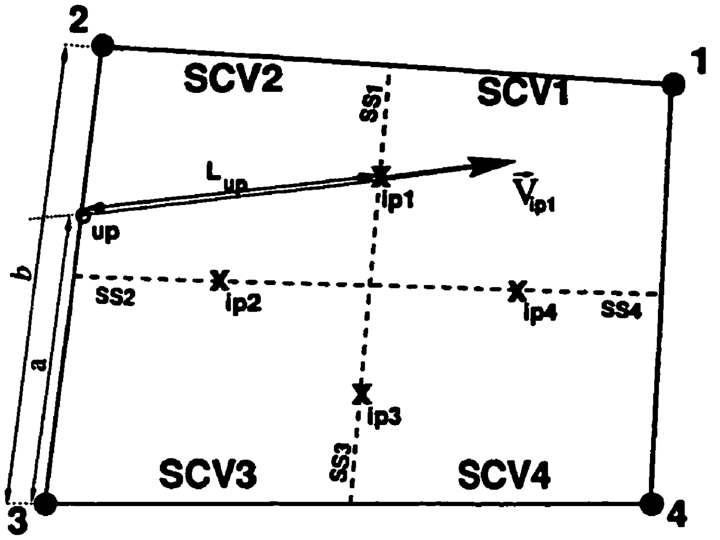

Figure 4.1: A schematic influence of upwind point.

ϕ_{up}, and then correct it by $\Delta\phi_{ip}$

$$\phi_{ip} = \phi_{up} + \Delta\phi_{ip} \tag{4.77}$$

The essence is that the connection is not only based on complex mathematical functions but also on the physical interpretation of the governing equations. Much effort has been expanded to determine better and simpler interpretations including all necessary influences. There are three basic points which must be remembered in determining integration point operators; 1-effect of directionality of the flow; 2-source (including pressure) term effects; and 3-the diffusion effects. The basic idea in modeling convective quantities is to treat the integration point values by the correct influence of upstream values. This is why different schemes like hybrid, power-law, upwind, exponential, etc. have been established over the years for their treatment.

The following sub-section present the methods of deriving the required integration point equations for different variables.

4.4.1 Momentum Components

In this section, we derive f and g integration point equations in an appropriate manner which considers the physics of the problem. More recently, control-volume-based methods have been concerned with the physics of the problem rather than complex mathematical approximations. Following this, Schneider and Raw [10] proposed a new scheme, Correct-Physical-Influence Scheme, which includes all the physics and relevant couplings for each variable. They have derived an algebraic approximation to the differential equations at each integration point. In Section 3.4.1, it was shown that this new scheme yields a physically well-behaved solution in the one-dimensional study. Following the one-dimensional investigation, the two-dimensional momentum integration point equations are derived by treating the non-conservative form of the momentum equations. In this way, the convection terms in the conservative form of the momentum equations are broken into two terms, combined with continuity equation and finally written in a streamwise direction, Appendix H. The following momentum equations are the result of this procedure:

$$\frac{\partial f}{\partial \theta} + V_{tot}\frac{\partial f}{\partial s} - \mu\nabla^2 u = -\frac{\partial p}{\partial x} + u(\frac{\partial \rho}{\partial \theta} + V_{tot}\frac{\partial \rho}{\partial s}) + \text{Viscous Terms} \tag{4.78}$$

$$\frac{\partial g}{\partial \theta} + V_{tot}\frac{\partial g}{\partial s} - \mu\nabla^2 v = -\frac{\partial p}{\partial y} + v(\frac{\partial \rho}{\partial \theta} + V_{tot}\frac{\partial \rho}{\partial s}) + \text{Viscous Terms} \tag{4.79}$$

where $V_{tot} = \sqrt{\bar{u}^2 + \bar{v}^2}$. *Viscous Terms* stand for the viscous terms which are not included at this point. In this section, f_{ip} is derived from Eq.(4.78) and the results are similarly extended to g_{ip} which must be equally derived from Eq.(4.79).

First of all, the transient term in Eq.(4.78) is written in backward form respect to time

$$\left(\frac{\partial f}{\partial \theta}\right)_{ipi} \approx \frac{f_{ipi} - f^o_{ipi}}{\Delta \theta} \tag{4.80}$$

where the subscript i denotes the integration point number. This discretization can be cast into matrix form for an arbitrary integration point of i

$$\left(\frac{\partial f}{\partial \theta}\right)_{ipi} \approx \sum_{j=1}^{4} c_{ij}^{ff\theta} f_j - C_i^{f\theta} \tag{4.81}$$

Here the notation of ip$i$ is switched to i which indicates integration point. The coefficients in question are

$$c_{i,j}^{ff\theta} = \begin{cases} \frac{1}{\Delta\theta} & j = i \\ 0 & j \neq i \end{cases} \tag{4.82}$$

$$C_i^{f\theta} = \frac{f_{ipi}^{o}}{\Delta\theta} \tag{4.83}$$

The key in this method is found in the convection term which has been written in the streamwise direction. This form provides the correct direction of upwinding in the streamwise direction. The one-dimensional investigation of this equation showed the flexibility of this formulation to predict the correct f for highly diffusive and convective flows, Section 3.4.1. The convection term is upwinded in the streamwise direction as

$$\left(V_{tot}\frac{\partial f}{\partial s}\right)_{ipi} \approx \left(\bar{V}_{tot}\frac{f - f_{up}}{L_{up}}\right)_{ipi} \tag{4.84}$$

where L_{up} and f_{up} are illustrated in Figure 4.1 for $ip1$. The upstream location, up, is found by intersecting the extension of the streamline direction at integration point with the edges of the same element. The value for f_{up} is interpolated between the two adjacent nodes which are nodes 2 and 3 for $ip1$ in Figure 4.1, i.e.,

$$(f_{up})_{ipi} = \frac{a}{b}(F_{upr})_{ipi} + (1 - \frac{a}{b})(F_{upl})_{ipi} \tag{4.85}$$

where $(F_{upr})_{ipi}$ and $(F_{upl})_{ipi}$ refer to the nodal values of F at right and left of the upstream point "up", respectively, when "up" point is watched from integration point i. Using this definition, a general form for integration point i is given by

$$\left(V_{tot}\frac{\partial f}{\partial s}\right)_{ipi} \approx \sum_{j=1}^{4} c_{ij}^{ffc} f_j + \sum_{j=1}^{4} C_{ij}^{ffc} F_j \tag{4.86}$$

where the matrix coefficients are

$$c_{i,j}^{ffc} = \begin{cases} \left(\frac{\bar{V}_{tot}}{L_{up}}\right)_{ipi} & j = i \\ 0 & j \neq i \end{cases} \tag{4.87}$$

$$C_{i,j}^{ffc} = \begin{cases} \left(\frac{\bar{V}_{tot}}{L_{up}}\frac{a}{b}\right)_{ipi} & j = (upr)_{ipi} \\ \left(\frac{\bar{V}_{tot}}{L_{up}}(1 - \frac{a}{b})\right)_{ipi} & j = (upl)_{ipi} \\ 0 & \text{else} \end{cases} \tag{4.88}$$

Here, the magnitude of C_{ij}^{ffc} depends only on the flow direction which is obtained by using Eq.(4.85).

The Mass-Weighted-Skew scheme of Schneider and Raw [69] is another accurate method for treating the convection terms. It reduces the possibility of negative coefficients in the formulation. This scheme models the local directionality of the flow in the manner that ensures positive coefficients in the convection terms of the discretized control volume equations. It finds the flow direction within the element and computes L_{up} and f_{up} based on the values and directions of flow parameters for both nodal and integration points. This results in a correct influence of flow in highly recirculating flows. We do not present the details of this scheme because the results which are presented in this study are only based on the previously discussed scheme.

Finite element shape function derivatives, Section A.3, are used to treat the pressure term in Eq.(4.78) as

$$-\left(\frac{\partial p}{\partial x}\right)_{ipi} \approx -\sum_{j=1}^{4}\left(\frac{\partial N_j}{\partial x}\right)_{ipi} P_j = \sum_{j=1}^{4} C_{ij}^{fpp} P_j \tag{4.89}$$

where the matrix coefficients are

$$C_{i,j}^{fpp} = -\left(\frac{\partial N_j}{\partial x}\right)_{ipi} \tag{4.90}$$

The role of the incompressible part of the diffusion term is considered as an active one in deriving the integration point equation for f. Again, the elliptic nature of diffusion promotes the use of finite element shape function derivatives. After linearization of the Laplacian operator in terms of momentum components, it can be approximated by

$$\left(\nabla^2 u\right)_{ipi} = \left(\nabla^2\left(\frac{f}{\rho}\right)\right)_{ipi} \approx \frac{\sum_{j=1}^{4} \frac{(N_j)_{ipi}}{\bar{\varrho}_j} F_j - \left(\frac{f}{\bar{\rho}}\right)_{ipi}}{(L_d^2)_{ipi}} \tag{4.91}$$

where L_d is an appropriate diffusion length scale, Appendix I. This approximation reduces to $f_i \approx \sum_{j=1}^{4} N_j F_j$ when diffusion dominates the convection in incompressible flows, i.e. $\nabla^2 u$=0. A general form of the Laplacian operator at an arbitrary integration point i can be written as

$$\mu\left(\nabla^2 u\right)_{ipi} \approx \sum_{j=1}^{4} C_{ij}^{ffd} F_j - \sum_{j=1}^{4} c_{ij}^{ffd} f_j \tag{4.92}$$

where the coefficient of the matrices are

$$c_{i,j}^{ffd} = \begin{cases} \mu\left(\frac{1}{\bar{\rho} L_d^2}\right)_{ipi} & j = i \\ 0 & j \neq i \end{cases} \tag{4.93}$$

$$C_{i,j}^{ffd} = \frac{\mu}{\bar{\varrho}_j}\left(\frac{N_j}{L_d^2}\right)_{ipi} \tag{4.94}$$

The last part of the discretization is the treatment of the terms inside the parenthesis in the right-hand-side of Eq.(4.78). This part is completely lagged and computed from the previous known values. The approximation of this part for an arbitrary integration point i is

$$u_{ipi}\left(\frac{\partial\rho}{\partial\theta}+V_{tot}\frac{\partial\rho}{\partial s}\right)_{ipi}\approx C_i^{fc}=\bar{u}_{ipi}\left(\frac{\bar{\rho}-\rho^o}{\Delta\theta}+\bar{V}_{tot}\frac{\bar{\rho}-\bar{\rho}_{up}}{L_{up}}\right)_{ipi} \tag{4.95}$$

With this discretization, the modeling of all terms in Eq.(4.78) is complete. If these models, including Eqs.(4.81, 4.86, 4.89, 4.92, and 4.95), are plugged into Eq.(4.78) and similar coefficients are combined together the complete integration point equation for f is written as

$$\sum_{j=1}^{4}(c_{i,j}^{ff\theta}+c_{i,j}^{ffc}+c_{i,j}^{ffd})f_j=\sum_{j=1}^{4}(C_{i,j}^{ffc}+C_{i,j}^{ffd})F_j+\sum_{j=1}^{4}C_{i,j}^{fpp}P_j+C_i^{f\theta}+C_i^{fc} \tag{4.96}$$

The matrix form of the algebraic equation for f is

$$[c^{ff\theta}+c^{ffc}+c^{ffd}]\{f\}=[C^{ffc}+C^{ffd}]\{F\}+[C^{fpp}]\{P\}+\{C^{f\theta}+C^{fc}\} \tag{4.97}$$

This integration point equation relates f at the integration point to its neighbouring nodal dependent variables. In order to derive a direct expression for f, the coefficient matrix of f is inverted and multiplied by the other coefficient matrices on the right hand side. The final form of the f operators at four integration points of the element could be summarized in the following fashion:

$$\{f\}=[C^{ff}]\{F\}+[C^{fp}]\{P\}+\{C^f\} \tag{4.98}$$

Comparing with Eq.(4.77), it denotes that the two last terms in Eq.(4.98) are responsible for the streamwise correction, i.e. $\Delta\phi$. The matrices on the right hand side are named *influence coefficient matrices* because they verify the correct physical influence of the nodal values on the integration point values. They are

$$[C^{ff}] = [c^{ff\theta} + c^{ffc} + c^{ffd}]^{-1}[C^{ffc} + C^{ffd}] \tag{4.99}$$

$$[C^{fp}] = [c^{ff\theta} + c^{ffc} + c^{ffd}]^{-1}[C^{fpp}] \tag{4.100}$$

$$\{C^{f}\} = [c^{ff\theta} + c^{ffc} + c^{ffd}]^{-1}\{C^{f\theta} + C^{fc}\} \tag{4.101}$$

where C^{ff} and C^{fp} are two 4×4 matrices which indicate the effect of F and P fields on f. The 4×1 array of $\{C^f\}$ includes all known parts of the assembled terms. The first and second superscripts of C indicates to which equation and parameter of equation it respectively belongs.

Similarly, an expression for g is derived by following the procedure that was just described for f but starting from Eq.(4.79). The final result can be written as

$$\{g\} = [C^{gg}]\{G\} + [C^{gp}]\{P\} + \{C^{g}\} \tag{4.102}$$

The elements of the referred matrices can be determined by comparing with the matrices of the f operator.

Now, these integration point expressions of f and g are substituted in the momentum parts of the arrays $\mathcal{F}$ and $\mathcal{G}$ in Eqs.(4.49, 4.50, and 4.76). According to our experience in the one-dimensional study, these expressions are not plugged into the continuity equation. Supplementary integration point equations are derived in Section 4.5 for continuity equation.

4.4.2 Pressure

The integration point pressure which appeared in the conservative discretization of governing equations has to be calculated as a function of nodal dependent variables in the element. The integration point pressure is needed for treating the pressure terms in the momentum and energy governing equations where velocity and temperature fields, respectively, are coupled with the pressure field. A strong coupling like that from the pressure Poisson equation, which can be derived by taking the divergence of the momentum equations, is not so critical in this study. On the contrary, a simple interpolation will provide the primary connection and provides a good representation of the pressure field. In this regard, bilinear finite-element shape functions are used to convey the elliptic nature of pressure at the integration points

$$p_{ipi} = \sum_{j=1}^{4} (N_j)_{ipi} P_j \tag{4.103}$$

Using the following definition

$$C_{ij}^{-p} = (N_j)_{ipi} \tag{4.104}$$

will result in the matrix form of the integration point operator for the pressure

$$\{p\} = [C^{-p}]\{P\} \tag{4.105}$$

The minus sign in the superscript means that p is not derived based on any governing equations but on physical reasoning.

4.4.3 Temperature Variable

Following the procedure discussed in Section 3.4.2, the non-conservative form of energy equation is used to derive the appropriate integration point operator for temperature. Either enthalpy or total energy as well as temperature are quantities which can be treated in the manner that convected quantities are dealt with.

On the other hand, the energy equation can be written in a number of ways to represent the transport of the parameter in question, i.e. h, e, and t. Here, we select the temperature form of this equation because the temperature is considered as a dependent variable in this study. The use of other forms, i.e. enthalpy and total energy, require more linearization for h and e according to their definitions, Eqs.(2.13 and 2.14). The temperature form of the energy equation could be formed by combining the continuity equation, Eq.(2.2), and the original form of the energy equation, Eq.(2.5). The final form after employing the definition of total energy, Eq.(2.13), assuming zero source term, and writing the convection terms in the streamwise direction, Appendix H, is

$$\frac{\partial t}{\partial \theta} + V_{tot}\frac{\partial t}{\partial s} - \frac{\mathbf{k}}{\rho c_v}\nabla^2 t = \frac{1}{\rho c_v}\left\{-p\vec{\nabla}\cdot\vec{V} + \mu\Theta\right\} \tag{4.106}$$

where the thermal dissipation function is

$$\Theta = 2(\frac{\partial u}{\partial x})^2 + 2(\frac{\partial v}{\partial y})^2 + (\frac{\partial v}{\partial x} + \frac{\partial u}{\partial y})^2 - \frac{2}{3}(\frac{\partial u}{\partial x} + \frac{\partial v}{\partial y})^2 \tag{4.107}$$

Comparing the left hand side of Eq.(4.106) with that of Eq.(4.78) shows that their transient and convection terms are identical if μ is replaced by $\frac{k}{\rho c_v}$ and f by t. Using this analogy and the general forms in Eqs.(4.81 and 4.86) will result in

$$\frac{\partial t}{\partial \theta} + V_{tot}\frac{\partial t}{\partial s} \approx \sum_{j=1}^{4} c_{i,j}^{tt\theta}\, t_j - C_i^{t\theta} - \sum_{j=1}^{4} c_{i,j}^{ttc}\, t_j + \sum_{j=1}^{4} C_{i,j}^{ttc}\, T_j \tag{4.108}$$

where the matrix elements are readily obtained by

$$c_{i,j}^{tt\theta} = c_{i,j}^{ff\theta} \tag{4.109}$$

$$C_i^{t\theta} = \frac{t_{ipi}^{o}}{\Delta\theta} \tag{4.110}$$

$$c_{i,j}^{ttc} = c_{i,j}^{ffc} \tag{4.111}$$

$$C_{i,j}^{ttc} = C_{i,j}^{ffc} \tag{4.112}$$

Contrary to Eq.(4.78), the energy diffusion term does not need linearization here, i.e.,

$$\left(\frac{\mathbf{k}}{\rho c_v}\nabla^2 t\right)_{ipi} \approx \frac{\mathbf{k}}{c_v\bar{\rho}_{ipi}}\frac{\sum_{j=1}^{4}(N_j)_{ipi}T_j - t_{ipi}}{(L_d^2)_{ipi}} = \sum_{j=1}^{4} C_{ij}^{ttd}T_j - \sum_{j=1}^{4} c_{ij}^{ttd}t_j \tag{4.113}$$

where the matrix coefficients are given by

$$c_{i,j}^{ttd} = \begin{cases} \frac{\mathbf{k}}{c_v}\left(\frac{1}{\bar{\rho}L_d^2}\right)_{ipi} & j = i \\ 0 & j \neq i \end{cases} \tag{4.114}$$

$$C_{i,j}^{ttd} = \frac{\mathbf{k}}{c_v}\left(\frac{N_j}{\bar{\rho}L_d^2}\right)_{ipi} \tag{4.115}$$

The pressure term is approximated by

$$-p\vec{\nabla}\cdot\vec{\mathbf{V}} \approx -\left\{\sum_{l=1}^{4}\left(\frac{\partial N_l}{\partial x}\right)_{ipi}\bar{U}_l + \sum_{l=1}^{4}\left(\frac{\partial N_l}{\partial y}\right)_{ipi}\bar{V}_l\right\}\sum_{j=1}^{4}(N_j)_{ipi}P_j \tag{4.116}$$

The related matrix coefficient is written

$$C_{i,j}^{tpp} = \frac{-1}{\bar{\rho}_{ipi}c_v}\left\{\sum_{l=1}^{4}\left(\frac{\partial N_l}{\partial x}\right)_{ipi}\bar{U}_l + \sum_{l=1}^{4}\left(\frac{\partial N_l}{\partial y}\right)_{ipi}\bar{V}_l\right\}\sum_{j=1}^{4}(N_j)_{ipi} \tag{4.117}$$

The dissipation term is completely approximated from previous known values

$$C_i^{ts} = \frac{\mu}{c_v\bar{\rho}_{ipi}}\bar{\Theta}_{ipi} \tag{4.118}$$

where

$$\bar{\Theta}_{ipi} = 2\left(\sum_{j=1}^{4}\left.\frac{\partial N_j}{\partial x}\right|_{ipi}\bar{U}_j\right)^2 + 2\left(\sum_{j=1}^{4}\left.\frac{\partial N_j}{\partial y}\right|_{ipi}\bar{V}_j\right)^2 + \left(\sum_{j=1}^{4}\left.\frac{\partial N_j}{\partial x}\right|_{ipi}\bar{V}_j\right.$$
$$\left. + \sum_{j=1}^{4}\frac{\partial N_j}{\partial y}\,|_{ipi}\bar{U}_j\right)^2 - \frac{2}{3}\left(\sum_{j=1}^{4}\left.\frac{\partial N_j}{\partial x}\right|_{ipi}\bar{U}_j + \sum_{j=1}^{4}\left.\frac{\partial N_j}{\partial y}\right|_{ipi}\bar{V}_j\right)^2 \tag{4.119}$$

Combining and rearranging the above terms will result in the matrix arrangement of the algebraic equation for t as

$$\sum_{j=1}^{4}(c_{i,j}^{tt\theta} + c_{i,j}^{ttc} + c_{i,j}^{ttd})t_j = \sum_{j=1}^{4}(C_{i,j}^{ttc} + C_{i,j}^{ttd})T_j + \sum_{j=1}^{4} C_{i,j}^{tpp}P_j + (C_i^{t\theta} + C_i^{ts}) \tag{4.120}$$

This equation can be written in matrix form. The integration point expression for temperature is

$$\{t\} = [C^{tt}]\{T\} + [C^{tp}]\{P\} + \{C^{t}\} \tag{4.121}$$

The influence coefficient matrices on the right-hand-side are

$$[C^{tt}] = [c^{tt\theta} + c^{ttc} + c^{ttd}]^{-1}[C^{ttc} + C^{ttd}] \tag{4.122}$$

$$[C^{tp}] = [c^{tt\theta} + c^{ttc} + c^{ttd}]^{-1}[C^{tpp}] \tag{4.123}$$

$$\{C^{t}\} = [c^{tt\theta} + c^{ttc} + c^{ttd}]^{-1}\{C^{t\theta} + C^{ts}\} \tag{4.124}$$

Eq.(4.121) is not the only choice that can be used to calculate integration point temperature. Bilinear interpolation and streamwise upwinding are two other simple methods which were applied in many cases to compute the integration point temperature. This will be discussed more in Chapter 5 for solving mixed subsonic-supersonic flow with shock through a convergent-divergent nozzle.

4.4.4 Other Integration Point Equations

Before closing Section 4.4, it is necessary to explain about the method of derivation of the other integration point quantities which do not directly appear in our discretized equation. One such variable is density which should provide information for deriving the velocity field from the computed momentum field at the integration points. Density behaves as a convected quantity in highly compressible flows. Density integration point equation could be calculated in a manner which was done in Section 3.4.2 in one-dimensional investigations. However, in this two-dimensional study, density was mostly computed by using the following expression

$$\rho_{ipi} = k\, \rho_{up} \; + \; (1 - k)\, \rho_{bi} \tag{4.125}$$

where ρ_{bi} is a simple bilinear interpolation and k is a weighting coefficient which measures the correct influence of the two approximations. It is defined by

$$k = \begin{cases} 0 & M < 1 \\ 1 - \frac{1}{M^2} & M > 1 \end{cases} \tag{4.126}$$

The two approximations return to pure upwinding and bilinear interpolating, respectively. The density at upwind point, ρ_{up}, is determined in a similar manner to Eq.(4.85) for approximating f_{up}.

The other integration point lagged values are computed by using the already derived integration point expressions, i.e., Eqs.(4.98, 4.102, 4.105, 4.121, and 4.125). In this regard, velocity integration point values are obtained by using the magnitudes of the momentum components and density, i.e.,

$$u = \frac{f}{\rho} \qquad v = \frac{g}{\rho} \tag{4.127}$$

The total energy and enthalpy integration point values are obtained by employing the new integration point values to their original definitions, Eqs.(2.13 and 2.14).

4.5 Mass Conserving Connections

In this section, the necessary remedy for removing the checkerboard problem which is a common problem for certain numerical methods with a colocated grid arrangement is explained. The expressions which we derived for f and g in Section 4.4.1 are called *convected* ones. As discussed before, Section 3.5, these expressions are not substituted into the control volume continuity equation. The continuity equation constrains mass through the surfaces of the control volume which is highly affected by the pressure field. Thus, the pressure field is indirectly specified by the continuity equation although there is no explicit effect of the pressure field on density in an incompressible formulation. The use of convected expressions for f and g should compensate for the absence of a pressure term in the continuity equation. However, the investigation shows that this remedy does not necessarily remove the possibility of velocity and pressure field decoupling, e.g. Darbandi and Schneider [13], Section 3.5.1. The missing point in this conclusion could be found by reviewing the derived expressions. Convected expressions for f and g were originally derived from the momentum equations. These expressions did not consider the effect of the continuity equation which considers satisfaction of the mass. The idea of using two integration point values for a colocated grid arrangement goes back to the work of Rhie and Chow [9]. There are also other works which emphasize the employment of the two types of the integration point velocities, Schneider and Karimian [12]. Darbandi and Schneider [13] employed a new formulation for deriving a second integration point equation for momentum-components. These new expressions are obtained not only from modeling of the differential form of the momentum equations at each integration point, but the continuity equation is required to be used in conjunction with the momentum equations. To derive a second integration point value for f or g, a velocity-weighted continuity-equation error is subtracted from the momentum governing equations. Similar to the one-dimensional study, the form of these equations is

$$(x\text{-Momentum Eq. Error}) - u\,(\text{Continuity Eq. Error}) = 0 \tag{4.128}$$

$$(y\text{-Momentum Eq. Error}) - v\ (\text{Continuity Eq. Error}) = 0 \tag{4.129}$$

Now, these equations consider the numerical errors of both the continuity and momentum equations at the integration point. For the sake of brevity, the method of discretization is explained only for convecting f which is derived from Eq.(4.128). The results can then be extended for g. By substituting the governing equations into Eq.(4.128) the following equation is obtained

$$\frac{\partial f}{\partial \theta} + V_{tot}\frac{\partial f}{\partial s} - \mu \nabla^2 u + \frac{\partial p}{\partial x} + \text{Viscous Terms} - u(\frac{\partial \rho}{\partial \theta} - V_{tot}\frac{\partial \rho}{\partial s})$$
$$-u\left[\frac{\partial \rho}{\partial \theta} + \frac{\partial f}{\partial x} + \frac{\partial g}{\partial y}\right] = 0 \tag{4.130}$$

All of the terms in the momentum part of this equation are treated as in Section 4.4.1. The method of discretization for the second bracket is explained here. The $u\frac{\partial \rho}{\partial \theta}$ term is treated in the same manner that it was treated in Eq.(4.95), i.e.,

$$u_{ipi}\left(\frac{\partial \rho}{\partial \theta}\right)_{ipi} \approx C_i^{fm} = \bar{u}_{ipi}\left(\frac{\bar{\rho} - \rho^o}{\Delta \theta}\right)_{ipi} \tag{4.131}$$

The two other terms are discretized using bilinear interpolation

$$u_{ipi}(\frac{\partial f}{\partial x} + \frac{\partial g}{\partial y})_{ipi} \approx \bar{u}_{ipi}\left[\sum_{j=1}^{4} \left.\frac{\partial N_j}{\partial x}\right|_{ipi} F_j + \sum_{j=1}^{4} \left.\frac{\partial N_j}{\partial y}\right|_{ipi} G_j\right] \tag{4.132}$$

This discretization is written in matrix form for an arbitrary control volume of i

$$u_{ipi}(\frac{\partial f}{\partial x} + \frac{\partial g}{\partial y})_{ipi} \approx \sum_{j=1}^{4} C_{i,j}^{ffm} F_j + \sum_{j=1}^{4} C_{i,j}^{fgm} G_j \tag{4.133}$$

where the coefficients are defined as

$$C_{i,j}^{ffm} = \bar{u}_{ipi} \left.\frac{\partial N_j}{\partial x}\right|_{ipi} \tag{4.134}$$

$$C_{i,j}^{fgm} = \bar{u}_{ipi} \left.\frac{\partial N_j}{\partial y}\right|_{ipi} \tag{4.135}$$

There is another method for treating these two terms. In this method, $\frac{\partial f}{\partial x}$ is replaced by reference to $\frac{\partial f}{\partial s}$, with suitable alternative of Eq.(4.133), and then $\frac{\partial f}{\partial s}$ is discretized in streamwise direction. Regarding Figure 4.2, it is written

$$\frac{\partial f}{\partial s} = \frac{f_{dn} - f_{up}}{L_{up} + L_{dn}} \tag{4.136}$$

where $L_{up}+L_{dn}$ is the distance between *up* and *dn* points. f_{dn} and f_{up} are properly interpolated between adjacent nodes, Eq.(4.85). We have tested both of these methods and the difference is not significant.

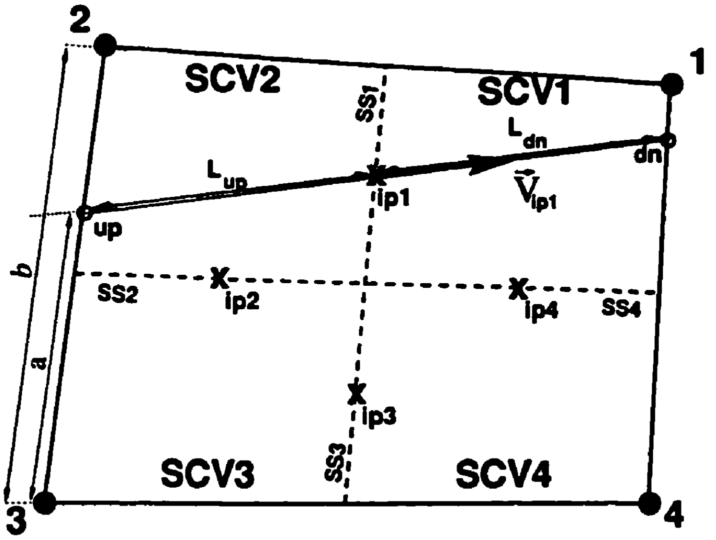

Figure 4.2: Element nomenclature and velocity upwinding.

Now, the new derived discretizations of this section are combined with the discretization results of Section 4.4.1. This will conclude with an equation for the convecting $\hat{f}$, similar to Eq.(4.98) which was derived for the convected f. After substitution of the terms of Eq.(4.130), they are categorized and combined together and the following expression is finally obtained

$$\{\hat{f}\} = [C^{\hat{f}f}]\{F\} + [C^{\hat{f}g}]\{G\} + [C^{\hat{f}p}]\{P\} + \{C^{\hat{f}}\} \tag{4.137}$$

This new integration point expression is called the *convecting momentum* for f. In order to distinguish it from the convected one we denote it by $\hat{f}$. The new influence coefficient matrices on right-hand-side are computed by adding the new matrix derivations to Eqs.(4.99-4.101), i.e.,

$$[C^{\hat{f}f}] = [c^{ff\theta} + c^{ffc} + c^{ffd}]^{-1}[C^{ffc} + C^{ffd} + C^{\hat{f}fm}] \tag{4.138}$$

$$[C^{\hat{f}g}] = [c^{ff\theta} + c^{ffc} + c^{ffd}]^{-1}[C^{\hat{f}gm}] \tag{4.139}$$

$$[C^{\hat{f}p}] = [c^{ff\theta} + c^{ffc} + c^{ffd}]^{-1}[C^{fpp}] \tag{4.140}$$

$$\{C^{\hat{f}}\} = [c^{ff\theta} + c^{ffc} + c^{ffd}]^{-1}\{C^{f\theta} + C^{fc} + C^{\hat{f}m}\} \tag{4.141}$$

A similar convecting could be derived for convecting $\hat{g}$. The procedure is started from Eq.(4.129) and the convecting expression is similar to Eq.(4.137), i.e.,

$$\{\hat{g}\} = [C^{\hat{g}f}]\{F\} + [C^{\hat{g}g}]\{G\} + [C^{\hat{g}p}]\{P\} + \{C^{\hat{g}}\} \tag{4.142}$$

These integration point expressions, i.e. Eqs.(4.137 and 4.142) are plugged into the continuity equation. Consequently, convecting velocities could be obtained by using the following definitions, $\hat{u} = \frac{\hat{f}}{\rho}$ and $\hat{v} = \frac{\hat{g}}{\rho}$. Regarding the discussion in Appendix C and respecting the two concepts of the convected and convecting velocities, the convecting expressions are used for computing lagged values in the convection terms of the conservative form of the momentum equations, i.e. Eq.(4.36). Either convected or convecting velocities could be plugged in the lagged velocities of the energy convection terms. However, in order to respect the consistancy it is better to use convecting ones.

4.6 Assembly

In Section 4.3, we discretized the governing equations by using a control-volume-based finite-element method. All discretizations were initially obtained for an arbitrary sub-control-volume and later extended for four sub-control-volumes of an element. The final results showed that the discretized equations involved unknowns at integration points in addition to the main nodal unknowns, see Eqs.(4.23, 4.49, 4.50, and 4.76). This difficulty resulted in deriving expressions for dependent variables at integration points, i.e. f, g, p, and t in Eqs.(4.98, 4.102, 4.105, and 4.121). These expressions not only connect the integration point variables to their neighbouring nodal variables but also model the possible relevant physics. In addition fo f and g, supplementary integration point expressions were derived for momentum components, i.e. $\hat{f}$ and $\hat{g}$ in Eqs.(4.137 and 4.142), in order to remove the pressure-velocity decoupling problem.

In this section, the discretized equations and the derived integration point expressions are combined and rearranged in order to provide a well-posed system of linear algebraic equations. We start the assembly procedure with treating the continuity equation. There are two integration point variables, f and g, in Eq.(4.23). Convecting momentum components, Eqs.(4.137 and 4.142), are plugged in the continuity equation. It results in

$$[D^{pf}]\{F\} + [D^{pg}]\{G\} + [D^{pp}]\{P\} + [D^{pt}]\{T\} = \{D^{p}\} \tag{4.143}$$

where

$$[D^{pf}] = [a^{pfm}][C^{\hat{f}f}] + [a^{pgm}][C^{\hat{g}f}] \quad (4.144)$$

$$[D^{pg}] = [a^{pfm}][C^{\hat{f}g}] + [a^{pgm}][C^{\hat{g}g}] \quad (4.145)$$

$$[D^{pp}] = [A^{pp\theta}] + [a^{pfm}][C^{\hat{f}p}] + [a^{pgm}][C^{\hat{g}p}] \quad (4.146)$$

$$[D^{pt}] = [A^{pt\theta}] \quad (4.147)$$

$$[D^{p}] = \{A^{p\theta}\} - [a^{pfm}]\{C^{\hat{f}}\} - [a^{pgm}]\{C^{\hat{g}}\} \quad (4.148)$$

The first and second superscripts of D indicates to which equation and parameter of equation it respectively belongs. Eqs.(4.49 and 4.50) show that the x-momentum and y-momentum equations involve pressure and momentum component unknowns at integration points. The integration point expression for pressure is given by Eq.(4.105). The convected momentum-component operators, Eqs.(4.98 and 4.102), are selected for unknown momentum-components at integration points. The procedure results in the following equation for the x-momentum

$$[D^{ff}]\{F\} + [D^{fg}]\{G\} + [D^{fp}]\{P\} + [D^{ft}]\{T\} = \{D^{f}\} \quad (4.149)$$

where

$$[D^{ff}] = [A^{ff\theta} + A^{ffd}] + [a^{ffc}][C^{ff}] \quad (4.150)$$

$$[D^{fg}] = [A^{fgd}] \quad (4.151)$$

$$[D^{fp}] = [a^{ffc}][C^{fp}] + [D^{fpp}][C^{-p}] \quad (4.152)$$

$$[D^{ft}] = 0 \quad (4.153)$$

$$[D^{f}] = \{A^{f\theta} + A^{fd}\} - [a^{ffc}]\{C^{f}\} \quad (4.154)$$

Similar procedure for the y-momentum equation will result in

$$[D^{gf}]\{F\} + [D^{gg}]\{G\} + [D^{gp}]\{P\} + [D^{gt}]\{T\} = \{D^{g}\} \tag{4.155}$$

where

$$[D^{gf}] = [A^{gfd}] \tag{4.156}$$

$$[D^{gg}] = [A^{gg\theta} + A^{ggd}] + [a^{ggc}][C^{gg}] \tag{4.157}$$

$$[D^{gp}] = [a^{ggc}][C^{gp}] + [a^{gpp}][C^{-p}] \tag{4.158}$$

$$[D^{gt}] = 0 \tag{4.159}$$

$$[D^{g}] = \{A^{g\theta} + A^{gd}\} - [a^{ggc}]\{C^{g}\} \tag{4.160}$$

The energy equation, Eq.(4.76), involves f, g, and t unknowns at integration points. The unknown temperature at the integration point is substituted from Eq.(4.121) and the convecting momentum-components, Eqs.(4.137 and 4.142), are plugged into unknown momentum-components at the integration points. It yields

$$[D^{tf}]\{F\} + [D^{tg}]\{G\} + [D^{tp}]\{P\} + [D^{tt}]\{T\} = \{D^{t}\} \tag{4.161}$$

where

$$[D^{tf}] = [A^{tf\theta} + A^{tfd}] + [a^{tfc}][C^{\hat{f}f}] + [a^{tgc}][C^{\hat{g}f}] \tag{4.162}$$

$$[D^{tg}] = [A^{tg\theta} + A^{tgd}] + [a^{tfc}][C^{\hat{f}g}] + [a^{tgc}][C^{\hat{g}g}] \tag{4.163}$$

$$[D^{tp}] = [a^{tfc}][C^{\hat{f}p}] + [a^{tgc}][C^{\hat{g}p}] + [a^{ttc}][C^{tp}] \tag{4.164}$$

$$[D^{tt}] = [A^{tt\theta} + A^{ttk}] + [a^{ttc}][C^{tt}] \tag{4.165}$$

$$[D^{t}] = \{A^{t\theta} + A^{td}\} - [a^{tfc}]\{C^{\hat{f}}\} - [a^{tgc}]\{C^{\hat{g}}\} - [a^{ttc}]\{C^{t}\} \tag{4.166}$$

The first stage of the assembly is finished now. We have already derived well-posed discretized equations for the continuity, Eq.(4.143), x-momentum, Eq.(4.149), y-momentum, Eq.(4.155), and energy, Eq.(4.161), equations. Each of these equations consist of four sub-equations for four sub-control-volume of an element. The number of unknowns in each sub-equation can be 16 or less. This number indicates the maximum number of unknowns at four nodes of element. They are four Fs, four Gs, four Ps, and four Ts.

In the second stage of the assembly, the derived elemental equations are put together

$$[D^{pf}]\{F\} + [D^{pg}]\{G\} + [D^{pp}]\{P\} + [D^{pt}]\{T\} = \{D^{p}\} \qquad (4.167a)$$

$$[D^{ff}]\{F\} + [D^{fg}]\{G\} + [D^{fp}]\{P\} + [D^{ft}]\{T\} = \{D^{f}\} \qquad (4.167b)$$

$$[D^{gf}]\{F\} + [D^{gg}]\{G\} + [D^{gp}]\{P\} + [D^{gt}]\{T\} = \{D^{g}\} \qquad (4.167c)$$

$$[D^{tf}]\{F\} + [D^{tg}]\{G\} + [D^{tp}]\{P\} + [D^{tt}]\{T\} = \{D^{t}\} \qquad (4.167d)$$

It could be written in the following matrix form as

$$\begin{bmatrix} [D^{pf}] & [D^{pg}] & [D^{pp}] & [D^{pt}] \\ [D^{ff}] & [D^{fg}] & [D^{fp}] & [D^{ft}] \\ [D^{gf}] & [D^{gg}] & [D^{gp}] & [D^{gt}] \\ [D^{tf}] & [D^{tg}] & [D^{tp}] & [D^{tt}] \end{bmatrix} \begin{Bmatrix} \{F\} \\ \{G\} \\ \{P\} \\ \{T\} \end{Bmatrix} = \begin{Bmatrix} \{D^{p}\} \\ \{D^{f}\} \\ \{D^{g}\} \\ \{D^{t}\} \end{Bmatrix} \qquad (4.168)$$

This 16×16 matrix is named *elemental stiffness matrix*. As seen, the procedure of the assembly resulted in a well-posed system of algebraic equations having 16 equations and 16 unknowns. It is important to note that this matrix does not provide information related to the conservation of the quantities because the assembly procedure is done for four sub-control-volumes of four different control-volumes. While the governing equations are conserved within individual control volumes rather than elements or sub-control-volumes.

At the third stage of assembly, the elemental stiffness matrix is assembled into the global matrix of all elements. In this regard, each derived sub-equation is added to the related global conservation equation. This global equation belongs to the control volume that the derived sub-equation belongs to one of its four sub-control-volumes. The assembly of four different sub-control-volumes of a control volume will result in the full conservation of the conserved quantities for that control volume. This is one of the most important advantages of the control-volume-based methods which provides the conservation laws for finite volumes.

The resulted system of algebraic equations has been solved by a direct sparse matrix solver, Chu et al [70].

4.7 Boundary Condition Implementation

Before presenting the results of the application of the numerical method, it is important to describe the techniques used to invoke boundary conditions. This not only eliminates repeating these discussions and thereby saving space but it also provides a collection of worthwhile detailed information for future reference.

The assembly of the elemental equations, Section 4.6, results in complete conservation of mass, momentum, and energy equations for all control volumes of the domain except those which have one or more surfaces coincident with solution domain boundary. The process of closing the conservation equations for a boundary control volume is completed if mass, momentum, and energy boundary flows are taken into account, i.e.

$$\text{(internal continuity equation)} + \quad Q_b^m \quad = 0 \tag{4.169}$$

$$\text{(internal } x\text{-momentum equation)} + \quad Q_b^f \quad = 0 \tag{4.170}$$

$$\text{(internal } y\text{-momentum equation)} + \quad Q_b^g \quad = 0 \tag{4.171}$$

$$\text{(internal energy equation)} + \quad Q_b^e \quad = 0 \tag{4.172}$$

where Q_b's represent the boundary mass, x-momentum, y-momentum, and energy flows which are indicated by m, f, g, and e, respectively. They consist of elementary convection and diffusion flux terms

$$Q_b^f = Q_b^{fc} + Q_b^{fp} - Q_b^{fd} \tag{4.173}$$

$$Q_b^g = Q_b^{gc} + Q_b^{gp} - Q_b^{gd} \tag{4.174}$$

$$Q_b^e = Q_b^{ec} + Q_b^{eq} - Q_b^{ed} \tag{4.175}$$

These fluxes are calculated by approximating the integration over the surfaces which are coincident with the domain boundary surfaces. These surfaces have been illustrated for the control volume in question in Figure 4.3. The crosses at the surface mid-points represent them, i.e. at *bip*1 and *bip*2 integration points. The resulting fluxes for the continuity equation are written

$$Q_b^m \;=\; \sum_{j=1}^{2} \int_{bipj} \rho \vec{V} \cdot d\vec{S} \tag{4.176}$$

Similarly, the resulting fluxes for the momentum equations are given by

$$Q_b^{fc} = \sum_{j=1}^{2} \int_{bipj} \rho u \vec{V} \cdot \vec{dS} \tag{4.177}$$

$$Q_b^{fp} \approx \sum_{j=1}^{2} [p(\Delta S)_x]_{bipj} \tag{4.178}$$

$$Q_b^{fd} \approx \sum_{j=1}^{2} [\sigma_n(\Delta S)_x - \sigma_t(\Delta S)_y]_{bipj} \tag{4.179}$$

$$Q_b^{gc} = \sum_{j=1}^{2} \int_{bipj} \rho v \vec{V} \cdot \vec{dS} \tag{4.180}$$

$$Q_b^{gp} \approx \sum_{j=1}^{2} [p(\Delta S)_y]_{bipj} \tag{4.181}$$

$$Q_b^{gd} \approx \sum_{j=1}^{2} [\sigma_n(\Delta S)_y + \sigma_t(\Delta S)_x]_{bipj} \tag{4.182}$$

And for the energy equation, they are are written

$$Q_b^{ec} = \sum_{j=1}^{2} \int_{bipj} \rho h \vec{V} \cdot \vec{dS} \tag{4.183}$$

$$Q_b^{eq} \approx \sum_{j=1}^{2} [q_x(\Delta S)_x + q_y(\Delta S)_y]_{bipj} \tag{4.184}$$

$$Q_b^{ed} \approx \sum_{j=1}^{2} [(u\tau_{xx} + v\tau_{xy})(\Delta S)_x + (u\tau_{yx} + v\tau_{yy})(\Delta S)_y]_{bipj} \tag{4.185}$$

where σ_n and σ_t are normal and tangential surface stresses. $(\Delta S)_x$ and $(\Delta S)_y$ were defined before by Eqs.(2.25).

A comprehensive discussion on the proper treatment of the above expressions and their combinations at boundary surfaces has been presented by Schneider [71].

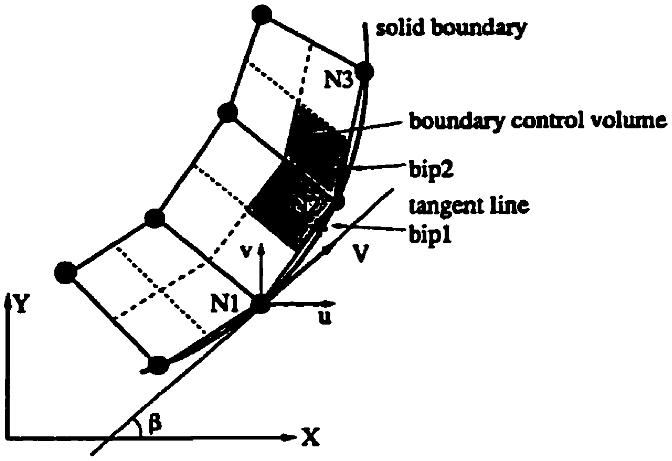

Figure 4.3: Boundary control volume and boundary condition implementation.

There are many different methods to implement the boundary conditions. However, we are not interested in presenting all possible boundary implementations; conversely, we are only concerned with those implementations which have been employed in the test problems of Chapter 5.

In the current study, the diffusion parts of the boundary conservation equations, i.e. Q_b^{fd},Q_b^{gd}, and Q_b^{ed}, are treated assuming zero viscous diffusion through the domain boundaries. The value of all other Q_b's are approximated by linear interpolation between adjacent boundary nodes unless the conservation equations are sacrificed to specify the known boundary values or their directions. For example, Equation (4.178) could be expanded for the control volume in question in Figure 4.3,

$$Q_b^{fp} \approx \sum_{j=1}^{2} [p \Delta S_x]_{bipj} = (\frac{1}{4}P_1 + \frac{3}{4}P_2)(\Delta S_x)_{bip1} + (\frac{1}{4}P_3 + \frac{3}{4}P_2)(\Delta S_x)_{bip2} \quad (4.186)$$

Generally speaking, the mass and momentum equations are used to treat pressure and velocity boundary conditions and energy is involved in treating temperature boundary conditions. The main purpose of the present boundary treatment is to conserve mass for all control volumes of the domain including the boundary. This is why the known pressure at the inflow and outflow boundaries of subsonic flow domains is specified by using the momentum equations. Two factors are important in boundary treatment. One is the nature of the flow and whether it is viscous or inviscid. The other relates to the physics of the boundary which could be classified into solid wall, inflow, outflow, etc. Based on these factors and sub-factors, several different boundary treatments could be constructed which are explained in the following sub-sections.

Viscous Solid Wall Modeling

No-slip boundary conditions are applied to model solid walls for solving the Navier-Stokes equations. In this regard, the x-momentum and y-momentum equations are replaced by F=0 and G=0 specifications for stationary walls and F=F_{wall} and G=G_{wall} for moving walls. Continuity is automatically closed for solid boundary because there is no mass flow through the solid boundary. Similarly, energy is not transmitted from boundary surfaces because boundary velocities are zero. Thus, an adiabatic boundary condition is applied to the energy equation, i.e. $q_n = \mathbf{k}\frac{\partial T}{\partial n} = 0$.

Inviscid Solid Wall Modeling

The flow tangency condition is considered for treating inviscid Euler flow over a solid wall. This condition restricts the direction of the flow to be tangent to the wall boundary, Figure 4.3. In this case, the x-momentum and y-momentum equations are completed normally for boundary control volumes assuming zero viscous diffusion. Then, they are combined to form the tangential momentum equation,

$$\cos(\beta)\ \{x\text{-momentum}\}\ +\ \sin(\beta)\ \{y\text{-momentum}\} = 0 \tag{4.187}$$

Now, the x-momentum equation is replaced by this new derived tangential momentum equation for such boundary control volumes. The y-momentum equation is simply replaced by the normal no-flow condition for the boundary control volumes,

$$\sin(\beta)\ F\ -\ \cos(\beta)\ G = 0 \tag{4.188}$$

Since there is no mass flow across the inviscid solid wall, continuity and energy equations are treated similar to those for a viscous solid wall.

Inflow Boundary Modeling

Most flow information is specified at an inlet section. In all subsonic, transonic, and incompressible cases, the x-component of mass or velocity is specified by replacing the x-momentum equation by an equation that simply specifies the mass component or x-velocity. The y-component of mass or velocity is not always specified. For those test cases which are consistent with a uniform inlet velocity distribution, the y-momentum equation is discarded for corresponding boundary control volumes and replaced by G=0 instead. However, for those inlets with non-uniform inflow, like the sloped inlet of a convergent-divergent nozzle, the y-momentum equation is completed normally considering zero shear for those control volumes. The result of this boundary implementation is illustrated and mentioned in applications. Contrary to the momentum equations, the continuity equation is always closed for the above flow cases.

A uniform inlet velocity specification does not necessarily describe a uniform mass distribution at the inlet and vice versa in compressible flow. In many cases, it is necessary to compare our results with those of other workers who solve using a velocity boundary condition. In order to have a uniform velocity at an x-inlet for our momentum variable procedure, F is specified via the x-momentum equation. Then, density is computed by using the equation of state and having the magnitude corresponding to the calculated pressure and temperature. This calculated density is used to correct the inlet mass, $F_{inlet} = \varrho_{new} U_{inlet}$. This new derived F is used to specify mass in the next iteration. Although this method of boundary implementation generally slows down convergence, it works well.

For supersonic cases, P, F, and G are specified at the inlet by replacing the continuity, x-momentum, and y-momentum equations, respectively. Temperature is always specified by replacing the energy equation by an equation that simply specifies the temperature. This latter implementation is applied for all investigated tests.

Outflow Boundary Modeling

At an outflow boundary in the x-direction, neither the x-velocity nor x-component of the mass is specified. Pressure is specified here by replacing the x-momentum equation with an equation specifying the desired pressure for subsonic and transonic flows. The method of treating the y-momentum equation is exactly similar to the one presented in inflow boundary modeling. The continuity equation is closed by an implicit treatment of the exit mass for subsonic and transonic flows.

Since pressure is specified at an upstream boundary in supersonic flow (see inflow boundary modeling) x-momentum equation is closed assuming zero shear. There are few test problems in supersonic flow which specify either pressure or mass at outflow by extrapolating specified values from the upstream of boundary nodal points and inside of the domain. However, this form of modeling does not cause significant improvement in the results.

Different techniques are used to deal with the energy equation for outflow boundary control volumes. In most cases, the energy equation is completed subject only to zero shear. In this modeling, dependent variables are implicitly involved in closing boundary values. In supersonic flows, the energy equation is either completed as before or temperature specified with magnitude extrapolated from neighboring upstream nodes. Another technique is to use an adiabatic boundary condition, $q_n = \mathbf{k}\frac{\partial T}{\partial n} = 0$. Such an equation relates each boundary node to its neighbouring nodes using finite element connectors or a direct backward differencing.

Symmetry Boundary Modeling

Symmetry boundary conditions are very beneficial for reducing computer time and memory requirements when appropriate. The mass, momentum, and energy flows do not intersect the symmetry boundary surface because the normal velocity and normal derivative of all other flow parameters are zero on that surface. This implements a normal closing of the continuity equation. In this modeling, the x-momentum is replaced by an equation which specifies zero gradient for tangential velocity at the boundary, i.e. $\frac{\partial U_t}{\partial n} = 0$. The y-momentum is also replaced by an equation, Eq.(4.188), which specifies the direction of the symmetry boundary. The adiabatic boundary condition is implemented for treating temperature as was done for viscous solid wall modeling.

4.8 Closure

The preliminary investigation on one-dimensional formulations has been extended in this chapter for two-dimensional application. In this regard, the two-dimensional Navier-Stokes equations were discretized using a control-volume-based finite-element method and selecting the momentum component variables as the dependent variables. The discretized form of conservation equations contained many nonlinearities and formed an ill-posed system of equations due to the integration point variables involved. Both of these difficulties were resolved using our one-dimensional experience. The velocity-pressure decoupling issue which was detected in the one-dimensional investigation was addressed following our previous methodology. The resulting equations in this chapter were cast in a general matrix form which will facilitate the future work. The details of the techniques which are employed to invoke boundary conditions were explained for different boundary condition implementation. The performance of this formulation will be studied and results presented in the next chapter.

Chapter 5

Two-Dimensional Results

5.1 Introduction

In this chapter, the performance of the developed two-dimensional method is examined. This examination comprises the investigation of several different kinds of flow and test problem. The main purpose of this chapter is to cover a wide range of flows and problems. Based on the title of this research, the primary concern in this route is to test the validity of the method for two major types of flow, i.e. incompressible and compressible flow. There are other factors like speed, viscosity, and time which break each type of flow into other categories. The time variable splits problems into steady and unsteady flows and viscosity into viscous and inviscid flows. Flow speed is a major parameter in compressible flows which divides it into many other subdivisions like subsonic and supersonic flows. Flow problems can be further categorized based on the flow boundary conditions.

The one-dimensional results were completely discussed in Section 3.7. Here, we are concerned only with two-dimensional flows and mainly with internal flows. In order to fulfill the objectives of this chapter, the flow problems are classified into three categories of incompressible, pseudo-compressible, and highly compressible flows. The first is limited to absolute constant density flows, the second addresses incompressible flows which are treated as compressible ones, and the last addresses highly compressible flows. Each component has specially been designed in such a manner that their assemblage would demonstrate the power of the method for a broad range of flows. Many other types of flow are examined in this chapter including viscous and inviscid flows. The factor of time was examined in Section 3.7.2 where the one-dimensional transient flow in a shock-tube was investigated.

Many different problems are modeled in this chapter including the driven cavity problem, channel entrance flow, converging-diverging nozzle flow, and flow over both a bump and a ramp. There are three major examples which are tested almost in all three parts. They are the cavity, entrance, and nozzle flows. This helps to follow the performance of the method through a wide range of flow parameters. The general common specifications of each sub-section is generally discussed before presenting the individual results of that sub-section.

In this chapter, the results of the present work are compared with those of other workers. Their results have been extracted either from the figures of their articles by using a digitizer or directly from the tables of their articles. These results may simply be indicated by symbols instead of continuous line distributions. The number and location of the symbols do not necessarily indicate the grid distributions.

In this chapter, all test problems are solved based on a time-dependent implicit algorithm. There are no internal iterations in each time step because we are concerned only with the steady-state solution. Marching in time is continued until a convergence criterion is reached. The Root Mean Square of the change from iteration (time step) to iteration is used as a measure of convergence for the dependent variables, i.e. F, G, P, and T. For a general unknown ϕ, the RMS is given by

$$RMS = \frac{1}{\phi_{avg}} \sqrt{\frac{\sum_{j=1}^{\aleph} (\phi_j - \phi_j^o)^2}{\aleph}} \tag{5.1}$$

where

$$\phi_{avg} = \sqrt{\frac{\sum_{j=1}^{\aleph} \phi_j^2}{\aleph}} \tag{5.2}$$

$\aleph$ is the total number of grid nodes. The RMS is evaluated for all four unknown dependent variables, however, experience shows that the RMS of F is slower than the other variables for the test cases investigated . The RMS values for the dependent variables at the integration points are also checked using similar definitions, however, experience shows that the convergence of the integration point variables is faster than that for the nodal values. The required criterion for convergence was set to 10^{-5} for all cases unless otherwise stated.

All pre and post processing of this chapter have been accomplished using either MATLAB software or author based tools. All figures which illustrate the results have been depicted by MATLAB. Since the intent of this work was to demonstrate the procedure, a direct sparse matrix solver was used for the computations [70]. Thus it is not relevant to present computational times for solutions in this work.

5.2 Incompressible Flow

As the first step of our method validation, the capabilities of the incompressible algorithm of the code are investigated. In this algorithm, the equation of state is reduced to Eq.(2.16) where absolute incompressible flow is specified. In this section, two test models are examined to reveal the characteristic of the method. They are the driven cavity problem and the entrance flow problem. They are addressed by solving the Navier-Stokes equations. Since viscous flow problems may be polluted by turbulence effects it is necessary to respect laminar restrictions for laminar flow solvers. The validity of the results is compared with the results of other numerical methods and available benchmark results. A mesh refinement study is accomplished for the cavity test problem which demonstrates the ability of the method to attain accurate results for coarse grid distributions. All test cases in this section are solved within a time-marching algorithm and the results are obtained by choosing huge time steps which results in an infinite CFL number.

5.2.1 Driven Cavity Problem

The first model problem is a classical problem to test the accuracy of numerical methods for incompressible viscous flows. It is the recirculating flow of a fluid in a square cavity which is bounded on three sides and whose fourth side moves at a constant speed, causing recirculation inside the cavity. The cavity problem is a difficult test problem because of two singularities at the corners of the lid and because of its several recirculation regions with their complexities dependent on the Reynolds number. This problem has been extensively studied as a benchmark problem, Ghia et al [72]. In order to demonstrate the effect of mesh size and Reynolds number on the results of the code, the study was done on five different uniform meshes, including 21×21, 31×31, 41×41, 51×51, and 71×71 grid nodes, and for three Reynolds numbers of 1000, 5000, and 7500. The length scale and density were considered to be unity. All velocities are nondimensionalized by the velocity of the lid. Figures 5.1, 5.3, and 5.5 depict the streamline contours for the three Reynolds number of 1000, 5000, and 7500 on three different uniform grids of 31×31, 51×51, and 71×71, respectively. Plotting the streamline contours requires the evaluation of the stream function within the solution domain. In this regard, the stream function values have been obtained by integrating the integration point velocities over control-volume surfaces. All the first and second level vortices have been successfully detected in these three figures despite using relatively coarse grids. As Reynolds number increases the central vortex becomes much rounder and the secondary vortices much stronger.

The u-velocity and v-velocity profiles at the centerlines of each cavity have been calculated and illustrated in Figures 5.2, 5.4, and 5.6 for three Reynolds number of 1000, 5000, and 7500, respectively. In order to study the effect of mesh refinement on the accuracy of the results, each Reynolds number was tested on up to three different grid distributions and compared with the benchmark results of Ghia et al [72] which are based on fine grid distributions. Their working grid is 129×129 for Reynolds 1000 and 257×257 for two other Reynolds numbers. Comparing with the results of benchmark work, this study shows that the accuracy of the solution is rapidly increased with relatively coarse grids.

Following the mesh refinement study, a comparative study on the validity of the method is performed. Reynolds number of 3200 is selected for this study because of available results. Figure 5.7 compares the results of the present method with three other references two of which are based on all-speed methods. The benchmark work [72], which has already been introduced, uses a grid resolution of 129×129. The grid resolution is 71×71 in [45] and 51×51 in [33]. The present method has used a grid distribution of 51×51 which generally shows better agreement comparing with the benchmark results. The streamline contour of this cavity flow is presented in Figure 5.8.

Certain cavity flow details have been studied and compared with those of the benchmark study. Table 5.1 shows a comprehensive survey of the primary and sec-

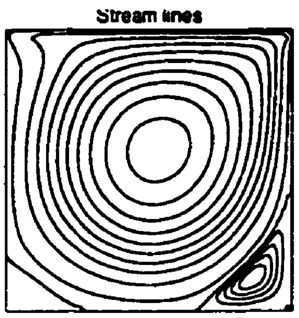

Figure 5.1: Cavity with a 31×31 grid and *Re* =1000.

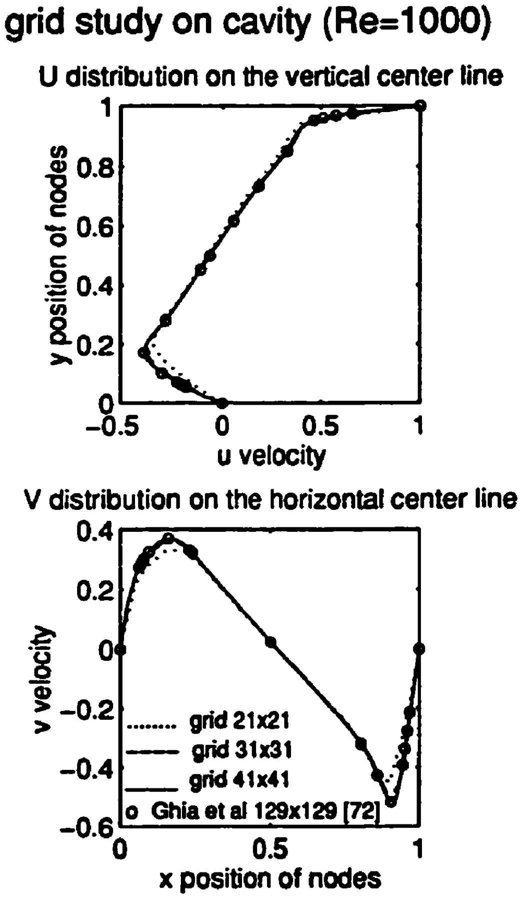

Figure 5.2: Mesh refinement study on centerline velocities.

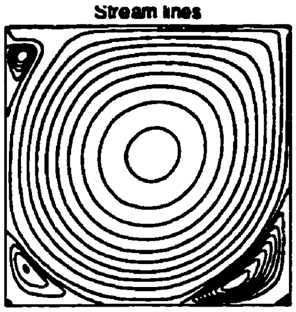

Figure 5.3: Cavity with a 51×51 grid and *Re* =5000.

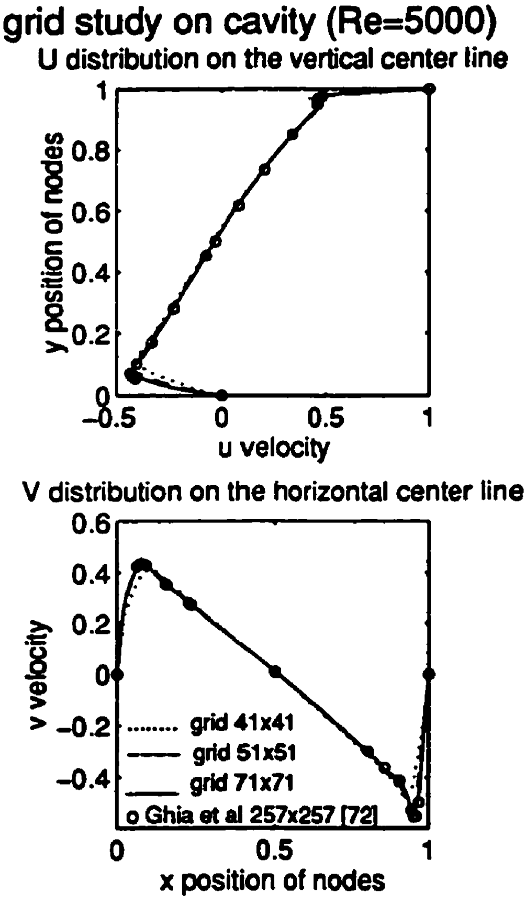

Figure 5.4: Mesh refinement study on centerline velocities.

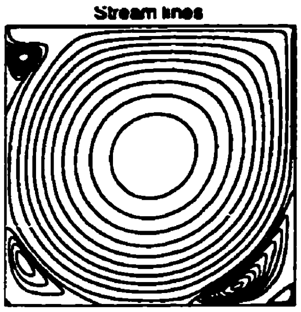

Figure 5.5: Cavity with a 71×71 grid and *Re* =7500.

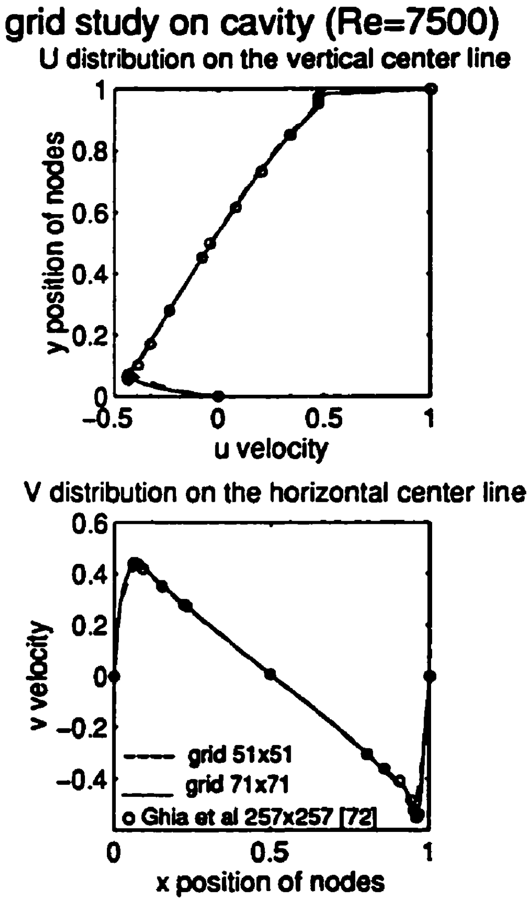

Figure 5.6: Mesh refinement study on centerline velocities.

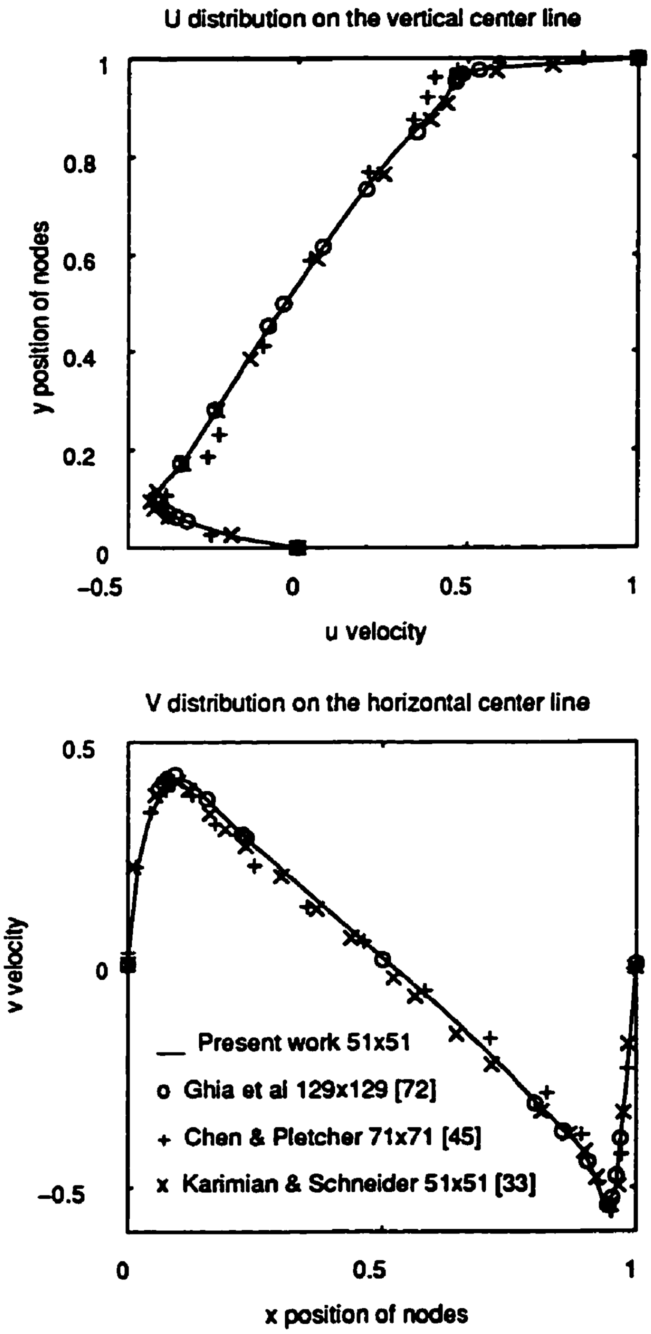

Figure 5.7: Comparative study on the centerline velocities in cavity, Re=3200.

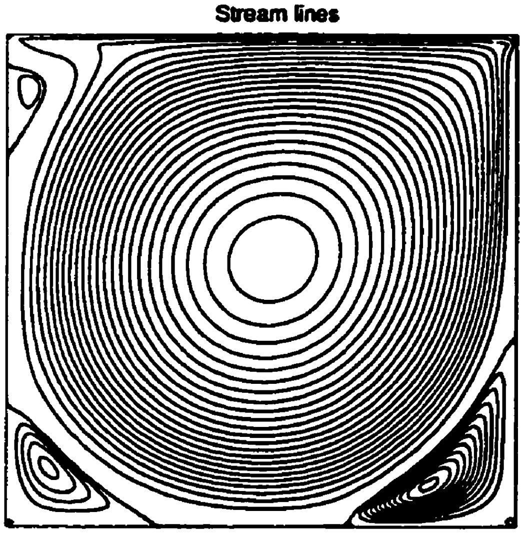

Figure 5.8: Cavity with a 51×51 grid and Re =3200.

ondary vortices of the flow inside the driven cavity for Reynolds number of 5000. This survey includes the strengths, dimensions, and locations of the main vortex and secondary vortices in the cavity. In this table, several abbreviations are used. P, T, BL, and BR represent primary, top, bottom left, and bottom right vortices. H and V represent the horizontal and vertical sizes of the vortex respectively measured along the corresponding wall surface. The summarized results in Table 5.1 demonstrate good quantitative agreement with the results of Ghia et al [72]. It must be noted that the grid size has a direct and strong effect on the order of errors and that vortices of smaller size would result in higher errors on coarser grids. The smaller vortices have not been presented in this table. Similar comparisons for other Reynolds numbers show similar results.

No-slip boundary conditions were applied on all solid walls of the cavity. The cavity problem was studied as a steady-state problem and the results of each case were obtained using several iterations in a huge time step. The number of itera-

	case	Ghia et al [72]	present method	Error %
Grid		257×257	51×51	
P	φ_{min}	-0.11897	-0.1120	5.86
	x, y	0.512, 0.535	0.514, 0.545	0.4, 1.87
T	φ_{max}	1.4564E-3	1.984E-3	36
	x, y	0.063, 0.910	0.069, 0.891	9.5, 2.1
	H, V	0.121, 0.269	0.113, 0.242	6.6, 10
BL	φ_{max}	1.3611E-3	1.23E-3	9.6
	x, y	0.070, 0.137	0.079, 0.149	12.9, 8.8
	H, V	0.318, 0.264	0.340, 0.274	6.9, 3.8
BR	φ_{max}	3.083E-3	3.17E-3	2.8
	x, y	0.809, 0.074	0.802, 0.080	0.87, 8.1
	H, V	0.357, 0.418	0.38 , 0.42	6.4, 0.5

Table 5.1: Comprehensive comparison of cavity details for Re =5000

tions was between 10 and 20 in each case to reach the required criterion which is RMS<10^{-5} for F and G.

5.2.2 Channel Entrance Flow

The second test problem is entrance flow between parallel plates. The parallel plates geometry is a limiting geometry for the family of both rectangular and concentric annular ducts. The velocity distribution at the inlet of a duct will undergo a development from some initial profile at the entrance to a fully developed profile at locations far downstream. The region of the duct in which this velocity development occurs is called the *entrance region*. There has been considerable interest in determining the fluid behaviour within the entrance region because of its general technical importance in engineering applications. The importance of this problem is also for developing laminar-flow theory and testing numerical schemes for solving elliptic conservation equations. There are no general exact solutions or experimental results for the entrance region. However, there are a variety of approximate analytical and numerical methods for the determination of the flow characteristics in this region, Darbandi and Schneider [73]. The development of a laminar flow at the entrance of two semi-infinite straight parallel plates is seen in Figure 5.9. The distance between two plates is $H = 1$. The entrance length, X_e, is defined as the

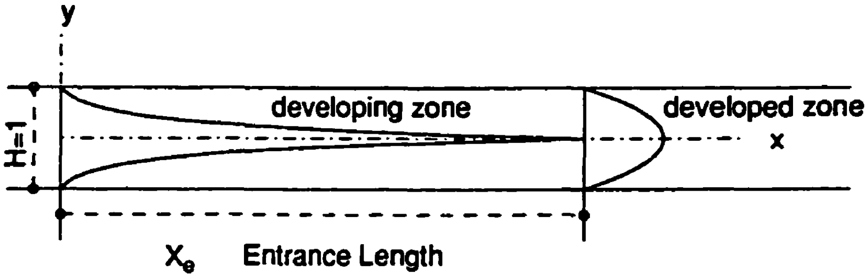

Figure 5.9: Developing and developed zones.

distance from the inlet boundary, with uniform inlet velocity profile, to the point where the centerline velocity reaches 99% of its asymptotic value. The entrance length divides the region into two zones. In the developing zone the velocity profile undergoes a transition from a flat to a parabolic profile. This developing profile may have two maxima at locations other than the centerline. The parabolic profile remains constant in the fully developed zone. All lengths are nondimensionalized by H and velocities by U_{inlet}. Because of the symmetrical nature of this problem, only the upper or lower half-channel could be calculated. However, in order to emphasize on the symmetry of the obtained solution, the calculation is done based on a full height of the channel.

The problem was investigated for Reynolds numbers 0, 1, 20, 200, 1000, and 2000. The first one is creeping flow and is approximated by specifying a very large value for viscosity. A 101×41 grid distribution was used for all Reynolds numbers. The first and second numbers show the longitudinal and the full transverse grid distributions, respectively. The distribution along the cross section was based on the hyperbolic sine and the longitudinal distribution was uniform.

Typical profiles of u-velocity for Reynolds numbers 200, 1000, and 2000 are shown in Figures 5.10 to 5.13 assuming a uniform velocity profile at the inlet. Qualitatively, the development of the velocity profiles were found to be quite similar at all Reynolds numbers although the off-centerline maxima appear to be the greatest at $Re=200$. As is seen, the velocity profiles have a peculiar behaviour close to the entrance. They show a local minimum at the center of the duct and symmetrically two maxima near the walls. These velocity overshoots are found at all Reynolds numbers while their magnitudes decrease and finally vanish with increasing Reynolds number. Shah and London [74] present a comprehensive discussion on the existence of these overshoots. They result from the condition that the velocity distribution at the inlet must be uniform. In order to maintain this condition, an adverse pressure gradient develops in a small region on the centerline near the entrance. Fluid parcels near the centerline are not accelerated immediately where as the fluid parcels next to the wall are forced to be stationary as soon as they enter the inlet region. To satisfy the continuity equation, velocity overshoots are thus formed.

There have been numerical [75], analytical [76, 77], and experimental [78] efforts to determine whether or not these overshoots are a part of the real behaviour of the

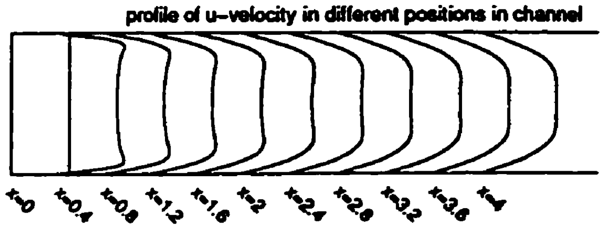

Figure 5.10: Entrance flow, Re=200, undeveloped.

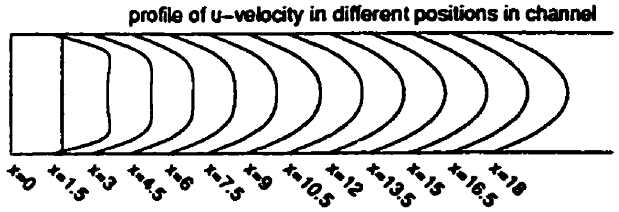

Figure 5.11: Entrance flow, Re=200, developed.

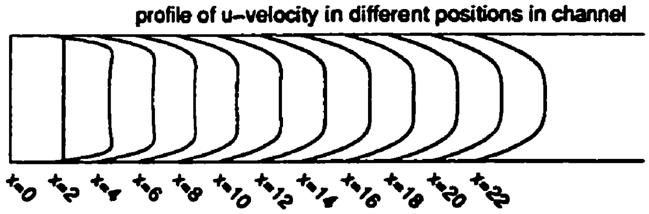

Figure 5.12: Entrance flow, Re=1000, undeveloped.

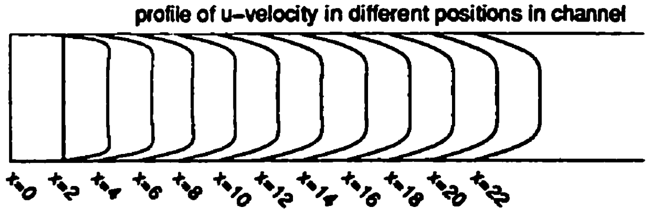

Figure 5.13: Entrance flow, Re=2000, undeveloped.

flow. Abarbanel [76] analytically solved the problem for Stokes flow and concluded that these bulges are indeed a real part of the mathematical solution. Berman and Santos [79] demonstrated with their experimental work that these velocity overshoots in the entrance region for pipe flow are not just a mathematical oddity but are real [80]. On the other hand, in the numerical category, AbdulNour and Potter [81] have solved the entrance flow of ducts by applying both uniform and actual inlet profiles and using vorticity and stream-function variables. They concluded that both improvement in the boundary conditions and the use of smoothing functions could minimize the magnitude of these overshoots. Darbandi and Schneider [73] have conducted a comprehensive study on the effect of mesh-refinement on velocity overshoot in the entrance region of a channel flow. They concluded that the velocity-overshoot distribution along the channel approaches asymptotic values with mesh refinements.

In order to study the effect of mesh size, the mesh size was changed from a non-uniform 101×41 grid to a 61×21 uniform grid distribution. The effect was low on the results of entrance length computation. Their changes were consistent with the change of mesh size at the end of developing region. The entrance length has been nondimensionalized with H and tabulated in Table 5.2 for different Reynolds numbers. The results of the present work are compared with those of Narang and Krishnamoorthy [82] who solved the boundary-layer equations and Morihara and Cheng [75] who solved the quasi-linear Navier-Stokes equations for incompressible flow. Although these results are based on the finer grid but they are not far from the results of the coarse grid which infers excellent result despite the use of a coarse grid.

Re	Present 101*(2*21)	Narang [82]	Morihara [75] 41*21
0	1.3	N.A.	1.282
1	1.3	1.282	1.302
20	2.2	2.220	2.237
200	18.0	16.70	18.060
1000	87.5	91.080	N.A.
2000	170.0	168.80	171.600

Table 5.2: Entrance or developing flow length

There is an empirical relationship for the hydrodynamic entrance length,

$$L_{hy}^{+} = \frac{X_e}{H\ Re} = 0.04 \tag{5.3}$$

This expression is not valid for Reynolds numbers under 100 because L_{hy}^{+} is a strong function of Re for low Re flows. This length has been calculated for our test problem and has been tabulated and compared with others' results in Table 5.3. The number of iterations for attaining the convergence criterion, i.e. RMS$<10^{-5}$ for F and G, did not exceed six iterations, for the highest Reynolds number, in all test cases.

Boundary Conditions

The Navier-Stokes equations for parallel plates may be solved for different inlet conditions. The selection mainly depends on the dependent variables. Those who solve for φ-ζ use irrotational entry conditions, IEC, at the inlet and those who solve using u-v use uniform entry condition, UEC. There is a third option which

Re	Present	Morihara [75]	AbdulNour [81]	empirical result
20	0.0558	0.0559	0.045	0.04
200	0.0456	0.0452	0.0442	0.04
1000	0.0441	N.A.	0.0442	0.04
2000	0.0436	0.0429	0.0443	0.04

Table 5.3: The hydrodynamic entrance length

considers the uniform-velocity far upstream of inlet section, e.g. [83], which is not considered here. Van Dyke [84] pointed out that the vorticity at the inlet is not zero for low or moderate Reynolds numbers because of its upstream diffusion as soon as the flow meets the entrance wall. Hence, the uniform entry velocity distribution is better than a zero vorticity distribution. Morihara [75] calculates and plots equi-vorticity lines in the duct and shows that the φ-ζ formulation is justified only for large Reynolds numbers.

There are works which apply both boundary conditions. Mcdonald [85] solved the complete set of Navier-Stokes equations for both the uniform and irrotational entries. He noted that the centerline velocities are higher for the irrotational entry than for uniform entry. This difference is higher for parallel plates compared to the circular tube. Ramos and Winowich [86] investigated magnetohydrodynamic channel flows. They showed that the primitive-variable formulation predicts either steeper axial velocity gradients at the channel walls or lower axial velocities at the channel centerline than the stream function-vorticity in finite-difference or finite-element methods. On the other hands, AbdulNour and Potter [81] show that the magnitude of overshoots could be minimized with improvement of boundary conditions in a φ-ζ formulation. All these comparisons between u-v and φ-ζ formulations show that there would be two different solutions considering either UEC or IEC. These solutions are not identical.

In this study the initial solution is always started with F=G=0 and P=P_0 at all mesh nodes throughout the domain. Then uniform entry condition, i.e. F=1 and G=0, is applied at the inlet. Almost all of the methods in the literature assume fully developed flow at infinity. Here, the uniform pressure and zero transverse velocity are specified far downstream of the entrance length, X_e, for boundary condition implementation. Since the problem is solved for the half height of the domain, symmetric boundary conditions are applied at the centerline. In this regard, mass flux and its related momentum are considered zero through the centerline. No-slip conditions are specified on the wall of the duct.

5.3 Pseudo-Compressible Flows

In this section, we are mainly concerned with the performance of the analogy to employ a compressible algorithm to solve for incompressible flows. Therefore, we are directly interested in evaluating the ability of the code to handle low-Mach-number flows known as pseudo-compressible flows. These flows definitely have the characteristics of real incompressible flow. In order to demonstrate the performance of the analogy, many pseudo-compressible flows are first solved using the compressible algorithm of the code, using Eq.(2.11) as the equation of state, and the results are compared with the results of the incompressible algorithm of the code, using Eq.(2.16).

In the following sections, there will appear a minimum low Mach number in each test case but this does not mean they are the lowest possible Mach numbers which could be solved by the compressible algorithm. It is the Mach number which definitely reveals the characteristic of real incompressible flow. Comparing the results of these sections shows that there is no difference between these results and those of incompressible flow although density was permitted to obey the ideal gas law. This high flexibility of the method in solving real incompressible flow as a compressible flow is not seen in compressible methods which are extended to solve incompressible flows. Volpe [30] has examined the performance of three two-dimensional compressible flow codes at low Mach numbers which did not exhibit this flexibility.

In this section, the performance of the analogy is investigated in three different test cases of cavity problem, entrance flow problem, and converging-diverging nozzle flow problem. The two first are solved by treating the Navier-Stokes equations and the last using the Euler equations. In order to complete the investigation, all compressible and pseudo-compressible results are compared with either analytical solutions or benchmark results.

5.3.1 Cavity Flow Problem

The first model problem is the two-dimensional cavity driven by the movement of the lid. The complexity in flow conditions is associated with well defined boundary conditions. This test problem was introduced in Section 5.2.1. The ability of the current work in detecting the separate recirculating regions of the incompressible cavity was previously demonstrated by solving high Reynolds number cavity flows, Section 5.2.1. Here, we are not directly concerned with the details of the solution but the ability of the analogy to employ compressible algorithms to solve for incompressible flows. Following this purpose, two cavity problems with grids of 19×19 and 31×31 are selected to study two Reynolds numbers of 100 and 1000, respectively. The cavity has a unit length scale and velocities are nondimensionalized by the lid velocity.

These problems are solved once by the incompressible algorithm and several times by the compressible algorithm. In the compressible case five different Mach numbers are investigated. These Mach numbers are divided into two categories of pseudo-compressible, $M<0.3$, and compressible, $M>0.3$, Mach numbers. Again, it must be noted that the lowest Mach number of $M=0.00001$ does not mean that it is the lowest possible Mach number for using the compressible algorithm. Figure 5.14 illustrates the u-velocity profiles at the vertical centerline of the cavity and Figure 5.15 similarly does for the v-velocity profiles at the horizontal centerline. These figures demonstrate the results of both absolute incompressible flow and compressible flows from very low Mach numbers up to sonic speed. These velocities have been nondimensionalized and compared with the incompressible results of Ghia et al [72]. As these two figures show all results are absolutely identical for both compressible and incompressible algorithms. There remains a question whether they are obtained under different solution conditions. Surprisingly, the answer is negative, i.e., all side conditions are definitely identical. Figure 5.16 compares the convergence history of F for different cases. As seen they are all identical. This is a feature not seen in the conventional compressible flow solvers and even in their modified versions which solve for incompressible flows.

One important issue which needs to be explained here, is the velocity profiles in highly compressible flows. The comparison shows that the velocity distributions are identical along cavity centerlines for both highly compressible and real incompressible flows. The reason behind this similarity returns to the velocity distribution inside the incompressible cavity. As Figures 5.14 and 5.15 show, most of the region inside the cavity is under incompressible conditions, i.e. Mach <0.3. This

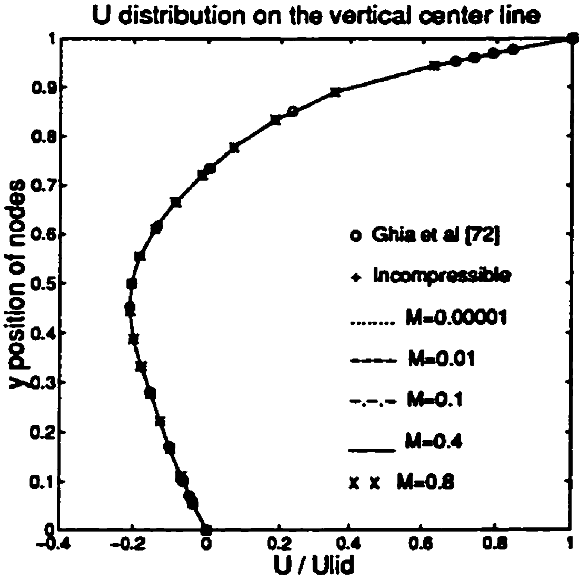

Figure 5.14: The velocity distributions for vertical center grid of the cavity problem, *Re*=100.

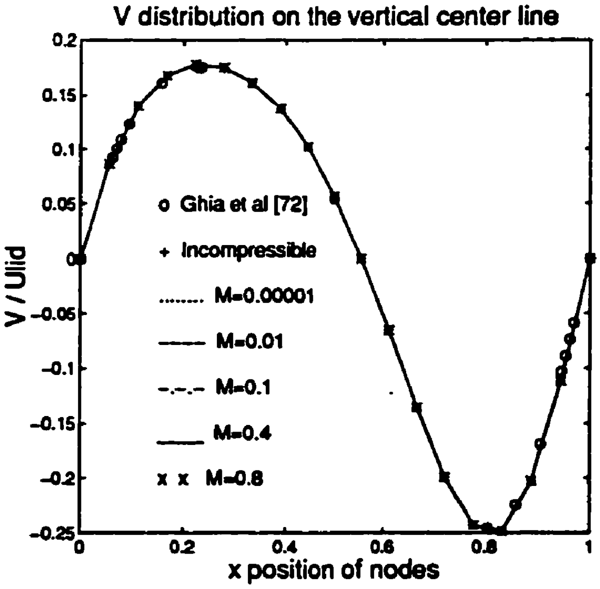

Figure 5.15: The velocity distributions for horizontal center grid of the cavity problem, *Re*=100.

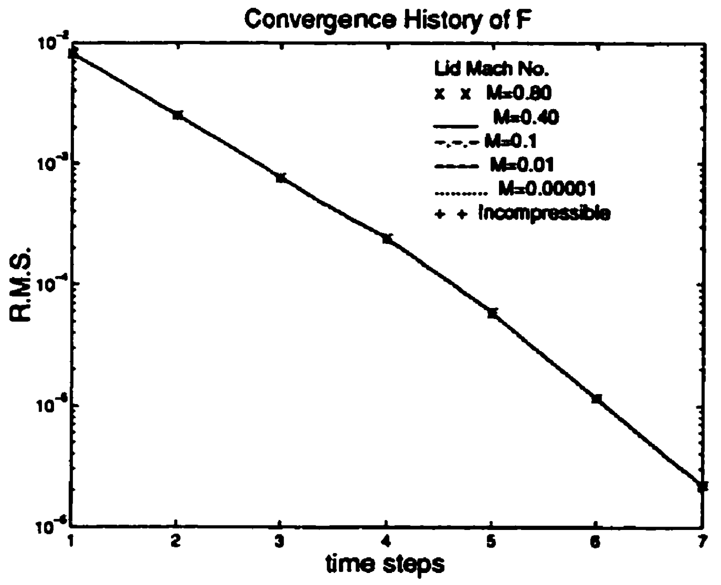

Figure 5.16: Comparison of the convergence histories in cavity with Re=100.

causes a sharp drop of compressibility effects beside the cavity lid. On the other hand, the cavity region is almost a constant pressure field except at the regions close to the leading and trailing edges of the moving lid. This has a direct effect in generating a constant density field. This independence of the solution from Mach number has also been reported by Pletcher and Cheng [38]. This is why we have included the results of high subsonic flows with those of pseudo-compressible flows. In another words, the behaviour of high Mach number subsonic flow is similar to that of very low Mach number flows and they could really be categorized in the pseudo-compressible branch.

The convergence study of the analogy is compared with that of Pletcher and Cheng [38] over a range of Mach numbers in Table 5.4. The comparison is performed for both preconditioning and no-conditioning procedures. In this table NOI stands for the Number-of-Iterations and NA means the case is Not-Available. For the

	No-Conditioning [38]		Preconditioning [38]	This Work
			$\Delta\theta=10^3$	$\Delta\theta=10^3$
Mach	$\Delta\theta$	NOI	NOI	NOI
10^{-5}	NA	NA	52	7
10^{-3}	NA	NA	52	7
10^{-2}	0.00025	2123	NA	7
0.1	0.03	264	52	7
0.2	0.1	138	52	7
0.4	0.2	68	52	7
0.8	0.3	51	52	7
1.0	NA	NA	53	7

Table 5.4: Comparison of the results of different compressible schemes for cavity flow, $Re = 100$, grid 19×19

no-conditioning scheme, it is not possible to use the same time step over a wide range of Mach numbers. They also could not reduce the number of iterations for the no-conditioning scheme to the level achieved with preconditioning for Mach numbers lower than 0.8. For the current study, the convergence was determined for the steady calculations when the Root-Mean-Square of all dependent variables reached 10^{-5}. The stability of the results of the current analogy in achieving the convergence characteristics are excellent in comparison with those of the reference. The low number of time steps is another issue which demonstrates the ability of this work. This is not seen in conventional compressible methods which are applied to very low speed flows. Volpe [30] examines three different Euler and Navier-Stokes solvers at different low Mach numbers and deduces that the number of iteration cycles to reach the convergence criterion is excessively high.

Many similar calculations were accomplished for other Reynolds numbers and grid resolutions and the similar results were achieved. As an example, Figures 5.17 to 5.19 demonstrate a similar investigation and comparison for a higher Reynolds number, Re=1000, in the same cavity. The mesh size is 31×31 in this model. In order to illustrate the trend of convergence for lower RMS criterion, this criterion has been diminished to 10^{-9}. The secondary recirculating regions become stronger at this Reynolds number. Despite this higher complexity of the flow, a similar conclusion which was derived for Re=100 is once more determined here for Re=1000. It is noted that all identical results show identical rates of convergence. Section 5.4.1 presents more results for compressible cavity with higher Reynolds numbers.

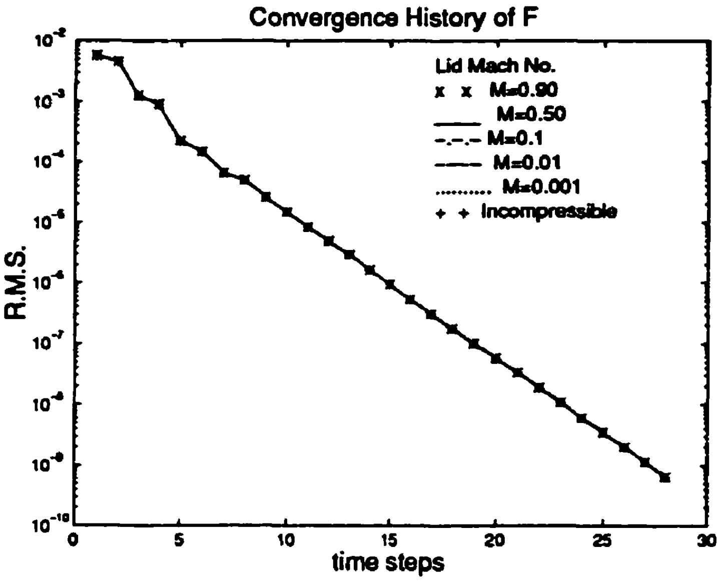

Figure 5.17: Comparison of the convergence histories in cavity with Re=1000.

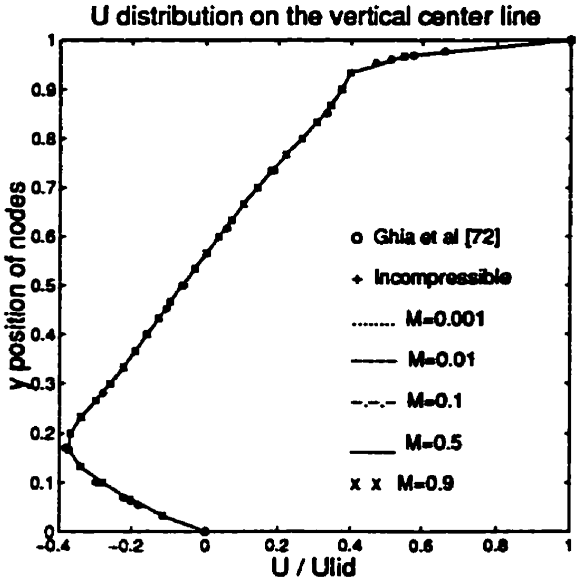

Figure 5.18: The velocity distributions for vertical center grid of the cavity problem, *Re*=1000.

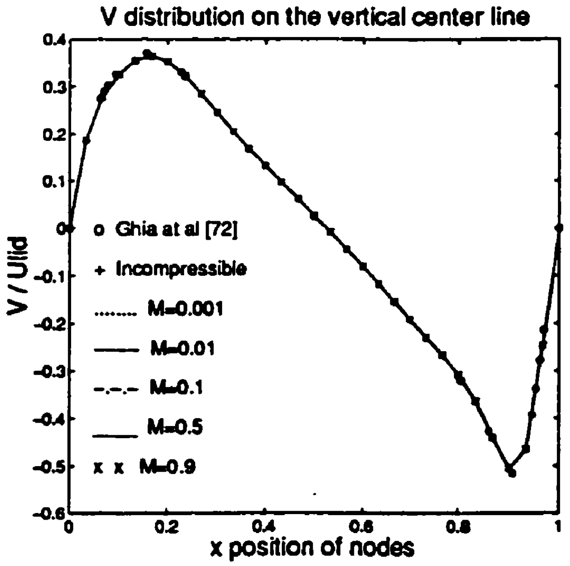

Figure 5.19: The velocity distributions for horizontal center grid of the cavity problem, *Re*=1000.

5.3.2 Channel Entrance Flow

The schematic development of a laminar flow at the entrance of two semi-infinite straight parallel plates was shown in Figures 5.10 to 5.13. This model problem has been investigated by the incompressible algorithm of the momentum-component procedure in Ref. [55] and Section 5.2.2. It has been shown that the velocity profile within the developing zone may have two maxima at locations other than the centerline. Here we are not directly interested in the overshoots or their magnitudes but in the performance of the analogy in solving both compressible and incompressible entrance flows.

Figure 5.20 illustrates the centerline velocities for incompressible flow and four compressible flows with inlet Mach numbers of 0.001, 0.01, 0.05, and 0.1 and a grid distribution of 41×21. As is seen, compressibility effects are not important for $M \leq 0.01$ and the results are identical with those for incompressible results. However, compressibility effects become noticeable as the inlet Mach number approaches 0.1. The derived results are compared with those of Morihara and Cheng [75] who solve the quasi-linear Navier-Stokes equations for incompressible flow. In addition, they are compared with the compressible results of Chen and Pletcher [45] at M=0.05. Generally speaking, the agreement between the results is excellent. Figure 5.21 compares the convergence histories of the investigated cases. The low number of time steps to achieve the criterion of 10^{-5} for all dependent variables is excellent. The deviation for M=0.1 is expected due to compressibility effects and the process of specifying the velocity at the inlet. The latter means that at the end of each time step the masses at inlet nodes are corrected by multiplying the specified values of velocity and the new calculated densities. These new masses are employed as specified masses at the inlet for the next time step. When compressibility effects

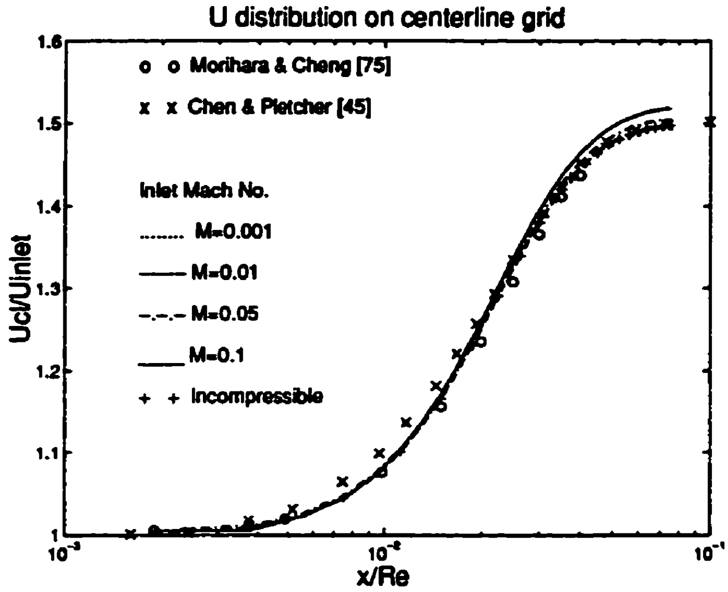

Figure 5.20: Centerline velocity distributions for incompressible and compressible flows in entrance region, *Re*=20.

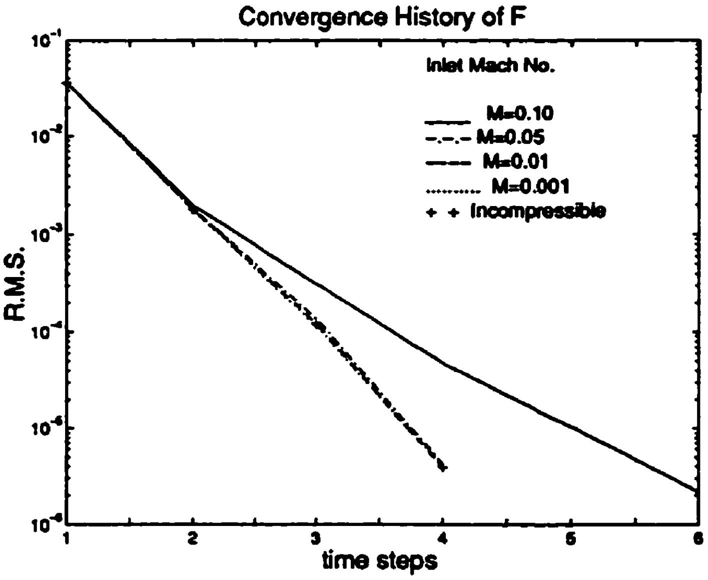

Figure 5.21: Comparing the convergence histories for entrance flow, *Re*=20.

become noticeable, this correction slows the convergence rate.

A similar presentation is given for Re=2000 in Figures 5.22 and 5.23. Here, the grid distribution is 101×11 which is considerably lower than that of references. The results of Morihara [75] and AbdulNour [87] have been included for comparison. AbdulNour solves the stream function-vorticity form of the Navier-Stokes equations with implementing a second-order boundary conditions. Although this distribution is not consistent with the results of the previous investigators it has been illustrated here to show the very recent attempts in this regard. The distribution shows abrupt jump at the inlet of the channel which is due to abrupt progress of the centerline velocity as soon as it enters the channel. The results of Carvalho et al [88] have also been shown here. Their method of solution, an integral transform method, is applicable to high Reynolds numbers, $Re \rightarrow \infty$. Moreover, the solutions in the entrance region approach asymptotic values when $Re \rightarrow \infty$. As is seen, the results of the present solution at high Reynolds numbers show excellent agreement with the results of the limiting values.

Finally, we examine the performance of the analogy with respect to convergence. In this regard, the entrance cases of Chen and Pletcher [45] who solve for all speed flows are selected and their reported results are compared with the results of our analogy. The test cases include four cases with inlet Mach numbers of 0.05. Grid distributions of 21×11, 21×11, 31×11, 41×11 are used with nondimensional channel lengths of 2, 4, 30, and 3000 to solve for Reynolds number of 0.5, 10, 75, and 7500, respectively. Here, the Reynolds number is based on the inlet velocity and half width of channel. The mesh distribution is a non-uniform one which is not similar to those used by the references. Table 5.5 presents the results of this comparison. The number of time steps to achieve the convergence criterion of 10^{-4} for all dependent variables is significantly lower for the analogy-based procedure.

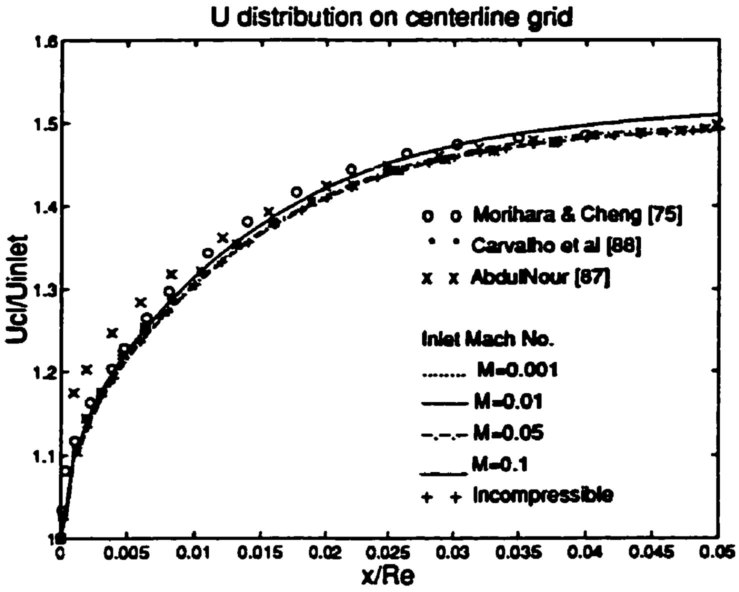

Figure 5.22: Centerline velocity distribution for incompressible and compressible flows in entrance region, *Re*=2000.

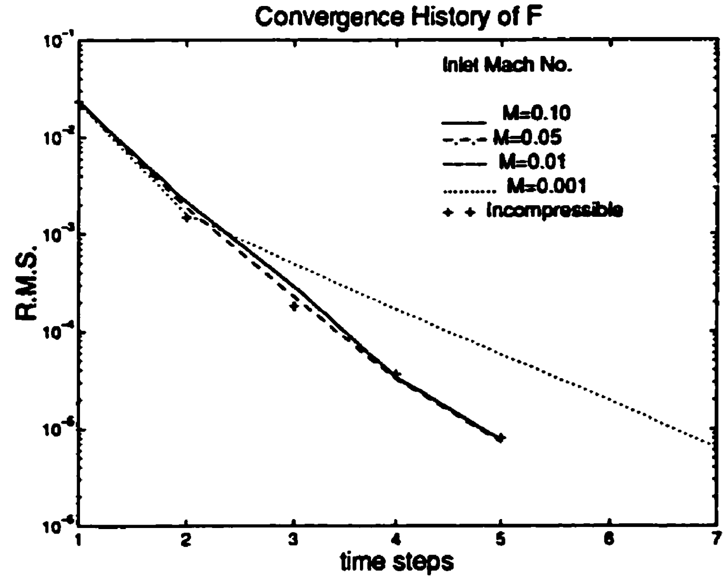

Figure 5.23: Comparing the convergence histories for entrance flow, *Re*=2000.

However for Re=0.5, the number of time steps is not as low as the others. In this regard, attention must be drawn toward the selected grid. This grid does not appropriately reveal the flow pattern in such a short length. Rapid convergence is recovered at higher Reynolds numbers.

Reynolds Grid	0.5 21×11	10 21×11	75 31×11	7500 41×11
Chen and Pletcher [45]	25	42	87	200
This work	6	3	3	3

Table 5.5: The number of time steps to achieve the criterion in compressible entrance flow, M=0.05

5.3.3 Converging-Diverging Nozzle Flow

The third test problem is hyperbolic planar converging-diverging nozzle flow. The geometry of this nozzle is seen in Figure 5.24. This symmetric planar nozzle has an aspect ratio of $AR = \frac{A_{in/out}}{A_{throat}}$ =2.0. Computations were performed for this model using the Euler equations. In this test, γ=1.4 and $T = 75^oC$ were considered for the fluid. The results have been obtained for the upper half-nozzle using a 51*11 uniform grid distribution. The grid lines are depicted by dotted lines in Figure 5.24. Slip boundary conditions were applied at the walls. Back pressure and mass flow were specified downstream and upstream of the nozzle respectively. Temperature was also specified at the inlet and the energy equation was closed for boundary control volumes at the outlet with zero diffusive flux. Adiabatic boundary conditions were applied to the walls. There was no condition on the y-component

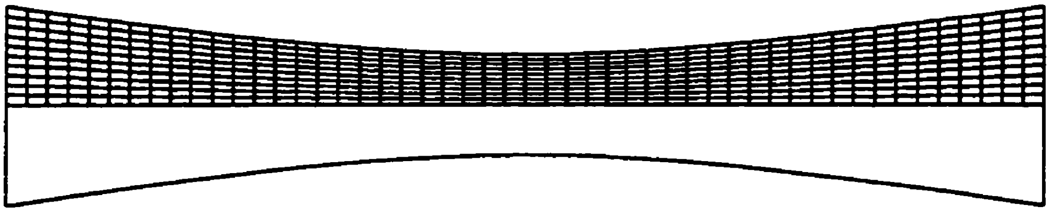

Figure 5.24: Hyperbolic converging-diverging nozzle configuration, AR=2.0.

of mass flux at either inlet or exit. In this study the mass flux and density variables are normally nondimensionalized with the values of the parameters at the inlet of the nozzle when they are plotted in figures. Pressure is nondimensionalized with the back pressure, P_{back}. For the initial condition, the flow is considered to be at rest and having ambient pressure at all grid locations.

This test problem is solved for incompressible flow and for a number of low Mach number compressible flows. The details of the procedure is quite similar to those for the cavity problem. The low Mach numbers are M=0.001, 0.01, 0.05, and 0.1 which approximate incompressible flow. Figure 5.25 shows the density distribution along the centerline of the nozzle for these test cases. As seen at lower Mach numbers, the density becomes uniform. Figure 5.26 compares the distribution of other flow parameters along the nozzle centerline for the tested low Mach number flows. These sub-figures illustrate the consistency of the other field parameters with the density field. Finally, the convergence histories for different low inlet Mach numbers have been depicted in Figure 5.27. It shows that the trend of convergence is similar to the trend in the cavity problem with slight differences. Since the pressure field changes are much sensitive at higher Mach numbers, the effect indirectly shows up in the convergence history. Although at the very low Mach number of M=0.001 the result is definitely identical with the incompressible

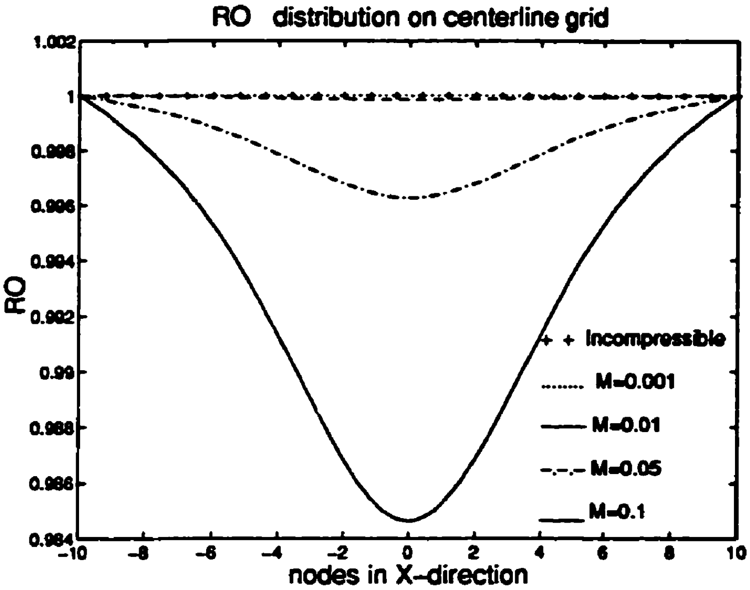

Figure 5.25: Density distributions for four different low inlet Mach numbers.

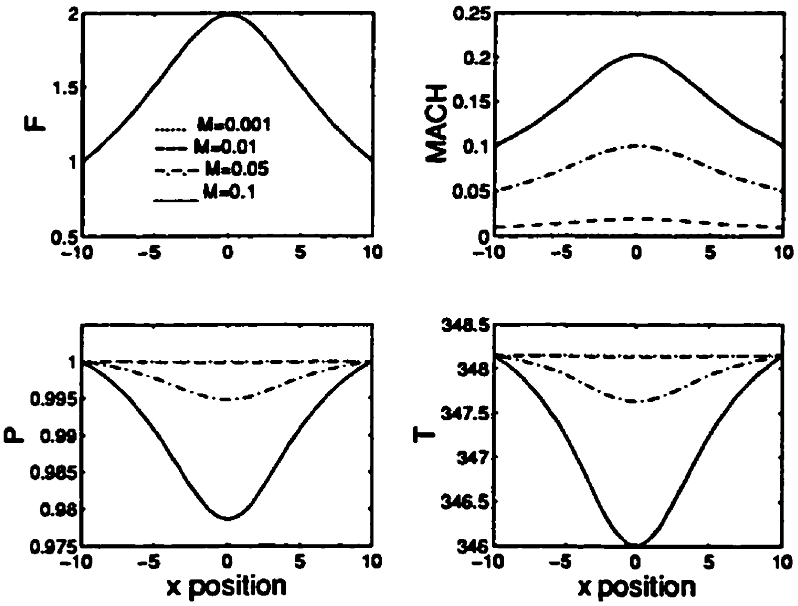

Figure 5.26: Mach distributions for four different low inlet Mach numbers.

one, a departure is seen for higher Mach number flow where the compressibility is slightly effective. This is more serious for M=0.1. Sesterhenn et al [44] has examined similar cases of low Mach number flows in a quasi one-dimensional Laval nozzle using 100 equally spaced control volumes. A total of 22 time steps was needed to achieve the specified criterion by changing the CFL number from 100 to 2000. Their method was restricted to only a one-dimensional study.

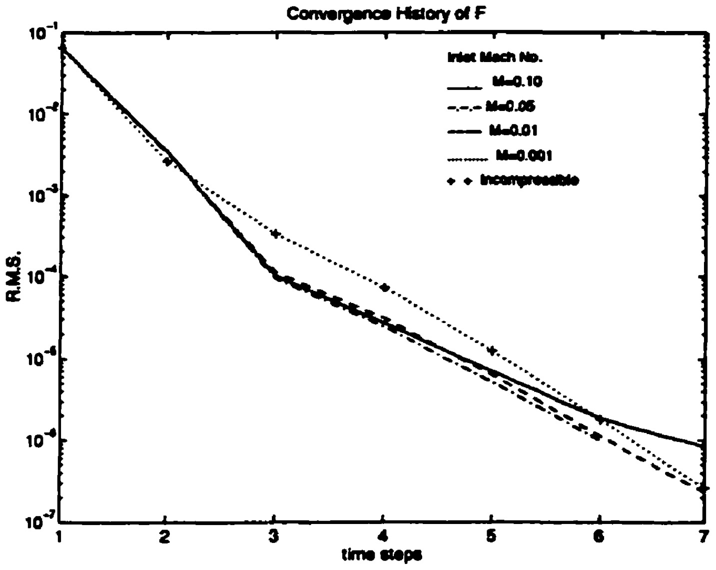

Figure 5.27: Comparison of convergence histories for low inlet Mach number flows in nozzle.

5.4 Compressible Flows

Contrary to the previous sections, highly compressible flows with considerable changes in density are investigated in this section. Highly compressible flows are mainly divided into subsonic, transonic, supersonic, and hypersonic flows. There are no shock waves in subsonic regimes while shock discontinuities become a major problem in treating the other regimes of flow. We start our testing with subsonic flow regimes. Later, this examination is extended to include the other flow regimes. In consequence of our studying compressible cavity and nozzle flows, these are two which are selected from the previous sections to be examined once more for high speed compressible flows. Different CFL numbers have been used to solve the problems in this section. They are provided for each case.

5.4.1 Compressible Cavity Problem

To demonstrate the performance of the present method in solving compressible flows, the cavity problem is recalled. This model problem was introduced in Section 5.2.1 and it has already been solved for both absolute incompressible flow, Section 5.2.1, and pseudo-compressible flow, Section 5.3.1. The cavity problem is once more tested here to emphasize the performance of the compressible algorithm of the code in solving high Reynolds number flows with high subsonic speeds. Section 5.3.1 and Ref. [55] provide more details.

In order to increase the compressibility effects within the cavity, the velocity of the lid is gradually increased. The effect is to raise the Mach number. Many cases were examined at different Mach numbers up to sonic speeds. Here we select M=0.8 to represent the related results. This test problem was also studied for several Reynolds numbers including high Reynolds number of 3200, 5000, and 7500 with a grid distribution of 51×51, 51×51, and 71×71, respectively. Figures 5.28 to 5.30 illustrate the centerline velocity distributions for these selected problems. The centerline velocities have been nondimensionalized by the velocity of the moving lid in all cases. The results have been compared with the incompressible

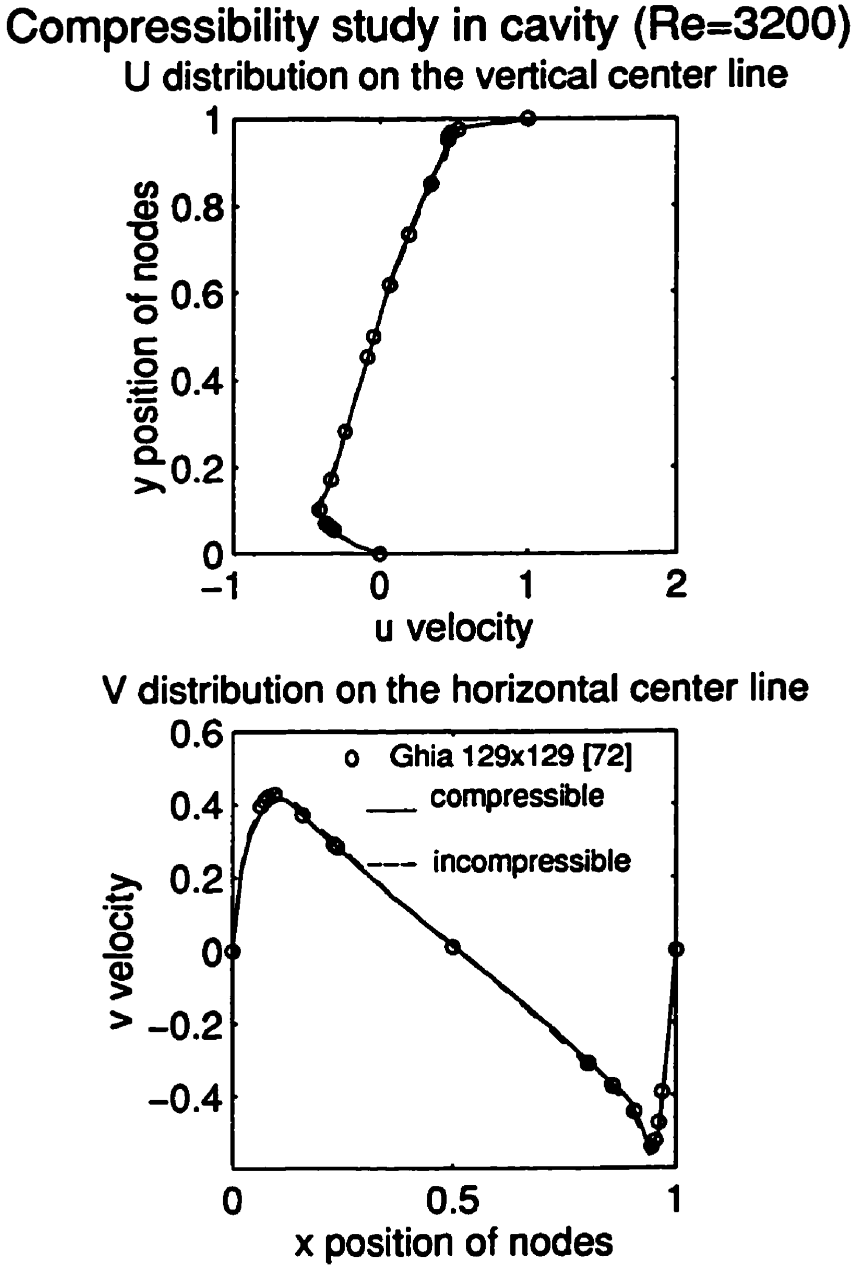

Figure 5.28: Compressible cavity, Re=3200, grid 51×51, $M \approx 0.8$.

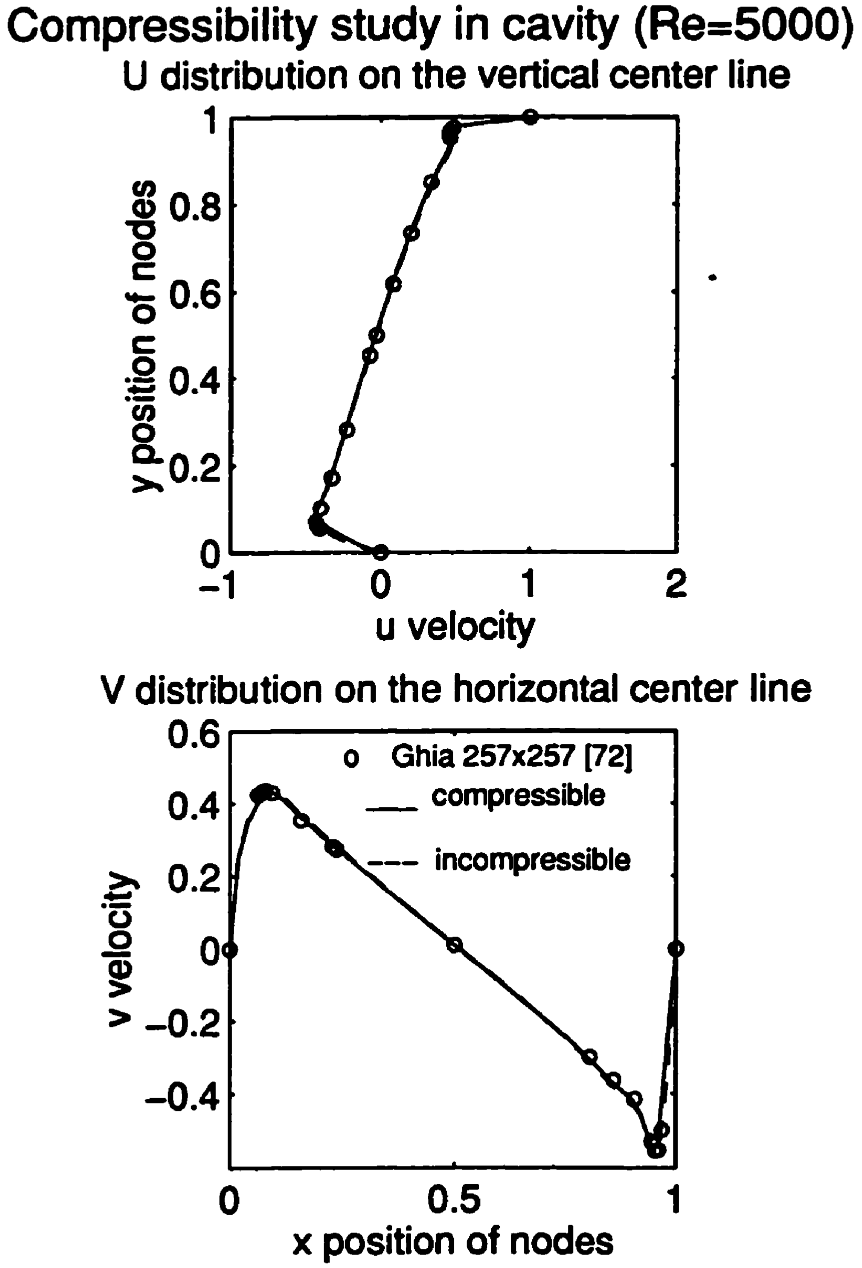

Figure 5.29: Compressible cavity, Re=5000, grid 51×51, $M \approx 0.8$.

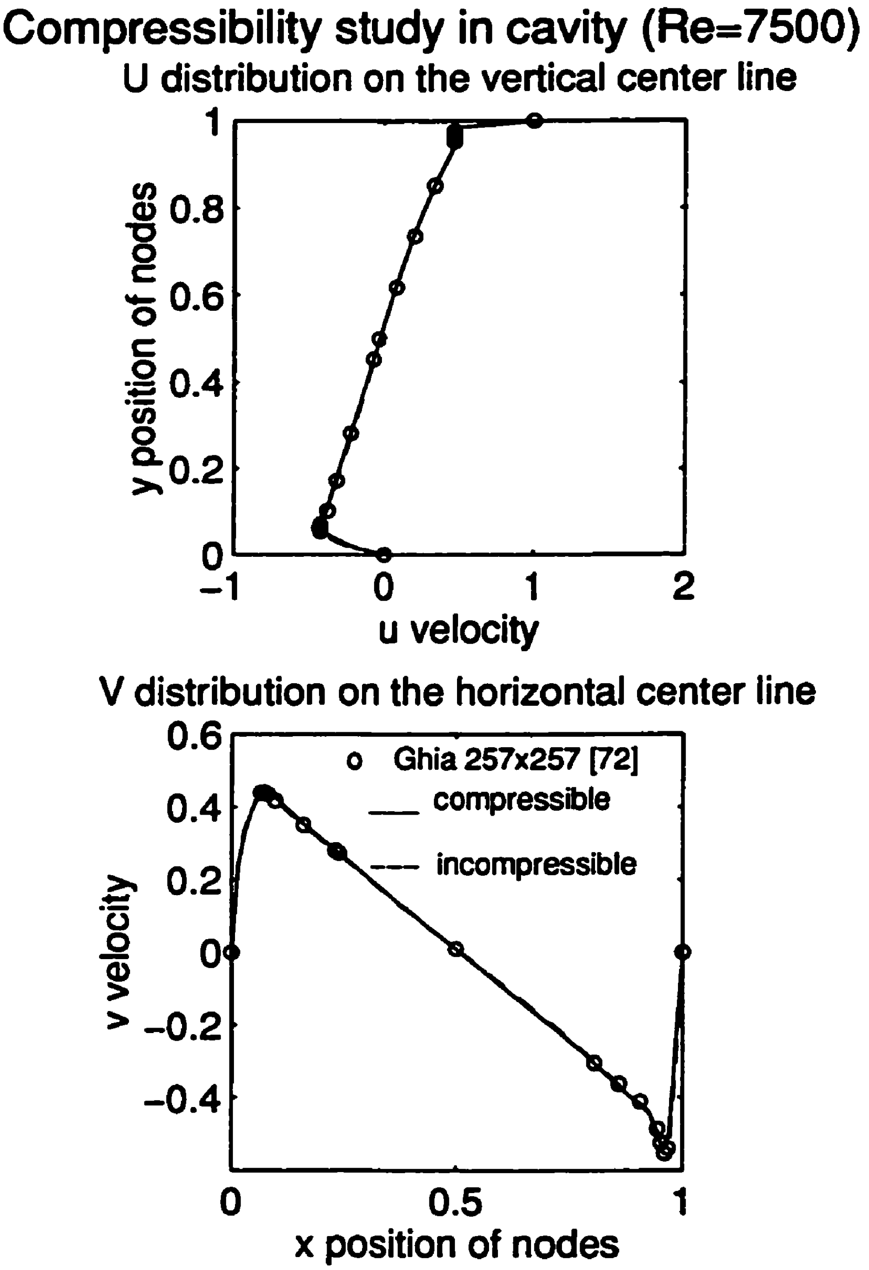

Figure 5.30: Compressible cavity, Re=7500, grid 71×71, $M\approx 0.8$.

results of Ghia et al [72]. At the same time, they have been compared with the incompressible results of the present method. There was a discussion about this agreement in Section 5.3.1 which is not repeated here.

These excellent results represent the performance of the method in solving Navier-Stokes equations for compressible flow with implementing a closed boundary condition. In the following sections, this performance is tested for solving Euler flow equations with other form of flow boundary conditions.

5.4.2 Converging-Diverging Nozzle Problem

In this part, converging-diverging nozzle configuration is tested for several different types of moderate and high compressible flows. They include subsonic, supersonic, and their combinations. Since most of the results of the current method in this section is compared with the analytical solution of the one-dimensional flow, the nozzle configuration has been selected in such a shape that its results are closer to the one-dimensional flow.

Subsonic Flow

The first step in subsonic flow investigation is to study the effect of nozzle configuration in the accuracy of the solution respect to the one-dimensional exact solution. This study is directed through an isothermal flow condition. The nozzle configuration in Figure 5.24 with all side conditions presented in Section 5.3.3 is recalled. Here, the flow is isothermal which eliminates the effect of temperature field changes. Figure 5.31 illustrates the distribution of Mach and pressure on the centerline of the nozzle. The highest subcritical Mach number in isothermal flow is less than that in isentropic flow. In an isothermal region, the flow becomes critical if $M > (\gamma)^{-1/2}$.

For air, this limit is $M > 0.85$. This has been emphasized in Figure 5.31 by drawing a horizontal solid line in the Mach plot. There is a good agreement between the results of the current method and that of the one-dimensional solution.

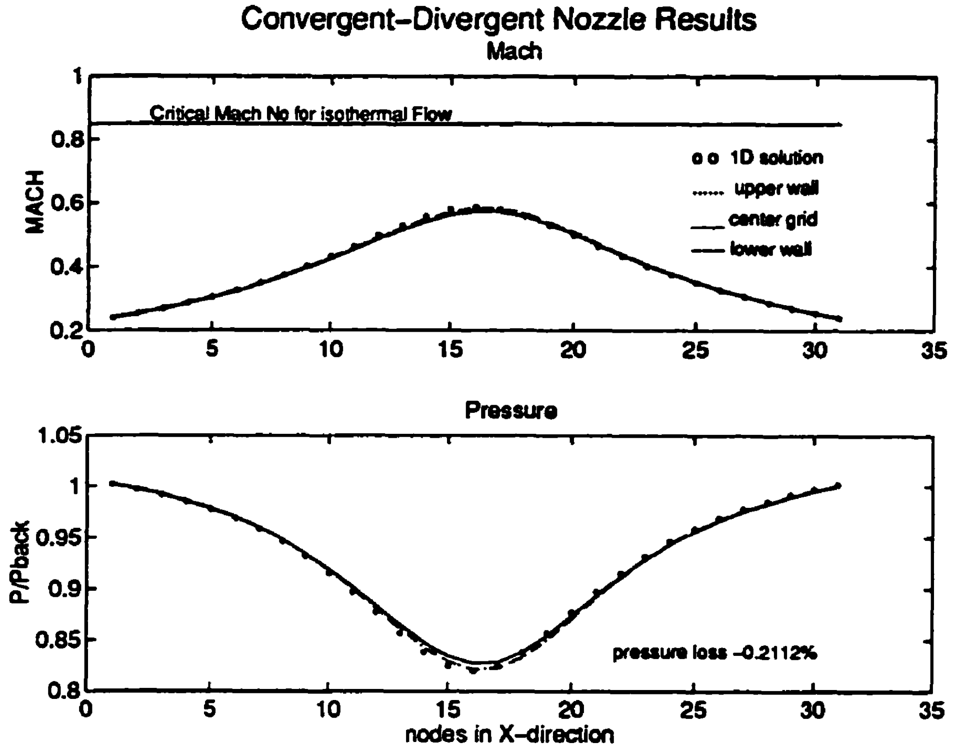

Figure 5.31: Mach and pressure distributions for an isothermal nozzle, $M_{in} \approx 0.25$.

Next, we change the nozzle configuration in order to study the effect of two-dimensionality of the configuration and flow. In this regard, the nozzle configuration is changed to a more realistic shape which is far from one-dimensional assumption. The geometry of this nozzle is seen in Figure 5.32. This symmetric planar nozzle has an aspect ratio of $AR = \frac{A_{in/out}}{A_{throat}} = 2.035$. We present the results of solving the Euler equations for this test problem and compare them with the available one-dimensional exact solution [89].

The test case was examined using a 31×11 uniform grid distribution. The grid lines are depicted by dotted lines in Figure 5.32. This figure also illustrates the Mach contours within the flow field. Since the flow field is totally subsonic, these contours are convex in the convergent part and concave in the divergent part. These schematic patterns are in good agreement with those of other predictions, Oswatitsch and Rothstein [90].

The isothermal Mach number and pressure distributions on the walls and the centerline are shown in Figure 5.33. These results are compared with the exact solution of the one-dimensional isothermal flow through a nozzle [89]. There is a good agreement between the two solutions. However, the effect of the two-dimensionality of the flow is much more critical in this test case than the one presented in Figure 5.31. The geometry of the nozzle shows how the one-dimensional solution could be far from the real solution. A comparison between the convergent and divergent parts shows that the deviation of the numerical solution from the one-dimensional solution is different in these two regions. The convergent part is much farther from the one-dimensional solution than the divergent part. This would cause more deviation from the one-dimensional solution in the convergent part which is consistent with the obtained results. This model was tested for longer lengths while retaining the aspect ratio constant. The results showed that the distribution along both walls and along the centerline approached the one-dimensional solution.

After this preliminary study on isothermal flow and the importance of the nozzle geometry, we recall the nozzle in Figure 5.24 to test the compressible algorithm for subsonic non-isothermal flows. In this regard, the inlet velocity is appropriately fixed upstream to capture three high subsonic Mach numbers of 0.5, 0.8, and 0.95 at the throat. The density, Mach, and temperature fields are depicted in Figures 5.34 to 5.36. These figures present the distribution at the walls and along the

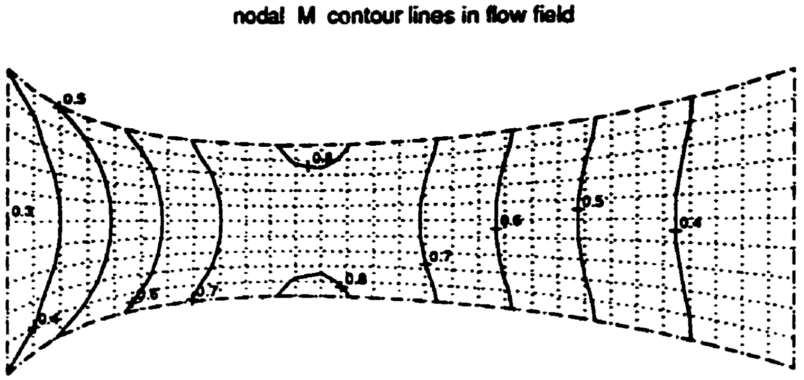

Figure 5.32: Mach contour lines in a converging-diverging nozzle with AR=2.035.

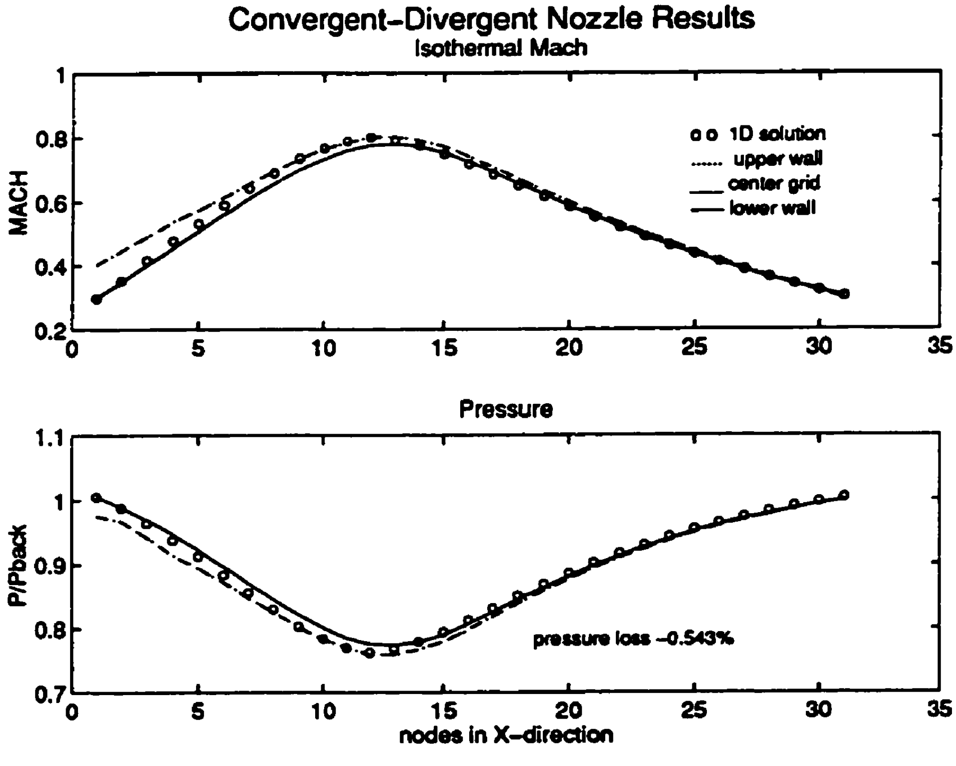

Figure 5.33: Isothermal Mach and pressure distributions for the nozzle presented in Figure 5.32 with M_{in} ≈0.3.

centerline of the nozzle. These results have been compared with the exact solution of the one-dimensional isentropic flow approximation through a nozzle. There is an excellent agreement between the two solutions. At first, it might be expected to see the one-dimensional solution always between the centerline and wall solutions. This is true until the throat reaches sonic speed. Then, the throat Mach number becomes highly sensitive to slight changes in inlet Mach number. Comparing the inlet Mach numbers for the cases with throat Mach numbers of M=0.8 and 0.95 reveals the high sensitivity of the throat values near sonic speeds. In another words, numerical errors will cause significant deviation from the exact solution near sonic speeds. On the other hand, a look at the geometry of the nozzle reveals how far it is from being one-dimensional. The two-dimensionality of the problem is another reason which causes deviation from the one-dimensional solution.

In addition to the two factors of the nozzle geometry and the sensitivity at high Mach numbers, there is the mesh size factor which affects the accuracy of the numerical solution. The effect of this factor has been illustrated in Figures 5.37 and 5.38 for the nozzle problem with $M_{throat} \approx 0.95$. This nozzle problem has been tested for three different mesh sizes of 101×11, 51×6, and 25×4. The Mach distributions on the centerline have been compared with the one-dimensional solution. As is seen, finer grid shows better accuracy comparing with the one-dimensional solution. The Mach contour lines have been depicted for these three different mesh sizes in Figure 5.37. Finer grid distribution demonstrates smoother distribution around the throat comparing with coarser distributions.

Generally speaking, Figures 5.34 to 5.36 present excellent performance of the compressible algorithm for solving high subsonic compressible flows. It is essential that the obtained solution presents a symmetric distribution left and right of the throat section. This symmetry is well demonstrated within these plots. Identical

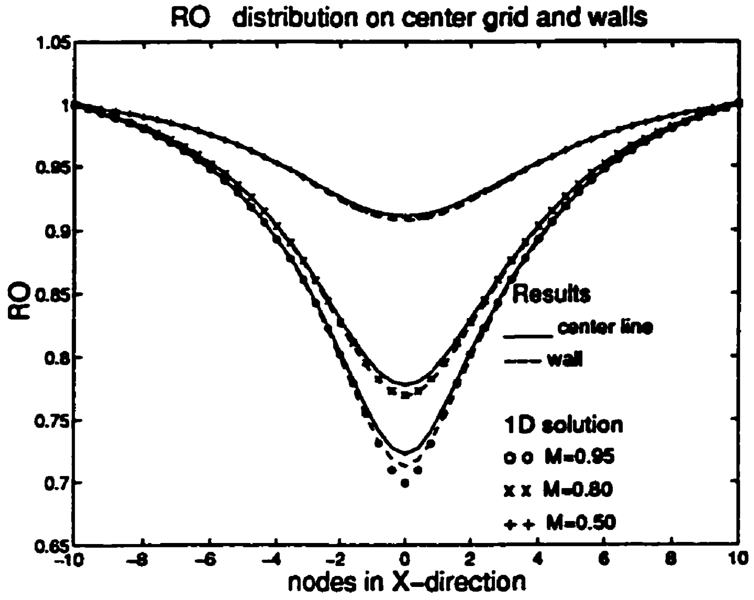

Figure 5.34: Density distribution for three different throat Mach numbers.

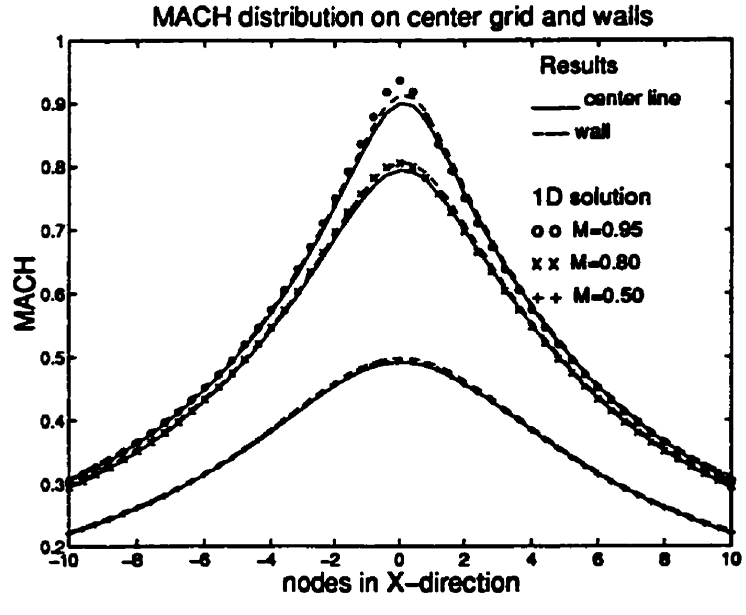

Figure 5.35: Mach distribution for three different throat Mach numbers.

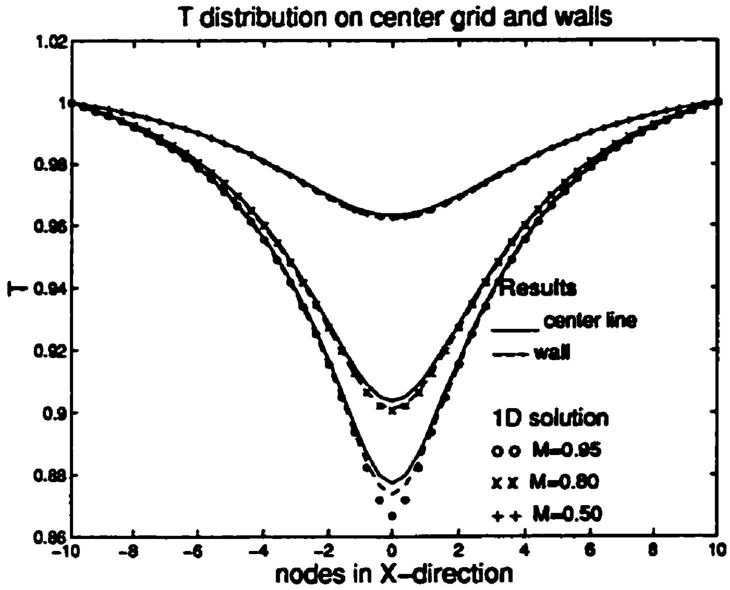

Figure 5.36: Temperature distribution for three different throat Mach numbers.

values of the parameters at the inlet and outlet of the domain supports the ability of the code in solving the Euler flow equations.

For the boundary condition implementation, the pressure was specified downstream, which is why all three lines of pressure distribution are matched at the exit of the nozzle. The upstream pressure was computed by the code. In an Euler flow, both upstream and downstream should attain the same pressure if their aspect ratios are the same. This was a good test for checking the pressure drop in this method. The pressure drops which are presented on Figures 5.31 and 5.33 report the pressure loss from inlet to outlet. These low numbers are another indication of the accuracy of the method for this subsonic flow.

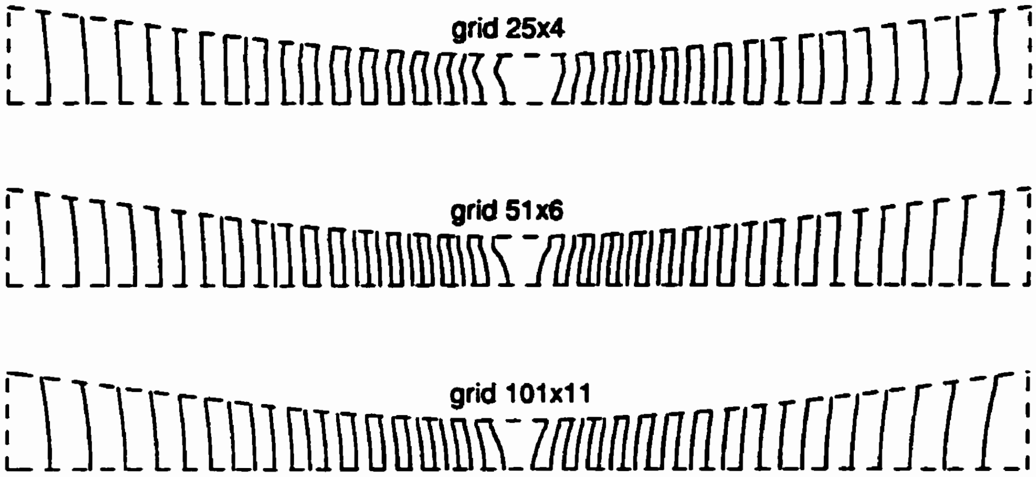

Figure 5.37: The effect of mesh size on the Mach contour distribution.

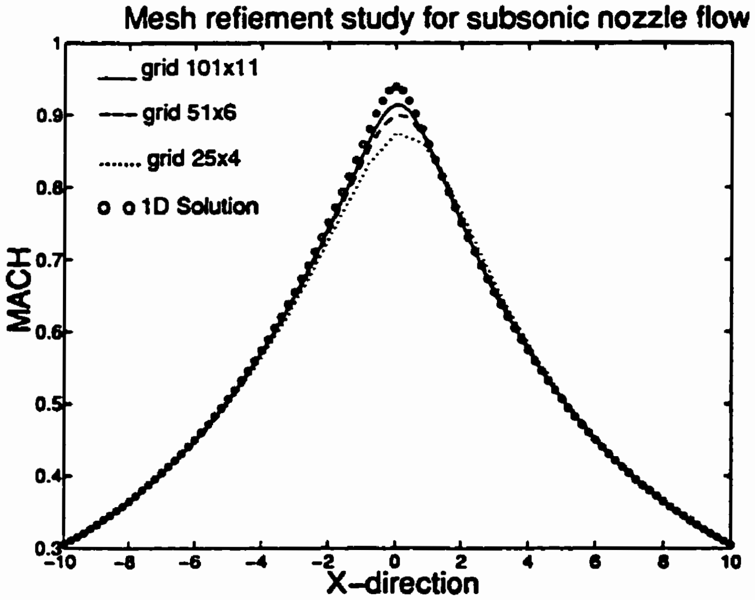

Figure 5.38: Mesh size effect on the accuracy of the numerical solution.

Mixed Subsonic-Supersonic Flow

In this part, the shock capturing capability of the current method is investigated by testing mixed subsonic-supersonic flow through a converging-diverging nozzle. There are two limiting cases for convergent-divergent nozzle flow when the Mach number of the throat is unity. The flow in divergent part of the nozzle can either be fully subsonic, with symmetric distribution of flow variables respect to the throat section, or supersonic, with a smooth decrease or increase of the flow parameters from inlet to exit. Between these two limiting cases, the flow is not stable unless there is a shock in the divergent part of the nozzle. In order to generate a shock in the nozzle, it is necessary to have sonic speed at the throat. In this regard, the inlet stagnation pressure is increased until the flow is choked. Then, the back pressure is decreased to a lower value than the inlet. This results in a normal shock wave within the divergent part of the nozzle. The ratio of $\frac{P_{exit}}{(P_0)_{in}}$ determines the location and the strength of the shock.

The nozzle figure is as before in Figure 5.24, while the grid distribution has been changed to a uniform 51×9 distribution for the whole nozzle. Initially, the inlet stagnation pressure was specified at the inlet and the exit pressure was selected in such a manner that a pressure ratio of $\frac{P_{exit}}{(P_0)_{in}}$=0.7932 produced shock at the particular section $\frac{A}{A^*}$=1.31 with strength, $\frac{M_{left}}{M_{right}}$=2.575. The results of the current method are depicted in Figures 5.39 and 5.40 and compared with that of the one-dimensional exact solution and Karki [91]. Karki solves the test case using a quasi-one-dimensional algorithm. Schneider and Karimian [12] have also solved this problem using a quasi-one-dimensional algorithm without mentioning the profile of the nozzle. Since the continuity equation is sacrificed to specify mass at the inlet, the control volumes which are placed at the inlet do not necessarily conserve mass.

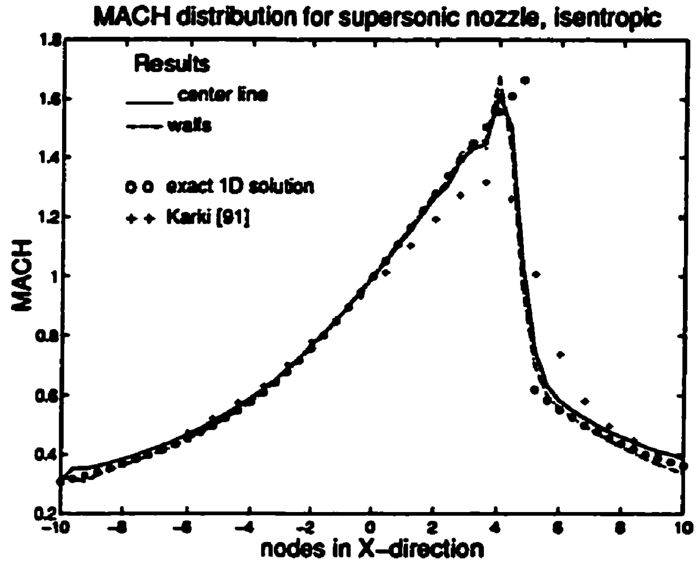

Figure 5.39: Mach distribution in nozzle with M_{max}=1.67.

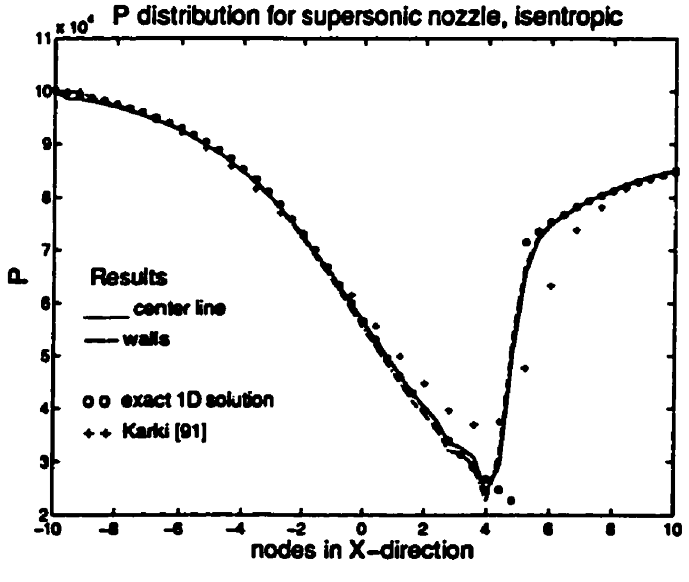

Figure 5.40: Pressure distribution in nozzle with M_{max}=1.67.

As observed in Figure 5.39, this defect causes some discrepancies in the solution close to the inlet. The exact solution has been computed right at the nodes and these values are shown by circles. The exact location of the shock is not necessarily at nodes but somewhere between two neighboring nodes in the vicinity of the shock discontinuity.

As seen, the shock has been captured very well in the divergent part despite using a coarse grid. The shock position and the exit Mach number have been predicted very well comparing with the one-dimensional solution. Lien and Leschziner [53] have solved a similar inviscid nozzle flow using either the quasi-one-dimensional or two-dimensional models in their all speed flow solver. They show that the two-dimensional results are farther than the quasi-one-dimensional solution to the one-dimensional exact solution around the shock. consistent with their experience, our results also show that the shock has been slightly smeared in the front of the shock and a minor undershoot is observed behind it. The source of this oscillation is from the temperature integration point calculation which is approximated by a bilinear interpolation in this case. The test problem was solved with a maximum Courant number of 1.25. This maximum occurs at the left-hand-side of the shock. A total of 222 time steps were executed to achieve the RMS of 10^{-5} for most of the dependent variables. It should be noted that no special treatment has been specified for the distribution in the vicinity of the shock wave.

In the second test, this nozzle configuration is examined for flow with stronger normal shock wave, Figures 5.41 to 5.43. In addition to that, the oscillation around the shock wave is investigated. In order to generate a stronger shock, the exit pressure is reduced to $\frac{P_{exit}}{(P_0)_{in}}=0.57$. This produces a shock at section $\frac{A}{A^*}=1.837$, with a strength of $\frac{M_{left}}{M_{right}}=3.74$. The maximum Mach number for this case is $M_{left}=2.1$ which is only 0.1 less than the maximum Mach number for a fully supersonic flow

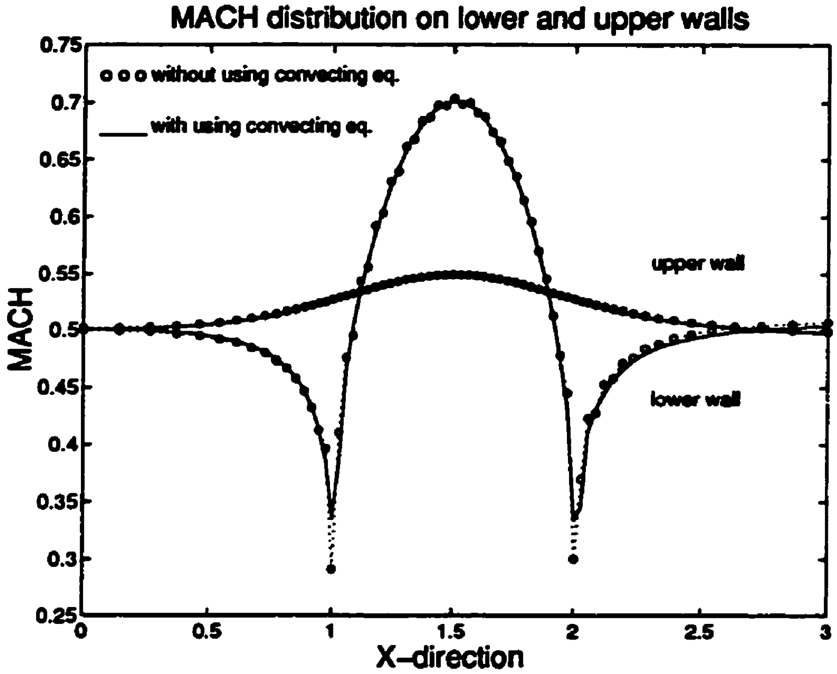

Figure 5.50: Mach distributions on the walls of channel with and without using convecting momentum equation, M_{in}=0.5.

Transonic Flow

In this part, the method is examined for more highly compressible flows, transonic flow. The test configuration and its grid arrangement are as before while the inlet Mach number of the flow is increased to a supercritical transonic case, i.e. M_{in}=0.675. This Mach number causes a supersonic region in the solution domain which is terminated by a shock. Figure 5.51 depicts Mach contour lines within the domain. These lines are no longer symmetric respect to the mid-chord line because there is a shock on the bump. The Mach contour lines are also not perpendicular to the wall downstream of the bump, as they are upstream, because the flow becomes rotational upon passing the shock. Figure 5.52 demonstrates the distributions of Mach number on the upper and lower walls of the channel and compares these

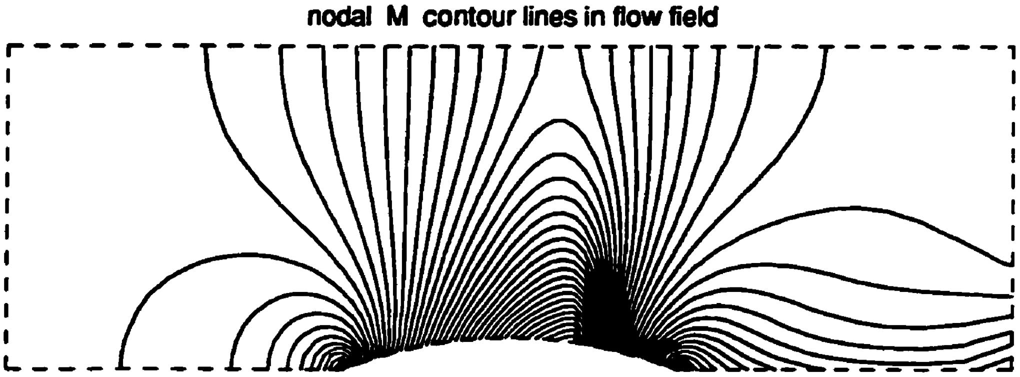

Figure 5.51: Mach contours for transonic flow in a channel with a bump, M_{in}=0.675.

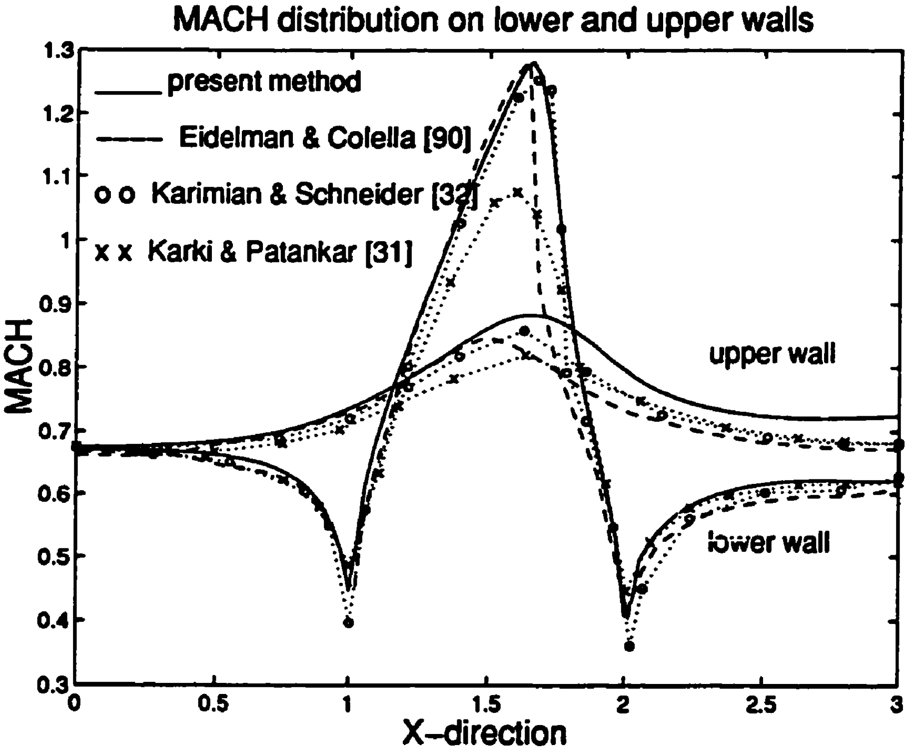

Figure 5.52: Mach distribution on the walls of channel and comparing with [92] using 89×33, [33] using 60×20, and [32] using 67×22 non-uniform grids, M_{in}=0.675.

with the results of other workers. The agreement of this work with the results of Eidelman [92] is very good although a little disparity is observed behind the shock.

In order to have a quantitative comparison as well as qualitative one, the location and magnitude of the captured shock have been determined and represented in Table 5.6. The results of the current work are compared with those of [33, 92, 93]. Ni [93] developed a multigrid scheme in the context of the density-based compressible flow algorithm. His results are more accurate. Since the shock for this work has a bit of spread its location has been calculated based on the midpoint between the upstream and downstream of the shock. The results of the current work compare favorably with those of the other researcher.

	Present method	Ni [93]	Eidelman [92]	Karimian [33]
Bump Chord%	75%	72%	72%	75%
Max. Mach No.	1.29	1.37	1.29	1.25

Table 5.6: Location of the shock in percentage of the bump chord length

The initial condition was F=G=0 for this case. The total of 50 time steps was required to reach the convergence criterion, i.e. RMS$<10^{-5}$ for all dependent variables, with $\Delta\theta$=0.1.

Supersonic Flow

The final case examined for the bump channel flow is for supersonic flow. The configuration of the test model remains the same except the bump thickness is reduced to 4%. The grid arrangement for this case is different from the previous one. It is a non-uniform 77×21 grid distribution which is shown in Figure 5.53. A coarser distribution has been considered for upstream of the bump because the flow in that region is not affected by the bump. The grid distribution along the channel over bump and its downstream are relatively uniform, however, non-uniform grid distribution has been considered for the cross sections to have better resolution of the shock on walls. The inlet Mach number of M_{in}=1.65 is selected to be compatible with the results of other workers.

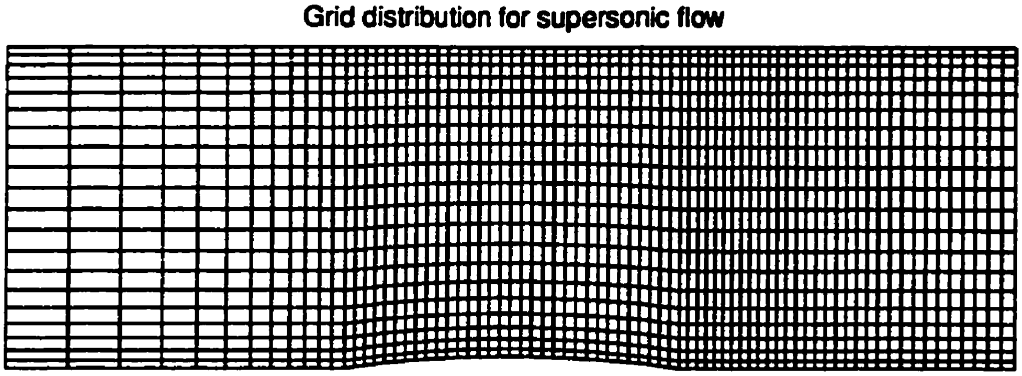

Figure 5.53: Grid distribution for supersonic flow in a channel with bump.

The isobar lines in Figure 5.54 show the position of the shock waves inside the channel. As observed, two oblique shock waves are formed at the corners of the bump. The leading edge shock is followed by expansion waves reflected from the bump's body. This shock later strikes the upper wall and is reflected back by the wall into the expanding flow field. The trailing edge shock leaves the computational domain from the exit boundary after intersecting the expansion waves. The number of intersections and reflections indicates that this supersonic problem is a difficult one.

The Mach distributions on the lower and upper walls are seen in Figure 5.55. The results of the current method are compared with those of the previous references for which the grid arrangements were different from the previous test cases. As seen

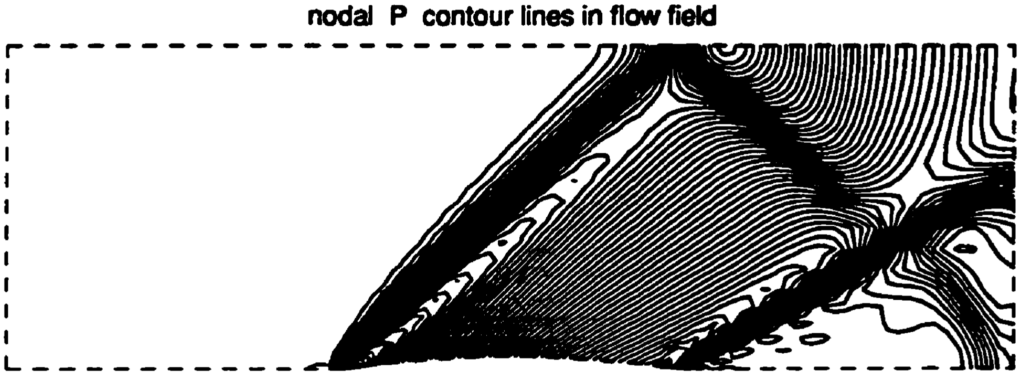

Figure 5.54: Mach contours for supersonic flow in a channel with a bump, M_{in}=1.65.

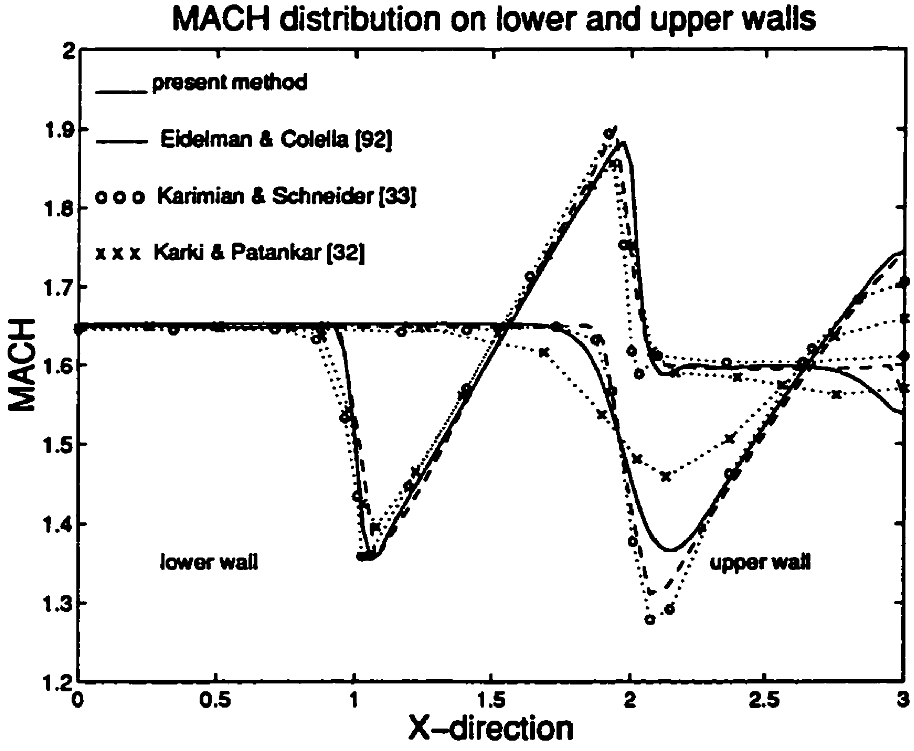

Figure 5.55: Mach distribution on the walls of channel and comparing with [92] using 89×33, [33] using 60×20, and [32] using 67×22 non-uniform grids, M_{in}=1.65.

from the figures, the agreement of the results on the lower wall is better than that of the upper wall, however, for the lower wall, the flow near the channel exit displays some oscillatory behaviour. This behaviour identifies the need for improvement in this region of the flow. Although the cause of this is not entirely clear, the intersection of the reflected shock with that corner might be an important factor.

The problem was started with initial conditions of F_0=500 kg/(m/s^2), G_0=0.0 kg/(m/s^2), P_0=86,100 Pa, and T_0=300 $^\circ K$. This non-zero F_0 speeds up the convergence. The number of time steps to reach the convergence criterion for RMS$<10^{-5}$ was 220. The maximum Courant number used for this test case was 0.86.

5.4.4 Supersonic Flow in a Channel with a Ramp

The purpose of this section is to study the performance of the current method in solving flow with strong oblique shock waves. The test model is a channel with a ramp mounted on its lower wall. This problem is very appropriate because of the availability of the exact solution. This enables us to evaluate the accuracy of the method. The geometry and grid distribution for this problem are shown in Figure 5.56. The longitudinal and transverse lengths are 1.3 and 1.2m, respectively. The ramp angle is 21.57-deg and its leading-edge is located at x=0.3m. The ramp angle creates an oblique shock wave with 45-deg angle if the inlet Mach number is M_{in}=2.5. This shock has an strength of M_2/M_1=0.628, P_2/P_1=3.497, and T_2/T_1=1.508. This shock will leave the solution domain without colliding the solid walls. A non-uniform grid distribution of 41×37 has been used for the computation, Figure 5.56.

Figure 5.57 depicts the Mach contour lines in the solution domain. As is seen, the main changes of the flow parameters occurs across the shock wave. The oblique

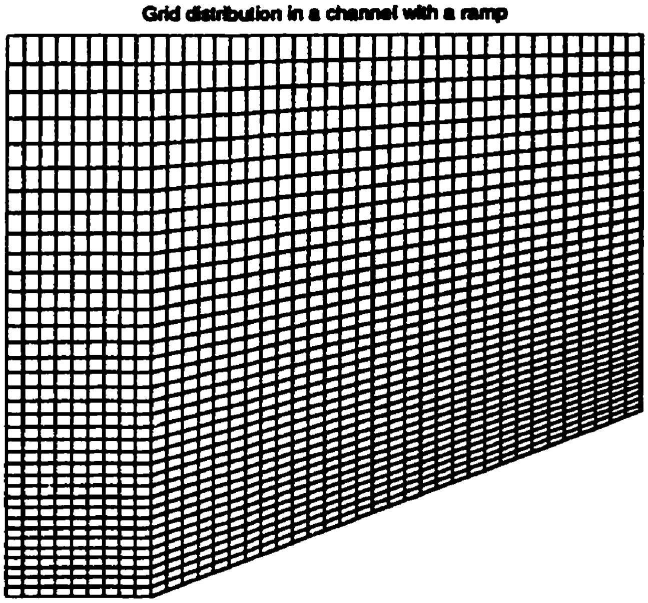

Figure 5.56: Grid distribution within a channel with a ramp.

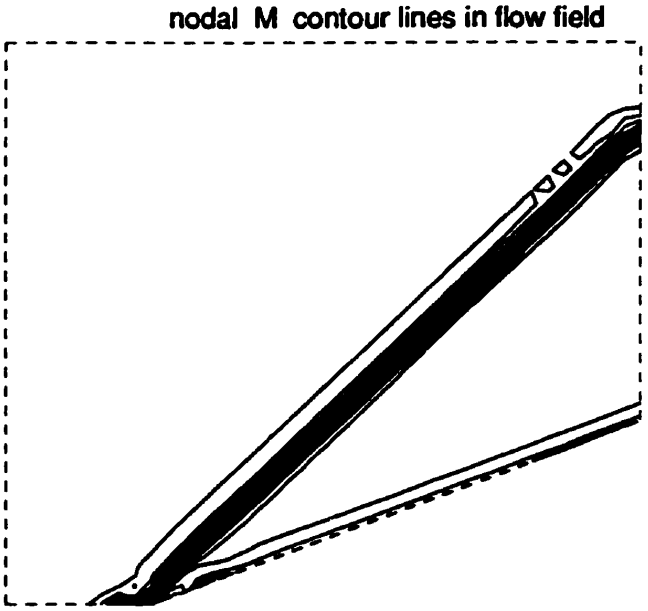

Figure 5.57: Mach contour lines plot for ramp with M_{in}=2.5.

shock wave leaves the domain with an angle of 45-deg which is identical with the analytical solution.

The details of the solution inside the channel have been provided in Figure 5.58. This figure shows the Mach distribution at a constant height of y=0.75m inside the channel and compares the results of the current method with that of Karimian and Schneider [33]. The comparison of these results with the exact solution shows that the shock wave has been captured within almost 6 nodes by the both methods. However, the current method shows an overshoot behind the shock. This is not seen in the results of the reference. This might be the effect of damping mechanism which is used by the reference. The results demonstrate the ability of the current method to capture strong oblique shock wave without using any implicit artificial viscosity or damping mechanism in its algorithm.

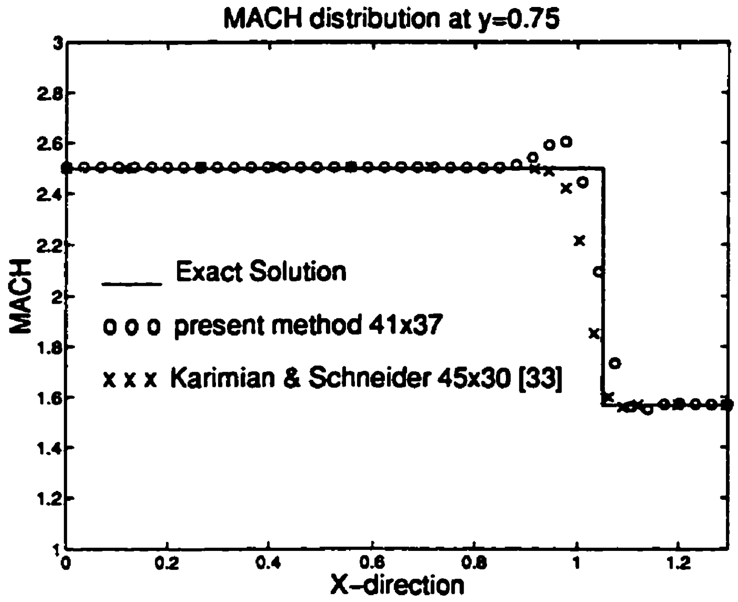

Figure 5.58: Comparing Mach distribution result at height y=0.75m with other results in a duct with a ramp.

In this test problem, the selected convergence criterion of $RMS<10^{-5}$ was decreased to $RMS<10^{-6}$ because the time step, or Courant number, for this problem was lower than that of the previous tested problems, Table 5.4. This small time step can lead to a wrong steady-state solution if RMS is not enough low. Since we are looking for the steady-state solution, we have to decrease the RMS criterion to be sure that the converged results performs the steady-state solution.

The problem was started with initial conditions of F_0=500 kg/(m/s^2), G_0=0.0 kg/(m/s^2), P_0=86,100 Pa, and T_0=300 °K. A non-zero F_0 speeds up the convergence. The problem was solved for an inlet Courant number of about 0.55. The total number of 416 time steps were needed to satisfy the $RMS<10^{-6}$ for F and G. This number is reduced to 265 if $RMS<10^{-5}$.

5.5 Comparison Between Velocity and Momentum Formulations

In this section, we present a comparison between the momentum-based and velocity-based formulations for high speed compressible flow. It is noted that there is no significant difference between the velocity-based and momentum-based formulation for absolute incompressible flow where density is a constant. The discussion on the performance of the current method in solving pseudo-compressible flows was presented in Section 5.3 and is not repeated here.

A literature review of the methods which solve for incompressible and compressible flows at all speeds was presented in Section 1.2.4. Zienkiewicz and Wu [49] solve subsonic and supersonic flows for a number of applications using an explicit or semi-explicit finite-element method. They solve the non-conservative form of the governing equations and admit that this may lead to different shock behaviour than that involving the full conservation form. They do not report the convergence histories for their steady-state solutions. Van Doormal et al [50] illustrates the applicability of segregated methods for solving flow at all speeds and evaluates the relative convergence behaviour of these methods for solving the one-dimensional and two-dimensional laminar compressible flows. This provides a good potential to compare the performance of the current method with that of the segregated ones. However, this comparison has been done for two-dimensional studies with a different segregated approaches. Karki and Patankar [32] have developed SIMPLE-based methods to solve for flow at all speeds. The density at the integration point is always upwind-biased. This provides an artificial damping which allows for the successful computation of transonic and supersonic flows. Their results have been compared with the results of the current formulation as illustrated in Figures 5.39 to 5.42, for the converging-diverging nozzle problem with shock, and Figures 5.49, 5.52, and 5.55, for flow in a channel with a bump. Their results show smearing in the vicinity of shocks due to excessive numerical dissipation. They do not report the convergence histories of their solutions.

Chen and Pletcher [38, 45] employ explicit/implicit second-order and explicit fourth-order smoothing terms in their time-marching method to solve transient flow and flow at all speeds. Their work is fully implicit and all variables, (u,v,p,t), are computed simultaneously. They report the convergence behaviour of their solutions which we compared with that of the current work. This comparison has been presented in Table 5.4 for solving the compressible cavity flow and in Table 5.5 for solving subsonic entrance flows. Generally speaking, the momentum-based procedure provides faster convergence and higher stability.

In addition to the above methods which solve for flow at all speeds, it is the method of Karimian and Schneider [27, 33] which enables us to provide a direct comparison between the performance of the momentum-based formulation and that of the velocity-based formulation. As was mentioned in Section 3.6, a difficulty with their method is the requirement of an explicit damping mechanism. This does not permit a neat and clear comparison between the two formulations. In a one-dimensional investigation, a comparison was performed by direct modeling of their method without considering the damping mechanism, Section 3.6. For the two-dimensional investigation, there remains a question of whether the velocity-based formulation can retain its characteristics of convergence and stability if the damping mechanism is eliminated from the scheme. Karimian [94] states that their velocity-based procedure would diverge without inclusion of the damping mechanism. This statement results in several important conclusions which are discussed subsequently in this section.

Table 5.7 provides an informative comparison between the velocity-based and momentum-based formulations for highly compressible flow problems which include flow through channels with a bump and with a ramp on the lower boundary. The number of iterations, NOI, and time step, $\Delta\theta$, are tabulated based on an RMS convergence criterion of 10^{-5} for the momentum formulation and of 10^{-3} for the velocity formulation. Although the initial and boundary conditions are the same for both formulations, the grid resolutions and distributions are not exactly identical.

Despite different RMS criterions for velocity-based and momentum-based formulations, a number of points could be resulted if we assume that they are the highest criterions to which steady-state solutions are botained in each of these formulations. For the subsonic flow, it is the momentum procedure which shows faster convergence in comparison with the velocity procedure in meeting a defined RMS. For transonic and supersonic flows, this fast convergence is diminishes with increas-

	momentum-based formulation with no damping this research	velocity-based formulation with artificial damping Karimian and Schneider [33]
R.M.S	0.00001	0.001
	Subsonic Bump, M_{in}=0.5	
NOI	8	8
$\Delta\theta$	huge	1.0
	Transonic Bump, M_{in}=0.675	
NOI	50	25
$\Delta\theta$	0.1	1.0
	Supersonic Bump, M_{in} =1.65	
NOI	220	10+18
$\Delta\theta$	0.0005	0.0002, 0.02
	Supersonic Ramp, M_{in} =2.5	
NOI	265	10+10+9
$\Delta\theta$	0.0002	0.0001, 0.001, 0.01

Table 5.7: Comparative study of the convergence histories between the velocity-based and momentum-based formulations.

ing Mach number. For supersonic flow, the performance of the velocity procedure with damping is superior to the momentum procedure without damping. Although both procedures start with small time steps, the velocity-based approach multiplies it after a number of preliminary steps. The time step increase speeds up the convergence toward the steady-state solution. If the time step is increased for the momentum-based formulation which is free from any explicit damping mechanisms, it cannot handle the acceleration produced by the force of the initial flow and of the boundary condition implementation.

Generally speaking, the momentum-based formulation has several advantages with respect to the velocity-based formulation without damping. The use of the momentum-component formulation does increase the stability of the method in comparison with the velocity-component formulation which requires a damping mechanism for all time steps in order to converge. Some under/overshoots are observed around strong shocks in the momentum-based formulation but do not cause serious difficulties in the convergence if the time step is small enough. It is the lack of a damping mechanism which does limit the time step to small values. Indeed, the momentum-based formulation does need improvement if it is desired to achieve faster convergence. This provides one possible area for future research.

At the end, it is noted that the advantages of the momentum-based formulation in obtaining better convergence without using a damping mechanism are supported by a number of factors. Two important factors were discussed in the research motivation. They are the stability of the mass flux in passing through shocks, Section 2.4.2, and the reduction in the linearization requirements, Section 2.4.3. However, the importance of each of these factors in promoting cannot be fully evaluated separately.

5.6 Closure

The proposed momentum variable procedure was examined for many different two-dimensional flows including incompressible, pseudo-compressible, and subsonic to supersonic compressible flows. The method showed excellent performance in solving flow at all speeds. There was no CFL number limit in solving incompressible and subsonic flows. The solution converged very rapidly within a small number of iterations. However, the convergence slowed down in supersonic flows with CFL numbers less than one. Despite not employing any explicit artificial viscosity or dissipation and in spite of using coarse grids, excellent solutions were obtained in comparison with the work of other references. However, the formulation still needs improvement to increase its convergence in comparison with the velocity-based formulation where damping is employed. The proposed formulation showed excellent performance in solving very low Mach number flows with respect to both the solution accuracy and the convergence history.

Chapter 6

Concluding Remarks

6.1 Summary

The difference in the nature of compressible and incompressible flows has resulted in the development of numerous numerical techniques to deal with each of these two types of flow separately. There have also been efforts to develop algorithms capable of solving both compressible and incompressible flows. In this thesis, a new two-dimensional unsteady viscous computational algorithm has been developed to solve flow at all speeds. A strong motivation for this development has been to explore the use of momentum component variables instead of the velocity components usually used in all speed solvers. Several reasons were behind this. A significant one of which is the strong analogy that exists between the two kinds of flow when such variables are used. This analogy, developed in this thesis, permits incompressible flow methods to be applied to compressible flow problems. In addition, using the momentum components improves stability around shocks and reduces the linearization difficulties.

The two-dimensional Navier-Stokes equations were selected to examine the performance of the proposed method. The method was developed using a control-volume-based finite-element scheme. The finite-element part of this scheme provides the benefits of finite-element geometric flexibility while the advantages of conservative discretization procedures are provided by the use of the control-volume formulation.

Initially, this proposed new direction was explored for one-dimensional flow modeling. In this one-dimensional investigation, momentum, pressure, and temperature were selected as the dependent variables in a colocated grid arrangement. The governing equations were treated in conservative manner. The integration point equation for the momentum component was derived by approximating the non-conservative form of the momentum equation at the integration point. Rearrangement of this equation enabled the integration-point momentum, or convected momentum, to be determined. If only this convected momentum component was employed in the conservative form of the discretized equations, it was found that a special form of the pressure checkerboard problem resulted. A number of different treatments to overcome this difficulty were examined. In this regard, a new integration point equation was derived by the combination of the momentum and continuity equation errors. This new equation was named the convecting equation which represented the convecting momentum component. The influence of the continuity error was examined by applying an appropriate factor. The use of both the convected and convecting momentum equations removed the possibility of the pressure-velocity decoupling problem. The resulting one-dimensional algorithm was then validated for incompressible flow by using several source/sink test cases. The algorithm was also validated for compressible flow by comparing with the analytical results for the shock tube problem. Finally, the performance of this one-dimensional momentum-component formulation was compared with that of the velocity-component formulation by direct modeling of the latter formulation.

Next, the procedure was extended for solving two-dimensional flows. Convected and convecting integration point equations were again derived by approximating the non-conservative form of momentum and the conservative form of continuity equations at the integration points. The stream-wise treatment of the convection terms had an important impact in achieving the correct physical modeling of the flow. The two-dimensional algorithm was validated for many different flows including incompressible and compressible ones. The flow models were classified into the three categories of incompressible, pseudo-compressible, and compressible flows. The results of the developed method were compared with those of several velocity-based procedures which solve flow for all speeds. The good to excellent performance of the method in achieving reliable results on coarse grids without using the explicit artificial viscosity and damping mechanisms are noteworthy. The following sections present the main conclusions of this work and recommendations for future research.

6.2 Conclusions

The main purpose of this PhD research has been to explore and find the advantages and disadvantages of the momentum-variable procedure in comparison with the velocity-based procedure. The potential advantages of the momentum-based formulation motivated this research: the existence of a flow analogy between the governing equations for compressible and incompressible flow, the stability of the mass flux through shocks, and reduced difficulty in linearizing the nonlinear terms.

It is almost impossible to recognize the degree to which each potential advantages is involved in gaining the superior results for the momentum-based procedure.

In a one-dimensional unsteady flow investigation, it was shown that the stability of the mass flux passing through shocks was not a crucial factor. However, this assessment was much more difficult in the two-dimensional study. Considering this difficulty, the advantages and disadvantages of the momentum-variable procedure are discussed in the following paragraphs mainly without reference to the factors which cause such advantage or disadvantage.

The conclusions are divided into two parts. In the first part, the characteristics and capabilities of the new method are presented. This part is developed mainly by comparing with exact solutions and the results of other workers. The second part compares the advantages and disadvantages of the momentum-variable procedure with those of the velocity-variable procedures. This part is concluded by a direct comparison with the results of the velocity-based procedures which solve flow for all speeds. Based on the method development and the demonstrated results of its application, the first part of the conclusions are

1. The benefits of the finite-element basis of the method facilitates domain discretization, and no difficulty was encountered in fitting the grid to the domain.
2. The integration point equations which were derived provide correct physical behavior of the flow variables. This ability was shown not only by the numerical solution but also by an analytical investigation. The Peclet and Courant numbers are two parameters which provide flexibility of the formulation for a wide range of flow parameters.
3. The proper consideration of the role of velocities at control-volume surfaces resulted in two sets of integration point equations; convected and convecting ones. The correct application of these equations generated a strong connection between the velocity and pressure fields and removed the possibility of the

checkerboard problem. This capability was demonstrated by numerous tests in both one-dimensional and two-dimensional studies.

4. The method showed good to excellent performance in solving flow at all speeds including: incompressible and compressible (pseudo-compressible to supersonic), viscous and inviscid, and steady and unsteady. Excellent results were obtained for incompressible and subsonic compressible flows despite using coarse grids. The demonstrated results confirm the excellent performance of the developed method in solving low and high Reynolds number flow cases. Very good results were obtained in supersonic flows despite the exclusion of explicit artificial viscosity or dissipation functions. This was clearly observed in solving high speed inviscid flows.

5. No CFL number limitation was encountered in solving incompressible, subsonic compressible, and transonic flows. This advantage enabled the present time dependent method to meet the convergence criterion within a relatively small number of iterations using large time steps.

6. The selection of pressure as a dependent variable and developing a pressure-based method enabled the method to be highly robust in treating very low Mach-number compressible flows. The results of solving the subsonic and transonic flows were noteworthy with regard to the coarse grid distribution and the number of time steps required to reach a steady-state solution.

7. Some difficulties were encountered in supersonic flow, which generally slowed down the convergence of the solution and limited the CFL number to close to one. This may be due to the lack of artificial dissipation and/or damping functions. Despite these restrictions, the results were fairly good.

8. An analogy between compressible and incompressible flow motivated the use of momentum-components as dependent variables. The pseudo-compressible and compressible models were used to demonstrate this analogy. The analogy worked well not only in deriving similar results for both compressible and incompressible flows but also in providing similar convergence histories.

9. The entire effort the current work was to develop the method as simple as possible. Complex and time-consuming techniques were avoided so that the conceptual aspects of the method could be emphasized. For example, all integration point equations were derived based only on the element nodal points. The other three integration point values were not involved in deriving the fourth. Despite excluding such a potential benefit, very good results were obtained for highly recirculating flows.

A direct comparison between the results of the momentum-variable and velocity-variable procedures which solve flow for all speeds results in the second part of the conclusions. The conclusions are categorized based on the characteristics of the different types of flow,

1. There is no significant difference between the velocity-variable formulation and momentum-variable formulation when density is constant. However, the momentum-based formulation involves and discretizes terms in the momentum equations which are not existent in the momentum equations of the velocity-based formulation. Although these terms are mathematically zero, they are numerically non-zero. These terms could be a source of difference between the above procedures.

2. The momentum-variable formulation is robust for pseudo-compressible flows. However, this may be accounted for as a direct advantages of using a pressure-based algorithm. Essentially, the pressure-based methods which solve compressible flows could be extended to solve for pseudo-compressible flows. However, there is no reason for a pressure-based method to show identical solution and convergence history behaviour for both the absolute incompressible and pseudo-compressible flows. The existence of these capabilities in the results of the momentum-component formulation could be accounted for as a direct effect of the existence of the flow analogy in that formulation.

3. Although both the velocity-based and momentum-based formulation successfully solve the subsonic compressible flows, the latter one generally shows better performance in comparison with the former one. This is concluded by comparing the number of iterations which they need to meet the preset convergence criterion.

4. In supersonic flow, the velocity-based procedure suffers from severe oscillations in the vicinity of the shock if no explicit damping mechanism or dissipation is included. This results in major time-step and Courant number restrictions. These oscillations subsequently results in instability and divergence if a lower convergence criterion is desired. However, the use of a damping mechanism in the velocity-based procedure could result in better stability and accuracy. The momentum-based procedure, on the other hand, had excellent stability and good accuracy, even without explicit damping, provided the time step and Courant number restrictions were satisfied.

6.3 Recommendations for Future Research

No single method contains all desirable features while avoiding any disadvantages. The following recommendations are suggested for the continuation of future research in this field:

1. There is a need to further investigate the problems encountered with supersonic flow. This investigation should generally address a number of issues. The first is to extend the ability of the supersonic application to solve for higher Courant numbers which will then result in faster convergence. The second is the use of artificial dissipation techniques and damping mechanisms ro remove undershoots and overshoots around the shock waves and improve convergence . The third is to extend the scheme to more accurate shock capturing techniques.

2. The possible unification of and the justification for the two convected and convecting momentum components is another interesting subject for future research. Although mathematically demonstrated, our understanding of this issue could be further enhanced.

3. While the discretization of the domain interior is fully conservative, the boundaries may not be. The modification of boundary condition treatment toward obtaining a fully conservative solution domain is another subject for future research.

4. A number of other extensions of the present method could also be pursued, such as extending the method to: three-dimensional flows, flows with more complicated geometries and boundaries, buoyant flows, heat transfer problems, and other types of finite elements (such as triangles).

Bibliography

1. Patankar, S.V., Numerical Heat Transfer and Fluid Flow, Hemisphere, Washington, D.C., 1980.
2. Harlow, F.M., and Welch, J.E., "Numerical Calculation of Time Dependent Viscous Incompressible Flow with Free Surface", Physics of Fluids, v.8, pp.2182-2189, 1965.
3. Raithby, G.D., and Schneider, G.E., "Numerical Solution of Problems in Incompressible Fluid Flow; Treatment of the Velocity-Pressure Coupling", Numerical Heat Transfer, v.2, pp.417-440, 1979.
4. Patankar, S.V., "A Calculation Procedure for Two-Dimensional Elliptic Situations", Numerical Heat Transfer, v.4, pp.409-425, 1981.
5. Zedan, M., and Schneider, G.E., "A Coupled Strongly Implicit Procedure for Velocity and Pressure Computation in Fluid Flow Problems", Numerical Heat Transfer, v.8, pp.537-557, 1985.
6. Patankar, S.V., and Spalding, D.B., "A calculation procedure for Heat, Mass, and Momentum Transfer in Three-Dimensional Parabolic Flows", International Journal of Heat and Mass Transfer, v.15, pp.1787-1806, 1972.

7. Baliga, B.R., and Patankar, S.V., "A Control-Volume Finite-Element Method for Two Dimensional Fluid Flow and Heat Transfer", Numerical Heat Transfer, v.6, pp.245-261, 1983.

8. Prakash, C., and Patankar, S.V., "A Control-Volume Based Finite-Element Method for Solving the Navier-Stokes Equation Using Equal Order Variable Interpolation", Numerical Heat Transfer, v.8, pp.259-280, 1985.

9. Rhie, C.M., and Chow, W.L., "Numerical Study of the Turbulent Flow Past and Airfoil with Trailing Edge separation" AIAA Journal, v.21, pp.1525-1532, 1983.

10. Schneider, G.E., and Raw, M.J., "Control Volume Finite Element Method for Heat Transfer and Fluid Flow Using Co-located Variables - 1. Computational Procedure", Numerical Heat Transfer, v.11, pp.363-390, 1987.

11. Schneider, G.E., and Raw, M.J. "Control Volume Finite Element Method for Heat Transfer and Fluid Flow Using Co-located Variables - 2. Application and Validation", Numerical Heat Transfer, v.11, pp.391-400, 1987.

12. Schneider, G.E., and Karimian, S.M.H., "Advances in Control-Volume Based Finite-Element Methods for Compressible flows", Computational Mechanics, v.14, pp.1-16, 1994.

13. Darbandi, M., and Schneider, G.E. "Momentum Component Variable Procedure for Flow at All Speeds", The Proceedings of the Third Annual Conference of the CFD of Society of Canada, Banff, Alberta, Canada, June 25-29, pp.145-156, 1995.

14. Peric, M., Kessler, R., and Scheuerer, G., "Comparison of Finite-Volume Numerical Methods with Staggered and Colocated Grids", Computers

and Fluids, v. 16, pp.389-403, 1988.

15. Alishahi, M.M., and Darbandi, M., "Multiple-Zone Potential Solution around Wing-Body Configurations", Journal of Aerospace Engineering, v.6, pp.329-346, 1993.

16. Palumbo, D.J., and Rubin, E.L., "Solution of two Dimensional Unsteady Compressible Navier-Stokes Equations Using a Second Order Accurate Numerical Scheme", Journal of Computational Physics, v.9, pp.466-495, 1972.

17. MacCormack, R.W., "The Effect of Viscosity in Hypervelocity Impact Cratering", AIAA Paper 69-354, 1969.

18. MacCormack, R.W., "A Numerical Method for Solving the Equations of Compressible Viscous Flows", AIAA Journal, v.20, pp.1275-1281, 1982.

19. Beam, R.M., and Warming, R.F., "An Implicit Finite Difference Algorithm for Hypersonic Systems in Conservation Law Forms", Journal of Computational Physics, v.22, pp.87-110, 1976.

20. Beam, R.M., and Warming, R.F., "An Implicit Factored Scheme for the Compressible Navier-Stokes Equations", AIAA Journal, v.16, pp.393-402, 1978.

21. Shamroth, S.J., Briley, W.R., and McDonald, H., "Prediction of Cascade Flow Fields Using the Averaged Navier-Stokes equations", Journal of Engineering for Gas Turbine and Power, v.106, pp.383-390, 1984.

22. Briley, W.R., and McDonald, H., "Solution of the Multidimensional Compressible Navier-Stokes Equations by a Generalized Implicit Method", Journal of Computational Physics, v.24, pp.372-392, 1977.

23. Baker, A.J., and Soliman, M.O., "A Finite Element Algorithm for Computational Fluid Dynamics", AIAA Journal, v.21, pp.816-827, 1983.

24. Issa, R.I., and Lockwood, F.C., "On the Prediction of Two Dimensional Supersonic Viscous Interactions Near Walls", AIAA Journal, v.15, pp.182-188, 1977.

25. Han, S.M., "A Generalized Finite Difference Method for Transient Analysis of Compressible and Incompressible Flows", Numerical Methods for Fluid Transient Analysis, presented at Applied Mechanics, Bioengineering, and Fluids Engineering Conference, ASME, Houston, Texas, June 20-22, 1983.

26. Rhie, C.M., "Pressure Based Navier-Stokes Solver Using the Multigrid Method", AIAA Journal, v.27, pp.1017-1018, 1989.

27. Karimian, S.M.H., and Schneider, G.E. "Numerical Solution of Two Dimensional Incompressible Navier-Stokes Equations: Treatment of Velocity-Pressure Coupling", AIAA Paper 94-2359, AIAA 25th Fluid Dynamics Conference, Colorado, June 20-23, 1994.

28. Issa, R.L., "Solution of the Implicit Discretized Fluid Flow Equations by Operator-Splitting", Journal of Computational Physics, v.61, pp., 1985.

29. Van Dyke, M., "Perturbation Methods in Fluid Mechanics", Academic Press, New York, Chapter 2, 1964.

30. Volpe, G., "Performance of Compressible Flow Codes at Low Mach Numbers", AIAA Journal, v.31, pp.49-56, 1993.

31. Hauke, G., and Hughes, T.J.R., "A Unified Approach to Compressible and Incompressible Flows", Computer Methods in Applied Mechanics and Engineering, v.113, pp.389-395, 1993.

32. Karki, K.C., and Patankar, S.V., "Pressure Based Calculation Procedure for Viscous Flows at All Speeds in Arbitrary Configurations", AIAA Journal, v.27, pp.1167-1173, 1989.

33. Karimian, S.M.H., and Schneider, G.E. "Pressure Based Control-Volume Finite-Element Method for Flow at All Speeds", AIAA Journal, v.33, pp.1611-1618, 1995.

34. Merk, C.L., and Venkateswaran, S., and Buelow, P.E.O., "The Relation Between Pressure-Based and Density-Based Algorithms", AIAA Paper 92-0425, 1992.

35. Ekaterinaris, J.A., and Giddens, D.P. "Numerical Solutions of Aerial Flows Using a Low Mach Number Compressible Approach", ASME Applied Mechanics Division (Publication) AMD v.84, Published by ASME, New York, pp.65-68, 1987.

36. Feng, J., and Merkle, C.L., "Evaluation of Preconditioning Methods for Time-Marching Systems", AIAA Paper 90-0016, 1990.

37. Briley, W.R., McDonald, H., and Sharmoth, S.J., "A Low Mach Number Euler Formulation and Application to Time-Iterative LBI Schemes", AIAA Journal, v.21, pp.1467-1469, 1983.

38. Pletcher, R.H., and Chen, K.H., "On Solving the Compressible Navier-Stokes Equations for Unsteady Flows at Very Low Mach Numbers", AIAA 93-3368, Proceedings of the 11th Computational Fluid Dynamics Conference, Orlando, FL, July 6-9, pp.765-775, 1993.

39. Chorin, A.J., "A Numerical Method for Solving Incompressible Viscous Flow Problems", Journal of Computational Physics, v.2, pp.12-26, 1967.

40. Steger, J.L., and Kutler, P., "Implicit Finite-Difference Procedures for the Computation of Vortex Wakes", AIAA Journal, v.15, pp:581-590, 1977.

41. Kwak, D., Chang, J.L.C., Shanks, S.P., and Chakrararthy, S.R., "A 3D Incompressible Navier-Stokes Flow Solver Using Primitive Variables", AIAA Journal, v.24, pp.390-396, 1986.

42. Choi, D., and Merkle, C.L., "Time-Derivative Preconditioning for Viscous Flows", AIAA Paper 91-1652, 1991.

43. Merkle, C.L., and Choi, Y.H., "Computation of Low Speed Flow with Heat Addition", AIAA J. v.25, pp.831-838, 1987.

44. Sesterhenn, J, Muller, B., and Thomann, H., "Flux-Vector Splitting for Compressible Low Mach Number Flow", Computers Fluids, v.22, pp.441-451, 1993.

45. Chen, K.H., and Pletcher, R.H., "Primitive Variable, Strongly Implicit Calculation Procedure for Viscous Flows at All Speeds", AIAA Journal, v.29, pp.1241-1249, 1991.

46. Darbandi, M., and Schneider, G.E. "Use of a Flow Analogy in Solving Compressible and Incompressible Flows", AIAA Paper 97-0706, 35th AIAA Aerospace Sciences Meeting & Exhibit, Reno, NV, January 6-9, 1997.

47. Harlow, F.M., and Amsden, A.A., "A Numerical Fluid Dynamics Calculation Method for All Flow Speeds", Journal of Computational Physics, v.8, pp.197-213, 1971.

48. Zienkiewicz, O.C., Szmelter, J., and Peraire, J., "Compressible and Incompressible Flows; An algorithm for all seasons", Computational Methods in Applied Mechanics and Engineering, v.78, pp:105-121, 1990.

49. Zienkiewicz, O.C., and Wu, J., "A General Explicit or Semi-Explicit Algorithm for Compressible and Incompressible Flows", International Journal for Numerical Methods in Engineering, v.35, pp.457-479, 1992.

50. Van Doormal, J.P., Raithby, G.D., and McDonald, B.H., "The Segregated Approach to Predicting Viscous Compressible Fluid Flows", Journal of Turbomachinery (Transaction of ASME), v.109, pp.268-277, 1987.

51. Demirdzic, I., Lilek, Z., and Peric, M., "A Colocated Finite Volume Method for Predicting Flows at All Speeds", International Journal for Numerical Methods in Fluids, v.16, pp.1029-1050, 1993.

52. Shyy, W., Chen, M.H., and Sun, C.S., "Pressure-Based Multigrid Algorithm for Flow at All Speeds", AIAA Journal, v.30, pp.2660-2669, 1992.

53. Lien, F.S., and Leschziner, M.A., "A General Non-Orthogonal Collocated Finite Volume Algorithm for Turbulent Flow at All Speeds", Computer Methods in Applied Mechanics and Engineering, v.114, pp.149-167, 1994.

54. Raw, M.J., Galpin, F.P., and Raithby, G.D., "The Development of an Efficient CFD Analysis Procedure", AIAA-89-2394, 25th Join Propulsion Conference, Monterey, July 10-12, 1989.

55. Darbandi, M., and Schneider, G.E. "Solving Compressible and Incompressible Flows Using a Momentum Variable Calculation Procedure", AIAA Paper 96-0605, AIAA 34th Aerospace Sciences Meeting & exhibit, Reno, NV, January 15-18, 1996.

56. Darbandi, M., and Schneider, G.E. "An Analogy-Based Momentum-Variable Procedure for Flow at all Speeds", to be presented in the 28th Fluid Dynamics Conference, Snowmass, CO, June 29-July 2, 1997.

57. White, F.M., Fluid Mechanics, McGraw-Hill Inc., New York, 1994.

58. Schneider, G.E., and Zedan, M., "Control-Volume-Based Finite Element Formulation for the Heat Conduction Equation", Spacecraft Thermal Control, Design, and Operation, Progress in Astronautics and Aeronautics, v.86, pp.305-327, 1983.

59. Kutler, P., "Computation of Three-Dimensional, Inviscid Supersonic Flows", in H.J. Wirz (ed), Progress in Numerical Fluid Dynamics, Springer-Verlag, Berlin, 1975, pp.293-374, 1975.

60. Anderson, W.K., Thomas, J.L., and Van Leer, B., "Comparison of Finite Volume Flux Vector Splittings for the Euler Equations", AIAA Journal, v.24, pp.1453-1460, 1986.

61. Anderson, J.D., Introduction to Computational Fluid Dynamics, Lecture Series, Von Karman Institute for Fluid Dynamics, 1987.

62. Anderson, D.A., Tannehill, J.C., and Pletcher, R.H. Computational Fluid Mechanics and Heat Transfer, Hemisphere Publishing Co., New York, 1984.

63. Baliga, B.R., Pham, T.T., and Patankar, S.V., "Solution of Some Two-Dimensional Incompressible Fluid Flow and Heat Transfer Problems Using a Control Volume Finite Element Method", Numerical Heat Transfer, v.6, pp.263-282, 1983.

64. Prakash, C., "An Improved Control Volume Finite Element Method for Heat and Mass Transfer and for Fluid Flow Using Equal-Order Velocity-Pressure Interpolation", Numerical Heat Transfer, v.9, pp.253-276, 1986.

65. Karimian, S.M.H., and Schneider, G.E. "Application of a New Control-Volume-Based Finite-Element Formulation to the Shock Tube Problem",

AIAA Paper 94-0131, 32nd Aerospace Sciences Meeting & Exhibit, Reno, January 10-13, 1994.

66. Patankar, N.S., "Private Communications", Banff, Alberta, June 1995.

67. Raithby, G.D., "A Critical Evaluation of Upstream Differencing Applied to Problems Involving Fluid Flow" Computer Methods in Applied Mechanics and Engineering, v.9, pp. 75-103, 1971.

68. Raithby, G.D., "Skew Upstream Differencing Schemes for Problems Involving Fluid Flow" Computer Methods in Applied Mechanics and Engineering, v.9, pp. 153-164, 1976.

69. Schneider, G.E., and Raw, M.J., "A Skewed Positive Influence Coefficient Upwinding procedure for Control-Volume-Based Finite-Element Convection-Diffusion Computation", Numerical Heat Transfer, v.8, pp.1-26, 1986.

70. Chu, E., George, A., Liu, J., and Ng, E. "SPARSPAK; Waterloo Sparse Matrix Package; User's Guide for SPARSPAK-A", Research Report CS-84-36, University of Waterloo, Department of Computer Science, Waterloo, Ontario, November 1984.

71. Minkowycz, W.J., Sparrow, E.M., Schneider, G.E., and Pletcher, R.H. "<u>Handbook of Numerical Heat Transfer</u>", John Wiley & Sons, New York, pp.379-421, 1988.

72. Ghia, U., Ghia, K.N., and Shin, C.T., "High-Re Solutions for Incompressible Flow Using the Navier-Stokes Equations and a Multigrid Method", Journal of Computational Physics, v.48, pp.387-411, 1982.

73. Darbandi, M., and Schneider, G.E. "A Study of the Overshoots of the Entrance Flow Using Control Volume Method", The Proceedings of the

Fourth Annual Conference of the CFD of Society of Canada, Ottawa, Ontario, Canada, June 2-6, pp.219-227, 1996.

74. Shah, R.K., and London. A.L., "Laminar Flow Forced Convection in Ducts", Academic Press, New York, 1978.

75. Morihara, H., and Cheng, R.T., "Numerical Solution of Viscous Flow in the Entrance Region of Parallel Plates", Journal of Computational Physics, v.11, pp.550-572, 1973.

76. Abarbanel, S., Bennet, A., Brandt, A., and Gillis, J., "Velocity Profiles of Flow at Low Reynolds Numbers", Journal of Applied Mechanics, v.37, pp.2-4, 1970.

77. Li, L.C., and Ludford, G.S.S., "The Overshoot in Entry Flow", Archives of Mechanics, v.32, pp.741-746, 1980.

78. Burke, T.P., and Berman, N.S., "Entrance Flow Development in Circular Tubes at Small Axial Distances", American Society of Mechanical Engineers, Paper 69-WA/FE-13, 1969.

79. Berman, N.S., and Santos, V.A., "Laminar Velocity Profiles in Developing Flows Using a Laser Doppler Technique", AICHE Journal, v.15, pp.323-327, 1969.

80. Berman, N.S., "Private Communications", Arizona State University, Tempe, Arizona, March 1996.

81. AbdulNour, B.S., and Potter, M.C. "A Stable, Iterative Finite-Difference Procedure for the Navier-Stokes Equations", ASME Fluids Engineering Division (Publication) FED v.93, Published by ASME, New York, pp.15-19, 1990.

82. Narang, B.S., and Krishnamoorthy, G., "Laminar Flow in Entrance Region of Parallel Plates", Journal of Applied Mechanics, v.43, pp.186-188, 1976.

83. Nguyen, T.V., and Maclaine-Cross, I.L., "Incremental Pressure Drop Number in Parallel-Plate Heat Exchangers", Journal of Fluids Engineering, v.110, pp.93-96, 1988.

84. Van Dyke, M., "Entry Flow in a Channel", Journal of Fluid Mechanics, v.44, pp.813-823, 1970.

85. Mcdonald, J.W., V.E., Denny, and Mills, A.F., "Numerical Solutions of the Navier-Stokes Equations in Inlet Region", Journal of Applied Mechanics, v.39, pp.873-878, 1972.

86. Ramos, J.I., and Winowich, N.S., "Finite Difference and Finite Element Methods for MHD Channel Flows", International Journal for Numerical Methods in Fluids, v.11, pp.907-934, 1990.

87. AbdulNour, B.S., "A Numerical Simulation for a Plane Viscous Entry Flow Problem", Proceedings of the ASME International Computers in Engineering Conference and Exposition, Boston, Aug. 5-9, v.2, pp.481-486, 1990.

88. Carvalho, T.M.B., Cotta, R.M., and Mikhailov, M.D., "Flow Development in Entrance Region of Ducts", Communications in Numerical Methods in Engineering, v.9, pp.503-509, 1993.

89. Zucrow, M.J., and Hoffman, J.D., Gas Dynamics; Volume I, John Wiley & Sons, Inc., New York, 1976.

90. Oswatitsch, K., and Rothstein, W., "Flow Patterns in a Converging-Diverging Nozzle", NACA TM No. 1215, 1949.

91. Karki, K.C., A Calculation Procedure for Viscous Flows at All Speeds in Complex Geometries, Ph.D. Thesis, University of Minnesota, Minneapolis, MN, 1986.

92. Eidelman, S., Colella P., and Shreeve, R.P., "Application of the Gudnov Method and Its Second-Order Extension to Cascade Flow Modeling", AIAA Journal, v.22, pp.1609-1615, 1984.

93. Ni, R.H., "A Multiple-Grid Scheme for Solving the Euler Equations", AIAA Journal, v.20, pp.1565-1571, 1982.

94. Karimian, S.M.H., "Private Communications", Amir Kabir University of Technology, Tehran, Iran, September 1996.

Appendix A

Element Geometric Relations

In this Appendix, after the introduction, we first discuss the discretization of solution domain into a number of elements using finite-element discretization. Next, the details of elemental geometric relations are presented. They provide necessary geometrical transformations between local and global coordinates are derived.

A.1 Introduction

Before discretizing the governing equations, it is necessary to discretize the calculation domain in some fashion. In the past two decades, different techniques have been developed for generating computational grids required in the finite-difference or finite element solutions of partial differential equations on arbitrary regions. Stability of the method, convergence speed, and accuracy of the solution are aspects which could be affected by choosing inappropriate grids. A poorly chosen grid may cause results to be erroneous or may fail to reveal critical aspects of the true solution.

Generally speaking, the accuracy of finite-difference methods is increased if the underlying mesh fits the region boundaries and is closely spaced in regions where the solution is rapidly varying. Transformation from orthogonal coordinate system to either non-orthogonal or orthogonal boundary-fitted coordinates will ensure the exact boundary fitting and arbitrary grid concentrating; however, this may cause more complexity in differential equations which need more numerical works, e.g. Alishahi and Darbandi [15]. Contrary to finite-difference method, there is finite-element method which has been widely selected for discretizing the solution domain because it is capable of modeling quite arbitrary and irregular geometries and has long been used to solve problems with complex geometries very successfully. No global topology or orthogonality restrictions is required for finite-element grid. Boundaries are automatically fitted and there is no restriction in concentrating the grid. Besides the finite-element and finite-difference methods, there are the control-volume approaches which have the advantage of providing a conservative discretization of the governing equations. Those approaches allow exact numerical conservation of the conserved quantities in each finite control volume.

A.2 Finite-Element Discretization

In the finite-element method, the solution domain is broken into a number of subregions which are called elements, Fig.A.1. The vertices of the element are nodal locations of the domain. They are the location of the problem unknowns. Different element shapes are used in finite-element method. Regarding the simplicity and economy of the solution, quadrilateral elements have been selected in this study.

In Fig.A.2, a single element is separated from the other elements in order to expand the finite-element relations for it. As seen, there are two coordinate systems, a global orthogonal coordinate system of (x,y) and a local non-orthogonal coordinate system of (ξ,η). The ranges of ξ and η are from -1 to $+1$ within the element. This local coordinate system permits each element to be treated individually and identically despite its shape, position, and location. In order to use the benefits of

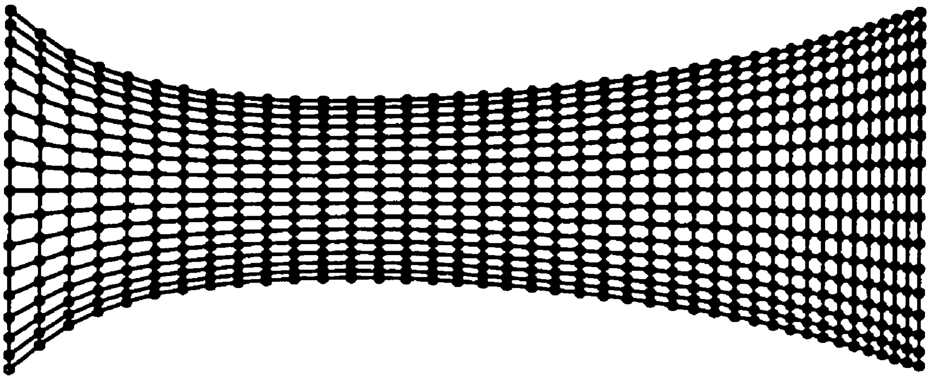

Figure A.1: Finite-element discretization within a nozzle domain.

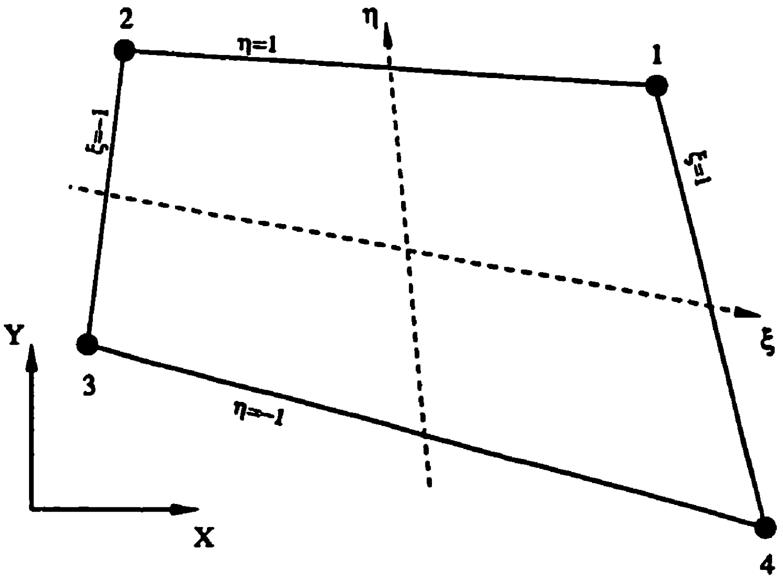

Figure A.2: An isolated element.

local system, it is necessary to relate local and global coordinates. Finite-element shape functions, N_i with i=1...4, are used to connect them, i.e.

$$x(\xi,\eta) = \sum_{i=1}^{4} N_i(\xi,\eta) \;\; x_i \tag{A.1a}$$

$$y(\xi,\eta) = \sum_{i=1}^{4} N_i(\xi,\eta) \;\; y_i \tag{A.1b}$$

where x_i and y_i are the coordinates of node i. In this study, we use bilinear shape-functions which are defined by

$$N_1(\xi,\eta) = \frac{1}{4}(1+\xi)(1+\eta) \tag{A.2a}$$

$$N_2(\xi,\eta) = \frac{1}{4}(1-\xi)(1+\eta) \tag{A.2b}$$

$$N_3(\xi,\eta) = \frac{1}{4}(1-\xi)(1-\eta) \tag{A.2c}$$

$$N_4(\xi,\eta) = \frac{1}{4}(1+\xi)(1-\eta) \tag{A.2d}$$

A.3 Local-Global Coordinate Transformation

The procedure of the discretization of the governing equations requires several differentiations and integrations to be performed within an element. Simple connection presented in Eq.(A.2) does not provide enough device to do that. In order to develop our local-global transformations we, start with differentiation of the dependent variable ϕ as

$$\left.\frac{\partial \phi}{\partial x}\right|_{\xi,\eta} = \sum_{i=1}^{4} \left.\frac{\partial N_i}{\partial x}\right|_{\xi,\eta} \phi_i \tag{A.3a}$$

$$\left.\frac{\partial \phi}{\partial y}\right|_{\xi,\eta} = \sum_{i=1}^{4} \left.\frac{\partial N_i}{\partial y}\right|_{\xi,\eta} \phi_i \tag{A.3b}$$

Since $\frac{\partial N_i}{\partial x}$ and $\frac{\partial N_i}{\partial y}$ are not known the chain rule is used to convert them to suitable form

$$\frac{\partial N_i}{\partial \xi} = \frac{\partial N_i}{\partial x}\frac{\partial x}{\partial \xi} + \frac{\partial N_i}{\partial y}\frac{\partial y}{\partial \xi} \tag{A.4a}$$

$$\frac{\partial N_i}{\partial \eta} = \frac{\partial N_i}{\partial x}\frac{\partial x}{\partial \eta} + \frac{\partial N_i}{\partial y}\frac{\partial y}{\partial \eta} \tag{A.4b}$$

Here all terms are known except $\frac{\partial N_i}{\partial x}$ and $\frac{\partial N_i}{\partial y}$ terms. Thus, we transform them into the following matrix structure

$$\left(\begin{array}{c} \frac{\partial N_i}{\partial \xi} \\ \frac{\partial N_i}{\partial \eta} \end{array} \right) = \left[\begin{array}{cc} \frac{\partial x}{\partial \xi} & \frac{\partial y}{\partial \xi} \\ \frac{\partial x}{\partial \eta} & \frac{\partial y}{\partial \eta} \end{array} \right] \left(\begin{array}{c} \frac{\partial N_i}{\partial x} \\ \frac{\partial N_i}{\partial y} \end{array} \right) \tag{A.5}$$

the solution of which is

$$\left(\begin{array}{c} \frac{\partial N_i}{\partial x} \\ \frac{\partial N_i}{\partial y} \end{array} \right) = \frac{1}{J} \left[\begin{array}{cc} \frac{\partial y}{\partial \eta} & -\frac{\partial y}{\partial \xi} \\ -\frac{\partial x}{\partial \eta} & \frac{\partial x}{\partial \xi} \end{array} \right] \left(\begin{array}{c} \frac{\partial N_i}{\partial \xi} \\ \frac{\partial N_i}{\partial \eta} \end{array} \right) \tag{A.6}$$

where J is the Jacobian of transformation and is defined by

$$J = \frac{\partial x}{\partial \xi}\frac{\partial y}{\partial \eta} - \frac{\partial y}{\partial \xi}\frac{\partial x}{\partial \eta} \tag{A.7}$$

Equation (A.6) is used to derive $\frac{\partial N}{\partial x}$ and $\frac{\partial N}{\partial y}$ forms as a function of $\frac{\partial N}{\partial \xi}$ and $\frac{\partial N}{\partial \eta}$ forms in the following manner. Initially, the following differential forms are obtained from Eq.(A.1) as

$$\begin{array}{ll} \frac{\partial x}{\partial \xi} = \sum_{i=1}^{4} \frac{\partial N_i}{\partial \xi} x_i & \frac{\partial x}{\partial \eta} = \sum_{i=1}^{4} \frac{\partial N_i}{\partial \eta} x_i \\ \frac{\partial y}{\partial \xi} = \sum_{i=1}^{4} \frac{\partial N_i}{\partial \xi} y_i & \frac{\partial y}{\partial \eta} = \sum_{i=1}^{4} \frac{\partial N_i}{\partial \eta} y_i \end{array} \tag{A.8}$$

Next, shape function derivatives with respect to ξ and η are derived from Eq.(A.2), i.e.,

$$\begin{array}{ll} \frac{\partial N_1}{\partial \xi} = \frac{1}{4}(1+\eta) & \frac{\partial N_1}{\partial \eta} = \frac{1}{4}(1+\xi) \\ \frac{\partial N_2}{\partial \xi} = -\frac{1}{4}(1+\eta) & \frac{\partial N_2}{\partial \eta} = \frac{1}{4}(1-\xi) \\ \frac{\partial N_3}{\partial \xi} = -\frac{1}{4}(1-\eta) & \frac{\partial N_3}{\partial \eta} = -\frac{1}{4}(1-\xi) \\ \frac{\partial N_4}{\partial \xi} = \frac{1}{4}(1-\eta) & \frac{\partial N_4}{\partial \eta} = -\frac{1}{4}(1+\xi) \end{array} \tag{A.9}$$

This completes the process of computing $\frac{\partial N}{\partial x}$ and $\frac{\partial N}{\partial y}$ forms.

In the next step, we pay attention to the process of integration over an arbitrary sub-domain $\xi = 0 \rightarrow \xi_1$ and $\eta = 0 \rightarrow \eta_1$. If the vector $\vec{r}$ is defined as

$$\vec{r} = x\hat{i} + y\hat{j} \tag{A.10}$$

its differential form is given by

$$d\vec{r} = \frac{\partial \vec{r}}{\partial \xi} d\xi + \frac{\partial \vec{r}}{\partial \eta} d\eta \tag{A.11}$$

The area or the volume per unit depth of this sub-domain is calculated by the product of $d\vec{\xi}$ and $d\vec{\eta}$, i.e.,

$$d\mathcal{V} = \mid d\vec{\xi} \times d\vec{\eta} \mid \tag{A.12}$$

or

$$d\mathcal{V} = \left| \frac{\partial \vec{r}}{\partial \xi} \times \frac{\partial \vec{r}}{\partial \eta} \right| d\xi \; d\eta \tag{A.13}$$

Considering Eq.(A.7), this equation is simplified to

$$d\mathcal{V} = \mid J \mid d\xi \; d\eta \tag{A.14}$$

The integration over the defined domain will yield

$$\mathcal{V} = \int_0^{\xi_1} \int_0^{\eta_1} \mid J \mid d\xi \; d\eta = \mid J \mid_{(\frac{\xi_1}{2}, \frac{\eta_1}{2})} \tag{A.15}$$

Appendix B

Density Linearization

Since density is not a major dependent variable it is necessary to connect it to the other major dependent variables. This variable appears in many terms of the governing equations and their discretized forms, e.g. the transient terms. The density in incompressible flow is constant and needs no treatment. There is no difficulty for computing the density if it is a lagged value. However, the density needs treatment whenever it appears as an unknown in our equations in compressible flow. The appropriate connection is provided by the equation of state and specifically the ideal gas law

$$\varrho = \frac{P}{RT} \tag{B.1}$$

As seen, the density is a function of both pressure and temperature. A simple linearization for this equation is provided by considering an active role for P and a lagged for T as

$$\varrho = \frac{1}{R\tilde{T}} P \tag{B.2}$$

This form of linearization is excellent for the compressible flows with isothermal assumptions. The overline denotes a lagged value from the previous inner/outer iterations. Another method of treatment is to employ a Taylor series expansion which considers active roles for both P and T. It is given by

$$\varrho = \bar{\varrho} + \overline{\frac{\partial \varrho}{\partial P}}(P - \bar{P}) + \overline{\frac{\partial \varrho}{\partial T}}(T - \bar{T}) \tag{B.3}$$

The density differential forms are derived from Eq.(B.1), i.e.,

$$\overline{\frac{\partial \varrho}{\partial P}} = \frac{1}{R\bar{T}} \qquad \overline{\frac{\partial \varrho}{\partial T}} = -\frac{\bar{P}}{R\bar{T}^2} \tag{B.4}$$

Now, these expressions are substituted in Eq.(B.3) and the results are simplified to

$$\varrho = \bar{\varrho} + \frac{1}{R\bar{T}}\, P - \frac{\bar{P}}{R\bar{T}^2}\, T \tag{B.5}$$

This linearization is similar to a Newton-Raphson linearization, Anderson et al [62]. In this form of linearization, a nonlinear product of two parameters of A and B is linearized to

$$AB = \bar{B}A + \bar{A}B - \overline{AB} \tag{B.6}$$

This form of linearization is called many times during this thesis.

Appendix C

Linearization of Momentum Convections

Before presenting the different possible linearizations for the nonlinear convection terms of the momentum equations, it is necessary to have an introduction to the concept of the individual elements in those terms. These terms need to be studied more carefully than the other terms because two different concepts could be defined for those individuals.

To expand those concepts, it is helpful to recall the method of derivation of those terms in the momentum equations. White [57] presents the basic differential equations by considering an elemental control volume, Figure C.1. The balance of the mass and the convection part of the linear-momentum conservation equations could be written for this infinitesimal fixed control volume as

$$\sum_i (\rho S V_n)_i \Big|_{out} - \sum_i (\rho S V_n)_i \Big|_{in} = 0 \qquad \text{(C.1)}$$

$$\sum \vec{\mathbf{R}} = \sum_i (\dot{m}_i \vec{V}_i)_{out} - \sum_i (\dot{m}_i \vec{V}_i)_{in} \qquad \text{(C.2)}$$

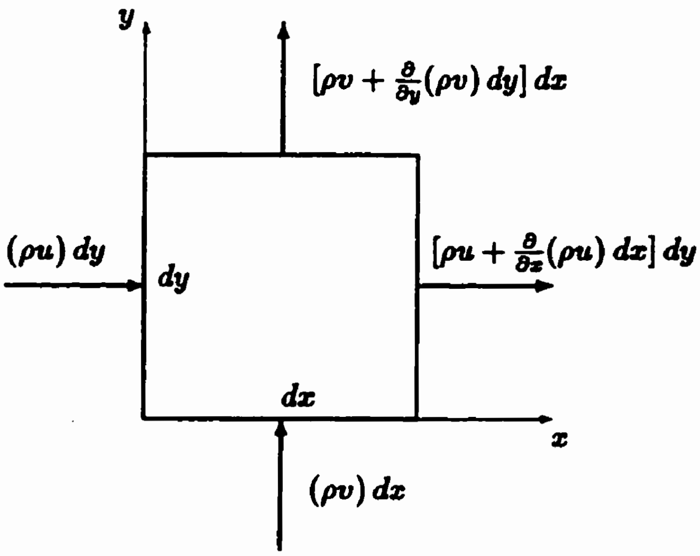

Figure C.1: A control volume showing inlet and outlet mass flows on the x faces.

where dx and dy present the control volume dimensions and S indicates the area of each control surface. Table C.1 presents the mass and momentum fluxes through the control volume faces. If these terms are plugged in Eq.(C.1) and Eq.(C.2) the results after some simplifications are given by

$$\frac{\partial}{\partial x}(\rho u) + \frac{\partial}{\partial y}(\rho v) = 0 \tag{C.3}$$

$$\frac{1}{dx\,dy}\sum \vec{\mathbb{R}} = \frac{\partial}{\partial x}(\rho u \vec{V}) + \frac{\partial}{\partial y}(\rho v \vec{V}) \tag{C.4}$$

As is seen, the velocity components appear in two positions in each term of Eq.(C.4), either as a part of the mass flux components or as a velocity components. This causes two different meanings for these two velocities. The velocity components which appear in the mass flux components are named *convecting velocities* or *mass conserving velocities*. This name returns to Eq.(C.3) where these velocity components numerically satisfy the mass conservation equation. They convect $\vec{V}$

Faces	Inlet mass flux	Outlet mass flux
x	$\rho u\, dy$	$[\rho u + \frac{\partial}{\partial x}(\rho u)\, dx]\, dy$
y	$\rho v\, dx$	$[\rho v + \frac{\partial}{\partial y}(\rho v)\, dy]\, dx$
Faces	**Inlet momentum flux**	**Outlet momentum flux**
x	$\rho u \vec{V}\, dy$	$[\rho u \vec{V} + \frac{\partial}{\partial x}(\rho u \vec{V})\, dx]\, dy$
y	$\rho v \vec{V}\, dx$	$[\rho v \vec{V} + \frac{\partial}{\partial y}(\rho v \vec{V})\, dy]\, dx$

Table C.1: Mass and linear momentum fluxes for control volume in Figure C.1.

through the control volume. On the other hand, the components of $\vec{V}$ in Eq.(C.4) are called *convected velocities*. These velocities are convected by the mass fluxes through the control volume surfaces. In order to distinguish these two types of velocities, The convecting is identified by a hat ($\hat{}$). Now, we can expand Eq.(C.4) in x and y directions while their original concepts are retained

$$x-\text{direction} \qquad \frac{1}{dx\, dy}\mathbf{R}_x = \frac{\partial}{\partial x}(\rho \hat{u}\ u) + \frac{\partial}{\partial y}(\rho \hat{v}\ u) \tag{C.5a}$$

$$y-\text{direction} \qquad \frac{1}{dx\, dy}\mathbf{R}_y = \frac{\partial}{\partial x}(\rho \hat{u}\ v) + \frac{\partial}{\partial y}(\rho \hat{v}\ v) \tag{C.5b}$$

It is worthful to note that an arbitrary switch from convected to convecting or from convecting to convected may destruct the original concepts which derivation of the equations are based on.

Generally speaking, we study two different forms of the linearization for the convection terms of the momentum equations. At this stage, we are concerned with the equations which are derived based on control volume discretization. Table 2.1 shows the result of simple linearization of the convection terms of the momentum equations which are repeated here with considering the above concepts

$$\rho\hat{u}\ u \approx \bar{\hat{u}}(\rho u) \tag{C.6a}$$

$$\rho\hat{v}\ u \approx \bar{\hat{v}}(\rho u) \tag{C.6b}$$

$$\rho\hat{u}\ v \approx \bar{\hat{u}}(\rho v) \tag{C.6c}$$

$$\rho\hat{v}\ v \approx \bar{\hat{v}}(\rho v) \tag{C.6d}$$

A second form of linearization is possible using a Newton-Raphson linearization rule, Eq.(B.6). This linearization considers more active roles for the individuals in the nonlinear term. We show the procedure for the linearization of the ρuu term which is linearized in the following manner

$$\rho\hat{u}\ u = \hat{u}\ (\rho u) \approx \bar{\hat{u}}\ (\rho u) + (\overline{\rho u})\ \hat{u} - \overline{\rho u\hat{u}} \tag{C.7}$$

Since $\hat{u}$ is not a major unknown in this study, one more Newton-Raphson linearization is used for $u = \frac{\rho u}{\rho}$, i.e.,

$$\hat{u} = \frac{(\rho\hat{u})}{\rho} \approx \frac{1}{\bar{\rho}}\ (\rho\hat{u}) - \frac{\bar{\hat{u}}}{\bar{\rho}}\ \rho + \bar{\hat{u}} \tag{C.8}$$

If Eq.(C.8) is plugged in Eq.(C.7) and some more simplifications are done the result is

$$\rho\hat{u}\ u \approx \bar{\hat{u}}\ (\rho u) + \bar{u}\ (\rho\hat{u}) - \overline{u\hat{u}\rho} \tag{C.9}$$

This linearization results in active roles for both convected and convecting velocities as well as density in x-momentum equation term. The density term is simply computed by the lagged values from the previous iterations. Considering this approximation and the definition of momentum components, we define a general equation in order to include both form of the simple and Newton-Raphson linearizations, i.e. Eq.(C.6) and Eq.(C.9),

$$\rho\hat{u}\ u \approx \bar{\hat{u}}\ f + k'(\bar{u}\ \hat{f} - \overline{u\hat{u}\rho}) \tag{C.10}$$

where k'=0 results in simple linearization and k'=1 represent Newton-Raphson linearization. This procedure could be similarly followed for the three other convection terms in the momentum equations. The results will be

$$\rho\hat{v}\ u \approx \bar{\hat{v}}\ f + k'(\bar{u}\ \hat{g} - \overline{u\hat{v}\rho}) \tag{C.11}$$

$$\rho\hat{u}\ v \approx \bar{\hat{u}}\ g + k'(\bar{v}\ \hat{f} - \overline{v\hat{u}\rho}) \tag{C.12}$$

$$\rho\hat{v}\ v \approx \bar{\hat{v}}\ g + k'(\bar{v}\ \hat{g} - \overline{v\hat{v}\rho}) \tag{C.13}$$

Eq.(C.10) was tested in the one-dimensional investigation with success. It generally showed better results than the simple linearization.

One more form of linearization was tested in the one-dimensional investigations. In this form the two concepts of convected and convecting were mixed up and the following linearization was derived,

$$\rho\hat{u}\ u \approx 2k'\ \bar{\hat{u}}\ f - k''\ \overline{\hat{u}^2\rho} \tag{C.14}$$

where k' and k'' are constants which make the two linearizations possible. The consideration of k'=k''=1 results in Newton-Raphson linearization and the consideration of $k'=\frac{1}{2}$ and k''=0 results in a simple linearization form. This form of linearization generally showed faster convergence than the previous ones.

The discussion in this appendix is important in colocated grid formulation where the decoupling of pressure and velocity fields may happen.

Appendix D

Linearization of Momentum Diffusion Terms

The terms involving the differential form of velocity components, i.e. $\frac{\partial u}{\partial x}$, $\frac{\partial u}{\partial y}$, $\frac{\partial v}{\partial x}$, and $\frac{\partial v}{\partial y}$ terms, are nonlinear if the momentum components are selected as the dependent variables. There are methods to linearize these nonlinearities. Here, we present the result of linearization only for $\frac{\partial u}{\partial x}$ with this knowledge that the other three forms are linearized in the same manner. The first method uses the advantages of the chain rule to derive an appropriate expression for $\frac{\partial u}{\partial x}$ as

$$\frac{\partial}{\partial x}(\rho u) = \rho\frac{\partial u}{\partial x} + u\frac{\partial \rho}{\partial x} \tag{D.1}$$

Rearrangement of this expression yields

$$\frac{\partial u}{\partial x} = \frac{1}{\bar{\rho}}\frac{\partial f}{\partial x} - \frac{\bar{u}}{\bar{\rho}}\frac{\partial \rho}{\partial x} \tag{D.2}$$

The nonlinear density variable, which is derived by the spatial discretization of the second term in the right-hand-side of the equation, could either be linearized using the methods presented in Appendix B or be lagged from the known values of the previous iterations. The latter has been chosen to treat the above density term throughout this thesis.

In the second method, the second term in right-hand-side of Eq.(D.2) is replaced by

$$\frac{\partial u}{\partial x} = \frac{1}{\bar{\rho}}\frac{\partial f}{\partial x} + f\frac{\partial}{\partial x}\left(\frac{1}{\rho}\right) \tag{D.3}$$

The next step is to linearize this term as

$$\frac{\partial u}{\partial x} = \frac{1}{\bar{\rho}}\frac{\partial f}{\partial x} + \overline{\frac{\partial}{\partial x}\left(\frac{1}{\rho}\right)}\, f \tag{D.4}$$

This form of linearization was not used in this thesis.

Appendix E

Convection in Non-conservative Momentum

The following investigation was performed for two terms of the one-dimensional momentum equation, i.e. $\rho u \frac{\partial u}{\partial x}$ and $u \frac{\partial(\rho u)}{\partial x}$. This investigation presents the possible weak forms of discretization for the above terms. One method for linearizing $\rho u \frac{\partial u}{\partial x}$ term in the momentum equation is the use of lagged values for $\frac{\partial u}{\partial x}$. This results in a direct transfer of this term to left hand side of the integration point equation. This form of linearization is studied for the steady-state Euler flow which is derived from Eq.(3.21) and linearized as

$$\bar{u}_e \frac{\partial f}{\partial x} + \overline{\frac{\partial u}{\partial x}} f_e + \frac{\partial p}{\partial x} = 0 \tag{E.1}$$

A central difference for $\frac{\partial f}{\partial x}$ will result in

$$f_e = \left. \frac{\bar{u}}{\Delta x \overline{\frac{\partial u}{\partial x}}} \right|_e [F_P - F_E] - \left[\overline{\frac{\partial u}{\partial x}} \right]_e^{-1} \left. \frac{\partial p}{\partial x} \right|_e \tag{E.2}$$

The investigation for a constant pressure field shows that this equation results in a wrong approximation for the integration point value.

In the next step, an upwind difference is considered for $\frac{\partial f}{\partial x}$ in Eq.(E.1). Now, if $\overline{\frac{\partial u}{\partial x}}$ is approximated by an upwind difference, the result is written as

$$f_e = \left[1 + \frac{\bar{U}_E - \bar{U}_P}{2\bar{u}}\right]_e^{-1} F_P + \left[\overline{\frac{\partial u}{\partial x}} + \frac{2\bar{u}}{\Delta x}\right]_e^{-1} \left.\frac{\partial p}{\partial x}\right|_e \tag{E.3}$$

and a central difference for $\overline{\frac{\partial u}{\partial x}}$ will result in

$$f_e = \left[2 - \frac{\bar{U}_P}{\bar{u}}\right]_e^{-1} F_P + \left[\overline{\frac{\partial u}{\partial x}} + \frac{2\bar{u}}{\Delta x}\right]_e^{-1} \left.\frac{\partial p}{\partial x}\right|_e \tag{E.4}$$

Similarly, the investigation for a constant pressure field shows that these two approximations are not appropriate approximations do result in wrong evaluations of the integration point values. Indeed, both of them are subject to negative or infinite coefficients for F_P.

Similarly, Equation (3.21) is recalled with the assumption of the steady-state inviscid flow in order to expand the investigation for $u\frac{\partial f}{\partial x}$ term of that equation,

$$\bar{u}_e \frac{\partial f}{\partial x} + \bar{f}_e \frac{\partial u}{\partial x} + \frac{\partial p}{\partial x} = 0 \tag{E.5}$$

A central difference for $\frac{\partial f}{\partial x}$ and an upwind difference for $\frac{\partial u}{\partial x}$ will finally result in

$$f_e = F_P + \frac{1}{2}[F_P - F_E] - \left[\frac{\Delta x}{2\bar{u}} \frac{\partial p}{\partial x}\right]_e \tag{E.6}$$

This expression also presents a wrong approximation for the integration point value. The correct approximation for the velocity at the integration point would be the average of the neighboring nodal velocity values if the pressure field is constant.

Appendix F

Linearization of Energy Transient Term

There are a number of techniques to deal with the nonlinear transient term of the energy equation in conservative treatment. In all cases the original form of this term is discretized by mass lumped approach and using backward scheme in time,

$$\frac{\partial(\rho e)}{\partial\theta} \approx \frac{1}{\Delta\theta}(\varrho E - \varrho^{o}E^{o}) \tag{F.1}$$

Here, the concern is on the nonlinear form of the first term inside the parenthesis. A simple way to linearize this term is to substitute E from Eq.(2.13) and try to linearize the equation appropriately as

$$\frac{\partial(\rho e)}{\partial\theta} \approx \frac{\bar{U}}{2\Delta\theta}F + \frac{\bar{V}}{2\Delta\theta}G + \frac{\bar{\varrho}c_v}{\Delta\theta}T - \frac{\varrho^{o}E^{o}}{\Delta\theta} \tag{F.2}$$

The other form of linearization is derived by the use of the Newton-Raphson linearization scheme, Eq.(B.6),

$$\varrho E \approx \bar{\varrho}E + \bar{E}\varrho - \overline{\varrho\bar{E}} \tag{F.3}$$

In this form, ϱ is substituted from Eq.(B.5) and E is treated as

$$E \approx c_v T + \frac{\bar{U}}{2\bar{\varrho}}F + \frac{\bar{V}}{2\bar{\varrho}}G \tag{F.4}$$

After the substitution of these nonlinear treatments in Eq.(F.3) and some rearrangement, the following form is resulted

$$\frac{\partial(\rho e)}{\partial\theta} \approx \frac{\bar{E}}{R\bar{T}\Delta\theta}P + \frac{\bar{U}}{2\Delta\theta}F + \frac{\bar{V}}{2\Delta\theta}G - \frac{\bar{\varrho}(\bar{U}^2+\bar{V}^2)}{2\bar{T}\Delta\theta}T - \frac{\varrho^o E^o}{\Delta\theta} \tag{F.5}$$

This form of linearization produces negative coefficient for temperature and cannot be reliable.

Another form of linearization is possible if Eq.(F.1) is treated in another form as

$$\frac{\partial(\rho e)}{\partial\theta} \approx \frac{\bar{U}}{2\Delta\theta}F + \frac{\bar{V}}{2\Delta\theta}G + \frac{c_v}{\Delta\theta}(\varrho T) - \frac{\varrho^o E^o}{\Delta\theta} \tag{F.6}$$

Similar to Eq.(F.3), nonlinear form of ϱT is changed to $\varrho\bar{T} + \bar{T}\varrho - \overline{\varrho T}$ and ϱ is linearized by Eq.(B.5) and is substituted in it. The final result is given by

$$\frac{\partial(\rho e)}{\partial\theta} \approx \frac{c_v}{R\Delta\theta}P + \frac{\bar{U}}{2\Delta\theta}F + \frac{\bar{V}}{2\Delta\theta}G - \frac{\varrho^o E^o}{\Delta\theta} \tag{F.7}$$

which does not include T term. This form was not used in this work.

Appendix G

Linearization of Energy Convection Terms

Regarding the conservative treatment of the convection terms in the energy equation, a number of approaches is applicable. The two convection terms can be written either in the enthalpy form $\frac{\partial(\rho uh)}{\partial x} + \frac{\partial(\rho vh)}{\partial y}$ or in the energy form $\frac{\partial(\rho ue+up)}{\partial x} + \frac{\partial(\rho ve+vp)}{\partial y}$. Here we are concerned only on enthalpy form and restrict the approaches to two possible form of linearizations. In this study, the original concepts of convected and convecting, which were described in Appendix C, are respected. For example,

$$\rho uh = \rho\hat{u}(c_p t + \frac{u^2}{2} + \frac{v^2}{2}) \tag{G.1}$$

The first linearization approach uses the definition of h, Eq.(2.14), and substitutes it directly in convection term. The remainder is to linearize the resulted expressions appropriately respect to the dependent variables,

$$\rho uh \approx \frac{\bar{\hat{u}}\bar{u}}{2}\, f + \frac{\bar{\hat{u}}\bar{v}}{2}\, g + c_p\bar{\rho}\bar{\hat{u}}\ t \tag{G.2a}$$

$$\rho vh \approx \frac{\bar{\hat{v}}\bar{u}}{2}\, f + \frac{\bar{\hat{v}}\bar{v}}{2}\, g + c_p\bar{\rho}\bar{\hat{v}}\ t \tag{G.2b}$$

If the concept of convected and convecting is not respected these equations are written as

$$\rho uh \approx \frac{\bar{u}}{2}(\bar{u}\ f + \bar{v}\ g + 2c_p\bar{\rho}\ t) \tag{G.3a}$$

$$\rho vh \approx \frac{\bar{v}}{2}(\bar{u}\ f + \bar{v}\ g + 2c_p\bar{\rho}\ t) \tag{G.3b}$$

A second linearization uses the Newton-Raphson scheme, i.e. Eq.(B.6), to linearize these convection terms. It is given by

$$\rho uh \approx \bar{f}h + \bar{h}f - \overline{hf} \tag{G.4a}$$

$$\rho vh \approx \bar{g}h + \bar{h}g - \overline{hg} \tag{G.4b}$$

Using the definition of enthalpy, substituting it in above equations, and treating them in an appropriate manner would result in

$$\rho uh \approx \frac{\bar{\hat{u}}\bar{u}}{2}\ f + \bar{h}\ \hat{f} + \frac{\bar{\hat{u}}\bar{v}}{2}\ g + c_p\bar{\hat{f}}\ t - \overline{hf} \tag{G.5a}$$

$$\rho vh \approx \frac{\bar{\hat{v}}\bar{u}}{2}\ f + \bar{h}\ \hat{g} + \frac{\bar{\hat{v}}\bar{v}}{2}\ g + c_p\bar{\hat{g}}\ t - \overline{hg} \tag{G.5b}$$

Ignoring the concepts of convecting and convected results in

$$\rho uh \approx (\frac{\bar{u}^2}{2} + \bar{h})\ f + \frac{\bar{u}\bar{v}}{2}\ g + c_p\bar{f}\ t - \overline{hf} \tag{G.6a}$$

$$\rho vh \approx \frac{\bar{v}\bar{u}}{2}\ f + (\frac{\bar{v}^2}{2} + \bar{h})\ g + c_p\bar{g}\ t - \overline{hg} \tag{G.6b}$$

All lagged values of these equations can be calculated from the previous iterations by using the known values of either convected or convecting variables.

Appendix H

Streamwise Discretization Approach

In two-dimensional flows, the direction of the flow has an important role in discretizing some differential terms of the governing equations. In a one-dimensional flow, grid lines and flow direction are coincident, however, this is not the case for the two-dimensional flows. The importance of the flow direction is in evaluating some differential terms in streamwise direction. The inconsistency between grid lines and flow directions does not allow discretization in streamwise direction. Fortunately, convection differential terms which are sensible to flow direction could be combined and written in streamwise direction as

$$\vec{\mathbf{V}} \,.\, \nabla\phi \equiv u\frac{\partial\phi}{\partial x} + v\frac{\partial\phi}{\partial y} \tag{H.1}$$

These terms can be written in the local streamwise direction as

$$\rho u\frac{\partial\phi}{\partial x} + \rho v\frac{\partial\phi}{\partial y} = \rho V_{tot}\frac{\partial\phi}{\partial s} \tag{H.2}$$

where

$$V_{tot} = \sqrt{u^2 + v^2} \tag{H.3}$$

and

$$ds = \frac{u}{V_{tot}} dx + \frac{v}{V_{tot}} dy \tag{H.4}$$

Eq.(H.2) provides a straightforward differential form to be used for discretization in streamwise direction like streamwise upwinding, central-differencing, etc.

Appendix I

Laplacian Operator Discretization

The procedure of computing integration point expressions requires the discretization of the diffusion terms which may take Laplacian form. Finite element discretization of the nonlinear Laplacian form is not straightforward. Here, the approach was taken by Schneider [71] is followed. In this regard, consider the Laplacian of an scalar ϕ which is given by

$$L(\phi) = \nabla^2 \phi = \frac{\partial^2 \phi}{\partial x^2} + \frac{\partial^2 \phi}{\partial y^2} \tag{I.1}$$

Considering Fig.I.1, we can obtain some approximations for terms of Eq.(I.1) at integration point of 1 as

$$\left(\frac{\partial^2 \phi}{\partial x^2}\right)_{ip1} = \frac{1}{\Delta x}\left\{\frac{(\frac{3}{4}\Phi_1 + \frac{1}{4}\Phi_4) - \phi_1}{\Delta x} - \frac{\phi_1 - (\frac{3}{4}\Phi_2 + \frac{1}{4}\Phi_3)}{\Delta x}\right\} \tag{I.2a}$$

$$\left(\frac{\partial^2 \phi}{\partial y^2}\right)_{ip1} = \frac{1}{\Delta y}\left\{\frac{(\frac{1}{2}\Phi_1 + \frac{1}{2}\Phi_2) - \phi_1}{\frac{1}{2}\Delta y} - \frac{\phi_1 - (\frac{1}{2}\Phi_3 + \frac{1}{2}\Phi_4)}{\frac{3}{2}\Delta y}\right\} \tag{I.2b}$$

If these expressions are substituted in Eq.(I.1) the following expression will be resulted after some rearrangement

$$\nabla^2 \phi_{ip1} = \frac{\sum_{j=1}^{4} N_j \Phi_j - \phi_{ip1}}{(L_d^2)_i} \tag{I.3}$$

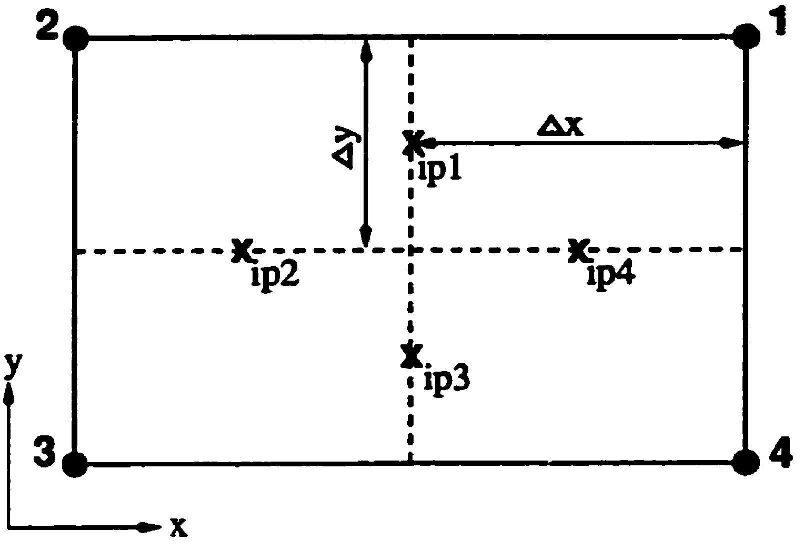

Figure I.1: Laplacian length scale.

Which the diffusion length scale is defined as

$$(L_d)_{ip1} = \left\{ \frac{2}{(\Delta x)^2} + \frac{8}{3(\Delta y)^2} \right\}_{ip1}^{-1} \tag{I.4}$$

As is observed, the derived approximation for the Laplacian Eq.(I.3) satisfactorily satisfy the limiting case of diffusion dominated flows. In another words, when

$$\nabla^2 \phi_{ip1} = 0 \tag{I.5}$$

Eq.(I.3) is reduced to the bilinear interpolation form of the nodal values, i.e.,

$$\phi_j = \sum_{j=1}^{4} N_j \Phi_j \tag{I.6}$$

Which is a correct approximation.

Eq.(I.3) was derived based on a rectangular element shape. However, it does not result in a correct approximation for general form of the quadrilateral finite elements which we use during this study. For a general form of elements, we use

Eq.(I.3) with a corrected L_d. Furthermore, Δx and Δy are replaced by the length scales perpendicular and tangential, respectively, to the face in question. This means Δy is considered as the length of the face in question and Δx is determined by,

$$\Delta x \rightarrow \frac{|J|}{\Delta y} \tag{I.7}$$

where $|J|$ is the magnitude of the Jacobian of transformation, Eq.(A.7).